UNIVERSITÀ
DEGLI STUDI
DI BRESCIA

DIPARTIMENTO DI INGEGNERIA MECCANICA E INDUSTRIALE

DOTTORATO DI RICERCA IN
TRANSIZIONE ENERGETICA E SISTEMI PRODUTTIVI SOSTENIBILI

SSD: **ING-IND/10** – Fisica Tecnica Industriale

CICLO
XXXVIII

REDUCED-ORDER MODELLING OF TRANSPORT PHENOMENA IN THIN-FILM FLOWS

Dottorando:
PAOLO BOTTICINI

Primo RELATORE: Prof. **DAVIDE PICCHI**

Primo CORRELATORE: Prof. **PIETRO POESIO**

Reduced-order modelling of transport phenomena in thin-film flows

Paolo Botticini

Thesis summary

Sommario

Questa tesi sviluppa modelli ad ordine ridotto per fenomeni di trasporto in flussi a film sottile, con particolare attenzione al trasferimento di calore e alla dinamica non lineare multifase, dal comportamento reologico in dominî porosi all'insorgenza di instabilità all'interfaccia. La ricerca si articola in quattro contributi complementari, che insieme delineano un quadro multiscala coerente vòlto ad far progredire la comprensione, sia teorica che applicata, del trasporto multifase. La logica di fondo risiede nell'individuazione di una gerarchia di scale caratteristiche di lunghezza o di tempo e nel mediare sistematicamente le variabili descrittive della microscala al fine di ottenere modelli monodimensionali. Tale strategia consente, in ultima analisi, di caratterizzare i sistemi attraverso proprietà effettive, preservando al contempo la fisica essenziale del problema originario.

Il primo ed il secondo contributo estendono lo schema perturbativo associato alla dispersione di Taylor-Aris in ambito termico a configurazioni bifase, nella fattispecie a flussi anulari e a film liquidi che si sviluppano attorno a bolle allungate, generalizzando così il classico problema di Graetz in condizioni di flusso termico uniforme. I meccanismi di interazione tra le fasi e la loro disposizione spaziale vengono descritti attraverso coefficienti effettivi, rendendo possibile la derivazione di espressioni analitiche in forma chiusa per il numero di Nusselt. Questi risultati offrono nuove prospettive sui meccanismi di scambio termico, con potenziali applicazioni nella gestione termica di dispositivi elettronici, nella progettazione di reattori biochimici e nell'ottimizzazione di scambiatori di calore.

Il terzo contributo indaga la reologia effettiva di flussi intermittenti, costituiti da una sequenza di bolle circondate da film liquidi a contatto con le pareti del canale. Lo studio mette in luce il carattere non lineare della curva pressione–portata ed estende l'analisi a mezzi porosi attraverso un modello costituito da un fascio di tubi capillari di raggio variabile. Questo modello semplificato di mezzo poroso identifica le cause delle deviazioni dalla legge di Darcy e propone un approccio analitico per la comprensione del complesso comportamento reologico multifase in dominî porosi, con rilevanza sia per flussi nel sottosuolo sia per sistemi biologici.

Infine, il quarto contributo riesamina la discesa di un film liquido soggetto all'azione della gravità nel caso di densità variabile, evidenziando come il carattere comprimibile del flusso promuova l'insorgenza di instabilità all'interfaccia nel limite di grande lunghezza d'onda. Attraverso un'approssimazione *shallow-water* (di acque basse), tale analisi arricchisce la consueta descrizione dell'instabilità di Kapitza ed amplia le basi teoriche per lo studio della stabilità di flussi stratificati.

Abstract

This thesis develops reduced-order models for transport phenomena in thin-film flows, with particular emphasis on heat transfer and nonlinear multiphase dynamics, from rheological behaviour in porous domains to the onset of interfacial instabilities. The research is articulated into four complementary contributions, which together establish a coherent multiscale framework for advancing both the theoretical and practical understanding of multiphase transport. The underlying rationale lies in identifying a hierarchy of characteristic length or time scales, and in systematically averaging out small-scale variables to obtain low-dimensional descriptions. This strategy ultimately enables system characterisation through effective properties, while retaining the essential physics of the original problem.

The first and second contributions extend the perturbation scheme associated with Taylor-Aris thermal dispersion to two-phase configurations, focusing on core–annular flows and liquid films around elongated bubbles, thereby generalising the classical Graetz problem under uniform heat flux conditions. The interplay between phases and the impact of flow topology are captured through effective coefficients, enabling the derivation of closed-form scaling laws for the Nusselt number. These results provide new insights into the heat transfer mechanisms at play, with potential applications in areas such as thermal management of electronic devices, the design of biochemical reactors, and the optimisation of heat exchangers.

The third contribution investigates the effective rheology of intermittent flows, composed of a chain of bubbles coated by wetting liquid films. The study highlights the nonlinear character of the pressure–flow relationship and extends the analysis to porous media by employing a capillary-bundle model with varying radii. This simplified analogue elucidates deviations from the Darcy law and offers an analytically tractable approach for understanding complex multiphase rheological behaviour in porous domains, with relevance for both subsurface and biological systems.

Finally, the fourth contribution revisits gravity-driven liquid films with variable density, showing how compressibility destabilises long-wave interfacial modes. By using a shallow-water approximation, this analysis enriches the classical picture of Kapitza instability and broadens the theoretical foundation for the stability of stratified flows.

Dedication

Alla Ricerca

SONETTO DEDICATORIO[‡]

« Per chi cerca il volume a foglio a foglio »

— GUIDO GOZZANO (1914)
Le Farfalle, II, Ep. vi, v. 133

 i se medesmo offrendo arguta mostra
alla pagina zero del quaderno,
campeggia un motto che mi prende a scherno:
« L'Indagine – ad un tempo – esalta e prostra ».

Dalle mie vene immite un senso alterno
il foglio macolò che qui s'inchiostra,
lusinga e croce al cuore che s'inostra,
ribelle all'eco sorda dell'esterno.

Così snudando me tra mute carte,
vagai gran pezza ed erro tuttavia
e, sbigottendo, riedomi in disparte:

al tutto alieno, un pellegrino in via,
teso a riandare le vestigia sparte
in traccia dell'identità più mia.

On Seeking for

DEDICATORY SONNET – TO QUEST ‡

« To those who seek the tome leaf after leaf »

— GUIDO GOZZANO (1914)
[*Butterflies*, II, Ep. vi, l. 133]

motto stands with wit and subtle grace
And mocks me slyly from the volume's start:
« The Quest uplifts and drains in equal pace »
– A jest that rends both reason and the heart.

From forth my veins there flows a wayward sense
Which stained this page with ink of mirth and pain,
A purple-seething burden, sole defense
To one whose heart holds scorn for worldly strain.

Thus baring self to silent, waiting leaves,
I wandered long, and still I roam astray,
Then, torn, I turn where solitude reprieves,
A stranger to the whole, and drift away:

A pilgrim tracing scattered signs once mine,
In search of what I am, through words in line.

Table of Contents

Chapter 1

Introduction

Both in natural and technological processes, modelling of thin film flows is of great importance, with applications ranging from coating and lubrication to biological and geophysical systems [1]. Their behaviour arises from the complex interplay of multiple physical mechanisms acting over disparate length and time scales [2], with capillary pressure gradients – generated by curvature variations along the interface – providing an additional contribution to the flow. Although the system is driven out of equilibrium, its behaviour can still be captured by assuming that sufficiently small portions of the film remain in local thermodynamic equilibrium [3], allowing the standard formalism of transport phenomena to be used to describe mass, momentum, and heat transfer.

1.1 Reduced-order modelling

Accurately characterising transport phenomena in thin-film flows poses significant challenges. In fact, their full dynamics are governed by the combined action of capillary, viscous, inertial, gravitational, and intermolecular forces, along with time- and space-dependent interfacial stresses. Dimensionless numbers, which quantify the relative importance of these effects and delineate the associated flow regimes, often span several orders of magnitude. As a result, the multiscale nature of the problem and the high dimensionality of the parameter space render direct numerical modelling computationally demanding [1]. In this context, *model order reduction* is emerging as a powerful strategy for the analysis of film flows. It provides a framework for capturing the essential physics of complex systems while maintaining computational feasibility. The basic idea is to approximate the original problem by deriving a simpler description of the system that retains its dominant modes of behaviour. Such reduced models not only enable efficient simulation but also facilitate controller design and optimisation, possibly allowing the induction of desired characteristics [4].

The conceptual foundation underlying many reduction procedures can be traced to the *slaving principle* [5], whose importance in nonlinear dynamics was emphasized by Haken in laser self-organization [6], and later extended within synergetics [7]. This principle states that rapidly damped (i.e., enslaved) variables can be expressed in terms of a few slowly

varying order parameters. Eliminating fast processes reduces the system's degrees of freedom, yielding evolution equations for the macroscopic variables alone [8]. Since the number of order parameters is typically much smaller than that of microscopic variables, the slaving principle provides a formal mechanism for information compression and coarse-graining [9].

1.1.1 Multiscale analysis

Capturing the essential dynamics of liquid films in low-dimensional models is far from trivial. The strong nonlinearities inherent to thin film dynamics – arising from nonlinear convective terms and geometric variability – cannot usually be treated through simple linearisation. Additional complications emerge when unsteady flows are considered, particularly when long-term evolution or coupled multiphysics effects (e.g., heat and mass transfer, surface deformation, or phase change) play a role [4].

In the case of thin-film flows, reduced models often take the form of depth-averaged or lubrication-type equations. Their derivation can rely on *perturbation theory*, a set of mathematical methods used to obtain approximate descriptions of systems for which exact analytical solutions are not available [10]. This framework provides a systematic way to analyse the global behaviour of solutions to differential equations by expanding them in terms of a small parameter, typically denoted by ε. When $\varepsilon = 0$, the problem becomes solvable, and the full solution can be expressed as a power-series expansion around this limit [11]. Regular perturbation problems are characterised by smooth variations of the solution as $\varepsilon \to 0$, whereas singular perturbation problems exhibit abrupt transitions or degeneracies, requiring more advanced analytical techniques such as coordinate transformations or matched asymptotics [12]. While often guided by heuristic considerations [13], the proper identification of the expansion parameter plays a crucial role in uncovering the hierarchy of scales and lies at the core of any reduced description.

Multi-scale analysis is a perturbation-based approach in which governing equations are expressed as asymptotic expansions with respect to a small parameter that represents the ratio of two characteristic time or length scales [14]. In this framework, the goal is to describe the slow (macroscale) dynamics while averaging out the effects of fast (microscale) variations. This is achieved by introducing two distinct characteristic lengths, ℓ and $\mathcal{L}$, such that $\varepsilon = \ell/\mathcal{L} \ll 1$. Alternatively, ε may represent the ratio between a microscopic and a macroscopic characteristic time, i.e., $\varepsilon = \tau/\mathcal{T} \ll 1$. The small parameter ε then serves as the basis for the subsequent perturbation analysis.

Upscaling techniques

In general, any mathematical procedure that aims to replace a fine-scale description with a coarser-scale one that yields equivalent behaviour may be referred to as *upscaling* [15]. To "upscale" differential equations and obtain macroscopic representations from microscale descriptions, two main mathematical strategies are commonly used: the representative elementary volume approach and homogenisation. The *volume averaging* technique smoothens a rapidly varying physical property by taking local averages over small neighborhoods corres-

ponding to representative volumes, thus capturing the macroscopic behaviour of the system from its microscale features [16]. In contrast, *homogenisation* considers a whole family of functions parameterised by the scale parameter and derives the macroscopic limit as the microscale tends to zero [17]. From a broader perspective, homogenisation may be viewed as the study of partial differential equations with rapidly oscillating coefficients [18, 19] and constitutes a natural application of the multiple-scale method to obtain coarse-grained, effective equations [20]. The goal is not to resolve the detailed microscale fields, but to describe the macroscopic behaviour through effective-medium equations and constitutive relations involving effective parameters, such as heat or mass diffusivities, which depend on the underlying microscale configuration [21, 22]. In general, the homogenisation procedure involves the following eight stages:

(i) representing the physical quantities as locally random functions depending simultaneously on macroscopic and microscopic coordinates;
(ii) identifying the scale separation, which yields the definition of the small parameter ε;
(iii) making the problem dimensionless;
(iv) expanding all variables as regular power series in the perturbation parameter;
(v) deriving a cascade of boundary-value problems by collecting terms of equal order;
(vi) solving each order sequentially while checking the *compatibility condition* [23];
(vii) identifying the effective coefficients by closing the problem through an appropriate *gauge-fixing condition* [24];
(viii) checking the consistency of the obtained results via a suitable error estimate [25].

1.1.2 Multiphase transport

Thin liquid films often arise from the coalescence of bubbles or droplets, thereby contributing to the formation of multiphase systems [1]. Notably, the use of multiple phases in internal forced convection within mini- and micro-channels has recently attracted growing attention as a promising strategy to enhance heat transfer [26], offering significant advantages by improving cooling performance while preserving system compactness. However, unlike single-phase flows – whose behaviour can be reliably predicted using well-established correlations [27] and computational models – the dynamics of two-phase flows in such confined geometries remain highly complex and difficult to characterise. This complexity is the result of several contributing factors, including elevated pressure drops [28], compressibility effects, and the emergence of flow instabilities [29].

Examples of two-phase heat transfer problems within confined geometries are numerous [31], including *flow condensation* and *flow boiling*. During in-tube film condensation, several flow regimes can emerge, depending on factors such as tube orientation and length, fluid properties, and the axial profile of the imposed wall heat flux. For example, in a long horizontal tube subjected to a circumferentially uniform heat flux, the flow typically transitions through the regimes shown in figure 1.1 (a). Consequently, the local heat transfer coefficient h varies significantly with the axial coordinate z, reflecting the evolving liquid–vapor distribution along the tube length [32]. Initially, an annular flow regime with a very thin liquid film in contact with the channel wall develops in the upstream section. Here, heat transfer

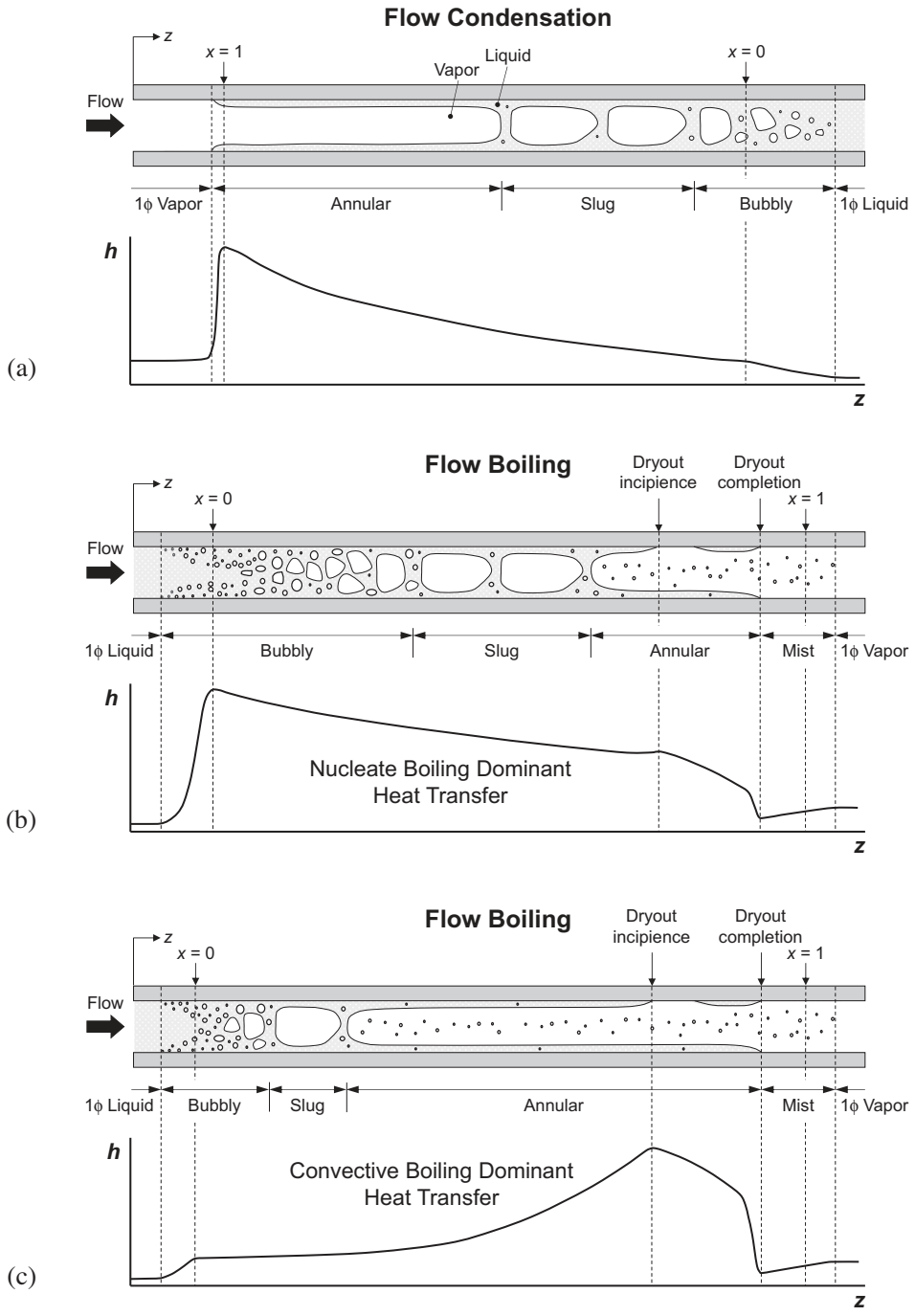

Figure 1.1: Schematics of flow regimes and axial evolution of the heat transfer coefficient in a circular mini-/micro-channel under iso-flux conditions, illustrating representative multiphase heat transfer scenarios: (*a*) condensation, (*b*) nucleate boiling, and (*c*) convective boiling; from [30].

is dominated by a very small conduction resistance, resulting in a heat transfer coefficient that increases along the channel, reaching a maximum slightly downstream of the point where the thermodynamic equilibrium quality x equals unity. As condensation proceeds, the liquid film gradually thickens, and the flow passes through the slug, bubbly, and fully liquid regimes, exhibiting a decreasing heat transfer coefficient. Flow boiling provides an additional example of heat transfer in internal multiphase flows [31, 33]. Panels (*b*) and (*c*) of figure 1.1 represent two distinct transport regimes associated with this process, and distinguished by the dominant mechanism upstream of the dryout location. Similarly to condensation in tubes, the local heat transfer strongly depends on the evolving distribution of liquid and vapor phases along the channel. Panel (*b*) illustrates the *nucleate boiling dominant* heat transfer regime, in which heat is primarily transferred through the formation and detachment of bubbles from the heated surface. In this regime, the bubbly and slug flow patterns occupy a significant portion of the channel length, while the heat transfer coefficient gradually decreases along the channel due to the progressive suppression of nucleate boiling. Panel (*c*) illustrates the *convective boiling dominant* heat transfer regime, in which heat transfer is primarily driven by the bulk motion of the fluid, with the liquid transporting thermal energy away from the heated surface. In this regime, annular flow prevails in a significant portion of the channel length, and the heat transfer coefficient increases along the channel due to the progressive thinning of the annular liquid film. For both heat transfer regimes, the heat transfer coefficient starts to decrease noticeably at the onset of dry patch formation, known as *dryout incipience*. Ultimately, *dryout completion*, associated to critical heat flux conditions, takes place further downstream, where the liquid film is entirely depleted.

Most studies on two-phase heat transfer in mini- and micro-channels rely on experimental or numerical approaches [34], which often result in semi-empirical correlations. For instance, numerous predictive models exist for the annular flow regime typical of in-tube condensation [32], which generally express the local Nusselt number as the product of the single-phase forced convection Nusselt number for the liquid and a two-phase multiplier – i.e., a corrective function dependent on the local vapor quality and other flow parameters. Although these correlations can yield reasonable approximations, they offer limited insight into the physical mechanisms of heat transfer. In this thesis, a reduced-order modelling framework is proposed as a rigorous strategy to capture the essential transport phenomena occurring in thin films, including heat transfer in core-annular flow and around elongated bubbles, thereby bridging the gap between simplified predictive models and a physics-based description of the system.

1.2 Outline of the thesis

This thesis is based on articles published or submitted for publication in peer-reviewed journals over the last three years. Each contribution addresses a specific aspect of thin-film transport phenomena approached through reduced-order modelling, ranging from heat transfer to rheological behaviour and flow instabilities. While each paper is, in principle, self-contained and can be read independently, brief comments are provided between them to offer the reader a coherent perspective on the overall research path and to highlight the logical progression

and connections among the different studies. The content of this thesis is organized around the articles listed below.

I. *Forced convection in two-phase core-annular flows* [P1]
II. *Convective heat transfer around an elongated bubble in the absence of phase change* [P2]
III. *Origin of pressure-flow non-linearity in two-phase intermittent flow in porous media* [P3]
IV. *Compressibility-induced destabilisation of falling liquid films: an integral approach* [P4]

Together, these works illustrate how a disparate class of transport phenomena can be interpreted within a unified multiscale framework, thereby advancing both the understanding and the practical applicability of reduced-order approaches to thin-film systems.

Paper I

P. Botticini, D. Picchi and P. Poesio, 'Forced convection in two-phase core-annular flows', *Journal of Fluid Mechanics*, vol. 1011, A41, May 2025, ISSN: 1469-7645. DOI: 10.1017/jfm.2025.360

Reduced-order modelling offers a powerful strategy to gain insight into multiphase heat transfer, particularly in capturing the mechanisms of interaction between distinct phases. This first study focuses on the effect of a uniform heat flux in a core–annular configuration, where two films flow in parallel. Interestingly, our analysis reveals that coupled advection appears as apparent diffusion terms, and clarifies how a reduced conductive resistance (i.e., small film thickness) enhances heat transfer in the annulus even in the absence of flow motion.

J. Fluid Mech. (2025), *vol.* 1011, A41, doi:10.1017/jfm.2025.360

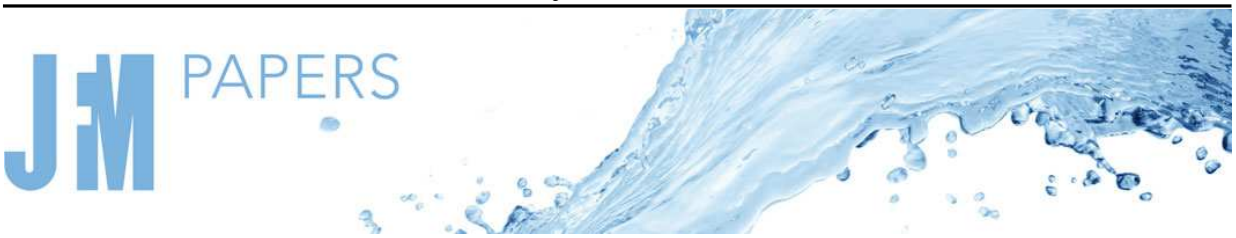

Forced convection in two-phase core-annular flows

P. Botticini[1], **D. Picchi**[1] **and P. Poesio**[1]

[1]Department of Mechanical and Industrial Engineering, Università degli Studi di Brescia, Brescia 25123, Italy

Corresponding author: D. Picchi, davide.picchi@unibs.it

(Received 2 December 2024; revised 17 February 2025; accepted 21 March 2025)

Predicting the temperature distribution in laminar two-phase flows is essential in a wide range of engineering applications, like heat dissipation of electronic equipment and thermal design of biological reactors. Motivated by this, we extend the classical Graetz problem, studying the heat transfer between two flowing phases in a core-annular flow configuration. Using a rigorous two-scale asymptotic analysis, we derived two coupled one-dimensional advection–diffusion heat-transfer equations (one for each phase) embedding the effects of advection, diffusion (both axial and transverse) and viscous dissipation. Specifically, the heat-transfer mechanisms are described through effective velocity and effective diffusion coefficients, while the interaction between the phases is accounted for via *ad hoc* coupling and source terms, respectively. The dynamics of the problem is controlled by seven dimensionless groups: the Péclet and Brinkman numbers, the heat flux, the viscosity, thermal diffusivity and thermal conductivity ratios, and the volume fraction. Our analysis reveals the existence of two main regimes, depending on the disparity in thermal conductivity between the phases. When the conductivity ratio is of order one, the problem is strongly coupled; otherwise, the phases are thermally decoupled. Interestingly, we investigate the evolution of the heat-transfer coefficient in the thin-film limit, shedding light on the most common assumptions underlying extensively used models in the context of film flows. Finally, we derived closed-form scaling laws for the Nusselt number clarifying the impact of the phases topology on heat-transfer dynamics. Since our model has been derived by first principles, we hope that it will improve the understanding of two-phase forced convection.

Key words: core-annular flow, multiphase flow

1. Introduction

Predicting heat transfer in laminar two-phase flows is of practical relevance, with applications ranging from heat sinks for electronic cooling (Mudawar 2011; Kottke *et al.* 2015), biomedical engineering (Wang & Fan 2010), building refrigeration (Armatis & Fronk 2017), thermal design of chemical reactors and heat exchangers (Neveu *et al.* 2013) to geophysical sciences (Hasan & Kabir 2010).

Among those challenges, the growing demand for high-performance computing and miniaturisation makes the effective heat flux removal the major ambition in the design and thermal management of electronic devices (Abdollahi, Sharma & Vatani 2017). Unfortunately, the penetration of well-established technologies, such as wire coil inserts, twisted tapes or helical ribs, is limited by fouling and high pressure losses (Ghajar & Tang 2010). A promising solution consists in promoting two-phase flow conditions to improve the heat transfer. This can be achieved either via the injection of gas bubbles into a pipe filled with refrigerant (e.g. the heat transfer coefficient can increase up to ten times as proposed by Celata *et al.* 1999), using mixtures of immiscible liquids (e.g. an aqueous and an organic phases (Brauner 2002)), or promoting evaporation/condensation (Kim *et al.* 2015; Adera *et al.* 2021). In these contexts, the design of heat exchangers is more complex than in the case of a single phase. The complexity arises from the fact that the heat transfer depends not only on the flow parameters (i.e. flow rate, pressure drop, slip ratio, etc.) and the pipe geometry, but also on the phase topology (i.e. the flow regime: core-annular, stratified, intermittent and dispersed). In addition, while gas–liquid systems are characterised by a low density and viscosity ratio, in liquid–liquid systems, the viscosity ratio can span several orders of magnitude. Thus, understanding how heat transfer is enhanced or retarded due to the presence of more than one phase becomes necessary for the design of modern heat exchangers.

So far, a wide range of investigations has focused primarily on forced convection of single-phase flow, starting from Graetz's and Nusselt's pioneering works (Graetz 1882; Nusselt 1910), where the thermal entrance length inside a circular pipe has been solved neglecting the effect of axial heat conduction and viscous dissipation. Thereafter, the Graetz problem has been studied extensively, see Shah & London (1978). For example, when the flow Péclet number is sufficiently small, streamwise conduction becomes important (see Pahor & Strnad (1956); Reynolds (1963)) as is the case of compact heat exchangers employing liquid metals as working fluids or in micro-channels (Nonino *et al.* 2009). The effect of viscous dissipation on forced convection leads to the so-called Graetz–Brinkman problem (Brinkman 1951; Ou & Cheng 1973), indicating that the internal friction becomes relevant only for highly viscous fluids in capillaries (Morini & Spiga 2006) even at moderate flow rates. Other generalisations include the case of hydrodynamically developing flows (Boussinesq 1890), non-circular arbitrary geometries (Barrera *et al.* 2016), non-Newtonian fluids (Cotta & Özişik 1986; Ali & Khan 2018; Asghar *et al.* 2023), specified-flux (Sellars, Tribus & Klein 1956) and mixed-type (Hsu 1968) boundary conditions or a combination of those (Colle 1988; Hirbodi, Yaghoubi & Warsinger 2022).

Extensions of the Graetz's problem to the case of two-phase flow are rather limited and, unfortunately, a generalised understanding of the effect of the presence of more that one phase on heat transfer dynamics is still missing. Most existing studies focus on core-annular flow and are restricted to steady-state conditions. Specifically, Leib, Fink & Hasson (1977) and Stockman & Epstein (2001) studied the steady-state and fully developed thermal problem of a vertical core-annular flow when a uniform heat flux is imposed at the pipe wall, while Bentwich & Sideman (1964*a*,*b*) proposed a simplified description

of stratified and core-annular liquid–liquid flows when the wall temperature is imposed. Nogueira & Cotta (1990) and Su (2006) solved the heat-transfer Sturm–Liouville-type problem for core-annular flows subjected to fixed temperature and mixed boundary conditions neglecting both axial conduction and viscous dissipation. Later on, Lindemer, Advani & Prasad (2015) studied the impact of convection-type boundary condition combining analytical and numerical solutions (using the method of quasi-orthogonal functions), while Chalhub, Corrêa & Teixeira (2022) proposed a solution of the steady-state Graetz's problem (neglecting axial diffusion) based on integral transform. In those solutions, the fluid temperature is obtained in the form of an infinite series and, therefore, macro-scale thermal parameters, such as the heat transfer coefficient (or the Nusselt number), cannot be obtained in a closed form, keeping the underlying physical scaling difficult to unravel. In fact, such macro-scale parameters are usually estimated using experiments and semi-empirical correlations (Dungan & Shapiro 1990). To sum up, a general theoretical framework that embeds both transient and steady-state effects, and all the relevant physical mechanisms (e.g. both axial and transverse diffusion), is still missing in the context of two-phase flows.

To fill this gap, the goal of this paper is to study the impact of the flow topology on heat transfer clarifying the competition between the main heat transfer mechanisms (diffusion, advection, an imposed heat flux at the channel walls and viscous dissipation) and flow parameters, like the volume fraction and the viscosity ratio. To do so, we extend the Graetz–Brinkman problem to core-annular flows (see figure 1, § 2) that represent the basic flow pattern in microchannel and it is often used as an idealisation of more complex flow regimes such as elongated bubbles (see Collier & Thome (1994); Thome, Dupont & Jacobi (2004); Picchi & Battiato (2018); Picchi, Ullmann & Brauner (2018)). Our goal is to derive an effective description of the heat-transfer problem addressing both transient and steady-state conditions.

With this aim, we generalise the Aris–Taylor dispersion theory to heat-transfer in the context of two-phase flows. In fact, this theory has the great advantage to be a satisfactory compromise between accuracy, compactness and physical interpretation of the final solution. Specifically, the long-standing theory of Taylor dispersion (Taylor 1953; Aris 1956) is a rigorous perturbation scheme that has been first applied to elementary geometries and later generalised to a disparate class of physical systems (Brenner 1980), including periodic obstructions (Farah *et al.* 2020), a non-premixed flame established in a narrow duct (Liñán *et al.* 2020), radiant pipes (Batycky, Edwards & Brenner 1994), soils (Auriault & Lewandowska 1996), capillary-tissue exchange kinetics (Levitt 1972; Fallon & Chauhan 2005), suspensions and porous media (Brenner & Stewartson 1980; Rubinstein & Mauri 1986; Battiato & Tartakovsky 2011; Parmigiani *et al.* 2011; Griffiths, Howell & Shipley 2013; Dejam, Hassanzadeh & Chen 2014; Bourbatache, Millet & Moyne 2020; Scholz & Bringedal 2022), and thin films (Picchi & Poesio 2022). Conveniently, it provides a reduced-order mathematical description where the competitive influence of advection, diffusion and boundary phenomena is taken into account via a set of effective coefficients (Frankel & Brenner 1989). So far, to the best of our knowledge, an attempt to adapt this approach to the case of core-annular flows has not been proposed yet.

Starting from transport equations (§ 2.1), we derive a set of coupled evolution equations for the average temperatures as functions of space and time by means of two-scale asymptotic expansions (§ 3). Our analysis (the full derivation is presented in Appendix C) is complemented by a rigorous specification of the theoretical bounds of validity of the model (§ 3.1). In the case of large thermal conductivity contrast between the phases, the system reduces to a single equation (§ 3.2), which admits an analytical solution (§ 4.1), including transient effects. Instead, when the thermal conductivities are of the same

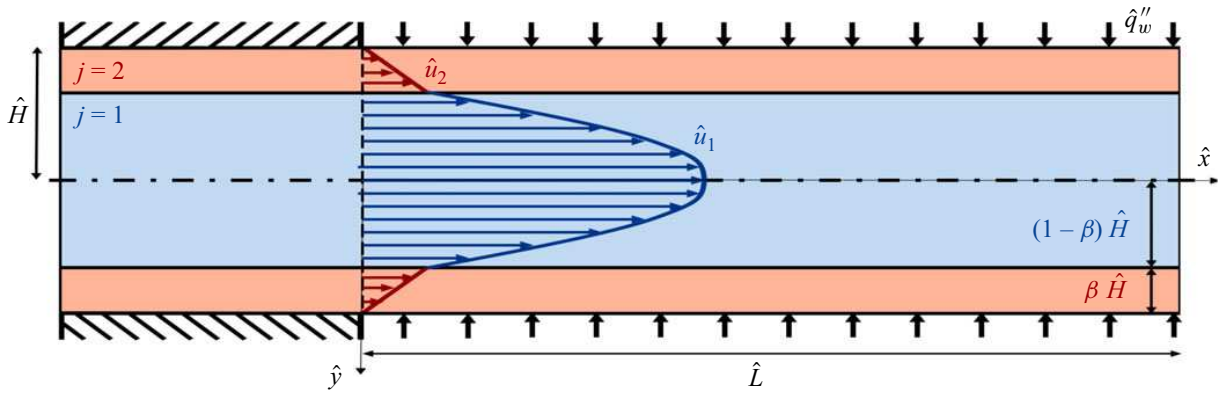

Figure 1. Schematic diagram of the extended Graetz–Brinkman problem for a laminar two-phase core-annular flow in a plane slender channel ($\hat{H} \ll \hat{L}$) with a semi-infinite heating section.

order of magnitude, the problem is described by two coupled advection–heat-transfer equations and an analytical solution only exists at the steady-state (§ 4.5). Finally, we derive analytical scaling laws for the asymptotic Nusselt number (§§ 4.2, 4.7) and discuss the thermal coupling between the phases (Brenner 1982; Chu, Sposito & Jury 1983; Auriault & Lewandowska 1994; Moyne & Murad 2006; Shelukhin, Yeltsov & Paranichev 2011). These results shed light on heat transfer phenomena in the context of multi-phase flows and may serve as a starting step to generalise the heat transfer model to other flow regimes.

2. Problem formulation

We consider an infinitely long and horizontal planar channel with a uniform cross-section of height $2\hat{H}$, as sketched in figure 1; the hat operator will be used to denote dimensional quantities. Two immiscible Newtonian fluids flow from left to right as a core-annular flow regime driven by a constant pressure gradient: the inner fluid, which is not in contact with the channel wall, will be denoted by subscript '1', while the outer fluid that is in contact with the channel wall will be denoted by subscript '2'. The fluid–fluid interface is supposed to be flat, and both velocity profiles are assumed to be fully developed and laminar. The channel is heated by a constant and uniform wall heat flux $\hat{q}''_w$ imposed at both plates ($\hat{y} = \pm\hat{H}$) over the entire semi-infinite domain ($\hat{x} \geqslant 0$). We primarily consider liquid–liquid systems or gas–liquid systems with sufficiently small temperature differences so that the thermal expansion of the gaseous phase can be neglected. The dimensional velocity profile in each fluid domain is derived from the incompressible Navier–Stokes equation for co-current core-annular flows in a planar geometry:

$$\hat{u}_1\left(\hat{y}\right) = \frac{1}{2\mu_1}\frac{\mathrm{d}\hat{p}}{\mathrm{d}\hat{x}}\left\{\hat{y}^2 - \frac{\hat{H}^2\left[\mu_2 - \beta(2-\beta)\left(\mu_2 - \mu_1\right)\right]}{\mu_2}\right\}, \quad \frac{\hat{y}}{\hat{H}} \in [0;\ 1-\beta], \tag{2.1a}$$

$$\hat{u}_2\left(\hat{y}\right) = \frac{1}{2\mu_2}\frac{\mathrm{d}\hat{p}}{\mathrm{d}\hat{x}}\left\{\hat{y}^2 - \hat{H}^2\right\}, \quad \frac{\hat{y}}{\hat{H}} \in [1-\beta;\ 1], \tag{2.1b}$$

where $\mathrm{d}\hat{p}/\mathrm{d}\hat{x} < 0$ is the axial pressure gradient, μ_j is the dynamical viscosity of the two fluids, $j = \{1,\ 2\}$, and β is the volume fraction of the outer phase ($0 < \beta < 1$); the detailed

derivation of the velocity profiles is given in Appendix A. Specifically, half the thickness of the inner and the outer phase is equal to $(1-\beta)\hat{H}$ and $\beta\hat{H}$, respectively.

We obtain the averaged speed of the inner and outer phase by integrating the velocity profiles (2.1),

$$\hat{U}_1 = \frac{\int_0^{(1-\beta)\hat{H}} \hat{u}_1\left(\hat{y}^*\right) \mathrm{d}\hat{y}^*}{(1-\beta)\,\hat{H}} = -\frac{\hat{H}^2}{6\,\mu_1\,\mu_2}\frac{\mathrm{d}\hat{p}}{\mathrm{d}\hat{x}}\left[2\mu_2 - \beta(2-\beta)\,(2\mu_2 - 3\mu_1)\right], \tag{2.2a}$$

$$\hat{U}_2 = \frac{\int_{(1-\beta)\hat{H}}^{\hat{H}} \hat{u}_2\left(\hat{y}^*\right) \mathrm{d}\hat{y}^*}{\beta\hat{H}} = -\frac{\hat{H}^2}{6\,\mu_2}\frac{\mathrm{d}\hat{p}}{\mathrm{d}\hat{x}}\left[\beta(3-\beta)\right], \tag{2.2b}$$

yielding an overall expression for the averaged speed over the entire channel,

$$\hat{U} = (1-\beta)\,\hat{U}_1 + \beta\,\hat{U}_2 = -\frac{\hat{H}^2}{3\,\mu_1\,\mu_2}\frac{\mathrm{d}\hat{p}}{\mathrm{d}\hat{x}}[\mu_2 - \beta(\beta^2 - 3\beta + 3)(\mu_2 - \mu_1)]. \tag{2.3}$$

2.1. *Governing equations for heat transfer*

The internal energy balance for each phase written in terms of temperature $\hat{T}_j(\hat{x},\ \hat{y},\ \hat{t})$ is given by

$$\rho_j\, c_{p,\,j}\left(\frac{\partial\hat{T}_j}{\partial\hat{t}} + \hat{u}_j\,\frac{\partial\hat{T}_j}{\partial\hat{x}}\right) = \kappa_j\left(\frac{\partial^2\hat{T}_j}{\partial\hat{x}^2} + \frac{\partial^2\hat{T}_j}{\partial\hat{y}^2}\right) + \hat{\mathcal{W}}_j, \tag{2.4}$$

with ρ_j, $c_{p,\,j}$, κ_j being the density, the isobaric mass heat capacity and the thermal conductivity of each phase, respectively. The term $\hat{\mathcal{W}}_j$ represents the rate of viscous dissipation of mechanical energy per unit mass and, for laminar unidirectional and fully developed flows, it reduces to

$$\hat{\mathcal{W}}_j = \mu_j\left(\frac{\mathrm{d}\hat{u}_j}{\mathrm{d}\hat{y}}\right)^2. \tag{2.5}$$

At the channel wall, $\hat{y} = \hat{H}$, we assume that a uniform heat flux (UWF) is imposed (Shah & London 1978), leading to

$$\hat{q}''_w = -\kappa_2\left(\hat{\boldsymbol{\nabla}}\hat{T}_2\cdot\boldsymbol{n}_2\right)\Big|_{\hat{y}=\hat{H}} = -\kappa_2\,\frac{\partial\hat{T}_2}{\partial\hat{y}}\bigg|_{\hat{y}=\hat{H}}, \tag{2.6}$$

where the unit vector is given by $\boldsymbol{n}_2 = (0;\ 1)$. From the practical point of view, an imposed uniform wall heat flux (for $\hat{x} \geqslant 0$) can be seen as an approximation of many experimental facilities where the channel is wrapped with a heat tape or wire resistance heater – see, for instance, Murphy, Alimohammadi & O'Shaughnessy (2024). In (2.6), we adopt as convention that the imposed heat flux is positive, $\hat{q}''_w > 0$, when it exits the fluid. At the fluid–fluid interface, $\hat{y} = (1-\beta)\hat{H}$, the normal vectors are given by $\boldsymbol{n}_1 = (0;\ 1) = -\boldsymbol{n}_2$, and the continuity of temperature and heat flux across the flat interface gives

$$\kappa_1\frac{\partial\hat{T}_1}{\partial\hat{y}}\bigg|_{\hat{y}=(1-\beta)\hat{H}} = \kappa_2\frac{\partial\hat{T}_2}{\partial\hat{y}}\bigg|_{\hat{y}=(1-\beta)\hat{H}}, \tag{2.7a}$$

$$\hat{T}_1\Big|_{\hat{y}=(1-\beta)\hat{H}} = \hat{T}_2\Big|_{\hat{y}=(1-\beta)\hat{H}}. \tag{2.7b}$$

In the duct cross-section at $\hat{y} = 0$, the symmetry of the thermal problem results in

$$\left.\frac{\partial \hat{T}_1}{\partial \hat{y}}\right|_{\hat{y}=0} = 0. \tag{2.8}$$

The problem is closed imposing the initial condition at the channel entry as a uniform temperature distribution at $\hat{t} = 0$ and $\hat{x} = 0$ for both phases:

$$\hat{T}_j\left(0,\ \hat{y},\ 0\right) = \hat{T}_{in,\,j}. \tag{2.9}$$

As it will be discussed in § 2.2, we are not focused on describing the early-time evolution of the system and, therefore, the initial condition (2.9) is unimportant for the purposes of our analysis.

Then, we recast the energy balance (2.4), written with respect to an absolute reference frame $(\hat{x},\ \hat{y})$, introducing a new axial coordinate $\hat{z} = \hat{x} - \hat{V}\,\hat{t}$ that advects in the direction of the flow with an arbitrary speed $\hat{V}$ (with $\hat{\tau} = \hat{t}$) yielding

$$\rho_j\, c_{p,\,j}\left[\frac{\partial \hat{T}_j}{\partial \hat{\tau}} + \left(\hat{u}_j - \hat{V}\right)\frac{\partial \hat{T}_j}{\partial \hat{z}}\right] = \kappa_j\left(\frac{\partial^2 \hat{T}_j}{\partial \hat{z}^2} + \frac{\partial^2 \hat{T}_j}{\partial \hat{y}^2}\right) + \hat{\mathcal{W}}_j. \tag{2.10}$$

In general, the choice of the reference frame speed $\hat{V}$ is arbitrary (Brady 1975), but it affects the definition of the integral variables (e.g. the effective diffusion coefficients). Specifically, $\hat{V} = 0$ corresponds to a description given in the absolute coordinate system; this reference frame will be adopted to compute the bulk temperature and the Nusselt number. Choosing $\hat{V} = \hat{U}$ identifies the volume-fixed reference frame, i.e. a relative coordinate system moving a speed equal to the mean flow velocity, see (2.3). This reference frame will be used when the focus is on revealing the impact of advection on multiphase heat transfer (i.e. the equivalent of hydrodynamic dispersion in mass transfer problems (Taylor 1953)). In cases where the two phases are thermally decoupled, it is convenient to choose a reference frame attached to the annulus with $\hat{V} = \hat{U}_2$. A rigorous justification of this argument is provided both in the framework of statistical moments (Aris 1956) or perturbation analysis enforcing the Fredholm-type solvability condition (Mauri 1991, 1995, 2015; Mikelić, Devigne & van Duijn 2006). Note that other choices of the reference frame can be made (e.g. molar or mass mean velocity), but their use is limited to multicomponent systems (Hooyman 1956; Brady 1975; Piña 1979; Taylor & Krishna 1993; Kozlova *et al.* 2019).

2.2. *Dimensionless formulation*

The governing equations introduced in § 2.1 are made dimensionless to facilitate the derivation of an effective description of two-phase flow heat transfer. The relevant scale along the $\hat{y}$-direction is chosen as the half-distance between the parallel plates $\hat{H}$, while we denote by $\hat{L}$ a characteristic macroscopic/observation length scale along the $\hat{x}$-axis. We look at systems that can be treated as a shallow geometry, $\hat{L} \gg \hat{H}$, and, therefore, a small scale parameter indicating the separation between transverse and axial variables arises naturally,

$$\varepsilon = \frac{\hat{H}}{\hat{L}} \ll 1. \tag{2.11}$$

The scale separation assumption, $\varepsilon \ll 1$, is a key requirement to simplify the momentum equations and ensures that the lubrication approximation for the flow holds (see Appendix A).

The determination of the relevant time scale is not unique (Mauri 1991; Auriault & Adler 1995; Mikelić *et al.* 2006; Battiato & Tartakovsky 2011; Bourbatache *et al.* 2020; Picchi & Poesio 2022). In fact, advection introduces three advective time scales depending on whether the focus is on a specific phase or the overall system. Assuming that the characteristic scale for the velocity is the overall flow speed $\hat{U}$ given in (2.3), we can define the axial advective time as $\hat{\tau}_a = \hat{L}/\hat{U}$, while using the phase speed, U_j, we can introduce two additional time scales as $\hat{\tau}_{a,\,j} = \hat{L}/\hat{U}_j$. Thermal diffusion introduces two additional time scales for each phase: the axial, $\hat{\tau}_{\hat{L},\,j} = \hat{L}^2/\alpha_j$, and the transverse, $\hat{\tau}_{\hat{H},\,1} = (1-\beta)^2\hat{H}^2/\alpha_1$, $\hat{\tau}_{\hat{H},\,2} = \beta^2\,\hat{H}^2/\alpha_2$, diffusion times, with $\alpha_j = \kappa_j/\rho_j\,c_{p,\,j}$ being the thermal diffusivity of the jth phase. Since we are primarily interested in transport dynamics in a time frame much larger than the transverse diffusion time and close to the advection time, we choose $\hat{\tau}_a$ as the reference scale for the time variable (Mauri 1991; Griffiths *et al.* 2013; Mauri 2015; Ling *et al.* 2016; Liñán *et al.* 2020). This choice allows the investigation of heat-transfer regimes characterised by the competition between advection and axial diffusion. In fact, as elucidated by Taylor's analysis of solute dispersion (Taylor 1953), the advective time scale corresponds to a time window that is intermediate between the times characterising transverse and axial diffusion, i.e. $\tau_{H,j} \ll \tau_a \ll \tau_{L,j}$, defining a hierarchy of time scales that can be uniquely determined in terms of the scale parameter ε and the Péclet number of the problem (see § 4.3). This choice of the relevant time window also implies that the model is not capable of describing the early-time relaxation of the system's initial configuration due to transverse diffusion (known as pre-asymptotic regime) and, therefore, the initial condition given in (2.9) will not be considered. Note that the description of the pre-asymtotic regime (see e.g. Taghizadeh, Valdés-Parada & Wood (2020)) is out of the scope of this work.

We can recast the energy balance (2.10) introducing the following dimensionless variables:

$$z = \frac{\hat{z}}{\hat{L}}, \quad y = \frac{\hat{y}}{\hat{H}}, \quad \tau = \frac{\hat{\tau}}{\hat{\tau}_a}, \quad \{u_j;\ V\} = \frac{\left\{\hat{u}_j;\ \hat{V}\right\}}{\hat{U}}, \quad \vartheta_j = \frac{\hat{T}_j - \hat{T}_{ref}}{\Delta\hat{T}_{ref}}, \qquad (2.12a\text{-}e)$$

where $\hat{T}_{ref}$ and $\Delta\hat{T}_{ref}$ are arbitrary reference values for the temperature and its variation, respectively. For example, the reference temperature $\hat{T}_{ref}$ can be chosen as the initial temperature at a given location ($\hat{x} = 0$), $\hat{T}_{in}$, while the reference temperature difference $\Delta\hat{T}_{ref}$ can be defined based on the condition of uniform heat flux at the wall, as $\hat{q}''_w\,\hat{L}/\kappa_2$ (Shah & London 1978) or $\hat{q}''_w\,\hat{L}/(\rho_2\,c_{p,\,2}\,\hat{U}\,\hat{H})$ (Chen *et al.* 2022). This procedure yields

$$\varepsilon\,\mathcal{A}\,Pe\left[\frac{\partial\vartheta_1}{\partial\tau} + (u_1 - V)\,\frac{\partial\vartheta_1}{\partial z}\right] = \left(\varepsilon^2\,\frac{\partial^2\vartheta_1}{\partial z^2} + \frac{\partial^2\vartheta_1}{\partial y^2}\right) + \frac{m}{\mathcal{K}}\,Br\left(\frac{\mathrm{d}u_1}{\mathrm{d}y}\right)^2, \quad y \in [0;\ 1-\beta]\,, \qquad (2.13a)$$

$$\varepsilon\,Pe\left[\frac{\partial\vartheta_2}{\partial\tau} + (u_2 - V)\,\frac{\partial\vartheta_2}{\partial z}\right] = \left(\varepsilon^2\,\frac{\partial^2\vartheta_2}{\partial z^2} + \frac{\partial^2\vartheta_2}{\partial y^2}\right) + Br\left(\frac{\mathrm{d}u_2}{\mathrm{d}y}\right)^2, \quad y \in [1-\beta;\ 1]\,, \qquad (2.13b)$$

where dimensionless absolute velocity profiles $u_j(y)$ are given in Appendix A.1. In the following, $V=0$ corresponds to a description given in the absolute coordinate system, $V=1$ identifies the relative coordinate system moving at the mean flow speed, while $V=U_2$ identifies the reference frame attached to the annulus. The normalisation introduces the viscosity ratio m, the thermal conductivity ratio $\mathcal{K}$ and the thermal diffusivity ratio $\mathcal{A}$:

$$m=\frac{\mu_1}{\mu_2},\qquad \mathcal{K}=\frac{\kappa_1}{\kappa_2},\qquad \mathcal{A}=\frac{\alpha_2}{\alpha_1}=\frac{1}{\mathcal{K}}\,\frac{\rho_1}{\rho_2}\,\frac{c_{p,1}}{c_{p,2}}. \tag{2.14a-c}$$

The viscosity ratio accounts for the different viscosity of the flowing phases: when $m\to 0$, the outer fluid is much more viscous compared with the inner one as typical of the majority of gas–liquid systems (see table 1); we will refer to this limit as the free-surface limit. When $m\to\infty$, the inner fluid is much more viscous than the outer one and it behaves like a rigid body, see figure 3(*a*); we will refer to this limit as the rigid-core limit. The product $\mathcal{K}\,\mathcal{A}$ can be seen as the thermal capacity ratio: gas–liquid systems are characterised by lower values of $\mathcal{K}\,\mathcal{A}$ with respect to liquid–liquid systems (see table 1). Note that, although in our model, the physical properties of the two phases appear in the three property ratios given in (2.14), other sets of dimensionless parameters can provide an equivalent description. For example, in Appendix B, we show how the property ratios (2.14) can be recast in terms of the heat-capacity flow rate ratio, commonly used to describe heat-exchanger problems.

In (2.13), the Péclet number Pe and the Brinkman number Br for the outer phase are given by

$$Pe_2=Pe=\frac{\hat{H}\,\hat{U}}{\alpha_2},\qquad Br=\frac{\mu_2\,\hat{U}^2}{\kappa_2\,\Delta\hat{T}_{ref}}. \tag{2.15a-b}$$

The Péclet number expresses the ratio between advection and axial diffusion. When $Pe\ll 1$, diffusion dominates over advection, while for $Pe\gg 1$, advection plays a major role with respect to diffusion. The Péclet number Pe_1 of the inner phase is given by the product $Pe_1=\mathcal{A}\,Pe$. The Brinkman number can be seen as the competition between the thermal power per unit mass produced by viscous dissipation and the one transferred due to conduction by the outer phase through the channel walls; $Br=0$ only in non-dissipative flows.

The dimensionless boundary conditions at the wall (2.6), at the interface (2.7) and at the channel axis (2.8) read

$$\left.\frac{\partial\vartheta_2}{\partial y}\right|_{y=1}=-\frac{\hat{q}''_w\,\hat{H}}{\kappa_2\,\Delta\hat{T}_{ref}}=q_w, \tag{2.16a}$$

$$\left.\frac{\partial\vartheta_2}{\partial y}\right|_{y=1-\beta}=\mathcal{K}\,\left.\frac{\partial\vartheta_1}{\partial y}\right|_{y=1-\beta}, \tag{2.16b}$$

$$\vartheta_2|_{y=1-\beta}=\vartheta_1|_{y=1-\beta}, \tag{2.16c}$$

$$\left.\frac{\partial\vartheta_1}{\partial y}\right|_{y=0}=0. \tag{2.16d}$$

Note that (2.16*a*) introduces the dimensionless wall heat flux q_w as a further governing dimensionless group.

3. Two-scale asymptotic analysis

The present work aims at obtaining a one-dimensional approximation of the energy equations (2.13) coupled with boundary conditions (2.16). Specifically, we look for one-dimensional advection–diffusion heat-transfer (ADHT) equations accounting for advection, diffusion and heat exchange between the two phases. To do so, we adopt a two-scale asymptotic expansion procedure (Hornung 1997; Boutin, Auriault & Geindreau 2010; Bensoussan, Lions & Papanicolaou 2011).

(i) The starting point is the local description of the dimensionless heat-transfer problem, see (2.13), (2.16), together with the definition of the scale parameter ε given in (2.11).

(ii) We focus on an asymptotic regime where the temperature profile can be considered almost uniform in the transverse direction (transverse diffusion has smeared out the initial profile) and axial diffusion is part of the game in the spirit of classical Taylor-dispersion theory (Taylor 1953). To this end, we look at axial variations in temperature in between the duct half-height, $\hat{H}$, and the duct length, $\hat{H}/\varepsilon$, of the order $1/\sqrt{\varepsilon}$. Therefore, the longitudinal coordinate z is re-scaled introducing a stretched spacial variable ξ (similarly to Griffiths *et al.* (2013); Ling *et al.* (2016); Liñán *et al.* (2020)):

$$\xi = \frac{z}{\sqrt{\varepsilon}}. \tag{3.1}$$

(iii) The dimensionless groups (2.15), (2.16*a*) and the property ratios are evaluated in asymptotic terms expressing their magnitude as integer or half-integer power of the scale parameter ε:

$$\mathcal{K} = K\,\varepsilon^{k} \quad \text{with} \quad K = \mathcal{O}(1) \quad \text{and} \quad k \in \frac{1}{2}\mathbb{Z}, \tag{3.2a}$$

$$\mathcal{A} = \varepsilon^{a} \quad \text{and} \quad Pe = \varepsilon^{-p} \quad \text{with} \quad a,\ p \in \frac{1}{2}\mathbb{Z}, \tag{3.2b}$$

$$Br = B\,\varepsilon^{b} \quad \text{with} \quad B = \mathcal{O}(1) \quad \text{and} \quad b \in \frac{1}{2}\mathbb{Z}, \tag{3.2c}$$

$$q_w = Q\,\varepsilon^{f} \quad \text{with} \quad Q = \mathcal{O}(1) \quad \text{and} \quad f \in \frac{1}{2}\mathbb{Z}. \tag{3.2d}$$

(iv) The temperature field ϑ_j in the energy equations (2.13), (2.16) is written as a half-integer power-series expansion in the scale parameter:

$$\vartheta_j(\xi, y, \tau;\ \varepsilon) = \vartheta_j^{(0)}(\xi, y, \tau) + \sqrt{\varepsilon}\,\vartheta_j^{(1)}(\xi, y, \tau) + \varepsilon\,\vartheta_j^{(2)}(\xi, y, \tau) + \mathcal{O}(\varepsilon\sqrt{\varepsilon}), \tag{3.3}$$

where $\vartheta_j^{(n)}$ is the nth-order term in the asymptotic expansion of the temperature field ϑ_j, with $j = \{1, 2\}$. We follow the classical multiscale approach where the main variables are expanded with respect to space and the axial coordinate is stretched according to (3.1) to properly describe the asymptotic regime (as explained in item (ii)) (Mauri 1991; Griffiths *et al.* 2013; Mauri 2015; Ling *et al.* 2016; Liñán *et al.* 2020). An equivalent approach would be to fully expand the independent variables in both time and space (Mauri 1995; Mazzino 1997; Mauri 2003; Mei & Vernescu 2010).

(v) Then, we collect the terms of the same order obtaining a cascade of boundary-value problems. These are sequentially solved to obtain the effective description of the original problem in terms of the depth-averaged temperatures, $\langle\vartheta_j\rangle(\xi, \tau)$,

plus higher-order corrections. To do so, we introduce the cross-sectional averaging operator over each fluid domain

$$\langle \star_j \rangle = \begin{cases} \dfrac{1}{1-\beta}\left(\displaystyle\int_0^{1-\beta} \star_j \, \mathrm{d}y\right) & \text{if } j = 1, \\ \dfrac{1}{\beta}\left(\displaystyle\int_{1-\beta}^{1} \star_j \, \mathrm{d}y\right) & \text{if } j = 2, \end{cases} \tag{3.4}$$

consistent with the classical two-scale asymptotic expansion procedure (Hornung 1997; Boutin *et al.* 2010; Bensoussan *et al.* 2011). Other types of mean relevant for heat-transfer problems, such as the mixing-cup (or bulk) temperature, require an *a priori* knowledge of the temperature field, and, therefore, they will be defined once the model's solution is determined, see § 3.3.
It will be shown, see Appendix C.2 and (C3*a*), that the leading-order term in (3.3) is independent on y and, therefore, $\vartheta_j^{(0)}(\xi,\ \tau) \equiv \langle \vartheta_j^{(0)} \rangle (\xi,\ \tau)$. In this type of approach, the goal is to describe the macroscopic behaviour of the system in terms of the zeroth-order terms $\vartheta_j^{(0)}$ while interpreting higher-order terms in (3.3) as small fluctuations around the zeroth-order values. Thus, without any lack of generality (Mauri 1995), we impose a gauge condition of the type

$$\left\langle \vartheta_j^{(n)}\ (\xi,\ y,\ \tau) \right\rangle \equiv 0 \qquad \text{for} \quad n \geqslant 1, \tag{3.5}$$

implying that the higher orders do not impact on the averaged temperature

$$\left\langle \vartheta_j^{(n)} \right\rangle \equiv \vartheta_j^{(0)}\ \delta_0^n, \tag{3.6}$$

where δ_0^n is the Kronecker delta indicator introduced to make the problem derivation more concise

$$\delta_{i_2}^{i_1} = \begin{cases} 0 & \text{if } i_1 \neq i_2, \\ 1 & \text{if } i_1 = i_2. \end{cases} \tag{3.7}$$

(vi) The effective model is obtained imposing the compatibility condition, (also known as solvability condition or Fredholm alternative) which is the sufficient and necessary condition for the existence of solutions to the successive boundary-value problems. Satisfying the compatibility condition results in setting to zero the average of the expanded governing equation over its domain (Rubinstein & Mauri 1986; Auriault 2002; Mikelić *et al.* 2006).

The full derivation following the aforementioned procedure is provided in Appendix C, while the final results are given in upcoming sections, distinguishing between two different scenarios based of the order of magnitude of the thermal conductivity ratio $\mathcal{K}$, see (3.2*a*).

3.1. *One-dimensional ADHT equations – coupled regime*

The system of ADHT equations, describing the spatial and temporal evolution of the averaged temperatures, is given in (C36), with the coefficients defined in (C37). The

corresponding equation in the core is

$$\mathcal{A}\,Pe\left(1+\frac{1-\beta}{K\,\beta}\right)\frac{\partial\langle\vartheta_1\rangle}{\partial\tau}+\mathcal{A}\,Pe\,\overbrace{\left(U_1-V+\omega_{11}^{\star}\right)}^{a_{11}^{\star}}\frac{\partial\langle\vartheta_1\rangle}{\partial z}+Pe\,a_{12}^{\star}\,\frac{\partial\langle\vartheta_2\rangle}{\partial z}$$
$$=\varepsilon\,\underbrace{\left[1+\frac{1-\beta}{K\,\beta}+\mathcal{A}^2Pe^2\left(D_1+\delta_{11}^{\star}\right)\right]}_{d_{11}^{*}}\frac{\partial^2\langle\vartheta_1\rangle}{\partial z^2}+\varepsilon\,Pe^2\,d_{12}^{\star}\,\frac{\partial^2\langle\vartheta_2\rangle}{\partial z^2}$$
$$+\frac{1}{\varepsilon}\left(g_1^{\star}\,q_w+w_1^{\star}\,Br\right)-\frac{1}{\varepsilon}\,e_1^{\star}\left(\langle\vartheta_1\rangle-\langle\vartheta_2\rangle\right),\tag{3.8}$$

while for the annulus, we get

$$Pe\left(1+\frac{K\,\beta}{1-\beta}\right)\frac{\partial\langle\vartheta_2\rangle}{\partial\tau}+Pe\,\overbrace{\left(U_2-V+\omega_{22}^{\star}\right)}^{a_{22}^{\star}}\frac{\partial\langle\vartheta_2\rangle}{\partial z}+\mathcal{A}\,Pe\,a_{21}^{\star}\,\frac{\partial\langle\vartheta_1\rangle}{\partial z}$$
$$=\varepsilon\,\underbrace{\left[1+\frac{K\,\beta}{1-\beta}+Pe^2\left(D_2+\delta_{22}^{\star}\right)\right]}_{d_{22}^{*}}\frac{\partial^2\langle\vartheta_2\rangle}{\partial z^2}+\varepsilon\,(\mathcal{A}\,Pe)^2\,d_{21}^{\star}\,\frac{\partial^2\langle\vartheta_1\rangle}{\partial z^2}$$
$$+\frac{1}{\varepsilon}\left(g_2^{\star}\,q_w+w_2^{\star}\,Br\right)+\frac{1}{\varepsilon}\,e_2^{\star}\left(\langle\vartheta_1\rangle-\langle\vartheta_2\rangle\right),\tag{3.9}$$

with $a_{jj}^{\star}(U_j,\ V,\ \beta,\ m,\ K)$ and $d_{jj}^{\star}(V,\ \beta,\ m,\ K,\ Pe)$ being the effective coefficients for advection and diffusion of the inner $(j=1)$ and the outer phase $(j=2)$. Those coefficients are a function of the speed of the reference frame, V, the phase speeds U_j, the volume fraction β, the viscosity ratio m, and the conductivity ratio $\mathcal{K}$ – their full expressions are given in Appendix C.6. The ADHT equations (3.8), (3.9) are coupled through diverse physical mechanisms, namely advection and diffusion of the other phase via the coefficients $a_{12}^{\star}(\beta,\ m,\ K)$ and $a_{21}^{\star}(\beta,\ m,\ K)$, and $d_{12}^{\star}(V,\ \beta,\ m,\ K)$ and $d_{21}^{\star}(V,\ \beta,\ m,\ K)$, respectively; heat exchange between the phases through storage terms $(\propto\pm(\langle\vartheta_1\rangle-\langle\vartheta_2\rangle))$ and source terms proportional to q_w. All these mechanisms will be discussed in detail in § 4.5.

The ADHT equations (3.8), (3.9) hold only in a specific range of the dimensionless groups (2.14), (2.15), (2.16*a*) to guarantee that the two scales can be decoupled. Such requirements are known as the applicability region and are sufficient (but not necessary) conditions for the effective model to be representative of the spatially averaged processes within the error bounds prescribed by the asymptotics. In our case, the upscaled equations hold only when:

(i) $\varepsilon\ll 1$;
(ii) $Pe\ll 1/\sqrt{\varepsilon}$;
(iii) $\mathcal{A}\,Pe\ll 1/\sqrt{\varepsilon}$;
(iv) $|q_w|\ll 1$;
(v) $Br\ll 1$.

Condition (a) ensures that the spatial scale separation exists. Conditions (b) and (c) provide the upper bounds to the Péclet number of each phase, ensuring that advection does not prevail over diffusion. Condition (d) restricts the rate at which heat is transferred by the

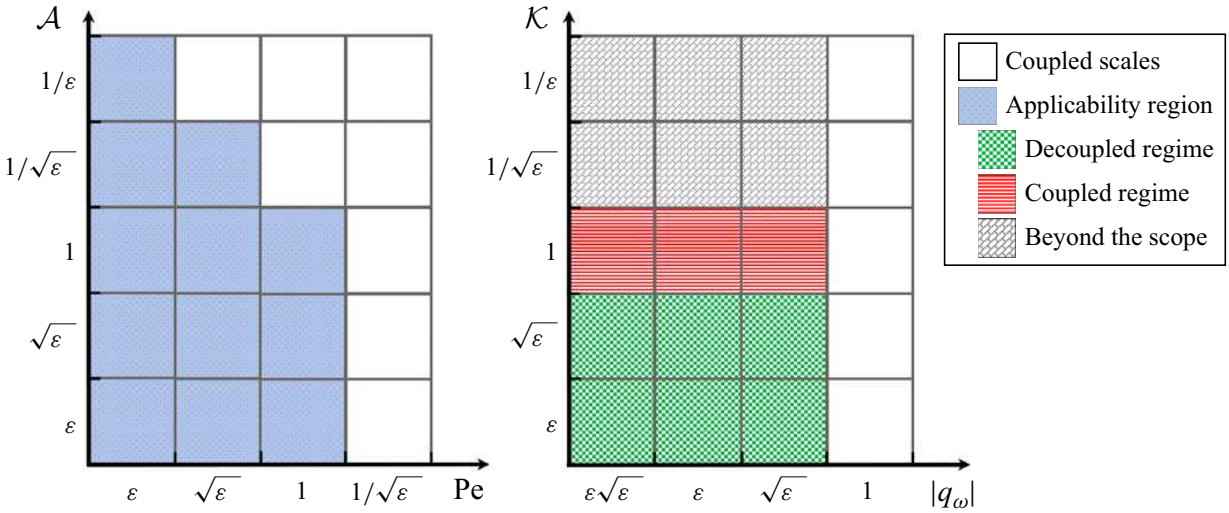

Figure 2. Parameter space of transport regimes in the (Pe, $\mathcal{A}$) (left) and in the (q_w, $\mathcal{K}$) (right) planes. Coloured areas of the maps correspond to regimes where the effective heat-transfer equation for the averaged temperatures can be formally written by means of two-scale expansion.

external energy source to/from the channel. Finally, condition (e) concerns the Brinkman number, guaranteeing that the impact of viscous shear heating is low enough not to conflict with the other transport phenomena.

The applicability region given by conditions (a)–(e) has been determined from the asymptotic solution developed in Appendix C selecting the order of the dimensionless parameters in such a way that they enter the problem at the highest order compatible with the separation of scales. In other words, the set of exponents p, a, k, b and f has been selected accordingly so that a given term enters into the corresponding order of magnitude depending on the transport regime. Those constraints are sufficient conditions which ensure a rigorous thermal decoupling between the transverse and the axial scales. If such constraints are not met, the idea of cross-sectional averaging (3.4) lacks significance and the accuracy of the upscaled model cannot be guaranteed (Boso & Battiato 2013). Note that there exists strategies to relax the applicability conditions, for example, using iterative hybrid numerical methods (see Battiato *et al.* (2011)).

Figure 2 shows the graphical representation of the conditions (b)–(d). Specifically, we can identify three main regimes based of the order of magnitude of the conductivity ratio $\mathcal{K}$. When $\mathcal{K} = \mathcal{O}(1)$, the thermal conductivities are of the same order of magnitude and the problem is described by two coupled ADHT equations (3.8), (3.9); this will be referred to as the coupled regime and it is typical of liquid–liquid systems (see table 1). Instead, when the thermal conductivity of the inner phase is small with respect to that of the outer one ($\mathcal{K} \leqslant \mathcal{O}(\sqrt{\varepsilon})$), the thermal interaction between the phases is negligible and the problem is described by a single ADHT equation for the outer phase, see § 3.2; this will be referred to as the decoupled regime, typical of gas–liquid systems and a few liquid–liquid systems, see table 1. There exists a third regime for $\mathcal{K} \geqslant \mathcal{O}(1/\sqrt{\varepsilon})$ that leads to a single equation for the core averaged temperature. In this work, the latest regime will not be considered, since we are mainly interested in two-phase forced-convection configurations where the inner phase is less conductive with respect to the outer phase.

3.2. *Decoupled regime*

When the thermal conductivity of the outer phase is greater than that of the inner phase, $\mathcal{K} \leqslant \mathcal{O}(\sqrt{\varepsilon})$, the thermal interaction is negligible and the fluid–fluid interface can be

Authors	Core (1)	Annulus (2)	m	ρ_1/ρ_2	$\mathcal{K}$	$\mathcal{A}$
Liquid–liquid						
Kruyer *et al.* (1967)	Transformer oil	Water	17	0.853	0.18	1.84
Hasson (1978)	Water	Kerosene	0.625	1.245	5.18	0.51
Arney *et al.* (1993)	No. 6 fuel oil	Water	2.70×10^{3}	0.989	0.20	2.31
Bannwart *et al.* (2004)	Heavy crude oil	Water	4.15×10^{4}	0.975	0.20	2.09
Gas–liquid						
Cioncolini (2023)	Air	Water	2.08×10^{-2}	1.19×10^{-3}	0.04	6.73×10^{-3}
Guevara & Gotham (1983)	Steam	Water	1.44×10^{-2}	6.00×10^{-4}	0.04	6.77×10^{-3}
Vuong *et al.* (2018)	Nitrogen	Isopar L	1.39×10^{-2}	2.19×10^{-2}	0.20	5.38×10^{-2}
Poesio *et al.* (2009)	Air	Turbine oil	1.54×10^{-5}	1.34×10^{-3}	0.19	3.44×10^{-3}

Table 1. Physical properties of liquid–liquid and gas–liquid core-annular systems taken from the literature. The property ratios m, $\mathcal{K}$, $\mathcal{A}$ denote the viscosity, thermal conductivity and thermal diffusivity ratios, respectively, as defined in (2.14).

considered adiabatic (see the derivation in Appendix C.5.1). Thus, in the moving reference frame $(z,\ \tau)$, (3.8), (3.9) reduce to a single ADHT for the averaged temperature of the outer phase $\langle\vartheta_2\rangle$:

$$\frac{\partial\,\langle\vartheta_2\rangle}{\partial\tau}+(U_2-V)\,\frac{\partial\,\langle\vartheta_2\rangle}{\partial z}=D_2^{\star}\,\frac{\partial^2\,\langle\vartheta_2\rangle}{\partial z^2}+S_2^{\star}, \tag{3.10}$$

where

$$D_2^{\star}=\frac{\varepsilon}{Pe}\left(1+Pe^2\,D_2\right),\qquad S_2^{\star}=\frac{q_w+Br\ W_2^{\star}}{\varepsilon\ Pe\ \beta}, \tag{3.11a–b}$$

are the effective diffusion coefficient and the effective source term, respectively, whose analytical expressions are given in Appendix C.6. The effective coefficients in (3.10) incorporate the impact of the non-uniformity of the velocity profile (2.1b) and thermal boundary conditions at the channel axis (2.8) and at the wall (2.6). Specifically, the shear flow spreads the temperature inhomogeneity along the axial direction, affecting axial heat diffusion at sufficiently large Péclet numbers via the coefficient $D_2^{\star}(V,\ \beta,\ m,\ Pe)$. The effective sink/source term $S_2^{\star}$ consists of two distinct contributions: q_w is the heat flux imposed at the wall, while $W_2^{\star}$ embeds the effect of viscous dissipation. The trends of the effective coefficients and the analytical solution of the thermal problem in the decoupled regime will be discussed in § 4.1.

3.3. *Determination of the convective heat-transfer coefficient*

The local convective heat-transfer coefficient h is defined via Newton's law of cooling as the ratio between the thermal power per unit area entering the system and the difference in temperature between the solid surface and a representative temperature for the fluid $\hat{T}_b$ (Incropera 2007):

$$h\left(\hat{x},\ \hat{t}\right)=\frac{-\,\hat{q}_w''}{\hat{T}_2\Big|_{\hat{y}=\hat{H}}-\hat{T}_b}, \tag{3.12}$$

where $\hat{T}_b$ is the bulk temperature; the estimation of h is provided in the absolute reference frame ($V=0$). The bulk (or mixing-cup or flow average) temperature is the temperature reached when a certain amount of fluid reaches the equilibrium without heat

loss to the surroundings (Tamir & Taitel 1972). It is defined as an enthalpy-weighted average of the phase temperature and for the core-annular flow configuration in figure 1, reads (Su 2006; Chalhub *et al.* 2022)

$$\hat{T}_b\left(\hat{x},\ \hat{t}\right) = \frac{\displaystyle\int_0^{(1-\beta)\hat{H}} \rho_1\, c_{p,\,1}\, \hat{u}_1\, \hat{T}_1\, \mathrm{d}\hat{y} + \int_{(1-\beta)\hat{H}}^{\hat{H}} \rho_2\, c_{p,\,2}\, \hat{u}_2\, \hat{T}_2\, \mathrm{d}\hat{y}}{\displaystyle\int_0^{(1-\beta)\hat{H}} \rho_1\, c_{p,\,1}\, \hat{u}_1\ \mathrm{d}\hat{y} + \int_{(1-\beta)\hat{H}}^{\hat{H}} \rho_2\, c_{p,\,2}\, \hat{u}_2\ \mathrm{d}\hat{y}}. \tag{3.13}$$

Equation (3.12) is made dimensionless using the same scales defined in § 2.2, which gives

$$h\,(x,\ t) = \frac{\kappa_2\ \left.\dfrac{\partial \vartheta_2}{\partial y}\right|_{y=1}}{\hat{H}\left(\vartheta_2|_{y=1} - \vartheta_b\right)}, \tag{3.14}$$

where the dimensionless bulk temperature ϑ_b is given combining (3.13) with (2.12), (3.4),

$$\vartheta_b\,(x,\ t) = \frac{\mathcal{K}\,\mathcal{A}\,(1-\beta)\left\langle u_1(y)\,\vartheta_1(y)\right\rangle + \beta\left\langle u_2(y)\,\vartheta_2(y)\right\rangle}{\mathcal{K}\,\mathcal{A}\,(1-\beta)\,U_1 + \beta\,U_2}. \tag{3.15}$$

Interestingly, the dimensionless group $\mathcal{K}\,\mathcal{A}$ in (3.15) is the volumetric heat capacity ratio: when $\mathcal{K}\,\mathcal{A} \ll 1$, the bulk temperature simplifies significantly and does not depend anymore on the core properties (this is true for the decoupled regime in § 4.2). Since the averaged temperature $\langle\vartheta_2\rangle$ is independent of y, the temperature (and its derivative) at the wall is calculated considering the power-series truncated to the first order as

$$\vartheta_2|_{y=1} = \langle\vartheta_2\rangle + \sqrt{\varepsilon}\ \left.\vartheta_2^{(1)}\right|_{y=1} + \mathcal{O}(\varepsilon), \tag{3.16a}$$

$$\left.\frac{\partial \vartheta_2}{\partial y}\right|_{y=1} = \sqrt{\varepsilon}\ \left.\frac{\partial \vartheta_2^{(1)}}{\partial y}\right|_{y=1} + \mathcal{O}(\varepsilon) = q_w + \mathcal{O}(\varepsilon). \tag{3.16b}$$

In problems of internal forced convection, the heat transfer coefficient is made dimensionless defining the local Nusselt number computed at the wall (Incropera 2007)

$$Nu\,(x,\ t) = \frac{h\,\mathcal{L}}{\kappa_2}, \tag{3.17}$$

where $\mathcal{L}$ is a characteristic length, typically the hydraulic diameter d_{eq}. For the planar configuration depicted in figure 1, the hydraulic diameter can be computed by considering a rectangular slit of width $\hat{w}$ and height $2\hat{H}$, and taking the limit for $\hat{w} \gg 2\hat{H}$ (see, for instance, Merritt 1991),

$$d_{eq} = \lim_{\hat{w}\to\infty} \frac{8\,\hat{H}\,\hat{w}}{2\left(\hat{w} + 2\,\hat{H}\right)} = 4\,\hat{H}. \tag{3.18}$$

Ultimately, the Nusselt number (3.17) can be expressed as

$$Nu\,(x,\ t) = \frac{4\ \left.\dfrac{\partial \vartheta_2}{\partial y}\right|_{y=1}}{\vartheta_2|_{y=1} - \vartheta_b}, \tag{3.19}$$

in view of (3.18) and (3.14). In the following, when the flow is thermally fully developed, we will refer to as the asymptotic (or limiting) Nusselt number Nu^{∞} (Shah & London 1978).

Finally, for the sake of comparison with the literature, we recast the Brinkman number defined in (2.15*b*) (Brinkman 1951; Bird, Stewart & Lightfoot 1960; Boucher & Alves 1963; Shah & London 1978) into

$$Br' = \frac{\mu_2 \, \hat{U}^2}{\left(-\hat{q}''_w\right) \mathcal{L}}. \tag{3.20}$$

In this work, the Brinkman numbers Br and Br' are linked to each other by the following relation:

$$Br = 4 \, q_w \, Br'. \tag{3.21}$$

4. Results and discussion

In this section, we will discuss the heat-transfer model illustrating the main physical mechanisms and deriving a closed-form expression for the Nusselt number for laminar core-annular flows, distinguishing between the decoupled and the coupled regime.

4.1. *Heat-transfer mechanisms and temperature field in the decoupled regime*

As described in § 3.2, the decoupled model (3.10) applies to cases where the thermal conductivity of the outer phase is much bigger compared with that of the inner phase, $\mathcal{K} \leqslant \mathcal{O}(\sqrt{\varepsilon})$. This implies that the inner and the outer phases are thermally decoupled and the model reduces to a 'one-side' approach. Such a scenario is typical of the majority of applications, including gas–liquid and liquid–liquid systems (see table 1).

By inspection of (3.10), we see that the temperature evolves in time and space due to three different mechanisms: advection equal to the average speed of the outer phase U_2, effective thermal diffusion through the coefficient $D_2^{\star}$, and a constant source term $S_2^{\star}$ due to the imposed heat flux at the channel wall and viscous dissipation. Specifically, $D_2^{\star}$ has the typical structure of the Aris–Taylor dispersion coefficient (it scales with the square of the Péclet number), being the sum of heat diffusivity, equal to the unity, and axial shear-induced diffusion, $D_2(V, \beta, m)$ whose expression is given in (C40*b*). The latter is an apparent diffusion mechanism for the averaged temperature and has its physical origin in the non-uniformity of the velocity in the outer phase: from the physical point of view, local advection enhances/reduces the axial diffusion in terms of the leading-order variables.

Figure 3(*a*) shows the evolution of D_2 in a coordinate system moving at the mean speed of the outer phase, $V = U_2$, according to Aris (Aris 1959). In fact, in the decoupled model, thermal dispersion is exclusively driven by the annulus. The presence of the other phase, which acts as a thermal insulator, reduces the effective heat-diffusion compared with the single-phase scenario where $D_2 = 2/105$; such a limit is reached only when the core vanishes, i.e. for $\beta \to 1$. The maximal shear-induced diffusion is obtained in the rigid core limit ($m \to \infty$), where the velocity profile of the annulus is almost linear (see figure 3*a*), maximising the spread of temperature in the axial direction. In the free surface limit ($m \to 0$), instead, the flow in the outer phase is so slow that the shear-induced diffusion becomes negligible.

Due to the many applications that involve confined thin-films (e.g. Craster & Matar (2009); Lavalle *et al.* (2021)), we highlight the thin-film region (TFR) in figure 3(*a*), defined arbitrarily as $\beta \leqslant \sqrt{\varepsilon} \ll 1$. In the TFR, the outer phase is 'thin' enough that D_2

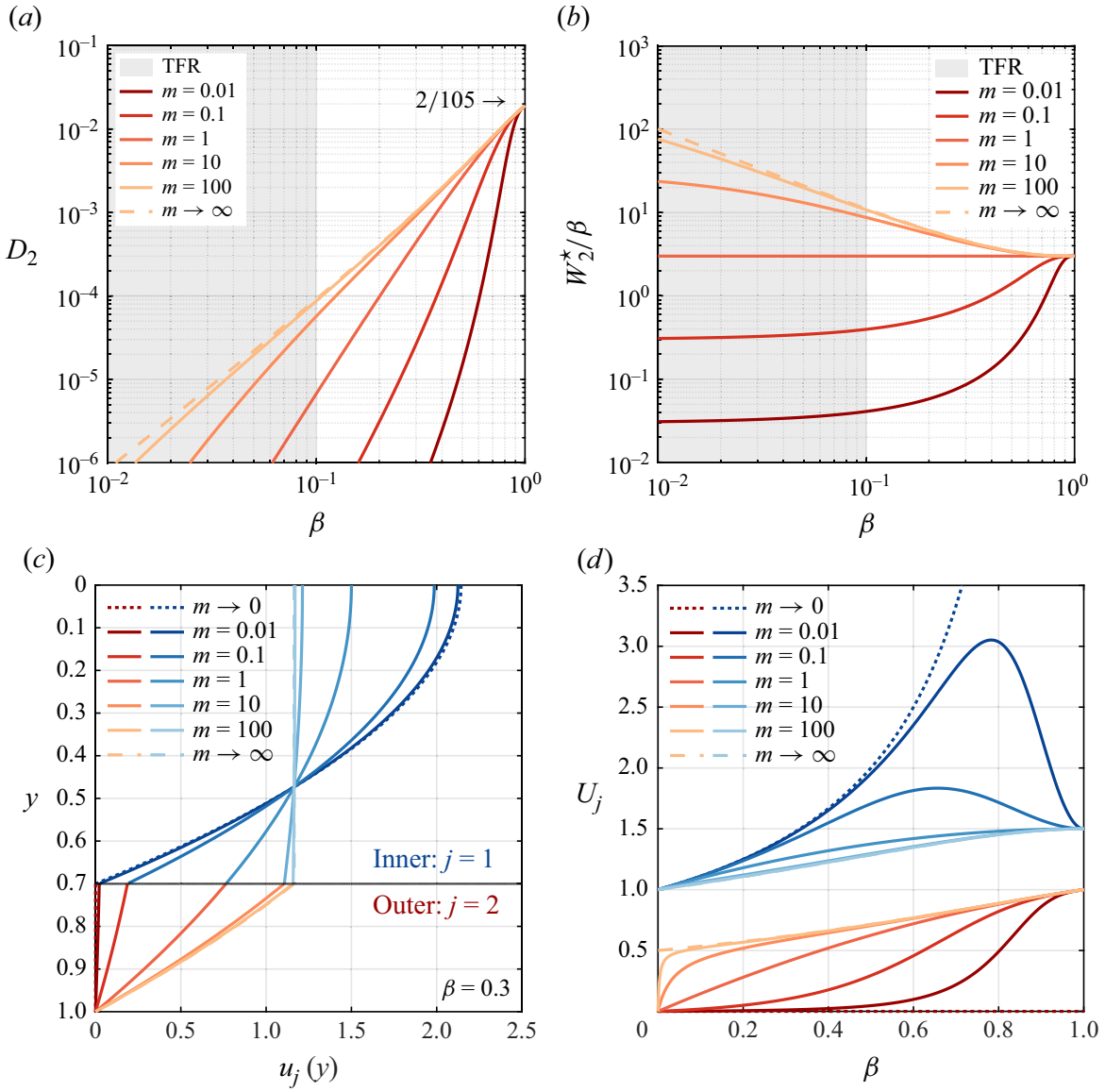

Figure 3. Effect of the viscosity ratio m on (a) D_2 (in the relative reference frame moving at the mean speed of the annulus, $V = U_2$) and (b) the source term related to viscous dissipation $W_2^\star/\beta$, as functions of the volume fraction of the outer phase β. The thin film region (TFR) is highlighted by the grey area. For both the inner ($j = 1$) and the outer ($j = 2$) phase: (c) dimensionless velocity profiles $u_j(y)$ for different values of the viscosity ratio m and a fixed volume fraction $\beta = 0.3$; (d) average speed U_j as a function of β and for different values of m.

can be expanded as

$$D_2(V = U_2,\ \beta \to 0,\ m) = \begin{cases} \dfrac{3\,m^2}{40}\,\beta^4 + \mathcal{O}(\beta^5) & \text{if } m \text{ finite}, \\ \dfrac{1}{120}\beta^2 + \mathcal{O}(\beta^3) & \text{if } m \to \infty, \end{cases} \tag{4.1}$$

showing that the shear-induced diffusion becomes negligibly small in thin films. This can be explained by looking at figure 3(d): when $\beta \to 0$, the speed of the liquid becomes so small that the system is dominated by diffusion.

In general, advection and diffusion compete in the transient dynamics described by (3.10). To quantify this, similarly to Dejam *et al.* (2014) and Ling *et al.* (2016), we introduce the ratio between the effective diffusivity (3.11a) and its single phase limit

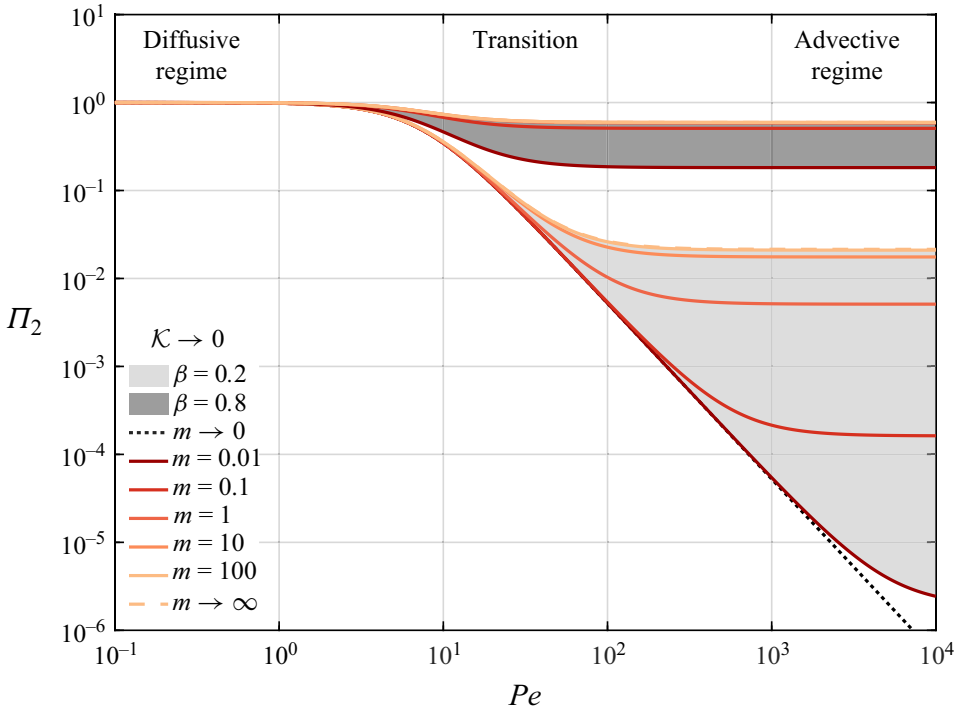

Figure 4. Normalised coefficient of shear-induced thermal diffusivity Π_2 for a decoupled system ($\mathcal{K} \to 0$) – see definition in (4.2) – against the flow Péclet number Pe, for different values of volume fraction β and viscosity ratio m.

(which corresponds to the analogous of the classical Aris–Taylor dispersion coefficient for the thermal problem), $\mathcal{D}_{AT} = 1 + \frac{2}{105}\, Pe^2$ (Horne & Rodriguez 1983; Berkowitz & Zhou 1996; Wang *et al.* 2012):

$$\Pi_2 = \frac{\varepsilon^{-1}\, Pe\, D_2^\star}{\mathcal{D}_{AT}} = \frac{1 + Pe^2\, D_2}{1 + \dfrac{2}{105}\, Pe^2}. \tag{4.2}$$

This normalisation facilitates the identification of different regimes, based on the competition between diffusion and advection, as shown in figure 4, where the evolution of Π_2 with respect to the Péclet number and the viscosity ratio at two fixed volume fractions, $\beta = \{0.2,\ 0.8\}$, is presented. Interestingly, for small Péclet numbers ($Pe < 1$), $\Pi_2 \to 1$ and it is independent of m and β, meaning that advective mixing of thermal energy in the outer phase is negligible compared with heat diffusion. When the Péclet number is sufficiently large, the advection dominates and Π_2 assumes always values lower than unity. This means that the core-annular flow pattern does not enhance heat diffusion compared with single-phase flow, in particular, when the volume fraction is small. Also, the mechanism of shear-induced diffusion becomes negligible in the free-surface limit ($m \to 0$) since the velocity in the outer layer is so small that, regardless of the film thickness β, Π_2 approaches zero without reaching a plateau as $Pe \to \infty$. The regime map in figure 4 can be used in transient multiphase heat-transfer applications to identify a specific set of operational conditions based on fluid and/or flow properties to enhance or reduce heat diffusion.

The source term $S_2^\star$ (3.11*b*) is affected by the dimensionless flux q_w and the Brinkman number Br. In particular, it scales with the inverse of the thickness of the outer phase $S_2^\star \sim q_w/\beta$, meaning that heating a thin film is very effective since thermal energy is delivered to a small volume of fluid. The viscous dissipation $W_2^\star = W_2^\star(\beta,\ m)$ defined in (C28*b, c*), see (C46*c*), contributes to the source term, accounting not only for the viscous

heating produced in the annulus, but also for the production into the core that is exchanged across the interface. As shown in figure 3(*b*), in the free-surface limit ($m \to 0$), the velocity in the annulus is so slow that viscous dissipation is negligible, while for iso-viscous fluids ($m = 1$), $W_2^\star/\beta = 3$ as for single-phase flow. However, in the rigid-core limit ($m \to \infty$), only the outer phase is dissipative and the heat generated due to friction becomes unbounded as the film gets thinner. Due to this singularity around $\beta = 0$, the scaling in the thin-film region can be obtained using Laurent series for $\beta \to 0$ as

$$\frac{W_2^\star}{\beta}\,(\beta \to 0,\ m) = \begin{cases} 3\,m + \mathcal{O}(\beta) & \text{if } m \text{ finite}, \\ \beta^{-1} + 1 + \mathcal{O}(\beta) & \text{if } m \to \infty. \end{cases} \tag{4.3}$$

The ADHT equation (3.10) for the decoupled regime admits an analytical solution, setting the initial temperature of the outer phase to a uniform value over the entire channel half-length $x > 0$ and imposing the same temperature at the inlet $x = 0$ for $t > 0$, i.e. $\langle\vartheta_2\rangle\,(x,\ 0) = \langle\vartheta_2\rangle\,(0,\ t) \equiv 0\ \forall\, x,\ t > 0$, we get – see Carslaw & Jaeger (1959) and Van Genuchten & Alves (1982) –

$$\begin{aligned} \langle\vartheta_2\rangle\,(x,\ t) \quad = \quad & S_2^\star \left\{ t + \frac{(x - U_2\,t)}{2\,U_2}\,\mathrm{erfc}\left[\frac{x - U_2\,t}{2\left(D_2^\star\,t\right)^{\frac{1}{2}}}\right] + \right. \\ & \left. - \frac{(x + U_2\,t)}{2\,U_2}\exp\!\left(\frac{U_2\,x}{D_2^\star}\right)\mathrm{erfc}\left[\frac{x + U_2\,t}{2\left(D_2^\star\,t\right)^{\frac{1}{2}}}\right]\right\}. \end{aligned} \tag{4.4}$$

At long times, the diffusion smears out the temperature profile and the steady-state temperature $\left\langle\vartheta_2^\infty\right\rangle$ becomes a linear function of x (like in classical internal forced-convection problems, see Incropera (2007)) with slope equal to $S_2^\star/U_2$, i.e.

$$\left\langle\vartheta_2^\infty\right\rangle(x) = \lim_{t\to+\infty}\langle\vartheta_2\rangle\,(x,\ t) = \frac{S_2^\star}{U_2}\,x. \tag{4.5}$$

This solution will be used in § 4.2 to derived a closed-form model for the heat-transfer coefficient. Note that, given the solution for the mean temperature (i.e. its leading order), higher order corrections can be easily calculated plugging (4.4) into (C15), (C23).

4.2. *Nusselt number in the decoupled regime*

In the decoupled regime, since $\mathcal{K} \to 0$ and $\mathcal{K}\,\mathcal{A} \lesssim \varepsilon$, the bulk temperature (3.15) simplifies to

$$\vartheta_b\,(x,\ t) = \langle\vartheta_2\rangle + \sqrt{\varepsilon}\,U_2^{-1}\left\langle u_2(y)\,\vartheta_2^{(1)}(y)\right\rangle + \mathcal{O}(\varepsilon). \tag{4.6}$$

Upon substitution of (4.6) in (3.14), the local Nusselt number (3.14) yields

$$Nu\,(x,\ t) = \frac{4\,q_w/\sqrt{\varepsilon}}{\vartheta_2^{(1)}\Big|_{y=1} - U_2^{-1}\left\langle u_2(y)\,\vartheta_2^{(1)}(y)\right\rangle}. \tag{4.7}$$

Equation (4.7) shows how the Nusselt number evolves in space and time and is calculated by plugging the analytical solution (4.4) into the first-order correction (C15) and using the velocity profile for $u_2(y)$, given in (A5*a*). Here, the Nusselt number is studied with respect to the fixed reference frame, in accordance with the literature, where the bulk temperature is always defined in systems with $V = 0$.

The Nusselt number in laminar decoupled core-annular flows with uniform wall heat flux is a function of space, time, the volume fraction, the viscosity ratio, the dimensionless heat-flux, the Brinkman and the Péclet numbers only, i.e. $Nu = Nu(x,\ t,\ \beta,\ m,\ q_w,\ Br',\ Pe)$. The Nusselt number and, as a consequence, the heat-transfer coefficient h depend on the Péclet number only in the transient regime, while at the steady-state, $Nu^\infty = Nu^\infty(\beta,\ m,\ Br')$. Note that, as typical in the heat transfer community (Shah & London 1978), the Péclet number can be seen as the product of the Prandtl and Reynolds numbers, i.e. $Pe = Pr\ Re$, where $Pr = \mu_2/(\rho_2\,\alpha_2)$ and $Re = \rho_2\,\hat{U}\,\hat{H}/\mu_2$, respectively.

When the thermal response reaches the steady state, we get the following expression for the asymptotic Nusselt number Nu^∞, obtained by combining (4.5), (C15) and (4.7),

$$Nu^\infty(\beta,\ m,\ Br') = \frac{280(3-\beta)^2}{\beta\left(\chi\ Br' + 45\,\beta^2 - 245\,\beta + 336\right)}, \tag{4.8}$$

where χ accounts for the contribution of viscous dissipation as

$$\chi = \frac{18\,m\left[3\,m\,\beta\,(7-3\,\beta)^2 - \left(5\,\beta^2 - 35\,\beta + 56\right)(1-\beta)^3\right]}{\left[1+\beta(\beta^2-3\,\beta+3)(m-1)\right]^2}. \tag{4.9}$$

Equation (4.8) shows that, in the absence of viscous dissipation ($Br' = 0$) or – equivalently – in the inviscid limit ($m \to 0$), the asymptotic Nusselt number is uniquely a function of the volume fraction of the outer phase β. Such an expression embeds the effects of viscous flow in both phases and heat-transfer (advection and diffusion) in the outer phase and it has been obtained starting from first principles. In figure 5(a), the Nusselt number in the non-dissipative regime is represented by the solid black line, which converges to the single phase limit of $140/17$ as $\beta \to 1$. Instead, in the dissipative regime, the single-phase limit of Nu^∞ approaches $140/(108\ Br' + 17)$ according to (278) of Shah & London (1978).

The viscosity ratio impacts Nu^∞ only in the dissipative regime, as shown in figure 5(a) for $Br' = 1$. Interestingly, when the viscosity ratio m is sufficiently large (but finite), there exists conditions where viscous heating ($Br' > 0$) prevails over the wall heat flux ($q_w > 0$), and the bulk temperature becomes greater than the wall temperature, $\vartheta_2|_{y=1} - \vartheta_b < 0$, reversing the direction of the heat exchange. When this happens, the heat-transfer coefficient h becomes negative, see (3.14), and the singularity of the Nusselt number represents the limiting situation where $\vartheta_2|_{y=1} = \vartheta_b$. The critical value of volume fraction $\overline{\beta} = \beta(m,\ Br')$ which determines the position of the vertical asymptote can be calculated by finding the zeros of the denominator in (4.8) numerically. To ensure that the Nusselt number remains positive in the entire film thickness range ($0 < \beta < 1$), the viscosity ratio and the Brinkman number have to satisfy the inequality $\chi\ Br' > -91/36$.

Finally, it is interesting to observe that the asymptotic Nusselt number in the TFR scales as follows:

$$Nu^\infty(\beta \to 0,\ m,\ Br' \neq 0) = \begin{cases} \dfrac{15}{2\left(1-3\,m\ Br'\right)}\,\beta^{-1} + \mathcal{O}(1) + \ldots & \text{if } m \text{ finite}, \\ \dfrac{60}{7\ Br'} + \mathcal{O}(\beta) & \text{if } m \to \infty, \end{cases} \tag{4.10}$$

while for non-dissipative flows ($Br' = 0$), we get that $Nu^\infty \sim 15/(2\,\beta)$. In the finite-viscosity regimes, the asymptotic Nusselt number Nu^∞ shows a singularity. Specifically,

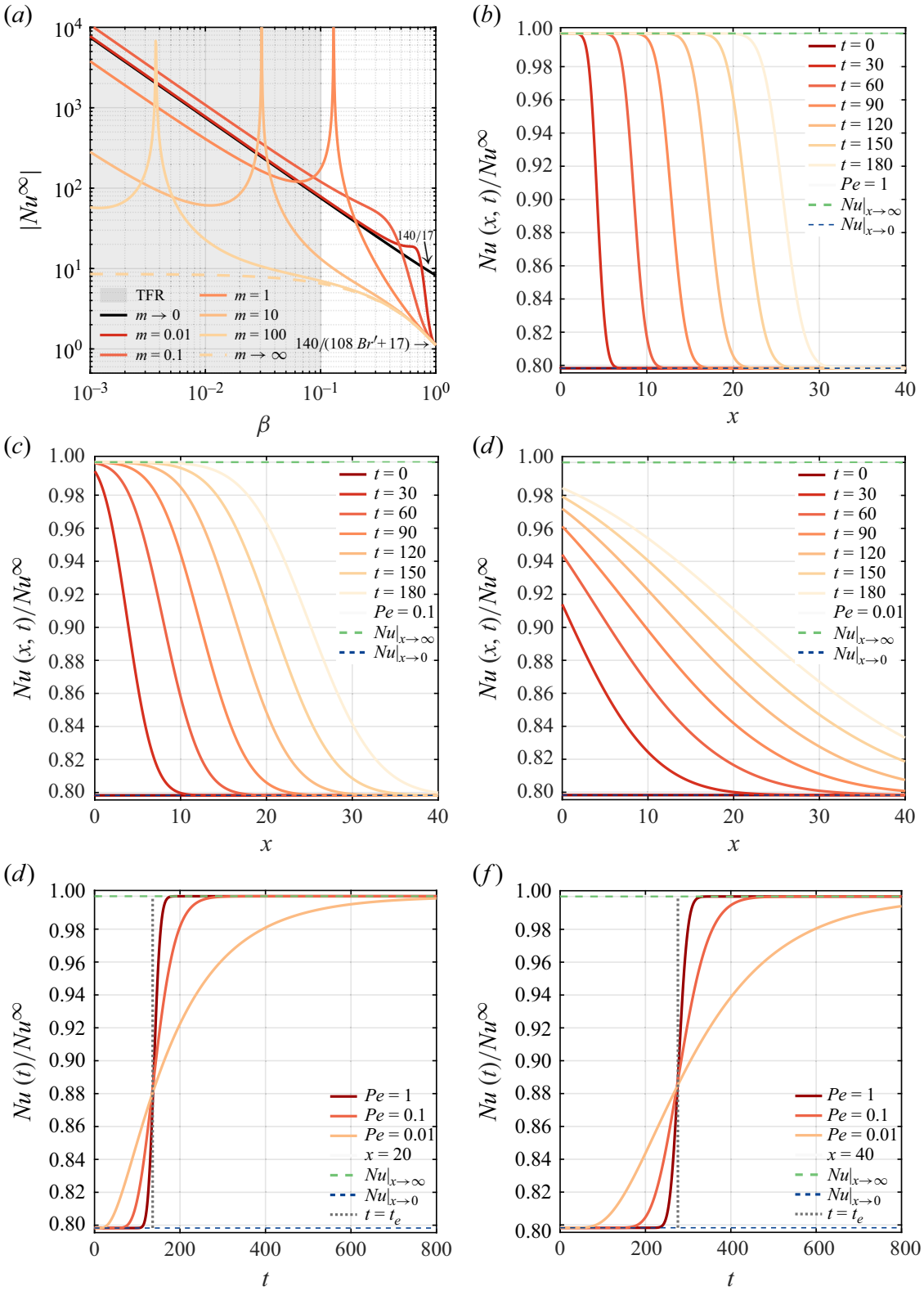

Figure 5. (*a*) Dependence of the asymptotic Nusselt number Nu^∞ (absolute value) on the volume fraction β, for fixed viscosity ratios m and $Br' = 1$. Evolution of the normalised Nusselt number Nu/Nu^∞: over space at fixed times and Péclet numbers – (*b*) $Pe = 1$, (*c*) $Pe = 0.1$, (*d*) $Pe = 0.01$ – over time and across the transport regimes at fixed axial locations – (*e*) $x = 20$, (*f*) $x = 40$, with $\varepsilon = 0.01$, $Br' = 0$, $q_w = \beta = 0.1$, $m = 1$.

increasing m shifts the position of the vertical asymptote towards lower values of β, and a larger number of terms in the expansion (4.10) is required to ensure the convergence of the series to (4.8).

The time and spatial evolution of the local Nusselt number, normalised with respect to its asymptotic value for $t \to \infty$, i.e. Nu/Nu^{∞}, is shown in figure 5(*b–d*) for different Péclet numbers. The resulting plots have the form of S-shaped breakthrough curves and they are bounded between two horizontal asymptotes: the upper one denotes the asymptotic Nusselt number, while the lower one corresponds to the Nusselt number predicted by (4.7) at the initial time instant, $t = 0$. At sufficiently high Péclet numbers, the S-shaped curves are almost rigidly transported by the flow over time, indicating an advective-dominated behaviour; a reduction of the Péclet number leads to a diffusion-dominated regime (see figure 4).

To determine how the advective and diffusive mechanisms compete in the transient dynamics, we plot the normalised Nusselt number for the different transport regimes considered in figure 5(*b–d*) over an extended time interval at two fixed positions along the channel: $x = 20$ (half-length of the channel) and $x = 40$ (end of the channel). At high Péclet numbers ($Pe = 1$), the heat is primarily advected downstream and the system quickly reaches the fully developed condition. This means that the heat transfer is quite efficient due to the strong influence of advection. Conversely, decreasing the Péclet number ($Pe = \{0.1,\ 0.01\}$) results in a slower increase of the Nusselt number due to the effect of diffusion. An interesting feature in both figures 5(*e*) and 5(*f*) is the existence of a common intersection point between all the curves at $t = t_e$ that is independent of the value of the Péclet number. For $t > t_e$, the Nusselt number increases with the Péclet number, whereas for $t < t_e$, the behaviour of the system is reversed. At a fixed axial position, the curves appear to pivot around this point.

4.3. *Hierarchy of time scales in thermal dispersion*

The trends illustrated in figure 5 also reflect the development of the forced-convective thermal boundary layer, similarly to the single-phase scenario (Siegel & Sparrow 1959; Siegel & Perlmutter 1963; Fakoor-Pakdaman *et al.* 2014). As time elapses, the thermal boundary layer progressively penetrates and fills up the thickness β occupied by the annulus. As a result, increasingly larger distances after $x = 0$ become thermally fully developed. In fact, since a finite amount of time, $t^* = x^*/U_2$, is required for the entrance fluid to be advected downstream and reach the axial position x^*, beyond this coordinate, $x \geqslant x^*$, there has not been any penetration of the fluid which was originally outside the channel before the start of the transient (at $t = 0$). For $x < x^*$, the thermal problem reaches its long-time thermal behaviour (linear temperature profile and constant Nusselt number).

Similarly to mass transfer (Allaire, Mikelić & Piatnitski 2010; Feder, Flekkøy & Hansen 2022), the thermal mixing is enhanced in regimes where diffusion has had time to even out the transverse variations of temperature (across the layer) while there are still longitudinal variations at the large scale (along it). Referring to the time scales introduced in § 2.2 and choosing the advective characteristic time scale $\hat{\tau}_a$ as the reference time, we obtain the following time scale hierarchy valid for the decoupled model (with $j = 2$ and $\mathcal{K} \to 0$):

$$\tau_{\hat{H},\,2} \ll \tau_{a,\,2} \ll \tau_{\hat{L},\,2} \qquad \Rightarrow \qquad \varepsilon\, Pe\, \beta^2 \ll U_2 \ll \frac{Pe}{\varepsilon}. \tag{4.11}$$

By inspection of (4.11), we can conclude that if the channel is sufficiently shallow ($\varepsilon \to 0$), these three times scales are sharply separated over a wide range of Péclet numbers, as shown in figure 6. In particular, since the mean velocity of the annulus is bounded between 0 and 1, i.e. $0 \leqslant U_2 \leqslant 1$ (see figure 3*d*), thermal dispersion is observed for times of the order of $\hat{\tau}_a$ whenever $Pe \gtrsim \varepsilon$. For smaller Péclet numbers, the problem approaches its purely diffusive limit, where mixing is not influenced by shear-induced mechanisms. Interestingly, in the inviscid limit ($m \to 0$), the outer phase is almost at rest

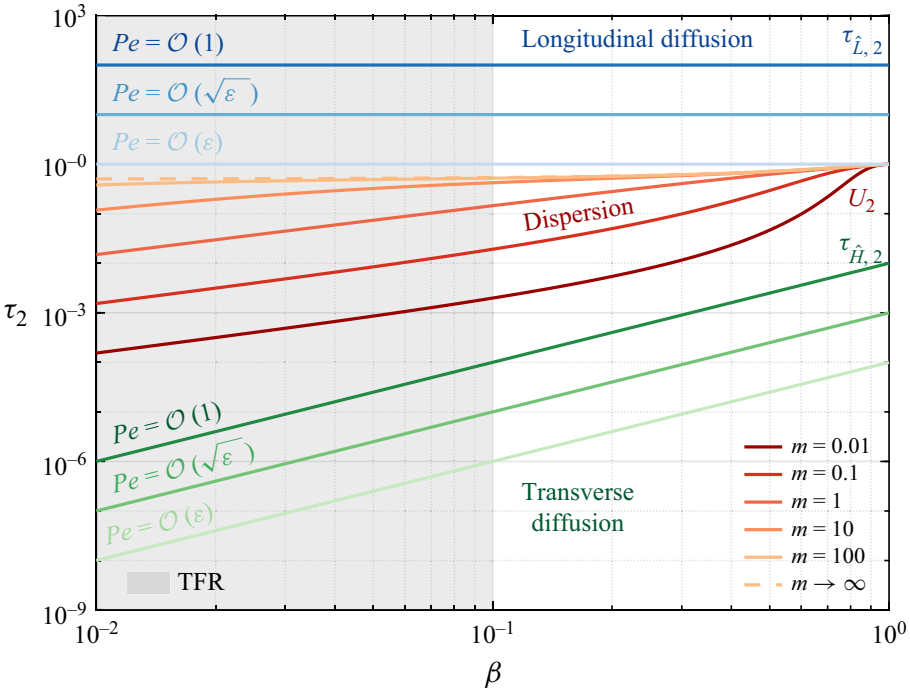

Figure 6. Time scale hierarchy and corresponding dominant heat-transfer mechanisms for the decoupled model ($\mathcal{K} \to 0$) as a function of the volume fraction β at different viscosity ratio m and Péclet number Pe. $\tau_2 = \{\tau_{\hat{H},2},\ U_2,\ \tau_{\hat{L},2}\}$ are the characteristic times of transverse diffusion, advection (average speed of the annulus) and longitudinal diffusion, see (4.11), respectively. The dispersion regime is characterised by the dynamical competition between longitudinal advection and diffusion. $\varepsilon = 0.01$.

($U_2 \to 0$) and does not experience any shear-induced mixing, while in the TFR limit, the outer phase is so thin that transverse diffusion is almost instantaneous ($\tau_{\hat{H},2} \to 0$ as $\beta \to 0$) at any Pe.

Finally, it is worth recalling that our analysis cannot describe the early-time dynamics of the system – which may be referred to as pre-asymptotic dispersion regime (Young & Jones 1991; Taghizadeh *et al.* 2020) – and the upscaled model (3.10) holds only at times that are much greater than $\tau_{\hat{H},2}$, i.e. $t \gg \varepsilon\, Pe\, \beta^2$, holding no memory from the initial conditions (Ananthakrishnan, Gill & Barduhn 1965; Sankarasubramanian, Gill & Benjamin 1973; Fallon & Chauhan 2005).

4.4. *Ramifications for the modelling of thin films and Taylor bubbles*

In some circumstances, the modelling of flow patterns, such as intermittent slug flow, relies on an idealisation of the liquid film region, borrowing closure relations from core-annular flows (see for example, Balestra, Zhu & Gallaire (2018); Picchi *et al.* (2018)). Taylor bubble flow, in fact, consists of a sequence of liquid slugs and elongated bubbles, and – if the bubble is sufficiently long – a region of uniform film thickness forms, which can be considered, as a first approximation, a (local) region of fully developed core-annular flow. This approach neglects the evolution of the thin-film typical of Bretherton's problem (Bretherton 1961), while preserving model simplicity. In the context of heat transfer, the widely used three-zone model developed by Thome *et al.* (2004) and Dupont, Thome & Jacobi (2004) assumes that the film region of an evaporating/condensing Taylor bubble can be treated in this way.

Specifically, the heat transfer coefficient between the thin film surrounding a Taylor bubble and the channel wall is modelled as $h = \kappa_2/\delta$ (where δ is the film thickness) considering only the heat conduction in the transverse direction (across the film) at the

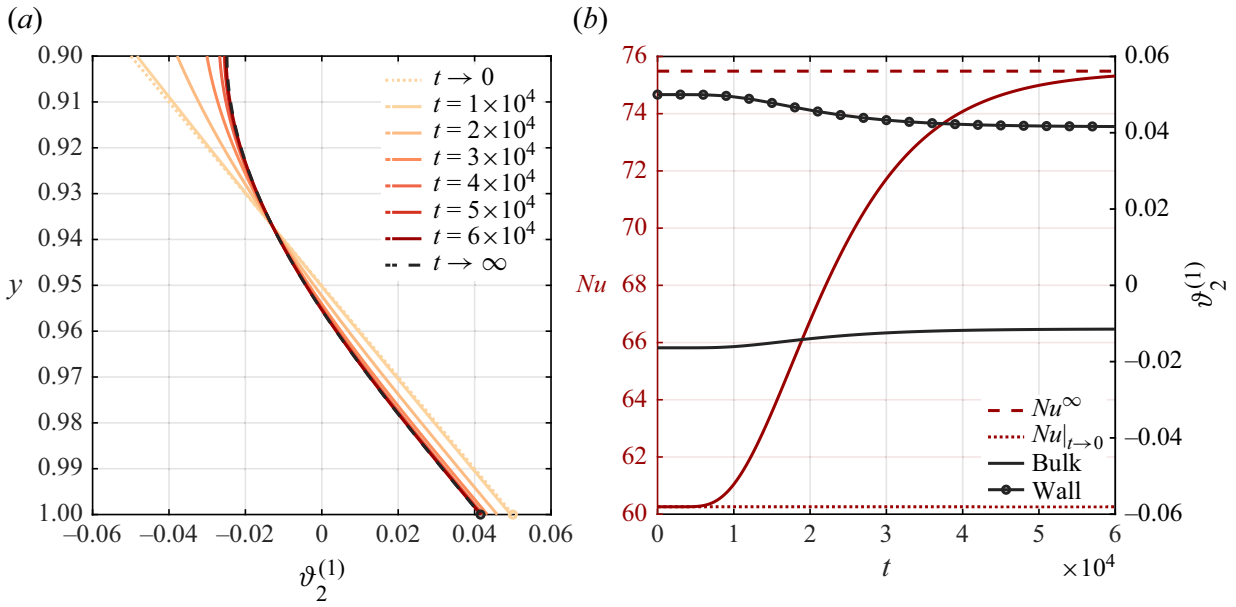

Figure 7. (*a*) Transient evolution of the first-order correction of the temperature profile of the annulus $\vartheta_2^{(1)}$ in the decoupled regime at $x = 40$, for $\beta = 0.1$, $m = 0.01$, $\varepsilon = 0.01$, $Pe = 1$, $q_w = 0.1$ and $Br = Br' = 0$. (*b*) Right ordinate: time evolution of the wall temperature ($\vartheta_2^{(1)}|_{y=1}$, black solid lines with circles) and the bulk temperature ($U_2^{-1}\,\langle u_2\,\vartheta_2^{(1)}\rangle$, black solid line). Left ordinate: Nusselt number (4.7). The lower asymptote (dotted line) identifies the starting Nusselt number, $Nu|_{t\to0} = 16(3-\beta)\beta^{-1}(8-3\,\beta)^{-1}$; the upper asymptote (dashed line) denotes the fully developed Nusselt number Nu^∞ (4.8).

steady-state and neglecting the impact of advection (see Dupont *et al.* (2004); Thome *et al.* (2004); Dai *et al.* (2015); Magnini & Thome (2017); Zhang & Nikolayev (2023)). In this way, the heat-transfer coefficient is obtained by assuming a linear temperature profile in the film. The results presented in § 4.2 can be used to check the validity of this hypothesis. Combining (4.10) with (3.14) and (3.19), we obtain the following scaling law for the steady-state heat-transfer coefficient of core-annular flows in a planar geometry:

$$h = \frac{15}{8}\,\frac{\kappa_2}{\beta\,\hat{H}}. \tag{4.12}$$

At the steady-state, h is a function of the fluid conductivity and the film thickness only, i.e. $h = h(\kappa_2,\ \beta\hat{H})$. Our analysis confirms that the heat-transfer is primarily driven by conduction in the film, and the temperature profile remains almost linear along the transverse direction: when the film is thin enough, the dynamic effects due to the flow are negligible, see figure 3(*d*), $U_2 \to 0$ as $\beta \to 0$. This can be easily shown combining (C15) with the steady-state axial derivative of the averaged temperature (4.4) for $Br = 0$,

$$\vartheta_2^{(1)}\Big|_{t\to\infty} = \frac{q_w}{\sqrt{\varepsilon}}\left[\frac{5\,(3+y)\,(1-y)^3 - \beta^3\,(5-\beta)}{20\,\beta^2\,(3-\beta)} + y + \frac{\beta}{2} - 1\right], \tag{4.13}$$

as plotted in figure 7(*a*). The temperature profile is almost linear in proximity of the wall, while it flattens out at the interface where the heat-flux is zero; this behaviour is embedded in the numerical factor 15/8 in (4.12).

However, in regimes where the film thickness is not small compared with the channel size (Aussillous & Quéré 2000), the flow in the film is not negligible, and the Nusselt number should be estimated using (4.8) instead of (4.12). In addition, accounting for transient effects would introduce the dependence of the Péclet number into the problem – see figure 7(*b*).

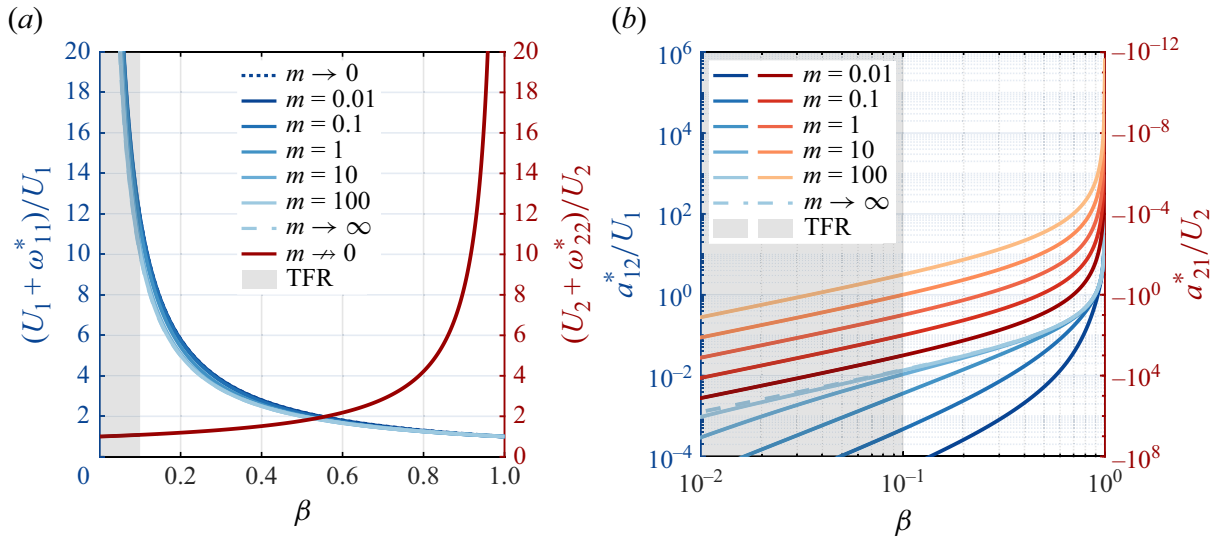

Figure 8. Effective coefficients of advection as functions of the volume fraction β, for different viscosity ratios m, when $\mathcal{K} = 1$ in the absolute reference frame ($V = 0$). (a) Advective coefficients normalised with the mean flow speed, i.e. $a^\star_{jj}/U_j$: $j = 1$ (left) and $j = 2$ (right). (b) Coefficients of coupled advection $a^\star_{12}/U_1$ (left) and $a^\star_{21}/U_2$ (right). Those coefficients are independent of the speed of the reference frame.

4.5. *Heat-transfer mechanisms and temperature field in the coupled regime*

When the thermal conductivities of the two phases are of the same order, $\mathcal{K} = \mathcal{O}(1)$, the heat transfer problem is described by two coupled ADHT equations (3.8), (3.9). Differently from the decoupled regime, the phases can exchange energy through the fluid–fluid interface. By inspection of (3.8), (3.9), we see that the temperatures evolve in time and space due to three different mechanisms: advection, diffusion and storage/source terms. Specifically, each ADHT equation shows (i) a canonical and a coupled effective advection term; (ii) a canonical and a cross-coupling effective diffusion term; (iii) storage and source terms. In the following, we elucidate the physical interpretation of those effective coefficients to describe the main heat-transfer mechanisms of the coupled regime.

The evolution of the advection coefficient $a^\star_{jj} = U_j + \omega^\star_{jj}$ is shown in figure 8(a) in the fixed reference frame ($V = 0$). For each phase, the advection can be written as the sum of the mean phase velocity and an extra contribution due to phase coupling. When β is small, the lubrication effect of the thin annulus enhances the effective advection of the core that scales as β^{-1} and it is not affected by the viscosity ratio. The coupling advective coefficients $a^\star_{ij}$ appear in each ADHT due to the continuity of temperature at the fluid–fluid interface (see § C.5.2) and link one phase with the advection of the other one. Those coupling coefficients are plotted in figure 8(b): when β is small (in the TFR), the coupled advection in the core becomes negligible, $a^\star_{12} \to 0$, and, therefore, axial temperature gradients of the annulus do not directly affect the core. Instead, regardless of the value of β, $a^\star_{21} \to 0$ in the rigid-core limit (for $m \to \infty$), where the velocity profile in the core is almost flat, see figure 3(c), and does not trigger any coupled advection mechanism.

To investigate the diffusive mechanisms, we can think of heat transfer in the flowing phases via an electrical circuit analogy, as shown in figure 9(a). Specifically, the core-annular flow is represented by a parallel connection of resistors with a specific thermal conductance equal to G_1 and G_2; the equivalent conductance is then $G_{eq} = G_1 + G_2$. In this framework, we can recast the diffusive coefficients in analogy with the Aris–Taylor

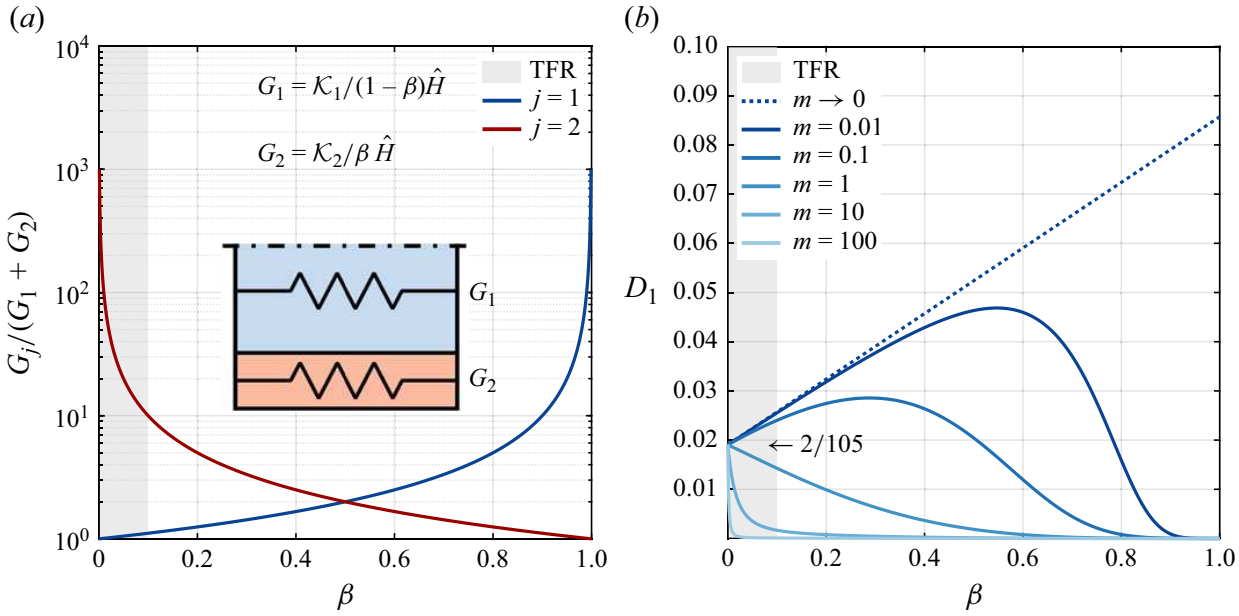

Figure 9. (*a*) Conductance ratios G_j/G_{eq} as functions of the volume fraction β, for $\mathcal{K} = 1$. (*b*) Effective coefficients of diffusion as functions of β, for different values of the viscosity ratio m, when $\mathcal{K} = 1$, in the reference frame moving at the mean flow speed ($V = 1$).

formalism to highlight the contribution of heat- and shear-induced diffusion as

$$d_{11}^\star = \underbrace{\frac{G_1}{G_{\mathrm{eq}}}}_{\text{(i)}} + Pe^2 \underbrace{\left(D_1 + \delta_{jj}^\star\right)}_{\text{(ii)}}, \qquad d_{22}^\star = \underbrace{\frac{G_2}{G_{\mathrm{eq}}}}_{\text{(i)}} + \mathcal{A}^2\, Pe^2 \underbrace{\left(D_2 + \delta_{22}^\star\right)}_{\text{(ii)}}, \tag{4.14a–b}$$

The first contribution, (i), is a volume-weighted average of the thermal conductivities of the individual phases and recalls the typical effective description proposed by Maxwell for the heat diffusion coefficient of composites (Maxwell 1873); its evolution with the volume fraction is shown figure 9(*a*), where we set $\mathcal{K} = 1$. Note that the ratio G_j/G_{eq} also appears in front of each time term in (3.8), (3.9), representing the thermal inertia of the phases, i.e. their capacity to store heat and delay its transmission. In the limit of $\mathcal{K} \to 0$, the ratio G_2/G_{eq} equals unity and the coefficient reduces to one discussed for the decoupled model. The second contribution in the effective diffusive coefficients, (ii), accounts for the shear-induced diffusion, D_1 and D_2, and the coupling between the phases via the terms $\delta_{jj}^\star$. Both the effective diffusion coefficients scale with the square of the Péclet number, while the extra contribution due to the interaction is specific of this class of coupled-layers problems since it enter the ADHT equations by imposing the continuity of temperatures at the fluid–fluid interface (see the derivation in § C.5.2). Those terms are quadratic expressions in the speed of the moving reference frame, V, see (C41), consistent with previous works in the context of mass diffusion, e.g. see Aris (1959).

The evolution of D_2 with β and m has been discussed in § 4.1, figure 3(*a*), while the shear-induced diffusion for the core, D_1, is plotted in figure 9(*b*) setting $V = 1$. Specifically, in the rigid-core limit, $m \to \infty$, the shear-induced diffusion becomes negligible since the inner phase has a flat velocity profile, see figure 3(*c*), preventing any extra spreading across the axial direction rather than heat diffusion. Conversely, in the free-surface limit, $m \to 0$, the outer phase is almost at rest and behaves like a static coating: D_1 increases linearly with the thickness β as

$$D_1(V = 1,\ m \to 0) = \frac{2}{105} + \frac{\beta}{15}, \tag{4.15}$$

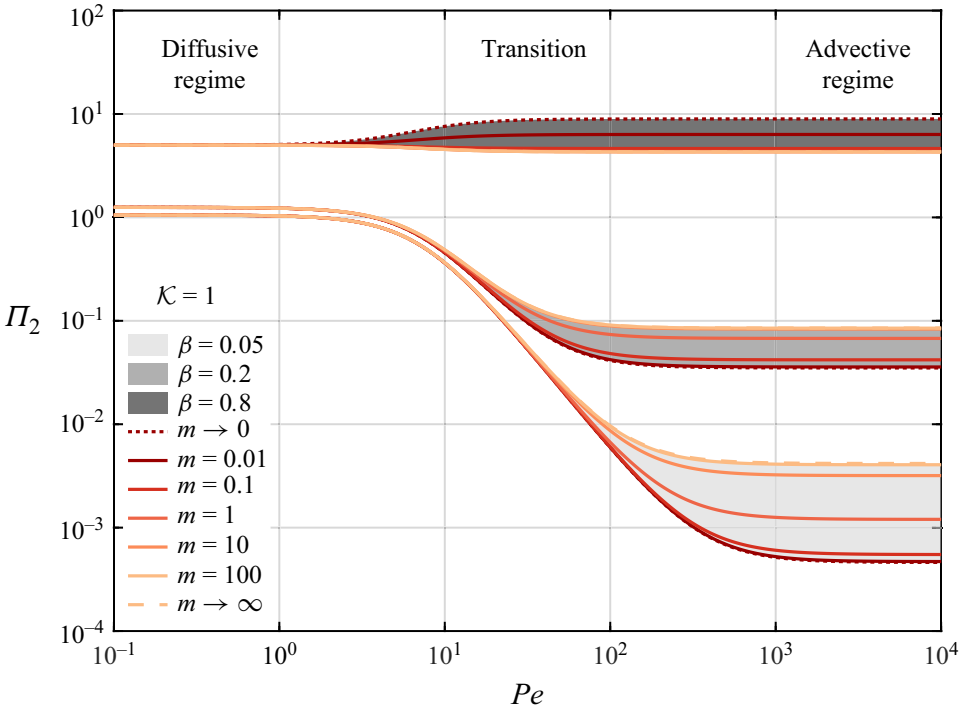

Figure 10. Normalised coefficient of shear-induced thermal conductivity Π_2 for the outer phase of core-annular flows ($\mathcal{K} = 1$) against the flow Péclet number Pe, for different values of volume fraction β and viscosity ratio m.

showing that a thinner core will result in higher transverse variations in its velocity profile, promoting the shear-induced axial diffusion mechanism. As expected, the single-phase limit of $2/105$ is recovered when $\beta \to 0$.

To explore the influence of the flow parameters (m, β, Pe, $\mathcal{K}$, $\mathcal{A}$) on the heat-transfer mechanisms in the coupled regime, we set $V = 1$ and study the ratio between the coefficient of shear-induced thermal diffusivity in (4.14) and its single-phase limit, $\Pi_j = d^\star_{jj}/\mathcal{D}_{\mathrm{AT},\,j}$, similarly to what done in § 4.1:

$$\Pi_1 = \frac{1 + \dfrac{1-\beta}{K\,\beta} + \mathcal{A}^2 Pe^2\left(D_1 + \delta^\star_{11}\right)}{1 + \dfrac{2}{105}\,\mathcal{A}^2\,Pe^2}, \qquad \Pi_2 = \frac{1 + \dfrac{K\,\beta}{1-\beta} + Pe^2\left(D_2 + \delta^\star_{22}\right)}{1 + \dfrac{2}{105}\,Pe^2}. \tag{4.16a–b}$$

The evolution of Π_2 against the Péclet number is shown in figure 10, varying the viscosity ratio m for three different volume fractions $\beta = \{0.05,\ 0.2,\ 0.8\}$; the conductivity ratio $\mathcal{K}$ has been set to unity. The normalised diffusion coefficient of the outer phase has the form of an S-shaped curve and allows the identification of a diffusion-dominated and an advection-dominated regime. Differently from the decoupled model, the purely diffusive regime is characterised by a limiting value that exceeds unity, i.e. $\Pi_2 \to 1 + K\,\beta/(1-\beta)$ for $Pe \to 0$, and equal to the conductance ratio G_2/G_{eq}, see the expression of $t^\star_2$ given in (C38). The advective limit is strongly affected by the viscosity ratio and the volume fractions. Specifically, when the thickness β is small, the combined effect of advection and the coupling between phases reduces the diffusion coefficients compared with the case of single-phase flow. This effect is more pronounced in the free-surface than in the rigid-core limit. When the annulus is thick enough, instead, Π_2 can overcome the purely diffusive limit for sufficiently small values of the viscosity ratio m. The shear-induced diffusion ratio

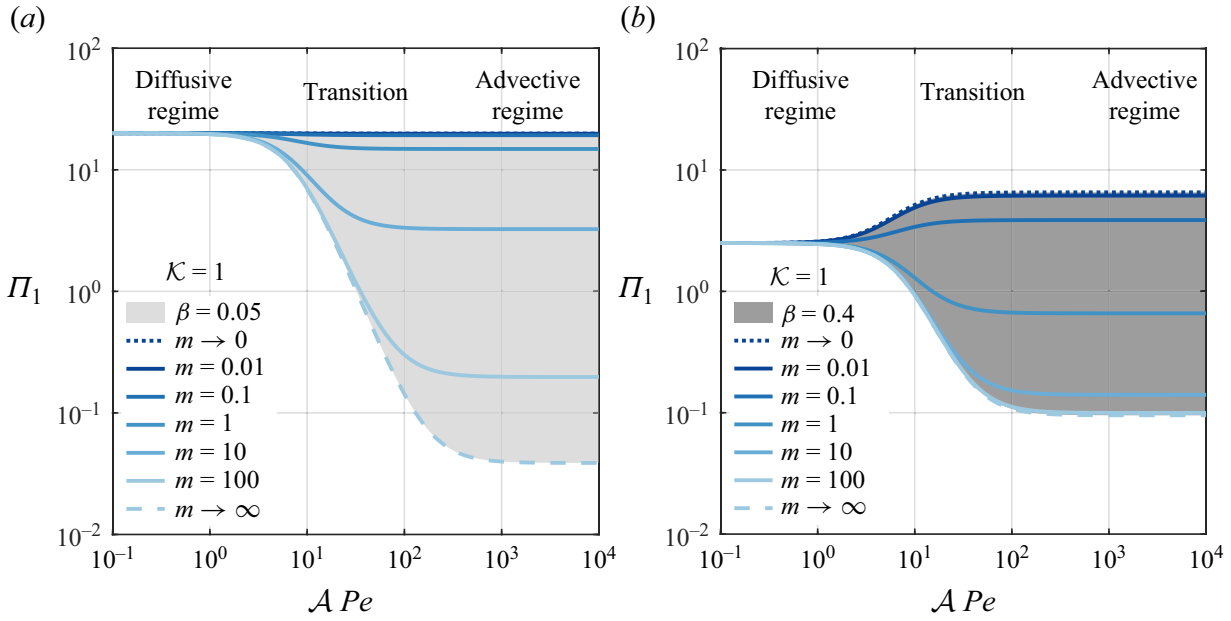

Figure 11. Normalised coefficient of shear-induced thermal diffusivity Π_1 for the inner phase of core-annular flows ($\mathcal{K} = 1$) against the flow Péclet number $\mathcal{A}\,Pe$, for different values of viscosity ratio m, setting the volume fraction to (*a*) $\beta = 0.05$ and (*b*) $\beta = 0.4$.

for the inner phase Π_1 shows a similar behaviour, as presented in figure 11: at low Péclet numbers, $\Pi_1 \to G_1/G_{\rm eq} = 1 + (1-\beta)/(K\,\beta)$, see the expression of $t_1^\star$ given in (C38). However, in the advective regime, the shear-induced diffusion in the core is minimal in the rigid-core limit, where transverse variations of velocity are negligible.

A similar analysis can be done for the cross-coupling diffusive terms $Pe^2\,d_{12}^\star$ and $\mathcal{A}^2\,Pe^2\,d_{21}^\star$ in (3.8), (3.9), introducing the following ratios:

$$\Pi_{12} = \frac{Pe^2\,d_{12}^\star}{1 + \dfrac{2}{105}\,Pe^2}, \qquad \Pi_{21} = \frac{\mathcal{A}^2\,Pe^2\,d_{21}^\star}{1 + \dfrac{2}{105}\,\mathcal{A}^2\,Pe^2}. \tag{4.17a-b}$$

The physical origin of these coupling terms is due to advection only, as can be seen in figure 12. Both coefficients, in fact, tend to zero in the purely diffusive regime ($Pe \to 0$) and play a role only when advection is important, i.e. at high Péclet numbers. Note that the coupling terms enter the model when the temperature continuity is enforced, see Appendix C.5.2, suggesting that, at high Péclet numbers, heat diffusion in one phase is influenced by diffusion in the other one and *vice versa*. This mechanism can either play as negative diffusion (with respect to a reference frame that moves with the mean flow $V = 1$, and, therefore, the core is always faster than the annulus), as in the case of the annulus, see figure 12(*a*), or either enhance or reduce diffusion depending on m and β in the case of the core, see figure 12(*b*).

Finally, we study the source terms in (3.8), (3.9) to interpret how the external source of energy q_w affects the model. To do so, observing that the source terms are identical up to a factor equal to K^2, i.e. $K^2\,e_1^\star = e_2^\star$, see (C45), and are opposite-signed, we consider the linear combination, K^2 (3.8) + (3.9), so that the exchange terms cancel out to obtain

$$\frac{q_w}{\varepsilon}\left(K^2 g_1^\star + g_2^\star\right) = \frac{q_w\,\hat{H}}{\varepsilon\,\kappa_2}\,(G_1 + G_2) = \frac{q_w\,\hat{H}}{\varepsilon\,\kappa_2}\,G_{eq}. \tag{4.18}$$

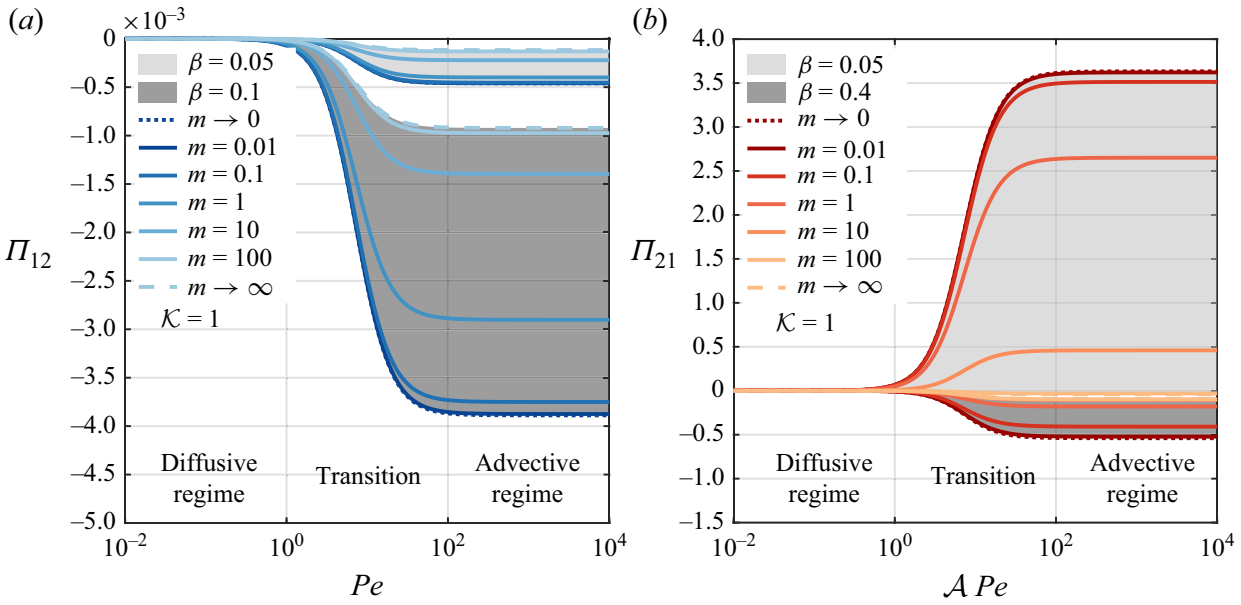

Figure 12. Normalised coefficients of cross-coupling diffusivity, (*a*) Π_{12} and (*b*) Π_{21}, for a core-annular system ($\mathcal{K}=1$) against the corresponding flow Péclet number, for different values of viscosity ratio m and volume fraction β.

The resulting source term is the imposed heat flux at the channel wall multiplied by the sum of the two thermal conductances, see figure 9(*a*), confirming the consistency of our model. In other words, in the equation for the annulus, the source term is positive and greater with respect to the decoupled model by a factor $3\,K/2(1-\beta)>0$ – see (C44) – while in the core, the source term is negative, $-K/2(1-\beta)<0$, so as to preserve the continuity of the temperature and the thermal flux across the interface. Overall, the energy entering both layers is equal to (4.18) and consistent with the imposed boundary conditions (2.16).

4.6. *Transient and steady-state temperature field in the coupled regime*

In the coupled regime, the system of coupled ADHT equations (3.8), (3.9) can be solved numerically and admits an analytical solution only at the steady state.

At the steady state, in fact, diffusion smears out any sharp differences of temperature, and the solution $\langle\vartheta_j^\infty\rangle(x)$, $j=\{1,\ 2\}$, can be derived by setting to zero the time derivatives and diffusive terms in (3.8), (3.9), yielding an inhomogeneous system of linear first-order ordinary differential equations (ODEs), which can be recast via a linear combination as

$$\begin{cases} \dfrac{\mathrm{d}\langle\vartheta_1^\infty\rangle}{\mathrm{d}x} = \eta_1\left(\langle\vartheta_1^\infty\rangle - \langle\vartheta_2^\infty\rangle\right) + \gamma_1, \\ \dfrac{\mathrm{d}\langle\vartheta_2^\infty\rangle}{\mathrm{d}x} = \eta_2\left(\langle\vartheta_1^\infty\rangle - \langle\vartheta_2^\infty\rangle\right) + \gamma_2, \end{cases} \tag{4.19a,b}$$

where

$$\lambda = \varepsilon\left(a_{11}^\star\, a_{22}^\star - a_{12}^\star\, a_{21}^\star\right), \quad \eta_1 = -\frac{a_{22}^\star\, e_1^\star + a_{12}^\star\, e_2^\star}{\mathcal{A}\,Pe\,\lambda}, \quad \eta_2 = \frac{a_{21}^\star\, e_1^\star + a_{11}^\star\, e_2^\star}{Pe\,\lambda}, \tag{4.20a}$$

$$\gamma_1 = \frac{\left(a_{22}^\star\, w_1^\star - a_{12}^\star\, w_2^\star\right) Br + \left(a_{22}^\star\, g_1^\star - a_{12}^\star\, g_2^\star\right) q_w}{\mathcal{A}\, Pe\, \lambda}, \tag{4.20b}$$

$$\gamma_2 = \frac{\left(-a_{21}^\star\, w_1^\star + a_{11}^\star\, w_2^\star\right) Br + \left(-a_{21}^\star\, g_1^\star + a_{11}^\star\, g_2^\star\right) q_w}{Pe\, \lambda}. \tag{4.20c}$$

A particular solution to system (4.19) (see Kamke (1977); Polyanin & Zaitsev (2017)) is represented by two parallel lines of slope M and intercepts Q_j:

$$\left\langle \vartheta_j^\infty \right\rangle (x) = Mx + Q_j, \quad \text{with} \quad M = \frac{\eta_1\, \gamma_2 - \eta_2\, \gamma_1}{\eta_1 - \eta_2}, \quad Q_j = -\frac{\eta_j\, (\gamma_1 - \gamma_2)}{(\eta_1 - \eta_2)^2}, \tag{4.21}$$

meaning that, at the steady state, the temperature of both phases increases linearly in the axial direction with slope equal to $M(q_w/Pe,\ \beta,\ m,\ \mathcal{K}\mathcal{A},\ Br')$ given by

$$M = \frac{2\, q_w}{\varepsilon\, Pe} \left\{ \frac{(1-\beta)^3 + m\left[\beta\left(\beta^2 - 3\,\beta + 3\right) + 12\, Br'\right]}{m\,\beta^2(3-\beta) + \mathcal{K}\mathcal{A}\left[2\,(1-\beta)^3 + 3\,m\,\beta\,(1-\beta)\,(2-\beta)\right]} \right\}, \tag{4.22}$$

where the dimensionless group $\mathcal{K}\mathcal{A}$ represents the volumetric heat capacity ratio. Remarkably, in the free-surface limit, $m \to 0$, M is independent of β and equals $q_w/(\varepsilon\, Pe\, \mathcal{K}\mathcal{A})$, whereas the single-phase limits are

$$\frac{\varepsilon\, Pe\, M}{q_w} = \begin{cases} \dfrac{1 + 12\, m\, Br'}{\mathcal{K}\mathcal{A}} & \text{if } \beta \to 0, \\ 1 + 12\, Br' & \text{if } \beta \to 1, \end{cases} \tag{4.23}$$

recovering, in the absence of viscous dissipation ($Br' = 0$), the expected steady-state thermal behaviour, i.e. $M \propto \{1/(\mathcal{K}\mathcal{A});\ 1\}$, see figure 13(*a*). The difference between the intercepts $Q_2 - Q_1$ corresponds to the steady-state thermal lag between the outer and the inner phase. Interestingly, in the free-surface limit, $m \to 0$, the normalised thermal lag increases linearly with β as $[4(1-\beta) + 5\,K\,\beta]/(10\,K)$.

The transient formulation of (3.8), (3.9) can be solved numerically, as shown in figure 14(*a, b*), choosing a liquid–liquid system from table 1; the numerical solution has been obtained using the *pdepe* solver of MATLAB, setting an initial temperature equal to zero in both phases and imposing the steady-state heat flux M, given in (4.22), at the right boundary of the domain ($x = 20$). A second-order accurate spatial discretisation scheme is employed to convert the original problem into a set of ODEs, which are then integrated to obtain approximate solutions at the specified times (Skeel & Berzins 1990). Time discretisation is performed using a multistep variable-step variable-order (VSVO) solver based on numerical differentiation formulae (NDFs) of orders 1–5 (Shampine & Reichelt 1997; Shampine, Reichelt & Kierzenka 1999). We use equally spaced meshes in the intervals $0 \leqslant x \leqslant 20$ and $0 \leqslant t \leqslant 18$, with 1001 and 501 points, respectively. To ensure highly accurate results, the relative and absolute errors at each integration step have been set to 10^{-12}, with norm control enabled to manage the overall error in the solution vector. As time elapses, the solution evolves and an increasing region of the channel reaches the steady state.

Interestingly, we can use the numerical solution to check the model consistency and verify that the continuity of temperature at the fluid–fluid interface has been properly enforced. This issue represents a key aspect of the model, since such a boundary condition has been imposed in asymptotic terms, see § C.5.2. From figure 14(*c*), we can see that the

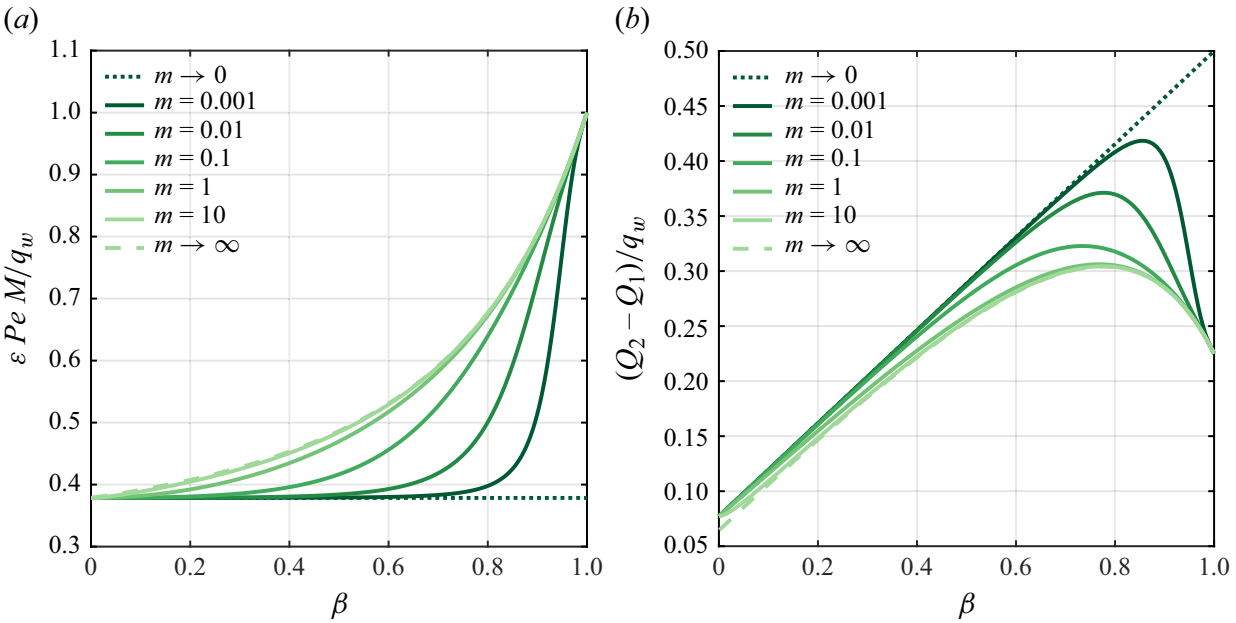

Figure 13. Normalised (*a*) slope and (*b*) difference in intercepts for the steady-state solutions (4.21) to the coupled model, as a function of the volume fraction of the outer phase β and for fixed values of the viscosity ratio m, corresponding to a liquid–liquid scenario with $\mathcal{A} = 0.51$ and $\mathcal{K} = 5.18$, see table 1.

temperature difference, $\vartheta_1 - \vartheta_2 = (\langle\vartheta_1\rangle + \sqrt{\varepsilon}\,\vartheta_1^{(1)} + \varepsilon\,\vartheta_1^{(2)}) - (\langle\vartheta_2\rangle + \sqrt{\varepsilon}\,\vartheta_2^{(1)} + \varepsilon\,\vartheta_2^{(2)})$ evaluated at the interface and keeping the first three terms of the expansions is within the $\mathcal{O}(\varepsilon\sqrt{\varepsilon})$ error, consistent with the two-scale asymptotic expansion in (3.3). Our model is in fact accurate up to the order $\mathcal{O}(\varepsilon)$.

4.7. *Nusselt number in the coupled regime*

In the coupled regime, the bulk temperature ϑ_b, see (3.15), simplifies to

$$\vartheta_b\,(x,\ t) = \frac{\mathcal{K}\,\mathcal{A}\,(1-\beta)\,U_1\left(\langle\vartheta_1\rangle + \sqrt{\varepsilon}\,\vartheta_1^{(1)}\right) + \beta\,U_2\left(\langle\vartheta_2\rangle + \sqrt{\varepsilon}\,\vartheta_2^{(1)}\right)}{\mathcal{K}\,\mathcal{A}\,(1-\beta)\,U_1 + \beta\,U_2} + \mathcal{O}(\varepsilon), \tag{4.24}$$

and the Nusselt number can be computed though the definition (3.19), using the numerical solution of (3.8), (3.9) for the averaged temperatures $\langle\vartheta_j\rangle$ to estimate the first-order terms in (4.24) via (C12) and (C15). The Nusselt number in laminar coupled core-annular flows with uniform wall heat-flux is a function only of $Nu = Nu(x,\ t,\ \beta,\ m,\ \mathcal{A},\ \mathcal{K},\ q_w,\ Br',\ Pe)$ and, based on the definition of the heat-transfer coefficient, see (3.12), it allows for obtaining the two-phase heat-transfer coefficient.

An example of the time and spatial evolution of $Nu(x,\ t)$ is given in figure 14(*d*): the Nusselt number evolves according to an S-shaped trend and is bounded between a lower and an upper horizontal asymptote, corresponding respectively to its limiting values for $t \to \infty$ and $t \to 0$. The impact of the Péclet number (i.e. the competition between advection and diffusion) is qualitatively similar to what is described in figure 5(*b–f*) for the decoupled regime and it is not shown here only for the sake of brevity.

At the steady state, the axial gradients of temperature $\partial\langle\vartheta_j\rangle/\partial x$ can be replaced by the slope M given in (4.21) and the Nusselt number $Nu^\infty = Nu^\infty(\beta,\ m,\ \mathcal{A},\ \mathcal{K},\ Br')$ can be written in a closed form (its full expression looks quite cumbersome and it is not reported here only for the sake of brevity). Figure 15 shows the evolution of Nu^∞ with respect to the volume fraction and the viscosity ratio for a liquid–liquid case, see table 1, keeping

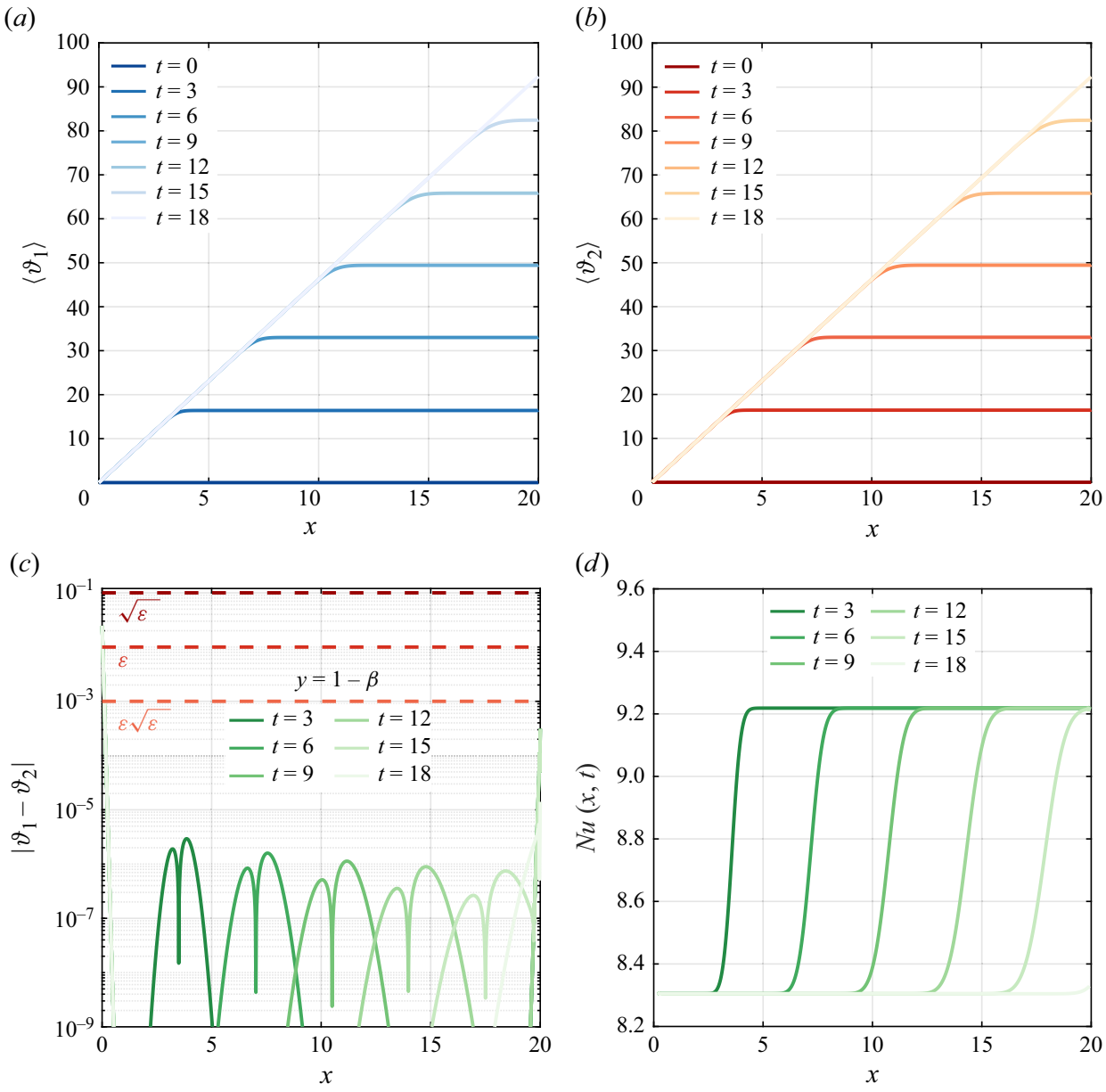

Figure 14. Transient evolution of the averaged temperature $\langle\vartheta_j\rangle(x,\,t)$ in the coupled regime, (a) $j=1$, (b) $j=2$. (c) Absolute value of the difference between the temperatures of the two phases at the interface $\vartheta_j|_{y=1-\beta}$, including corrections up to the second order. Dashed horizontal lines represent the $\mathcal{O}(\varepsilon^{1/2},\ \varepsilon,\ \varepsilon^{3/2})$ tolerances choosing $\varepsilon=0.01$. (d) Time evolution of the Nusselt number $Nu(x,\,t)$ against the axial coordinate x. For this liquid–liquid scenario (see table 1), the simulation parameters are: $Pe=1$, $\mathcal{A}=0.51$, $\mathcal{K}=5.18$, $m=0.625$, $q_w=0.1$, $\beta=0.5$, $Br'=0$. Mesh resolution: $\Delta x=0.02$.

the conductivity ratio as $\mathcal{K}=1$; the panels (a)–(c) show the effect of the diffusivity ratio $\mathcal{A}$. First, the single-phase limits of the steady-state Nusselt number for a vanishing core (i.e. the channel section is entirely occupied by the outer phase) yields to

$$Nu^{\infty}\left(\beta\to 1,\ m,\ \mathcal{A},\ \mathcal{K},\ Br'\right)=\begin{cases}4+\mathcal{O}(1-\beta) & \text{if } m\to 0,\\ \dfrac{140}{108\,Br'+17}+\mathcal{O}(1-\beta) & \text{otherwise,}\end{cases}\tag{4.25}$$

confirming that the result obtained as $m\not\to 0$ is consistent with the single-phase benchmark expression given by (278) of Shah & London (1978) ($Nu^{\infty}=140/17$) for a

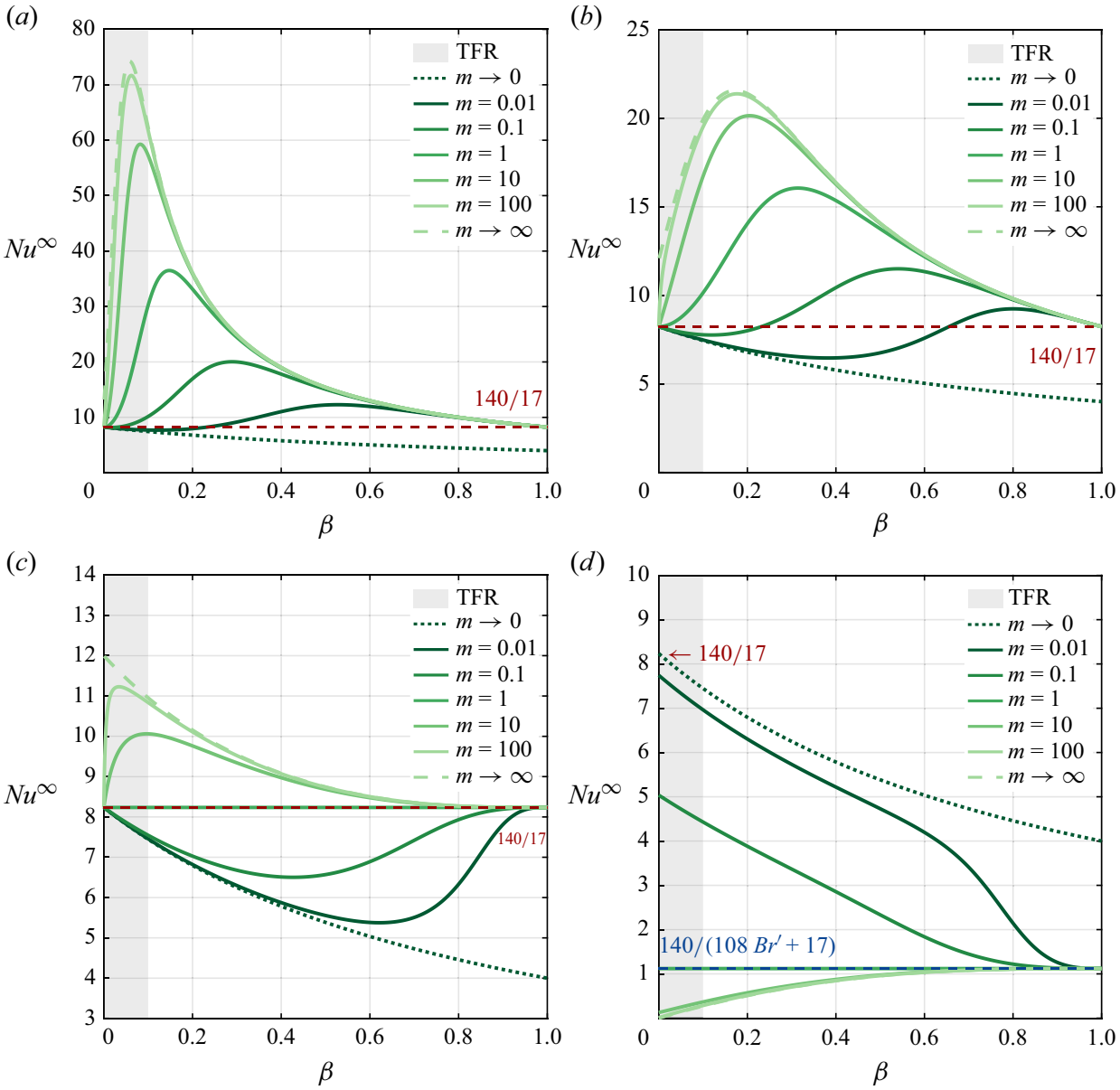

Figure 15. Limiting two-phase Nusselt number for a core-annular flow of unitary conductivity ratio, $\mathcal{K} = 1$, as a function of the volume fraction β, for fixed values of the viscosity ratio m. Panels (a) to (c) refer to a non-dissipative core-annular flow ($Br' = 0$) with increasing diffusivity ratios as increasing powers of the small-scale parameter, $\varepsilon = 0.01$: (a) $\mathcal{A} = \varepsilon$, ($b$) $\mathcal{A} = \sqrt{\varepsilon}$, ($c$) $\mathcal{A} = 1$. In (d), $\mathcal{A} = Br' = 1$.

uniform heat flux boundary condition imposed in a planar channel. Note that in the free-surface limit, $m \to 0$, the outer phase moves so slowly (see figure 3d) that the heat flux cannot be convected downstream and the Nusselt number converges to the value of 4, in agreement with the case of two different temperatures specified at each boundary, see (268) of Shah & London (1978).

Interestingly, when $m \to 0$, the convective heat-transfer is less efficient compared with the single-phase flow and $Nu^\infty < 140/17$ in the whole range of volume fractions, see figure 15(a–c). In the free-surface limit, in fact, the annulus moves so slowly (see figure 3c) that the asymptotic Nusselt number is unaffected by the thermal diffusivity ratio $\mathcal{A}$:

$$Nu^\infty\ (\beta,\ m \to 0,\ \mathcal{K}) = \frac{140\ K}{35\ K\ \beta + 17\ (1-\beta)}. \tag{4.26}$$

Notice that, in the coupled regime ($k = 0$), the use of K or $\mathcal{K} = K\,\varepsilon^k$ is equivalent in (4.26). In the rigid core limit, instead, convective heat-transfer is favoured and is always enhanced compared with the single-phase flow, namely $Nu^\infty > 140/17$, in the whole range of β. This can be explained by the shape of the velocity profile (linear in the annulus and flat in the core, see figure 3*c*), that maximises heat transfer ensuring the most efficient replacement of fluid over the heated surface. This effect is amplified by lowering the diffusivity ratio $\mathcal{A}$. Specifically, the thermal diffusivity represents the promptness of a material in dissipating a temperature inhomogeneity relative to its tendency to store thermal energy, and, therefore, when $\mathcal{A}$ is less than one, the diffusivity of the core is greater than that of the annulus. In our case, a lower value of $\mathcal{A}$ results in a greater tendancy of the outer phase to accumulate the heat received from the surroundings rather than diffusing it, enhancing the heat-transfer coefficient. This behaviour is favoured at low volume fractions, i.e. when the fluid in contact with the channel wall is sufficiently thin. In contrast, increasing β leads to a larger thermal resistance in the annulus and gives a greater difference between the wall and the bulk temperature defined in (4.24), reducing the heat-transfer coefficient h and the Nusselt number.

In other words, two-phase flows enhance convective heat transfer only under certain conditions. Specifically, only if the viscosity ratio is finite and the diffusivity ratio is small enough, we observe an enhanced heat-transfer coefficient, in particular at low volume fractions.

Finally, the effect of viscous dissipation on the Nusselt number is shown in figure 15(*d*), setting $Br' = 1$ while keeping $\mathcal{A} = 1$. When the two fluids have the same viscosity, i.e. $m = 1$, the Nusselt number does not depend on the volume fraction and viscous dissipation lowers the value of $140/(108\,Br' + 17)$. The curves obtained for values of m larger than 1 are located below this threshold, while those where $0 < m < 1$ lie above it. In any case, viscous heating ($Br' > 0$) reduces the efficiency of convective heat-transfer and the dependence on the viscosity ratio is flipped compared with the non-dissipative scenario. This can be attributed to the combination of two factors (Shah & London 1978): (i) a reduction in the wall temperature gradient near the wall region due to viscous heating; and (ii) a slower rise of the bulk temperature along the channel axis, due to a reduced amount of heat transferred through the wall.

5. Conclusions

Forced convection in two-phase channel flows arises in a large variety of applications. In this paper, we derived an asymptotic one-dimensional model to describe the heat transfer in laminar core-annular flows in a planar geometry heated by a uniform heat-flux (extended Graetz-type problem).

The main heat-transfer mechanisms (advection and diffusion) occurring along the transversal and the longitudinal direction has been modelled via effective coefficients, which depend on the Péclet and Brinkman numbers, the dimensionless heat flux, the viscosity, thermal diffusivity and thermal conductivity ratios, and the volume fraction only. Specifically, the resulting diffusion coefficients provide a generalisation of the classical Aris–Taylor dispersion theory to two-phase flows. The model reveals the existence of two main regimes, depending on the thermal capacity of the two phases.

When the thermal conductivities of the two fluids are of the same order of magnitude, as in liquid–liquid systems, the system is described by two-coupled advection–diffusion heat-transfer equations. The coupling between the phases results in a canonical and a coupled effective advection term, a canonical and a cross-coupling effective diffusion term, and storage and source terms for each phase. We derived an analytical model for the

Nusselt number revealing that the heat transfer is enhanced with respect to the single-phase scenario only if the viscosity ratio is finite and the diffusivity ratio is small enough. In addition to that, we identified the dominant regime controlling thermal mixing depending on the magnitude of the Péclet number. In particular, at small *Pe*, the transport of thermal energy is dominated by diffusion. For intermediate values of the Péclet number, advection and diffusion compete, leading to a strong influence of both the flow condition (i.e. Péclet number) and the properties of the system (i.e. volume fraction, viscosity, thermal conductivity and thermal diffusivity ratios) on the dispersion coefficient. At high *Pe*, heat transport is fully dominated by advection.

When the annulus is more conductive than the core, as in most liquid–gas systems, the phases are thermally decoupled and the averaged temperature of the core evolves according to a single one-dimensional advection–diffusion heat-transfer equation. In this case, the limiting Nusselt number scales as the inverse of the annulus thickness and it is independent of the viscosity ratio. If the annulus is thin, our model confirms that, within the film, the heat-transfer is primarily driven by conduction and the temperature profile remains almost linear along the transverse direction. Interestingly, in the advection-dominated regime, the core-annular flow pattern does not enhance thermal mixing compared with single-phase flow, in particular when the volume fraction is small. Our analysis is complemented by the identification of a hierarchy between the characteristic time scales of advection and diffusion, helping in understanding the proper time window where thermal dispersion can be observed.

Our work clarifies the impact of the phases topology on forced convection and we hope that it may be extended with the aim of offering a more rigorous interpretation of the heat-transfer phenomena taking place in more complex two-phase flow patterns.

Funding. This study has received funding from the European Union 'NextGenerationEU', Ministero dell'Università e della Ricerca (MUR) 'Italiadomani' Piano Nazionale di Ripresa e Resilienza (PNRR), Mission 4, Research Project PRIN 2022 'Predictive forecasting and risk assessment for CO_2 transport in pipelines', MUR code: 20229JPN53; CUP Master code: J53D23002000006; CUP code: D53D23003250006.

Declaration of interests. The authors report no conflict of interest.

Appendix A. Velocity profiles

Consider a core-annular flow as shown in figure 1 at laminar and steady-state conditions: the system is composed by two immiscible and incompressible fluids with no interfacial instabilities or entrainment of one phase into the other (Joseph, Nguyen & Beavers 1984) and in the absence of any body forces (such as buoyancy). The channel is assumed to be shallow enough ($\hat{H}/\hat{L} \ll 1$) so that the momentum equations of each phase are simplified using the lubrication approximation and the flow is treated as one-dimensional (the velocity components in the transverse and normal directions are neglected). The momentum equation for each jth-Newtonian fluid, then, reduces to

$$0 = -\frac{\mathrm{d}\hat{p}}{\mathrm{d}\hat{x}} + \mu_j \frac{\mathrm{d}^2\hat{u}_j}{\mathrm{d}^2\hat{y}^2} \qquad j = \{1,\ 2\}\,, \tag{A1}$$

subjected to the following boundary conditions:

$$\left.\frac{\mathrm{d}\hat{u}_1}{\mathrm{d}\hat{y}}\right|_{\hat{y}=0} = 0, \tag{A2a}$$

$$\mu_1 \left.\frac{\mathrm{d}\hat{u}_1}{\mathrm{d}\hat{y}}\right|_{\hat{y}=(1-\beta)\hat{H}} = \mu_2 \left.\frac{\mathrm{d}\hat{u}_2}{\mathrm{d}\hat{y}}\right|_{\hat{y}=(1-\beta)\hat{H}}, \tag{A2b}$$

$$\hat{u}_1\big|_{\hat{y}=(1-\beta)\hat{H}} = \hat{u}_2\big|_{\hat{y}=(1-\beta)\hat{H}}, \tag{A2c}$$

$$\hat{u}_2\big|_{\hat{y}=\hat{H}} = 0, \tag{A2d}$$

namely, the symmetry of the inner velocity profile with respect to the channel axis (A2*a*), the continuity of tangential stresses (A2*b*) and velocities (A2*c*) at the interface, and, the no-slip condition at the channel wall. The set of equations (A1) admits the following analytical solution

$$\hat{u}_j(\hat{y}) = \frac{1}{2\mu_j}\frac{\mathrm{d}\hat{p}}{\mathrm{d}\hat{x}}\,\hat{y}^2 + \hat{A}_j\,\hat{y} + \hat{B}_j \qquad j = \{1,\ 2\}, \tag{A3}$$

where $\hat{A}_j$, $\hat{B}_j$ are constants to be determined imposing the boundary conditions given in (A2):

$$\hat{A}_1 = 0, \qquad \hat{A}_2 = 0, \tag{A4a}$$

$$\hat{B}_1 = -\frac{1}{2}\frac{\mathrm{d}\hat{p}}{\mathrm{d}\hat{x}}\frac{\hat{H}^2\left[\mu_2 - \beta(2-\beta)\,(\mu_2-\mu_1)\right]}{\mu_1\,\mu_2}, \qquad \hat{B}_2 = -\frac{1}{2}\frac{\mathrm{d}\hat{p}}{\mathrm{d}\hat{x}}\frac{\hat{H}^2}{\mu_2}, \tag{A4b}$$

leading to the dimensional velocity fields expressed in (2.1). Effects related to thermo-capillary Marangoni convection have not been considered in this work.

A.1 *Dimensionless velocity profiles*

The dimensionless velocity profiles $u_j(y)$ normalised using (2.12*b*,*d*) are given by

$$u_1(y) = 3\,\Lambda[1+\beta(2-\beta)(m-1)-y^2], \qquad u_2(y) = 3\,\Lambda\,m(1-y^2), \tag{A5a}$$

$$U_1 = \Lambda[2+\beta(2-\beta)(3m-2)], \qquad U_2 = \Lambda\,m\beta(3-\beta), \tag{A5b}$$

with

$$\Lambda^{-1} = 2[1+\beta(\beta^2-3\beta+3)(m-1)]. \tag{A6}$$

Figure 3(*c*) shows the velocity profiles (A5*a*) as a function of the viscosity ratio m. When $m \to \infty$, the inner fluid approaches the constant plug-like profile and we will refer to it as the rigid-core limit; conversely, the outer velocity profile becomes linear in the free-surface limit when $m \to 0$ (Balestra *et al.* 2018).

The evolution of the average speed U_j, see (A5*b*), against the volume fraction of the outer phase for different values of the viscosity ratio is presented in figure 3(*d*).

Appendix B. Heat capacity flow rate ratio

In Graetz-type heat exchange problems, the heat capacity flow rate ratio (or capacitance ratio) Cr is widely used. This dimensionless number is the ratio between the heat capacity rates (the product of mass flow rate $\dot{m}_j$ and specific heat capacity at constant pressure $c_{p,\,j}$)

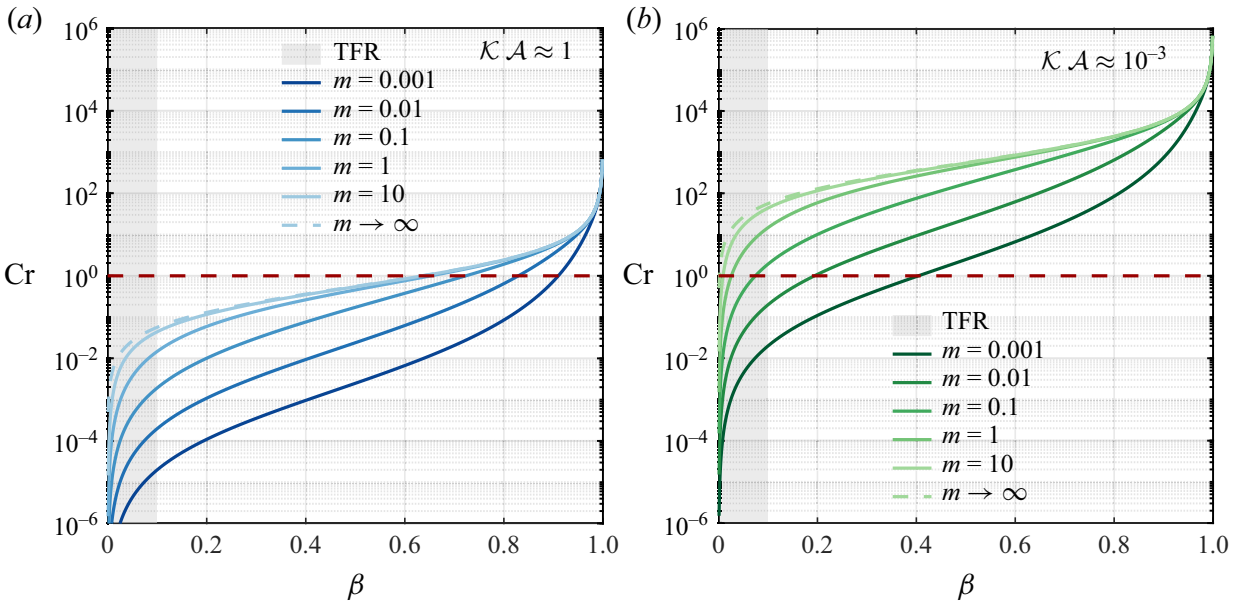

Figure 16. Evolution of the heat capacity flow rate ratio Cr as a function of the dimensionless thickness of the outer layer β for different values of the viscosity ratio m in (*a*) liquid–liquid and (*b*) gas–liquid systems. The two set of curves differ for the thermal capacity ratio $\mathcal{K}\mathcal{A}$. The TFR is highlighted by the grey area.

of the two phases flowing in a heat exchanger (Bai *et al.* 2018). For the core-annular configuration depicted in figure 1, Cr is computed combining (2.14*c*, A5*b*, A6) as

$$\mathrm{Cr} = \frac{\dot{m}_2\, c_{p,\,2}}{\dot{m}_1\, c_{p,\,1}} = \frac{\rho_2}{\rho_1}\,\frac{\beta}{1-\beta}\,\frac{U_2}{U_1}\,\frac{c_{p,\,2}}{c_{p,\,1}} = \frac{1}{\mathcal{K}\mathcal{A}}\,\frac{\beta^2\, m(3-\beta)}{(1-\beta)\left[2\,(1-\beta)^2 + 3\,m\,\beta(2-\beta)\right]}. \tag{B1}$$

From the physical point of view, the heat capacity ratio governs the distribution of heat between the two phases and plays a crucial role in determining the overall effectiveness of heat transfer. Specifically, Cr describes how efficiently the energy is transferred from one phase to the other: the optimal performance is obtained when $\mathrm{Cr} \approx 1$, while for $\mathrm{Cr} \to 0$ or $\mathrm{Cr} \to \infty$, its effectiveness is limited due to one phase dominating the heat transfer process. The Cr is typically related to the design and the optimisation of heat exchangers, e.g. the NTU (number of transfer units) method (Langerova & Matuska 2023).

In figure 16, we plot the capacitance ratio against the volume fraction of the outer phase for different values of the viscosity ratio for liquid–liquid and gas–liquid systems, identified by the order of magnitude of the thermal capacity ratio (i.e. the product $\mathcal{K}\mathcal{A}$). Referring to table 1, we can assume that $\mathcal{K}\mathcal{A} \approx 1$ in liquid–liquid and $\mathcal{K}\mathcal{A} \approx 10^{-3}$ for gas–liquid systems. Interestingly, Cr increases with m while keeping β fixed for both liquid–liquid and gas–liquid systems, and the optimal condition of $\mathrm{Cr} = 1$ shifts to lower β, see figure 16.

Appendix C. Derivation of the heat-transfer model using two-scale asymptotic expansion

In the following sections, the derivation of the effective equations is carried out following the procedure discussed in § 3.

C.1 *Expanded governing equations*

After making the axial-coordinate stretching (3.1) and using (3.2), the governing equations (2.13) become

$$\varepsilon^{-p+\delta_1^j a}\left[\varepsilon\,\frac{\partial \vartheta_j}{\partial \tau}+\sqrt{\varepsilon}\,\left(u_j-V\right)\frac{\partial \vartheta_j}{\partial \xi}\right]=\left(\varepsilon\,\frac{\partial^2 \vartheta_j}{\partial \xi^2}+\frac{\partial^2 \vartheta_j}{\partial y^2}\right)+B\,\varepsilon^{b+\delta_1^j\left[\log_\varepsilon(m/K)-k\right]}\left(\frac{\mathrm{d}u_j}{\mathrm{d}y}\right)^2, \tag{C1}$$

where $u_j(y)$ is the velocity profile of the j-phase given in (A5), V is the velocity of the moving reference frame, and $\delta_1^j=1-\delta_2^j$ is the Kronecker delta defined in (3.7) and introduced to make the model derivation more compact. Plugging the expansion (3.3) into (C1) leads to

$$\begin{aligned}&-\varepsilon^{-p+\delta_1^j a}\left[\varepsilon\,\frac{\partial \vartheta_j^{(0)}}{\partial \tau}+\varepsilon\sqrt{\varepsilon}\,\frac{\partial \vartheta_j^{(1)}}{\partial \tau}+\sqrt{\varepsilon}\,\left(u_j-V\right)\frac{\partial \vartheta_j^{(0)}}{\partial \xi}+\varepsilon\,\left(u_j-V\right)\frac{\partial \vartheta_j^{(1)}}{\partial \xi}\right.\\&\left.+\varepsilon\sqrt{\varepsilon}\,\left(u_j-V\right)\frac{\partial \vartheta_j^{(2)}}{\partial \xi}\right]+\varepsilon\,\frac{\partial^2 \vartheta_j^{(0)}}{\partial \xi^2}+\varepsilon\sqrt{\varepsilon}\,\frac{\partial^2 \vartheta_j^{(1)}}{\partial \xi^2}\\&+\left(\frac{\partial^2 \vartheta_j^{(0)}}{\partial y^2}+\sqrt{\varepsilon}\,\frac{\partial^2 \vartheta_j^{(1)}}{\partial y^2}+\varepsilon\,\frac{\partial^2 \vartheta_j^{(2)}}{\partial y^2}\right)+B\,\varepsilon^{b+\delta_1^j\left[\log_\varepsilon(m/K)-k\right]}\left(\frac{\mathrm{d}u_j}{\mathrm{d}y}\right)^2=\mathcal{O}(\varepsilon^2).\end{aligned} \tag{C2}$$

Since the employed asymptotic expansion (3.3) was truncated to its first three terms, a cascade of equations for the unknown functions $\vartheta_j^{(n)}$, with $n=\{0,\ 1,\ 2\}$, originates from (C2). Specifically, we obtain

$$\mathcal{O}(1):\frac{\partial^2 \vartheta_j^{(0)}}{\partial y^2}=0, \tag{C3a}$$

$$\mathcal{O}(\sqrt{\varepsilon}):\frac{\partial^2 \vartheta_j^{(1)}}{\partial y^2}=\varepsilon^{-p+\delta_1^j a}\left(u_j-V\right)\frac{\partial \vartheta_j^{(0)}}{\partial \xi}-B\,\varepsilon^{b-\frac{1}{2}+\delta_1^j\left[\log_\varepsilon\left(\frac{m}{K}\right)-k\right]}\left(\frac{\mathrm{d}u_j}{\mathrm{d}y}\right)^2, \tag{C3b}$$

$$\mathcal{O}(\varepsilon):\frac{\partial^2 \vartheta_j^{(2)}}{\partial y^2}=\varepsilon^{-p+\delta_1^j a}\left[\frac{\partial \vartheta_j^{(0)}}{\partial \tau}+\left(u_j-V\right)\frac{\partial \vartheta_j^{(1)}}{\partial \xi}\right]-\frac{\partial^2 \vartheta_j^{(0)}}{\partial \xi^2}, \tag{C3c}$$

$$\mathcal{O}(\varepsilon\sqrt{\varepsilon}):0=\varepsilon^{-p+\delta_1^j a}\left[\frac{\partial \vartheta_j^{(1)}}{\partial \tau}+\left(u_j-V\right)\frac{\partial \vartheta_j^{(2)}}{\partial \xi}\right]-\frac{\partial^2 \vartheta_j^{(1)}}{\partial \xi^2}, \tag{C3d}$$

where the order of magnitude of the governing parameters is within the applicability region discussed in § 3.1 and has been chosen in a way that ensures the least degeneracy of the closure problem (Van Dyke 1964). In other words, we keep the maximum possible number of non-vanishing small terms (Feuillebois & Lasek 1977) when equal powers of ε are gathered from the expanded governing equation (C2). Doing so, all the relevant physical effects enter the problem as soon as practicable and not beyond (Richard *et al.* 2016).

C.1.1 *Boundary conditions*

The boundary conditions (2.16) have to be expanded so that at each order in (C3), we obtain a boundary-value problem in the form of a second-order linear partial differential equation (PDE) that can be solved integrating twice in y.

The continuity of thermal fluxes across the interface (2.16*b*) reads

$$\left(\frac{\partial \vartheta_2^{(0)}}{\partial y}+\sqrt{\varepsilon}\frac{\partial \vartheta_2^{(1)}}{\partial y}+\varepsilon\frac{\partial \vartheta_2^{(2)}}{\partial y}\right)\bigg|_{y=1-\beta}=\mathcal{K}\left(\frac{\partial \vartheta_1^{(0)}}{\partial y}+\sqrt{\varepsilon}\frac{\partial \vartheta_1^{(1)}}{\partial y}+\varepsilon\frac{\partial \vartheta_1^{(2)}}{\partial y}\right)\bigg|_{y=1-\beta}, \tag{C4}$$

suggesting the identification of several regimes based on the order of magnitude of the thermal conductivity ratio $\mathcal{K}$. In this work, we will focus on regimes where the inner phase exhibits a comparable ($k=0$) or lower ($k>0$) thermal conductivity with respect to that of the outer phase only. Therefore, depending on the order of magnitude of the conductivity ratio, the terms on the right-hand side of (C4) shift between orders.

The continuity of temperatures across the interface (2.16*c*) is not imposed order-by-order, *viz.* $\vartheta_1^{(n)}|_{y=1-\beta}=\vartheta_2^{(n)}|_{y=1-\beta}$, because it is not compatible with the chosen gauge (3.6) (namely, that the leading-order temperature coincides with the averaged temperature). Instead, similarly to Ling *et al.* (2016), we interpret the temperature continuity as an asymptotic equivalence of the type

$$\left(\vartheta_1^{(0)}-\vartheta_2^{(0)}\right)\Big|_{y=1-\beta}+\sqrt{\varepsilon}\,\left(\vartheta_1^{(1)}-\vartheta_2^{(1)}\right)\Big|_{y=1-\beta}+\varepsilon\,\left(\vartheta_1^{(2)}-\vartheta_2^{(2)}\right)\Big|_{y=1-\beta}=\mathcal{O}\left(\varepsilon\sqrt{\varepsilon}\right). \tag{C5}$$

The adiabatic condition (2.16*d*) at $y=0$ is straightforward and consistent with the symmetry of the problem, giving

$$\frac{\partial \vartheta_1^{(n)}}{\partial y}\bigg|_{y=0}=0, \qquad n=\{0,\ 1,\ 2\}. \tag{C6}$$

Lastly, to satisfy the gauge condition (3.6), the dimensionless external heat flux imposed at $y=1$ needs necessarily to appear as an $\mathcal{O}(\sqrt{\varepsilon})$ quantity, which is equivalent to writing (2.16*a*) as

$$\frac{\partial \vartheta_2^{(n)}}{\partial y}\bigg|_{y=1}=\begin{cases}0 & \text{if } n=0\ \vee\ n\geqslant 2,\\ Q\,\varepsilon^{f-\frac{1}{2}} & \text{if } n=1.\end{cases} \tag{C7}$$

C.2 *Order* $\mathcal{O}(1)$*:* $\vartheta_j^{(0)}$ *solutions*

The leading-order equation (C3*a*) and the boundary conditions (C6), (C7) for $n=0$ are homogeneous. This ensures that the boundary-value problem

$$\begin{cases}\dfrac{\partial^2 \vartheta_j^{(0)}}{\partial y^2}=0,\\[2ex] \dfrac{\partial \vartheta_j^{(0)}}{\partial y}\bigg|_{y=\delta_2^j}=0,\end{cases} \tag{C8a,b}$$

admits a trivial solution (i.e. that $\vartheta_j^{(0)}$ is independent of y), and, therefore, $\vartheta_j^{(0)}(\xi,\ \tau)$ corresponds to the average dimensionless temperature $\langle\vartheta_j\rangle(\xi,\ \tau)$ defined by (3.4). This is

true as long as $p < 1/2$, $p - a < 1/2$ and $f > 0$, namely $Pe \ll 1/\sqrt{\varepsilon}$, $\mathcal{A}\,Pe \ll 1/\sqrt{\varepsilon}$ and $q_w \ll 1$ – viscous dissipation also has to enter the problem as an $\mathcal{O}(\sqrt{\varepsilon})$ contribution or lower.

C.3 *Order* $\mathcal{O}(\sqrt{\varepsilon})$*:* $\vartheta_j^{(1)}$ *solutions*

At the order $\mathcal{O}(\sqrt{\varepsilon})$, the derivation will be carried out without choosing a specific value for the velocity of the reference frame V, which will remain arbitrary. This issue will be discussed in § 4.

Starting from the inner phase, (C3*b*) and (C6) with $n = 1$ and $j = 1$ give the following boundary-value problem:

$$\begin{cases} \dfrac{\partial^2 \vartheta_1^{(1)}}{\partial y^2} = \varepsilon^{-p+a}\,(u_1 - V)\,\dfrac{\partial \vartheta_1^{(0)}}{\partial \xi} - \dfrac{m\,B}{K}\,\varepsilon^{b-k-\frac{1}{2}}\left(\dfrac{\mathrm{d}u_1}{\mathrm{d}y}\right)^2, \\ \left.\dfrac{\partial \vartheta_1^{(1)}}{\partial y}\right|_{y=0} = 0. \end{cases} \tag{C9a,b}$$

Integrating (C9*a*) with respect to y gives

$$\frac{\partial \vartheta_1^{(1)}}{\partial y}(y) = \frac{\varepsilon^a}{\varepsilon^p}\left(\int \left(u_1(y^*) - V\right)\mathrm{d}y^*\right)\frac{\partial \vartheta_1^{(0)}}{\partial \xi} - \frac{m\,B}{K}\,\frac{\varepsilon^{b-k}}{\sqrt{\varepsilon}}\int\left(\frac{\mathrm{d}u_1(y^*)}{\mathrm{d}y^*}\right)^2\mathrm{d}y^* + A_1^{(1)}, \tag{C10}$$

where the integration constant $A_1^{(1)} = 0$ is determined by using the thermal symmetry condition (C9*b*) along with the corresponding velocity profiles (A5).

Then, we proceed by integrating (C10), obtaining

$$\vartheta_1^{(1)}(y) = \frac{\varepsilon^a}{\varepsilon^p}\left(\iint\left(u_1(y^*) - V\right)\mathrm{d}^2y^*\right)\frac{\partial \vartheta_1^{(0)}}{\partial \xi} - \frac{m\,B}{K}\,\frac{\varepsilon^{b-k}}{\sqrt{\varepsilon}}\iint\left(\frac{\mathrm{d}u_1(y^*)}{\mathrm{d}y^*}\right)^2\mathrm{d}^2y^* + B_1^{(1)}, \tag{C11}$$

where the integration constant $B_1^{(1)}$ is determined enforcing the gauge-fixing condition of the type of (3.5), i.e. $\left\langle \vartheta_1^{(1)} \right\rangle = 0$ (see Mikelić *et al.* (2006)). Doing so, we get an expression for the first-order correction of the temperature of the inner phase

$$\vartheta_1^{(1)}(\xi,\ y,\ \tau;\ \varepsilon) = \varepsilon^{-p+a}\,\mathcal{M}_1(y)\,\frac{\partial \vartheta_1^{(0)}}{\partial \xi} - \frac{m\,B}{K}\,\varepsilon^{b-k-\frac{1}{2}}\,\mathcal{M}_1^{\mathcal{W}}(y), \tag{C12}$$

where the functions

$$\mathcal{M}_1(y) = \left[\frac{(1-\beta)^2 - 3\,y^2}{6}\right]V + \frac{\Lambda}{20}\left\{-5\,y^4 + 30\left[\beta\,m(2-\beta) + (1-\beta)^2\right]y^2 + \right.$$

$$\left. -(1-\beta)^2\left[10\,\beta\,m(2-\beta) + 9\,(1-\beta)^2\right]\right\}, \tag{C13a}$$

$$\mathcal{M}_1^{\mathcal{W}}(y) = \frac{3\,\Lambda^2\left[5\,y^4 - (1-\beta)^4\right]}{5}, \tag{C13b}$$

are traditionally named B-fields after the seminal works of H. Brenner (Brenner & Stewartson 1980; Brenner & Edwards 1993) on Taylor dispersion. These functions represent the mean axial displacement at long times of a fluid particle located at y within

the channel cross-section, under the assumption that its initial positions are all equally probable (Mauri 2015).

For the outer phase, $j = 2$, (C3*b*) and (C7) for $n = 1$ give

$$\begin{cases} \dfrac{\partial^2 \vartheta_2^{(1)}}{\partial y^2} = \varepsilon^{-p}\,(u_2 - V)\,\dfrac{\partial \vartheta_2^{(0)}}{\partial \xi} - B\,\varepsilon^{b-\frac{1}{2}}\left(\dfrac{\mathrm{d}u_2}{\mathrm{d}y}\right)^2, \\ \left.\dfrac{\partial \vartheta_2^{(1)}}{\partial y}\right|_{y=1} = Q\,\varepsilon^{f-\frac{1}{2}}. \end{cases} \tag{C14}$$

Following the same mathematical procedure illustrated earlier yields a solution for $\vartheta_2^{(1)}$ in a similar form:

$$\vartheta_2^{(1)}(\xi,\ y,\ \tau;\ \varepsilon) = \varepsilon^{-p}\,\mathcal{M}_2(y)\,\frac{\partial \vartheta_2^{(0)}}{\partial \xi} - B\,\varepsilon^{b-\frac{1}{2}}\,\mathcal{M}_2^{\mathcal{W}}(y) + Q\,\varepsilon^{f-\frac{1}{2}}\,\mathcal{M}_2^{q}(y), \tag{C15}$$

where

$$\mathcal{M}_2(y) = \left[\frac{\beta^2 - 3\,(1-y)^2}{6}\right] V + \frac{\Lambda\, m}{20}\left(-5\,y^4 + 30\,y^2 - 40\,y + \beta^4 - 5\,\beta^3 + 15\right), \tag{C16a}$$

$$\mathcal{M}_2^{\mathcal{W}}(y) = \frac{3\,\Lambda^2\, m^2}{5}\left(-5\,y^4 + 20\,y + \beta^4 - 5\beta^3 + 10\beta^2 - 15\right), \tag{C16b}$$

$$\mathcal{M}_2^{q}(y) = y + \frac{\beta}{2} - 1. \tag{C16c}$$

C.4 *Order* $\mathcal{O}(\varepsilon)$*:* $\vartheta_j^{(2)}$ *solutions*

At the order $\mathcal{O}(\varepsilon)$, the procedure to find $\vartheta_j^{(2)}$ can be simultaneously applied to both phases using the Kronecker delta defined in (3.7). First, since the previous-order solutions $\vartheta_j^{(1)}$, see (C12), (C15), depend on the axial coordinate ξ only via the leading-order temperatures $\vartheta_j^{(0)}$, we have

$$\frac{\partial \vartheta_j^{(1)}}{\partial \xi} = \varepsilon^{-p+\delta_1^j a}\,\mathcal{M}_j(y)\,\frac{\partial^2 \vartheta_j^{(0)}}{\partial \xi^2}. \tag{C17}$$

Then, we can replace (C17) into (C3*c*) and use the boundary conditions (C6), (C7) to obtain

$$\begin{cases} \dfrac{\partial^2 \vartheta_j^{(2)}}{\partial y^2} = \varepsilon^{-p+\delta_1^j a}\,\dfrac{\partial \vartheta_j^{(0)}}{\partial \tau} + \left[\varepsilon^{2\,(-p+\delta_1^j\, a)}\left(u_j(y) - V\right)\mathcal{M}_j(y) - 1\right]\dfrac{\partial^2 \vartheta_j^{(0)}}{\partial \xi^2}, \\ \left.\dfrac{\partial \vartheta_j^{(2)}}{\partial y}\right|_{y=\delta_2^j} = 0. \end{cases} \tag{C18a,b}$$

Integrating (C18*a*) between δ_2^j and y and making use of (C18*b*) lead to

$$\frac{\partial \vartheta_j^{(2)}}{\partial y}(y) = \varepsilon^{-p+\delta_1^j a}\,\varphi_j(y)\,\frac{\partial \vartheta_j^{(0)}}{\partial \tau} + \left[\varepsilon^{2\,(-p+\delta_1^j\,a)}\,\psi_j(y) - \varphi_j(y)\right]\frac{\partial^2 \vartheta_j^{(0)}}{\partial \xi^2}, \tag{C19}$$

with

$$\varphi_j(y) = \int_{\delta_2^j}^{y} \mathrm{d}y^*, \qquad \psi_j(y) = \int_{\delta_2^j}^{y} \mathcal{I}_j(y^*)\,\mathrm{d}y^*, \qquad \mathcal{I}_j(y) = \big(u_j(y) - V\big)\,\mathcal{M}_j(y). \tag{C20}$$

Integrating (C19) indefinitely gives

$$\vartheta_j^{(2)}(y) = \varepsilon^{-p+\delta_1^j a}\,\tilde{\Phi}_j(y)\,\frac{\partial \vartheta_j^{(0)}}{\partial \tau} + \left[\varepsilon^{2\,(-p+\delta_1^j\,a)}\,\tilde{\Psi}_j(y) - \tilde{\Phi}_j(y)\right]\frac{\partial^2 \vartheta_j^{(0)}}{\partial \xi^2} + B_j^{(2)}, \tag{C21}$$

where

$$\tilde{\Phi}_j(y) = \int \varphi_j(y^*)\mathrm{d}y^*, \qquad \tilde{\Psi}_j(y) = \int \psi_j(y^*)\,\mathrm{d}y^*, \tag{C22}$$

and $B_j^{(2)}$ is an integration constant, which can be found via the gauge-fixing condition $\langle \vartheta_j^{(2)} \rangle = 0$. Finally, we obtain the full expression for the second-order correction of the temperature for both phases:

$$\vartheta_j^{(2)}(\xi,\ y,\ \tau;\ \varepsilon) = \varepsilon^{-p+\delta_1^j a}\,\Phi_j(y)\,\frac{\partial \vartheta_j^{(0)}}{\partial \tau} + \left[\varepsilon^{2\,(-p+\delta_1^j\,a)}\,\Psi_j(y) - \Phi_j(y)\right]\frac{\partial^2 \vartheta_j^{(0)}}{\partial \xi^2}, \tag{C23}$$

with

$$\Phi_j(y) = \tilde{\Phi}_j - \big\langle \tilde{\Phi}_j \big\rangle, \qquad \Psi_j(y) = \tilde{\Psi}_j - \big\langle \tilde{\Psi}_j \big\rangle. \tag{C24}$$

By inspection of (C23), we can notice that the $\mathcal{O}(\varepsilon)$ temperature profile describes the temporary thermal fluctuations occurring within the system through a time-derivative and a diffusive term. We do not report here the full analytic expression for the y-dependent functions that define the $\mathcal{O}(\varepsilon)$ solution, since we will follow the approach presented by Ling *et al.* (2016) for closing the problem (see § C.5), where we will make use only of the value that (C19), (C23) assume at the interface. To lighten notation, the inverted circumflex accent will be employed to denote the evaluation of a given function at the interface, namely $\check{\mathcal{M}}_j \equiv \mathcal{M}_j(y)\big|_{y=1-\beta}$.

C.5 *Closure of the upscaled model*

To derive the upscaled model, the cross-sectional average operator (3.4) is applied to (C2) while accounting for the boundary conditions. This is a necessary and sufficient condition for the cascade of linear equations (C3) to be solvable, thereby enforcing the solvability condition.

Thus, applying the gauge condition (3.6) to the expanded energy equation for the outer phase (C2), $j=2$, we obtain

$$\varepsilon^{-p}\left[\varepsilon\,\frac{\partial\,\langle\vartheta_2\rangle}{\partial\tau}+\sqrt{\varepsilon}\,\langle u_2-V\rangle\,\frac{\partial\,\langle\vartheta_2\rangle}{\partial\xi}+\varepsilon\overbrace{\left\langle(u_2-V)\,\frac{\partial\vartheta_2^{(1)}}{\partial\xi}\right\rangle}^{\text{(i)}}+\varepsilon\sqrt{\varepsilon}\overbrace{\left\langle(u_2-V)\,\frac{\partial\vartheta_2^{(2)}}{\partial\xi}\right\rangle}^{\text{(ii)}}\right]$$

$$=\varepsilon\,\frac{\partial^2\,\langle\vartheta_2\rangle}{\partial\xi^2}+\frac{\sqrt{\varepsilon}}{\beta}\left(\frac{Q\,\varepsilon^f}{\sqrt{\varepsilon}}-\underbrace{\left.\frac{\partial\vartheta_2^{(1)}}{\partial y}\right|_{y=1-\beta}}_{\text{(iii)}}\right)+\frac{\varepsilon}{\beta}\left(0-\underbrace{\left.\frac{\partial\vartheta_2^{(2)}}{\partial y}\right|_{y=1-\beta}}_{\text{(iv)}}\right)$$

$$+\frac{B\,\varepsilon^b}{\beta}\int_{1-\beta}^{1}\left(\frac{\mathrm{d}u_2(y^*)}{\mathrm{d}y^*}\right)^2\mathrm{d}y^*, \tag{C25}$$

where we used the wall boundary conditions (C7) at $\mathcal{O}(\sqrt{\varepsilon},\ \varepsilon)$. Four terms in (C25) need to be closed: two non-local advective terms (i, ii), and two interfacial boundary terms (iii, iv). By means of (C17) and (C20), the term labelled by (i) can be expressed in terms of macro-scale quantities as $\varepsilon^{-p}\,\langle\,\mathcal{I}_2\,\rangle\,\partial^2\,\langle\vartheta_2\rangle/\partial\xi^2$, while the term (ii) is found to be zero by averaging (C3*d*) with $j=2$.

Based on the disparity in the thermal conductivities of the two phases, the continuity condition of thermal fluxes at the interface, see (C4), has different expressions depending on the order of magnitude of thermal conductivity ratio and, therefore, different closure relations are valid for terms (iii) and (iv). This leads to the identification of two different thermal models which may incorporate one or two equations (similarly to Quintard & Whitaker (1993); Lewandowska & Auriault (2004); Lewandowska, Szymkiewicz & Auriault (2005)): the cases where $k>0$ (decoupled model) and the case where $k=0$ (coupled model).

C.5.1 *Decoupled model*

When $k\geqslant 1$, term (iii) is obtained by replacing (C12) into (C4)

$$\text{(iii)}:\quad -\frac{m\,B\,\varepsilon^b}{\sqrt{\varepsilon}}\,\frac{\mathrm{d}\check{\mathcal{M}}_1^{\mathcal{W}}}{\mathrm{d}y}, \tag{C26}$$

while term (iv) is zero. Thus, the upscaled energy equation describing how temperature evolves in the outer phase does not directly contain any information related to the inner flow temperature, and the resulting model is termed decoupled:

$$\varepsilon^{-p}\,\frac{\partial\langle\vartheta_2\rangle}{\partial\tau}+\frac{\varepsilon^{-p}}{\sqrt{\varepsilon}}\langle u_2-V\rangle\frac{\partial\langle\vartheta_2\rangle}{\partial\xi}=\left[1+\varepsilon^{-2p}\,D_2\right]\frac{\partial^2\langle\vartheta_2\rangle}{\partial\xi^2}+\frac{Q}{\beta}\,\varepsilon^{f-1}+\frac{B}{\beta}\,\varepsilon^{b-1}\,W_2^{\star}, \tag{C27}$$

where the integral contributions to effective diffusivity and viscous dissipation have been denoted for brevity as follows:

$$D_2=-\,\langle\,\mathcal{I}_2\,\rangle\,,\qquad W_2^{\star}=W_2+m\,\frac{\mathrm{d}\check{\mathcal{M}}_1^{\mathcal{W}}}{\mathrm{d}y},\qquad W_2=\int_{1-\beta}^{1}\left(\frac{\mathrm{d}u_2(y^*)}{\mathrm{d}y^*}\right)^2\mathrm{d}y^*. \tag{C28a–c}$$

The full expressions of the above effective coefficients are give later on in Appendix C.6, see (C40*b*) and (C46*c*). After multiplying both sides of (C27) by ε^p, reintroducing dimensionless groups according to (3.2) and scaling back the spatial variable $\xi \mapsto z$ via (3.1), we obtain a one-dimensional ADHT equation for the averaged temperature of the outer phase whose full expression is given in (3.10).

A special scenario is represented for the case where $k = 1/2$: the $\mathcal{O}(\sqrt{\varepsilon})$ solution for the inner phase (C12) yields the following closure:

$$\text{(iv)}: \quad K\,\varepsilon^{-p+a}\,\frac{\check{\mathcal{M}}_1}{\mathrm{d}y}\,\frac{\partial\,\langle\vartheta_1\rangle}{\partial\xi}, \tag{C29}$$

while term (iii) is the same as for the case where $k = 0$. Using (C29) leads to a single-equation model of the form of (C25) but requires an *a priori* knowledge of the axial gradient of the temperature of the inner phase $\partial\,\langle\vartheta_1\rangle/\partial\xi$, reducing to the ADHT equation valid for $k \geqslant 1$ only if the inner phase has a uniform temperature. Thus, this case will not be addressed in this work.

C.5.2 *Coupled model*

When $k = 0$, the thermal conductivities of the two phases are comparable and the upscaled model consists of two coupled equations in the unknowns $\langle\vartheta_j\rangle$. Specifically, the boundary terms (iii), (iv) in (C25) are closed using (C4), obtaining

$$\text{(iii)}: \quad K\,\frac{\partial\vartheta_1^{(1)}}{\partial y}\bigg|_{y=1-\beta} = K\,\varepsilon^{-p+a}\,\frac{\check{\mathcal{M}}_1}{\mathrm{d}y}\,\frac{\partial\,\langle\vartheta_1\rangle}{\partial\xi} - m\,B\,\varepsilon^{b-1}\frac{\mathrm{d}\check{\mathcal{M}}_1^{\mathcal{W}}}{\mathrm{d}y}, \tag{C30a}$$

$$\text{(iv)}: \quad K\,\frac{\partial\vartheta_1^{(2)}}{\partial y}\bigg|_{y=1-\beta} = K\left[\varepsilon^{-p+a}\,\check{\varphi}_1\,\frac{\partial\,\langle\vartheta_1\rangle}{\partial\tau} \underbrace{+\left(\varepsilon^{2(-p+a)}\,\check{\psi}_1 - \check{\varphi}_1\right)\frac{\partial^2\,\langle\vartheta_1\rangle}{\partial\xi^2}}_{(\mathrm{c_{iii}})}\right], \tag{C30b}$$

where we used (C12) and (C19) with $j = 1$. Using (C30*b*) in (C25) introduces a coupled-derivative term, i.e. $\propto \varepsilon^{-p+a}\,\partial\,\langle\vartheta_1\rangle/\partial\tau$, giving an upscaled equation including the time derivative of $\langle\vartheta_1\rangle$ and $\langle\vartheta_2\rangle$ simultaneously. To avoid this issue, we can derive the $\mathcal{O}(\varepsilon)$ solution of (C23) for the inner phase, $\vartheta_1^{(2)}$, and, evaluating it at the interface, we get an expression for replacing the time derivative in (C30*b*):

$$\varepsilon^{-p+a}\,\frac{\partial\,\langle\vartheta_1\rangle}{\partial\tau} = \frac{1}{\check{\Phi}_1}\left\{\vartheta_1^{(2)}\Big|_{y=1-\beta} \underbrace{-\left[\varepsilon^{2\,(-p+a)}\,\check{\Psi}_1 - \check{\Phi}_1\right]\frac{\partial^2\,\langle\vartheta_1\rangle}{\partial\xi^2}}_{(\mathrm{c_{ii}})}\right\}. \tag{C31}$$

The last step is to enforce the continuity of temperature at the interface (C5) asymptotically, replacing the interfacial temperature in (C31) as the following power series:

$$\vartheta_1^{(2)}\Big|_{y=1-\beta}$$

$$= \frac{1}{\varepsilon}\left\{\underbrace{(\langle\vartheta_2\rangle - \langle\vartheta_1\rangle)}_{\text{(a)}} + \underbrace{\sqrt{\varepsilon}\,\left(\vartheta_2^{(1)} - \vartheta_1^{(1)}\right)\Big|_{y=1-\beta}}_{\text{(b)}} + \underbrace{\varepsilon\,\vartheta_2^{(2)}\Big|_{y=1-\beta}}_{(\mathrm{c_i})} + \mathcal{O}\left(\varepsilon\sqrt{\varepsilon}\right)\right\}. \tag{C32}$$

This procedure shows that three different mechanisms are needed to adequately capture the thermal interplay between the phases, namely a storage-type term (a), coupled advective contributions due to axial gradients, term (b), and time-dependent/diffusive contributions, term (c). Specifically, term (b) is obtained as the difference between the $\mathcal{O}(\sqrt{\varepsilon})$ solutions, see (C12), (C15), evaluated at the interface, whereas term (c) can be detailed as follows: term ($\mathrm{c_i}$) follows from (C23) (with $j=2$), thus containing a time-derivative ($\propto \partial\,\langle\vartheta_2\rangle\,/\partial\tau$) and a direct-diffusive term ($\propto \partial^2\,\langle\vartheta_2\rangle\,/\partial\xi^2$), while terms($\mathrm{c_{ii}}$) and ($\mathrm{c_{iii}}$) results in cross-diffusion ($\propto \partial^2\,\langle\vartheta_1\rangle\,/\partial\xi^2$). Note that existing transport models between coupled layers have postulated the coupling only in the form of a storage term (Reichert & Wanner 1991; Kazezyılmaz-Alhan 2008) or, additionally, an advective contribution due to axial gradients (Ling *et al.* 2016, 2021, 2024), but our analysis highlights that also cross-diffusive terms emerge naturally from the derivation of the model via asymptotic expansions and should be accounted for to preserve the model consistency.

The upscaled energy equation for the inner phase can be obtained following the same procedure shown in § C.5 with $j=1$ and using the symmetry condition (C6) at the channel centre line (the detailed derivation is not shown here for the sake of brevity); this gives

$$\varepsilon^{-p+a}\left[\varepsilon\,\frac{\partial\langle\vartheta_1\rangle}{\partial\tau} + \sqrt{\varepsilon}\,\langle u_1 - V\rangle\frac{\partial\langle\vartheta_1\rangle}{\partial\xi} + \varepsilon\overbrace{\left\langle(u_1-V)\frac{\partial\vartheta_1^{(1)}}{\partial\xi}\right\rangle}^{\text{(i)}} + \varepsilon\sqrt{\varepsilon}\overbrace{\left\langle(u_1-V)\frac{\partial\vartheta_1^{(2)}}{\partial\xi}\right\rangle}^{\text{(ii)}}\right]$$

$$= \varepsilon\,\frac{\partial^2\,\langle\vartheta_1\rangle}{\partial\xi^2} + \frac{\sqrt{\varepsilon}}{1-\beta}\left(\underbrace{\frac{\partial\vartheta_2^{(1)}}{\partial y}\Big|_{y=1-\beta}}_{\text{(iii)}} - 0\right) + \frac{\varepsilon}{1-\beta}\left(\underbrace{\frac{\partial\vartheta_2^{(2)}}{\partial y}\Big|_{y=1-\beta}}_{\text{(iv)}} - 0\right)$$

$$+ \frac{m\,B\,\varepsilon^{b-k}}{K\,(1-\beta)}\int_0^{1-\beta}\left(\frac{\mathrm{d}u_1(y^*)}{\mathrm{d}y^*}\right)^2\mathrm{d}y^*, \tag{C33}$$

where, in analogy with (C28), we can define the following effective coefficients for diffusion and viscous dissipation – the full expressions are given in Appendix C.6, see (C40*a*) and (C46*c*):

$$D_1 = -\,\langle\,\mathcal{I}_1\,\rangle\,, \qquad W_1 = \int_0^{1-\beta}\left(\frac{\mathrm{d}u_1(y^*)}{\mathrm{d}y^*}\right)^2\mathrm{d}y^*. \tag{C34a–b}$$

The closure of two advective terms (i), (ii) and two boundary terms (iii), i(v) in (C33) is obtained as before: regardless of the value of k, by means of (C17) and (C20), we find that term (i) is equal to $\varepsilon^{-p+a}\,\langle\,\mathcal{I}_1\,\rangle\,\partial^2\,\langle\vartheta_1\rangle/\partial\xi^2$, while term (ii) is zero by averaging equation (C3d) with $j=1$. Again, the closure of terms (iii) and (iv) is accomplished via the boundary conditions at the interface: for term (iii), it is sufficient to enforce at $\mathcal{O}(\sqrt{\varepsilon})$ the continuity of thermal fluxes, see (C4), while for term (iv), this condition at $\mathcal{O}(\varepsilon)$ has to be combined with the continuity of temperatures written in asymptotic terms, in analogy with (C32):

$$\vartheta_2^{(2)}\Big|_{y=1-\beta} = \frac{1}{\varepsilon}\left\{(\langle\vartheta_1\rangle-\langle\vartheta_2\rangle)+\sqrt{\varepsilon}\,\left(\vartheta_1^{(1)}-\vartheta_2^{(1)}\right)\Big|_{y=1-\beta}+\varepsilon\;\vartheta_1^{(2)}\Big|_{y=1-\beta}+\mathcal{O}\left(\varepsilon\sqrt{\varepsilon}\right)\right\}. \tag{C35}$$

Finally, we obtain that heat-transfer between two flowing phases is described by the following two coupled ADHT equations:

$$\begin{cases} \varepsilon^{-p+a}\,t_1^\star\,\dfrac{\partial\langle\vartheta_1\rangle}{\partial\tau}+\dfrac{1}{\sqrt{\varepsilon}}\,\varepsilon^{-p+a}\,a_{11}^\star\,\dfrac{\partial\langle\vartheta_1\rangle}{\partial\xi}+\dfrac{1}{\sqrt{\varepsilon}}\,\varepsilon^{-p}\,a_{12}^\star\,\dfrac{\partial\langle\vartheta_2\rangle}{\partial\xi}= \\ \quad d_{11}^\star\,\dfrac{\partial^2\langle\vartheta_1\rangle}{\partial\xi^2}+\dfrac{1}{\varepsilon^{2p}}\,d_{12}^\star\,\dfrac{\partial^2\langle\vartheta_2\rangle}{\partial\xi^2}+\dfrac{1}{\varepsilon}\,g_1^\star\,Q\,\varepsilon^f+\dfrac{1}{\varepsilon}\,w_1^\star\,B\,\varepsilon^b-\dfrac{1}{\varepsilon}\,e_1^\star\left(\langle\vartheta_1\rangle-\langle\vartheta_2\rangle\right), \\ \varepsilon^{-p}\,t_2^\star\,\dfrac{\partial\langle\vartheta_2\rangle}{\partial\tau}+\dfrac{1}{\sqrt{\varepsilon}}\,\varepsilon^{-p}\,a_{22}^\star\,\dfrac{\partial\langle\vartheta_2\rangle}{\partial\xi}+\dfrac{1}{\sqrt{\varepsilon}}\,\varepsilon^{-p+a}\,a_{21}^\star\,\dfrac{\partial\langle\vartheta_1\rangle}{\partial\xi}= \\ \quad d_{22}^\star\,\dfrac{\partial^2\langle\vartheta_2\rangle}{\partial\xi^2}+\dfrac{\varepsilon^{2a}}{\varepsilon^{2p}}\,d_{21}^\star\,\dfrac{\partial^2\langle\vartheta_1\rangle}{\partial\xi^2}+\dfrac{1}{\varepsilon}\,g_2^\star\,Q\,\varepsilon^f+\dfrac{1}{\varepsilon}\,w_2^\star\,B\,\varepsilon^b+\dfrac{1}{\varepsilon}\,e_2^\star\left(\langle\vartheta_1\rangle-\langle\vartheta_2\rangle\right), \end{cases} \tag{C36a,b}$$

where the effective coefficients are defined as follows and their explicit expressions are given in Appendix C.6:

$$t_1^\star=1-\frac{\check{\varphi}_2\,\check{\Phi}_1}{K\,(1-\beta)\,\check{\Phi}_2},\qquad t_2^\star=1+\frac{K\,\check{\varphi}_1\,\check{\Phi}_2}{\beta\,\check{\Phi}_1}, \tag{C37a}$$

$$a_{11}^\star=\langle u_1-V\rangle+\omega_{11}^\star,\quad a_{22}^\star=\langle u_2-V\rangle+\omega_{22}^\star, \tag{C37b}$$

$$\omega_{11}^\star=-\frac{\check{\varphi}_2\,\check{\mathcal{M}}_1}{K\,(1-\beta)\,\check{\Phi}_2},\quad \omega_{22}^\star=\frac{K\,\check{\varphi}_1\,\check{\mathcal{M}}_2}{\beta\,\check{\Phi}_1}, \tag{C37c}$$

$$a_{12}^\star=\frac{1}{K\,(1-\beta)}\left(\frac{\check{\varphi}_2\,\check{\mathcal{M}}_2}{\check{\Phi}_2}-\frac{\mathrm{d}\check{\mathcal{M}}_2}{\mathrm{d}y}\right),\quad a_{21}^\star=\frac{K}{\beta}\left(\frac{\mathrm{d}\check{\mathcal{M}}_1}{\mathrm{d}y}-\frac{\check{\varphi}_1\,\check{\mathcal{M}}_1}{\check{\Phi}_1}\right), \tag{C37d}$$

$$d_{11}^\star=t_1^\star+\frac{\varepsilon^{2a}}{\varepsilon^{2p}}\left(D_1+\delta_{11}^\star\right),\quad d_{22}^\star=t_2^\star+\frac{1}{\varepsilon^{2p}}\left(D_2+\delta_{22}^\star\right), \tag{C37e}$$

$$\delta_{11}^{\star} = \frac{\check{\varphi}_2\,\check{\Psi}_1}{K\,(1-\beta)\,\check{\Phi}_2}, \quad \delta_{22}^{\star} = -\frac{K\,\check{\varphi}_1\,\check{\Psi}_2}{\beta\,\check{\Phi}_1}, \tag{C37f}$$

$$d_{12}^{\star} = \frac{1}{K\,(1-\beta)}\left(\check{\psi}_2 - \frac{\check{\varphi}_2\,\check{\Psi}_2}{\check{\Phi}_2}\right), \quad d_{21}^{\star} = \frac{K}{\beta}\left(\frac{\check{\varphi}_1\,\check{\Psi}_1}{\check{\Phi}_1} - \check{\psi}_1\right), \tag{C37g}$$

$$g_1^{\star} = \frac{1}{K\,(1-\beta)}\left(\frac{\mathrm{d}\check{\mathcal{M}}_2^q}{\mathrm{d}y} - \frac{\check{\varphi}_2\,\check{\mathcal{M}}_2^q}{\check{\Phi}_2}\right), \quad g_2^{\star} = \frac{1}{\beta}\left(1 - \frac{K\,\check{\varphi}_1\,\check{\mathcal{M}}_2^q}{\check{\Phi}_1}\right), \tag{C37h}$$

$$\begin{aligned} w_1^{\star} &= \frac{1}{K\,(1-\beta)}\left[m\left(W_1 - \frac{\check{\varphi}_2\,\check{\mathcal{M}}_1^{\mathcal{W}}}{K\,\check{\Phi}_2}\right) - \frac{\mathrm{d}\check{\mathcal{M}}_2^{\mathcal{W}}}{\mathrm{d}y} + \frac{\check{\varphi}_2\,\check{\mathcal{M}}_2^{\mathcal{W}}}{\check{\Phi}_2}\right], \\ w_2^{\star} &= \frac{1}{\beta}\left[W_2 + m\,\frac{\mathrm{d}\check{\mathcal{M}}_1^{\mathcal{W}}}{\mathrm{d}y} + \frac{\check{\varphi}_1}{\check{\Phi}_1}\left(K\,\check{\mathcal{M}}_2^{\mathcal{W}} - m\,\check{\mathcal{M}}_1^{\mathcal{W}}\right)\right], \end{aligned} \tag{C37i}$$

$$e_1^{\star} = -\frac{\check{\varphi}_2}{K\,(1-\beta)\,\check{\Phi}_2}, \quad e_2^{\star} = \frac{K\,\check{\varphi}_1}{\beta\,\check{\Phi}_1}. \tag{C37j}$$

Reintroducing dimensionless groups and scaling back the spatial variable, we obtain the coupled model in its final form, see (3.8), (3.9).

Note that the ADHT equations of the coupled model (C37) reduce to the decoupled model in the limit of $K \to 0$. This requires that in $w_2^{\star}$, we artificially remove the contribution originated by the dissipative function within the inner stream $\check{\mathcal{M}}_1^{\mathcal{W}}$, which is not part of the decoupled formulation.

C.6 *Model coefficients*

The full expressions of the effective coefficients (C37) are reported below, while their physical interpretation will be given in § 4.

In particular, transient effects are taken into account via the following coefficients:

$$t_1^{\star} = 1 + \frac{1-\beta}{K\,\beta}, \quad t_2^{\star} = 1 + \frac{K\,\beta}{1-\beta}. \tag{C38}$$

Advective coefficients appearing in (3.8), (3.9) read

$$\omega_{11}^{\star} = \frac{3\,\Lambda\,(1-\beta)\left[5\,m\,\beta(2-\beta) + 4\,(1-\beta)^2\right]}{5\,K\,\beta} - \frac{1-\beta}{K\,\beta}\,V, \tag{C39a}$$

$$\omega_{22}^{\star} = \frac{3\,K\,\Lambda\,m\,\beta^2\,(15-4\,\beta)}{20\,\,(1-\beta)} - \frac{K\,\beta}{1-\beta}\,V, \tag{C39b}$$

$$a_{12}^{\star} = \frac{\Lambda\,m\,\beta^2\,(15-8\,\beta)}{20\,K\,(1-\beta)}, \quad a_{21}^{\star} = -\frac{2\,\Lambda\,K\,(1-\beta)^3}{5\,\beta}; \tag{C39c}$$

while effective diffusion is described by the following set of coefficients:

$$D_1 = -\frac{2\,\Lambda\,(1-\beta)^4}{15}\,V + \frac{2\,\Lambda^2\,(1-\beta)^4\left[7\,m\,\beta\,(2-\beta)+6\,(1-\beta)^2\right]}{35}, \tag{C40a}$$

$$D_2 = \frac{\Lambda\,m\,\beta^3\,(15-8\beta)}{60}\,V - \frac{\Lambda^2\,m^2\,\beta^4\left(8\,\beta^2-49\,\beta+63\right)}{140}; \tag{C40b}$$

$$\delta^\star_{11} = \frac{(1-\beta)^3}{15\,K\,\beta}\,V^2 + \frac{2\,\Lambda\,(1-\beta)^3\left[(1-m)\,\beta\,(2-\beta)-1\right]}{5\,K\,\beta}\,V + \\ + \frac{\Lambda^2\,(1-\beta)^3\left[105\,m^2\,\beta^2\,(2-\beta)^2+210\,m\,\beta\,(2-\beta)\,(1-\beta)^2+104\,(1-\beta)^4\right]}{175\,K\,\beta}, \tag{C41a}$$

$$\delta^\star_{22} = \frac{K\,\beta^3}{15\,(1-\beta)}\,V^2 + \frac{K\,\Lambda\,m\,\beta^4}{8\,(1-\beta)}\,V - \frac{K\,\Lambda^2\,m^2\,\beta^5\left(32\,\beta^2-105\,\beta-270\right)}{5600\,\,(1-\beta)}, \tag{C41b}$$

$$d^\star_{12} = -\frac{\beta^3}{15\,K(1-\beta)}\,V^2 + \frac{\Lambda\,m\,\beta^4(45-16\,\beta)}{120\,K(1-\beta)}\,V - \frac{\Lambda^2\,m^2\,\beta^5(288\,\beta^2-1855\,\beta+2790)}{5600\,K(1-\beta)}, \tag{C42a}$$

$$d^\star_{21} = -\frac{K\,(1-\beta)^3}{15\,\beta}\,V^2 + \frac{2\,K\,\Lambda\,(1-\beta)^3\left[3\,m\,\beta\,(2-\beta)+2\,(1-\beta)^2\right]}{15\,\beta}\,V + \\ - \frac{K\,\Lambda^2\,(1-\beta)^3\left[105\,m^2\,\beta^2\,(2-\beta)^2+140\,m\,\beta\,(2-\beta)\,(1-\beta)^2+44\,(1-\beta)^4\right]}{175\,\beta}. \tag{C42b}$$

Among the effective coefficients, see (C37), the speed of the reference frame V only impacts effective diffusion and direct-coupling advection $a^\star_{jj}$. Specifically, shifting from moving to the fixed reference frame via the inverse transformation $x = z + V\,\tau$ has no net impact on diffusion, i.e. $\partial^2\langle\vartheta_j\rangle/\partial z^2 \equiv \partial^2\langle\vartheta_j\rangle/\partial x^2$, but offers significant advantages in terms of the physical interpretation of the advective coefficients. In fact, each of these could be recast as the phase-averaged velocity augmented by a specific factor, namely $U^\star_j = a^\star_{jj} + V\,t^\star_{jj} = U_j - V + \omega^\star_{jj} + V\,t^\star_{jj} = U_j + \Delta U^\star_j$, where

$$\Delta U^\star_1 = \frac{3\,\Lambda\,(1-\beta)\left[5\,m\,\beta(2-\beta)+4\,(1-\beta)^2\right]}{5\,K\,\beta}, \quad \Delta U^\star_2 = \frac{3\,K\,\Lambda\,m\,\beta^2\,(15-4\,\beta)}{20\,\,(1-\beta)}. \tag{C43}$$

Interestingly, the final expressions for $\Delta U^\star_j$ defined in (C43) are independent of V, implying that effective extra-advection is invariant with respect to the choice of the reference frame, i.e. $\omega^\star_{jj}\big|_{V=0} \equiv \Delta U^\star_j$.

The effective coefficients in front of the source terms in (C36) read

$$g^\star_1 = -\frac{1}{2\,K\,(1-\beta)}, \qquad g^\star_2 = \frac{1}{\beta} + \frac{3\,K}{2\,(1-\beta)}; \tag{C44}$$

whereas those concerning storage are

$$e_1^\star = \frac{3}{K\,\beta\,(1-\beta)}, \qquad e_2^\star = \frac{3\,K}{\beta\,(1-\beta)}. \tag{C45}$$

Finally, the analytical expressions for the effective coefficients related to viscous dissipation are

$$w_1^\star = \frac{3\,\Lambda^2\,m\left\{4\,(1-\beta)^3\,[5\,K\beta+3\,(1-\beta)]-K\,m\,\beta^3\,(15-8\,\beta)\right\}}{5\,K^2\,\beta\,(1-\beta)}, \tag{C46a}$$

$$w_2^\star = \frac{3\,\Lambda^2\,m\left\{m\left[3\,\beta^2\,K\left(4\,\beta^2-15\,\beta+20\right)+20\,\beta\,(1-\beta)\left(\beta^2-3\beta+3\right)\right]+8\,(1-\beta)^4\right\}}{5\,\beta\,(1-\beta)}, \tag{C46b}$$

$$W_1 = 12\,\Lambda^2\,(1-\beta)^3\,, \qquad W_2 = 12\,\Lambda^2\,m^2\,\beta\left(\beta^2-3\,\beta+3\right), \qquad W_2^* = 6\,\Lambda\,m. \tag{C46c}$$

Appendix D. Model validation

To check the accuracy of the ADHT equations (3.8), (3.9), we present the validation against the steady-state solution of the problem. At the steady-state, in fact, the temperature gradients along the channel length are uniform and diffusion becomes negligible so that (in the absolute reference frame, $V = 0$)

$$\frac{\mathrm{d}\vartheta_1}{\mathrm{d}x} = \frac{\mathrm{d}\vartheta_2}{\mathrm{d}x} = J. \tag{D1}$$

Consequently, the energy balances (2.13) reduce to

$$\varepsilon\,\mathcal{A}\,Pe\,J\,u_1 = \frac{\mathrm{d}^2\vartheta_1}{\mathrm{d}y^2} + \frac{m}{\mathcal{K}}\,Br\left(\frac{\mathrm{d}u_1}{\mathrm{d}y}\right)^2, \quad y\in[0;\;1-\beta]\,, \tag{D2a}$$

$$\varepsilon\,Pe\,J\,u_2 = \frac{\mathrm{d}^2\vartheta_2}{\mathrm{d}y^2} + Br\left(\frac{\mathrm{d}u_2}{\mathrm{d}y}\right)^2, \qquad y\in[1-\beta;\;1]\,, \tag{D2b}$$

subjected to boundary conditions (2.16). Integrating (D2) gives

$$\frac{\mathrm{d}\vartheta_1(y)}{\mathrm{d}y} = \varepsilon\,\mathcal{A}\,Pe\,J\int u_1(y^*)\,\mathrm{d}y^* - \frac{m}{\mathcal{K}}\,Br\int\left(\frac{\mathrm{d}u_1(y^*)}{\mathrm{d}y^*}\right)^2\mathrm{d}y^* + C_1, \tag{D3a}$$

$$\frac{\mathrm{d}\vartheta_2(y)}{\mathrm{d}y} = \varepsilon\,Pe\,J\int u_2(y^*)\,\mathrm{d}y^* - Br\int\left(\frac{\mathrm{d}u_2(y^*)}{\mathrm{d}y^*}\right)^2\mathrm{d}y^* + C_2, \tag{D3b}$$

where C_1 and C_2 are integration constants. The value of C_1 is determined via the symmetry boundary condition (2.16*d*), whereas the boundary condition at the wall (2.16*a*) allows to express the other constant of integration as a function of the steady-state axial gradient J and the external heat flux q_w, i.e. implicitly $C_2 = C_2(q_w,\;J,\;\ldots)$. The expression for J can be found using the thermal flux continuity condition at the interface (2.16*b*) and solving for $J = J(q_w,\ldots)$. These calculations have been carried out using a

symbolic tool and are not reported here for the sake of brevity. It can be easily checked that J is equivalent to the slope of the steady-state solution, M, of the leading-order model given in (4.21), obtaining that $M|_{V=0} = \sqrt{\varepsilon}\, J$.

Finally, aiming at validating the steady-state Nusselt number with the analytical solution of (D2), we can first integrate (D3) to obtain the steady-state temperature profile. Then, the continuity of temperatures at the interface (2.16*c*) is used to eliminate one of the two additional integration constants. It is convenient to leave the constant for the outer phase temperature undetermined since it does not affect the definition of the Nusselt number (3.19): at the denominator of the local heat-transfer coefficient, only the difference between the wall and the bulk temperature appears. Doing so, the expressions of the steady-state Nusselt number obtained using the steady-state analytical solution and the upscaled model match exactly, confirming the consistency of our model.

References

Abdollahi, A., Sharma, R.N. & Vatani, A. 2017 Fluid flow and heat transfer of liquid-liquid two phase flow in microchannels: a review. *Intl Commun. Heat Mass Transfer* **84**, 66–74.

Adera, S., Naworski, L., Davitt, A., Mandsberg, N.K., Shneidman, A.V., Alvarenga, J. & Aizenberg, J. 2021 Enhanced condensation heat transfer using porous silica inverse opal coatings on copper tubes. *Sci. Rep.* **11** (1), 10675.

Ali, N. & Khan, M.W.S. 2018 The graetz problem for the ellis fluid model. *Z. Naturforsch.* **74** (1), 15–24.

Allaire, G., Mikelić, A. & Piatnitski, A. 2010 Homogenization approach to the dispersion theory for reactive transport through porous media. *SIAM J. Math. Anal.* **42** (1), 125–144.

Ananthakrishnan, V., Gill, W.N. & Barduhn, A.J. 1965 Laminar dispersion in capillaries: Part I. Mathematical analysis. *AIChE J.* **11** (6), 1063–1072.

Aris, R. 1956 On the dispersion of a solute in a fluid flowing through a tube. *Proc. R. Soc. Lond. A Math. Phys. Sci.* **235**, 67–77.

Aris, R. 1959 On the dispersion of a solute by diffusion, convection and exchange between phases. *Proc. R. Soc. Lond. A Math. Phys. Sci.* **252** (1271), 538–550.

Armatis, P.D. & Fronk, B.M. 2017 Evaluation of governing heat and mass transfer resistance in membrane-based energy recovery ventilators with internal support structures. *Sci. Technol. Built Environ.* **23** (6), 912–922.

Arney, M.S., Bai, R., Guevara, E., Joseph, D.D. & Liu, K. 1993 Friction factor and holdup studies for lubricated pipelining—I. Experiments and correlations. *Intl J. Multiphase Flow* **19** (6), 1061–1076.

Asghar, Z., Khan, M.W.S., Shatanawi, W. & Gondal, M.A. 2023 Semi-analytical solution of Graetz–Brinkman problem combined with non-Newtonian Ellis fluid flow in a passive channel. *Eur. Phys. J. Plus* **138** (11), 978.

Auriault, J.-L. 2002 Upscaling heterogeneous media by asymptotic expansions. *J. Engng Mech.* **128** (8), 817–822.

Auriault, J.-L. & Adler, P.M. 1995 Taylor dispersion in porous media: analysis by multiple scale expansions. *Adv. Water Resour.* **18** (4), 217–226.

Auriault, J.-L. & Lewandowska, J. 1994 On the cross-effects of coupled macroscopic transport equations in porous media. *Transp. Porous Med.* **16** (1), 31–52.

Auriault, J.-L. & Lewandowska, J. 1996 Diffusion/adsorption/advection macrotransport in soils. *Eur. J. Mech. A-Solid* **15**, 681–704.

Aussillous, P. & Quéré, D. 2000 Quick deposition of a fluid on the wall of a tube. *Phys. Fluids* **12** (10), 2367–2371.

Bai, H.Y., Zhu, J., Chen, Z. & Chu, J. 2018 State-of-art in modelling methods of membrane-based liquid desiccant heat and mass exchanger: a comprehensive review. *Intl J. Heat Mass Transfer* **125**, 445–470.

Balestra, G., Zhu, L. & Gallaire, F. 2018 Viscous taylor droplets in axisymmetric and planar tubes: from bretherton's theory to empirical models. *Microfluid Nanofluid* **22** (6), 67.

Bannwart, A.C., Rodriguez, O.M.H., Trevisan, F.E., Vieira, F.F. & de Carvalho, C.H.M. 2004 Flow patterns and pressure gradients in horizontal, upward inclined and vertical heavy oil–water–gas flows: experimental investigation and full-scale experiments. In *Proceedings of the 3rd International Symposium on Two-Phase Flow Modelling and Experimentation* (ed. G.P. Celata, P. Di Marco, A. Mariani & R.K. Shah), vol. 4, pp. 2605–2614. Edizioni ETS.

BARRERA, C., LETELIER, M., SIGINER, D. & STOCKLE, J. 2016 The Graetz problem in tubes of arbitrary cross section. *Acta Mechanica* **227** (11), 3239–3246.
BATTIATO, I. & TARTAKOVSKY, D.M. 2011 Applicability regimes for macroscopic models of reactive transport in porous media. *J. Contam. Hydrol.* **120-121**, 18–26.
BATTIATO, I., TARTAKOVSKY, D.M., TARTAKOVSKY, A.M. & SCHEIBE, T.D. 2011 Hybrid models of reactive transport in porous and fractured media. *Adv. Water Resour.* **34** (9), 1140–1150.
BATYCKY, R.P., EDWARDS, D.A. & BRENNER, H. 1994 Thermal Taylor dispersion phenomena in nondiabatic systems. *Chem. Engng Commun.* **130** (1), 53–104.
BENSOUSSAN, A., LIONS, J.-L. & PAPANICOLAOU, G. 2011 *Asymptotic Analysis for Periodic Structures*. American Mathematical Society.
BENTWICH, M. & SIDEMAN, S. 1964*a* Temperature distribution and heat transfer in annular two-phase (liquid-liquid) flow. *Can. J. Chem. Engng* **42** (1), 9–13.
BENTWICH, M. & SIDEMAN, S. 1964*b* Temperature distribution in cocurrent two-phase (liquid-liquid) laminar flow on inclined surfaces. *J. Heat Transfer* **86** (4), 476–480.
BERKOWITZ, B. & ZHOU, J. 1996 Reactive solute transport in a single fracture. *Water Resour. Res.* **32** (4), 901–913.
BIRD, R.B., STEWART, W.E. & LIGHTFOOT, E.N. 1960 *Transport Phenomena*. Wiley.
BOSO, F. & BATTIATO, I. 2013 Homogenizability conditions for multicomponent reactive transport. *Adv. Water Resour.* **62**, 254–265.
BOUCHER, D.F. & ALVES, G.E. 1963 Dimensionless numbers: for fluid mechanics heat transfer, mass transfer and chemical reaction. *Chem. Engng Prog.* **59** (8), 75–83.
BOURBATACHE, M.K., MILLET, O. & MOYNE, C. 2020 Upscaling diffusion–reaction in porous media. *Acta Mechanica* **38** (4), 1262–1287.
BOUSSINESQ, J. 1890 Hydrodynamique. *C. R. Acad. Sci.* **110** (1160-1170), 1238–1242.
BOUTIN, C., AURIAULT, J.-L. & GEINDREAU, C. 2010 *Homogenization of Coupled Phenomena in Heterogenous Media*. Wiley.
BRADY, J.B. 1975 Reference frames and diffusion coefficients. *Am. J. Sci.* **275** (8), 954–983.
BRAUNER, N. 2002 Heat transfer to a liquid-liquid mixture - which of the liquids is in contact with the tube wall? *Heat Transfer Engng* **23** (3), 1–2.
BRENNER, H. 1980 A general theory of taylor dispersion phenomena. *Physico-Chem. Hydrodyn.* **1** (2-3), 91–123.
BRENNER, H. 1982 A general theory of Taylor dispersion phenomena IV. Direct coupling effects. *Chem. Engng Commun.* **18** (5-6), 355–379.
BRENNER, H. & EDWARDS, D.A. 1993 *Macrotransport Processes*. Butterworth-Heinemann.
BRENNER, H. & STEWARTSON, K. 1980 Dispersion resulting from flow through spatially periodic porous media. *Phil. Trans. R. Soc. Lond. A Math. Phys. Sci.* **297** (1430), 81–133.
BRETHERTON, F.P. 1961 The motion of long bubbles in tubes. *J. Fluid Mech.* **10** (2), 166–188.
BRINKMAN, H.C. 1951 Heat effects in capillary flow I. *Appl. Sci. Res.* **2** (1), 120–124.
CARSLAW, H.S. & JAEGER, J.C. 1959 *Conduction of Heat in Solids*. Oxford science publications, Clarendon Press.
CELATA, G.P., CHIARADIA, A., CUMO, M. & D'ANNIBALE, F. 1999 Heat transfer enhancement by air injection in upward heated mixed-convection flow of water. *Intl J. Multiphase Flow* **25** (6-7), 1033–1052.
CHALHUB, D.J.N.M., CORRÊA, L.M. & TEIXEIRA, R.DE S. 2022 Analytical solution for thermally developing laminar core-annular flow with two immiscible liquids considering axial diffusion in semi-infinite ducts. *Chem. Engng Res. Des.* **178**, 1–12.
CHEN, K., COTTA, R.M., NAVEIRA-COTTA, C.P. & PONTES, P.C. 2022 Heat transfer analysis of compressible laminar flow in a parallel-plates channel via integral transforms. *Intl Commun. Heat Mass Transfer* **138**, 106368.
CHU, S.-Y., SPOSITO, G. & JURY, W.A. 1983 The cross-coupling transport coefficient for the steady flow of heat in soil under a gradient of water content. *Soil Sci. Soc. Am. J.* **47** (1), 21–25.
CIONCOLINI, A. 2023 Liquid entrainment in annular gas–liquid two-phase flow: a critical assessment of experimental data and prediction methods. *Phys. Fluids* **35** (11), 111303.
COLLE, S. 1988 The extended graetz problem with arbitrary boundary conditions in an axially heat conducting tube. *Appl. Sci. Res.* **45** (1), 33–51.
COLLIER, J.G. & THOME, J.R. 1994 *Convective Boiling and Condensation*. Oxford University Press.
COTTA, R.M. & ÖZIŞIK, M.N. 1986 Laminar forced convection to non-newtonian fluids in ducts with prescribed wall heat flux. *Intl Commun. Heat Mass Transfer* **13** (3), 325–334.
CRASTER, R.V. & MATAR, O.K. 2009 Dynamics and stability of thin liquid films. *Rev. Mod. Phys.* **81** (3), 1131–1198.

DAI, Z., GUO, Z., FLETCHER, D.F. & HAYNES, B.S. 2015 Taylor flow heat transfer in microchannels—unification of liquid–liquid and gas–liquid results. *Chem. Engng Sci.* **138**, 140–152.

DEJAM, M., HASSANZADEH, H. & CHEN, Z. 2014 Shear dispersion in a fracture with porous walls. *Adv. Water Resour.* **74**, 14–25.

DUNGAN, S.R., SHAPIRO, M. & BRENNER, H. 1990 Convective-diffusive-reactive taylor dispersion processes in particulate multiphase systems. *Proc. R. Soc. Lond. A Math. Phys. Sci.* **429** (1877), 639–671.

DUPONT, V., THOME, J.R. & JACOBI, A.M. 2004 Heat transfer model for evaporation in microchannels. part ii: comparison with the database. *Intl J. Heat Mass Transfer* **47** (14-16), 3387–3401.

FAKOOR-PAKDAMAN, M., ANDISHEH-TADBIR, M. & BAHRAMI, M. 2014 Unsteady laminar forced-convective tube flow under dynamic time-dependent heat flux. *J. Heat Transfer* **136** (4), 041706.

FALLON, M.S. & CHAUHAN, A. 2005 Dispersion in core–annular flow with a solid annulus. *AIChE J.* **51** (9), 2415–2427.

FARAH, Y., LOGHIN, D., TZELLA, A. & VANNESTE, J. 2020 Diffusion in arrays of obstacles: beyond homogenization. *Proc. R. Soc. Lond. A: Math. Phys. Engng Sci.* **476**, 2244.

FEDER, J., FLEKKØY, E.G. & HANSEN, A. 2022 *Physics of Flow in Porous Media*. Cambridge University Press.

FEUILLEBOIS, F. & LASEK, A. 1977 Computer aided application of the principle of least degeneracy. *Z. Angew. Math. Phys.* **28** (6), 1141–1146.

FRANKEL, I. & BRENNER, H. 1989 On the foundations of generalized Taylor dispersion theory. *J. Fluid Mech.* **204** (1), 97–119.

GHAJAR, A.J. & TANG, C.C. 2010 Importance of non-boiling two-phase flow heat transfer in pipes for industrial applications. *Heat Transfer Engng* **31** (9), 711–732.

GRAETZ, L. 1882 Ueber die wärmeleitungsfähigkeit von flüssigkeiten (on the thermal conductivity of liquids). *Annalen der Physik* **254** (1), 79–94.

GRIFFITHS, I.M., HOWELL, P.D. & SHIPLEY, R.J. 2013 Control and optimization of solute transport in a thin porous tube. *Phys. Fluids* **25** (3), 3.

GUEVARA, E. & GOTHAM, D.H.T. 1983 Entrainment in condensing annular flow. *Intl J. Multiphase Flow* **9** (4), 411–419.

HASAN, A.R. & KABIR, C.S. 2010 Modeling two-phase fluid and heat flows in geothermal wells. *J. Petrol. Sci. Engng* **71** (1-2), 77–86.

HASSON, D. 1978 Scale prevention by annular flow of an immiscible liquid along the walls of a heated tube. In *Proceeding of International Heat Transfer Conference*, pp. 6. Begellhouse.

HIRBODI, K., YAGHOUBI, M. & WARSINGER, D.M. 2022 New Nusselt number correlations for developing and fully developed laminar flows in concentric circular annular ducts. *Intl J. Heat Mass Transfer* **134**, 105936.

HOOYMAN, G.J. 1956 Thermodynamics of diffusion in multicomponent systems. *Physica* **22** (6-12), 751–759.

HORNE, R.N. & RODRIGUEZ, F. 1983 Dispersion in tracer flow in fractured geothermal systems. *Geophys. Res. Lett.* **10** (4), 289–292.

HORNUNG, U. 1997 *Homogenization and Porous Media*. Springer.

HSU, C.-J. 1968 Exact solution to entry-region laminar heat transfer with axial conduction and the boundary condition of the third kind. *Chem. Engng Sci.* **23** (5), 457–468.

INCROPERA, F.P. 2007 *Fundamentals of Heat and Mass Transfer*. Wiley.

JOSEPH, D.D., NGUYEN, K. & BEAVERS, G.S. 1984 Non-uniqueness and stability of the configuration of flow of immiscible fluids with different viscosities. *J. Fluid Mech.* **141**, 319–345.

KAMKE, E. 1977 *Differentialgleichungen Lösungsmethoden und Lösungen*. Vieweg+Teubner Verlag Wiesbaden.

KAZEZYILMAZ-ALHAN, C.M. 2008 Analytical solutions for contaminant transport in streams. *J. Hydrol.* **348** (3-4), 524–534.

KIM, D.E., YU, D.I., JERNG, D.W., KIM, M.H. & AHN, H.S. 2015 Review of boiling heat transfer enhancement on micro/nanostructured surfaces. *Exp. Therm. Fluid Sci.* **66**, 173–196.

KOTTKE, P.A., YUN, T.M., GREEN, C.E., JOSHI, Y.K. & FEDOROV, A.G. 2015 Two-phase convective cooling for ultrahigh power dissipation in microprocessors. *J. Heat Transfer* **138** (1), 011501.

KOZLOVA, S., MIALDUN, A., RYZHKOV, I., JANZEN, T., VRABEC, J. & SHEVTSOVA, V. 2019 Do ternary liquid mixtures exhibit negative main fick diffusion coefficients? *Phys. Chem. Chem. Phys.* **21** (4), 2140–2152.

KRUYER, J., REDBERGER, P.J. & ELLIS, H.S. 1967 The pipeline flow of capsules. Part 9. *J. Fluid Mech.* **30** (3), 513–531.

LANGEROVA, E. & MATUSKA, T. 2023 One-dimensional modelling of sensible heat storage tanks with immersed helical coil heat exchangers: a critical review. *J. Energy Storage* **72**, 108507.

LAVALLE, G., MERGUI, S., GRENIER, N. & DIETZE, G.F. 2021 Superconfined falling liquid films: linear versus nonlinear dynamics. *J. Fluid Mech.* **919**, R2.
LEIB, T.M., FINK, M. & HASSON, D. 1977 Heat transfer in vertical annular laminar flow of two immiscible liquids. *Intl J. Multiphase Flow* **3** (6), 533–549.
LEVITT, D.G. 1972 Capillary-tissue exchange kinetics: an analysis of the Krogh cylinder model. *J. Theor. Biol.* **34** (1), 103–124.
LEWANDOWSKA, J. & AURIAULT, J.-L. 2004 Modelling of unsaturated water flow in soils with highly permeable inclusions. *C. R. Méc* **332** (1), 91–96.
LEWANDOWSKA, J., SZYMKIEWICZ, A. & AURIAULT, J.-L. 2005 Upscaling of Richards' equation for soils containing highly conductive inclusions. *Adv. Water Resour.* **28** (11), 1159–1170.
LIÑÁN, A., RAJAMANICKAM, A., WEISS, P., A., D. & SÁNCHEZ, A.L. 2020 Taylor-diffusion-controlled combustion in ducts. *Combust. Theor. Model.* **24** (6), 1054–1069.
LINDEMER, M.D., ADVANI, S.G. & PRASAD, A.K. 2015 Graetz–Brinkman problem in laminar core-annular flow of two immiscible liquids. *Intl J. Therm. Sci.* **89**, 362–371.
LING, B., RIZZO, C.B., BATTIATO, I. & DE BARROS, F.P.J. 2021 Macroscale transport in channel-matrix systems via integral transforms. *Phys. Rev. Fluids* **6** (4), 044501.
LING, B., SHAN, R. & DE BARROS, F.P.J. 2024 Dispersion control in coupled channel-heterogeneous porous media systems. *Phys. Rev. Fluids* **9** (6), 064502.
LING, B., TARTAKOVSKY, A.M. & BATTIATO, I. 2016 Dispersion controlled by permeable surfaces: surface properties and scaling. *J. Fluid Mech.* **801**, 13–42.
MAGNINI, M. & THOME, J.R. 2017 An updated three-zone heat transfer model for slug flow boiling in microchannels. *Intl J. Multiphase Flow* **91**, 296–314.
MAURI, R. 1991 Dispersion, convection, and reaction in porous media. *Phys. Fluids A: Fluid Dyn.* **3** (5), 743–756.
MAURI, R. 1995 Heat and mass transport in random velocity fields with application to dispersion in porous media. *J. Engng Maths* **29** (1), 77–89.
MAURI, R. 2003 Heat and mass transport in nonhomogeneous random velocity fields. *Phys. Rev. E* **68** (6), 066306.
MAURI, R. 2015 *Transport Phenomena in Multiphase Flows, Fluid Mechanics and Its Applications*, vol. 112, Springer International Publishing.
MAXWELL, J.C. 1873 A treatise on electricity and magnetism. *Clarendon Press* **1**, 365–366.
MAZZINO, A. 1997 Effective correlation times in turbulent scalar transport. *Phys. Rev. E* **56** (5), 5500–5510.
MEI, C.C. & VERNESCU, B. 2010 *Homogenization Methods for Multiscale Mechanics*. World Scientific.
MERRITT, H.E. 1991 *Hydraulic Control Systems*. Wiley.
MIKELIĆ, A., DEVIGNE, V. & VAN DUIJN, C.J. 2006 Rigorous upscaling of the reactive flow through a pore, under dominant peclet and Damkohler numbers. *SIAM J. Math. Anal.* **38** (4), 1262–1287.
MORINI, G.L. & SPIGA, M. 2006 The role of the viscous dissipation in heated microchannels. *J. Heat Transfer* **129** (3), 308–318.
MOYNE, C. & MURAD, M.A. 2006 A two-scale model for coupled electro-chemo-mechanical phenomena and Onsager's reciprocity relations in expansive clays:I homogenization analysis. *Trans. Porous Med.* **62** (3), 333–380.
MUDAWAR, I. 2011 Two-phase microchannel heat sinks: theory, applications, and limitations. *J. Electron. Packag.* **133** (4), 041002.
MURPHY, P.J., ALIMOHAMMADI, S. & O'SHAUGHNESSY, S.M. 2024 Experimental investigation of dual jet flow past a heated surface: effect of Reynolds number. *Intl J. Heat Mass Transfer* **218**, 124786.
NEVEU, P., TESCARI, S., AUSSEL, D. & MAZET, N. 2013 Combined constructal and exergy optimization of thermochemical reactors for high temperature heat storage. *Energy Convers. Manage.* **71**, 186–198.
NOGUEIRA, E. & COTTA, R.M. 1990 Heat transfer solutions in laminar co-current flow of immiscible liquids. *Wärme-Stoffübertrag.* **25** (6), 361–367.
NONINO, C., SAVINO, S., DEL GIUDICE, S. & MANSUTTI, L. 2009 Conjugate forced convection and heat conduction in circular microchannels. *Intl J. Heat Fluid Flow* **30** (5), 823–830.
NUSSELT, W. 1910 Die abhängigkeit der wärmeübergangszahl von der rohrlänge (the dependence of the heat-transfer coefficient on the tube length). *VDI Z.* **54** (28), 1154–1158.
OU, J.W. & CHENG, K.C. 1973 Viscous dissipation effects on thermal entrance region heat transfer in pipes with uniform wall heat flux. *Appl. Sci. Res.* **28** (1), 289–301.
PAHOR, S. & STRNAD, J. 1956 Die Nusseltsche Zahl für laminare Strömung im zylindrischen Rohr mit konstanter Wandtemperatur (the Nusselt number for laminar flow in a cylindrical pipe with constant wall temperature). *Z. Angew. Math. Phys.* **7** (6), 536–538.

PARMIGIANI, A., HUBER, C., BACHMANN, O. & CHOPARD, B. 2011 Pore-scale mass and reactant transport in multiphase porous media flows. *J. Fluid Mech.* **686**, 40–76.

PIÑA, E. 1979 On the De Donder-Meixner transformations in non-equilibrium thermodynamics. *Phys. A: Stat. Mech. Applics.* **98** (3), 613–619.

PICCHI, D. & BATTIATO, I. 2018 The impact of pore-scale flow regimes on upscaling of immiscible two-phase flow in porous media. *Water Resour. Res.* **54** (9), 6683–6707.

PICCHI, D. & POESIO, P. 2022 Dispersion of a passive scalar around a Taylor bubble. *J. Fluid Mech.* **951**, A22.

PICCHI, D., ULLMANN, A. & BRAUNER, N. 2018 Modeling of core-annular and plug flows of Newtonian/non-Newtonian shear-thinning fluids in pipes and capillary tubes. *Intl J. Multiphase Flow* **103**, 43–60.

POESIO, P., STRAZZA, D. & SOTGIA, G. 2009 Very-viscous-oil/water/air flow through horizontal pipes: pressure drop measurement and prediction. *Chem. Engng Sci.* **64** (6), 1136–1142.

POLYANIN, A.D. & ZAITSEV, V.F. 2017 *Handbook of Ordinary Differential Equations: Exact Solutions, Methods, and Problems*. CRC Press.

QUINTARD, M. & WHITAKER, S. 1993 *One- and Two-Equation Models for Transient Diffusion Processes in Two-Phase Systems*. Elsevier, 369–464.

REICHERT, P. & WANNER, O. 1991 Enhanced one-dimensional modeling of transport in rivers. *J. Hydraul. Engng* **117** (9), 1165–1183.

REYNOLDS, W.C. 1963 Effect of wall heat conduction on convection in a circular tube with arbitrary circumferential heat input. *Intl J. Heat Mass Transfer* **6** (10), 925.

RICHARD, G.L., RUYER-QUIL, C. & VILA, J.P. 2016 A three-equation model for thin films down an inclined plane. *J. Fluid Mech.* **804**, 162–200.

RUBINSTEIN, J. & MAURI, R. 1986 Dispersion and convection in periodic porous media. *SIAM J. Appl. Maths* **46** (6), 1018–1023.

SANKARASUBRAMANIAN, R., GILL, W.N. & BENJAMIN, T.B. 1973 Unsteady convective diffusion with interphase mass transfer. *Proc. R. Soc. Lond. A Math. Phys. Sci.* **333** (1592), 115–132.

SCHOLZ, L. & BRINGEDAL, C. 2022 A three-dimensional homogenization approach for effective heat transport in thin porous media. *Transp. Porous Med.* **141** (3), 737–769.

SELLARS, J.R., TRIBUS, M. & KLEIN, J.S. 1956 Heat transfer to laminar flow in a round tube or flat conduit—the Graetz problem extended. *J. Fluids Engng* **78** (2), 441–447.

SHAH, R.K. & LONDON, A.L. 1978 *Laminar Flow Forced Convection in Ducts*. Elsevier.

SHAMPINE, L.F. & REICHELT, M.W. 1997 The matlab ode suite. *SIAM J. Sci. Comput.* **18** (1), 1–22.

SHAMPINE, L.F., REICHELT, M.W. & KIERZENKA, J.A. 1999 Solving Index-1 DAEs in MATLAB and Simulink. *SIAM Rev.* **41** (3), 538–552.

SHELUKHIN, V., YELTSOV, I. & PARANICHEV, I. 2011 The electrokinetic cross-coupling coefficient: two-scale homogenization approach. *World J. Mech.* **01** (03), 127–136.

SIEGEL, R. & PERLMUTTER, M. 1963 Laminar heat transfer in a channel with unsteady flow and wall heating varying with position and time. *J. Heat Transfer* **85** (4), 358–365.

SIEGEL, R. & SPARROW, E.M. 1959 Transient heat transfer for laminar forced convection in the thermal entrance region of flat ducts. *J. Heat Transfer* **81** (1), 29–36.

SKEEL, R.D. & BERZINS, M. 1990 A method for the spatial discretization of parabolic equations in one space variable. *SIAM J. Sci. Stat. Comput.* **11** (1), 1–32.

STOCKMAN, G.E. & EPSTEIN, N. 2001 Uniform flux heat transfer in concentric laminar flow of two immiscible liquids. *Can. J. Chem. Engng* **79** (6), 990–994.

SU, J. 2006 Exact solution of thermal entry problem in laminar core-annular flow of two immiscible liquids. *Chem. Engng Res. Des.* **84** (11), 1051–1058.

TAGHIZADEH, E., VALDÉS-PARADA, F.J. & WOOD, B.D. 2020 Preasymptotic taylor dispersion: evolution from the initial condition. *J. Fluid Mech.* **889**, A5.

TAMIR, A. & TAITEL, Y. 1972 On the concept of the "mixing cup" temperature in flows with axial conduction. *Can. J. Chem. Engng* **50** (3), 421–424.

TAYLOR, G.I. 1953 Dispersion of soluble matter in solvent flowing slowly through a tube. *Proc. R. Soc. Lond. A Math. Phys. Sci.* **219** (1137), 186–203.

TAYLOR, R. & KRISHNA, R. 1993 *Multicomponent Mass Transfer*. Wiley Series in Chemical Engineering. Wiley.

THOME, J.R., DUPONT, V. & JACOBI, A.M. 2004 Heat transfer model for evaporation in microchannels. Part I: presentation of the model. *Intl J. Heat Mass Transfer* **47** (14-16), 3375–3385.

VAN DYKE, M. 1964 *Perturbation Methods in Fluid Mechanics. Applied mathematics and mechanics*. Academic Press.

VAN GENUCHTEN, M.T. & ALVES, W.J. 1982 *Analytical solutions of the one-dimensional convective-dispersive solute transport equation*. Technical Bulletin 1661. U.S. Department of Agriculture, Agricultural Research Service.

VUONG, D.H., SARICA, C., PEREYRA, E. & AL-SARKHI, A. 2018 Liquid droplet entrainment in two-phase oil-gas low-liquid-loading flow in horizontal pipes at high pressure. *Intl J. Multiphase Flow* **99**, 383–396.

WANG, L., CARDENAS, M.B., DENG, W. & BENNETT, P.C. 2012 Theory for dynamic longitudinal dispersion in fractures and rivers with Poiseuille flow. *Geophys. Res. Lett.* **39** (5), L05401.

WANG, L. & FAN, J. 2010 Modeling bioheat transport at macroscale. *J. Heat Transfer* **133** (1), 011010.

YOUNG, W.R. & JONES, S. 1991 Shear dispersion. *Phys. Fluids A: Fluid Dyn.* **3** (5), 1087–1101.

ZHANG, X. & NIKOLAYEV, V.S. 2023 Physics and modeling of liquid films in pulsating heat pipes. *Phys. Rev. Fluids* **8** (8), 084002.

Paper II

P. Botticini, D. Picchi and P. Poesio, *Convective heat transfer around an elongated bubble in the absence of phase change*, submitted to *Physical Review Fluids*, Jan. 2026

While the previous work focused on flat films and examined the competition between advection and diffusion without accounting for interfacial instabilities, this second study explores the non-trivial influence of interfacial geometry in shaping the thermal behaviour of the system. Specifically, heat transfer is investigated in the liquid film region surrounding an elongated inviscid bubble, under the assumption that the gas phase is non-conductive, which represents a particular instance of the decoupled regime identified earlier. Our analysis confirms that film thickness is the key factor governing convective efficiency, with the Nusselt number decreasing as the film becomes thicker. This outcome reaffirms the dominant influence of conductive resistance on heat transfer in thin films, extending the theoretical framework of two-scale asymptotics to curved geometries.

Convective heat transfer around an elongated bubble in the absence of phase change

Paolo Botticini,[1] Davide Picchi,[1,*] and Pietro Poesio[1]

[1] *Department of Mechanical and Industrial Engineering, Università degli Studi di Brescia, Brescia 25123, Italy*

(Dated: January 28, 2026)

The injection of an elongated bubble into a micro-channel is a well-established strategy for enhancing convective heat transfer, with applications ranging from electronics cooling to miniaturized heat exchangers. So far, a rigorous characterization of the heat removal capabilities of elongated bubbles (also known as Bretherton's or Taylor's bubbles) is still lacking. To address this gap, we investigate the forced convection problem around an elongated bubble under uniform wall heat flux, examining the competition between advection, diffusion, viscous dissipation, and an imposed heat flux at the channel walls. By means of two-scale asymptotic analysis, we derive a one-dimensional advection-diffusion–heat-transfer equation with shape-dependent effective coefficients. This model generalizes the classical Graetz problem to capillary-driven flows and extends the Aris-Taylor dispersion to the case of an elongated bubble, clarifying the interplay between the imposed heat flux and the recirculating flow patterns at both front and rear menisci. Interestingly, the model recovers the Péclet-squared scaling of the effective diffusion coefficient and can be used to determine the heat transfer coefficient in the film region. In fact, we derive a closed-form scaling law for the Nusselt number, revealing the influence of the problem parameters (i.e., the bubble profile and the axial temperature gradient) and the dimensionless groups (Péclet, Brinkman, and capillary numbers) on forced convection. Comparison with numerical simulations from the literature shows good agreement and supports the model's predictive capability beyond its formal domain of applicability. Grounded in first principles, our analysis contributes to a deeper understanding of capillary-driven forced convection in confined environments.

* Contact author: davide.picchi@unibs.it

CONTENTS

I. INTRODUCTION

Understanding the dynamics of two-phase gas-liquid flows in micro-channels is relevant to many engineering application, ranging from heat-exchangers to small-scale reactors. In these contexts, the topology of the flowing phases determines the existence of several flow patterns (i.e., stratified, core-annular, intermittent or slug, and dispersed flows) that profoundly affect the heat transfer rate. In particular, due to the dominant effect of surface tension, the most common flow pattern is characterized by the presence of elongated bubbles surrounded by a thin liquid film and separated by liquid plugs [see for example, 1]. When a long bubble flows in a capillary tube, in fact, it assumes the typical bullet shape and is often referred to as a Bretherton or Taylor bubble after their seminal works in the early 1960s [2, 3]. Historically, the name "Taylor bubble" was proposed for the first time by Griffith and Wallis [4] and Brown [5], referring to large gas volumes rising in a large-diameter tube after the work of Davies and Taylor [6], but, later on, it has also been used to denote trains of elongated bubbles in small-diameter tubes [see Taylor flow in 7, 8].

So far, most of the studies have focused on heat transfer enhancement closed to an elongated bubble in the context of boiling and cooling applications such as in the context of heat-pipes [9, 10]. These results are summarized in recent review papers [just to mention a few 11–13] where the evaporating/condensing elongated bubble is often investigated experimentally [14, 15], or in terms of mechanistic models, such as the widely used three-zone model developed by Thome *et al.* [16], Dupont *et al.* [17], Szczukiewicz *et al.* [18], or by means of numerical simulations [19, 20]. Also, there is a growing interest in the dynamics of evaporation in very thin-films, known as microlayer [21–25].

However, the heat transfer problem in the absence of phase change, where the elongated bubbles are obtained by injection of an immiscible dispersed phase, has received limited attention. Although this class of two-phase flows finds application in compact heat exchangers embedded in printed circuit boards [26, 27] and micro-reactors [1], most of the existing works is primarily experimental or numerical [see the recent reviews in 27–30]. A theoretical framework, able to provide a better understanding of the relevant physical mechanisms playing in forced convection around a non evaporating/condensing elongated bubble, is still lacking. Specifically, experimental evidences point out that the presence of elongated bubbles enhances heat transfer compared to single-phase flow but the impact of flow characteristics (e.g., the velocity field, the slug length, the liquid fraction, fluid thermal properties, and thermal boundary conditions) on thermal performance [31] is still not fully understood.

In fact, it is common practice is to model the heat transfer coefficient using semi-empirical correlations [e.g., 32–37] formulating the Nusselt number in analogy with the single-phase scenario [38, 39]. Unfortunately, the predictions of these correlations presents a large variability [27]. Only recently, Che *et al.* [40] proposed a model for a train of elongated bubbles, but, since the bubbles are treated as a sequence of rectangular wall-wetting plugs, the effect of the the thin-film surrounding the bubble on forced convection is not accounted for.

One way to deal with this thermal problem is to take inspiration from hydrodynamic dispersion, which has been extensively investigated from a theoretical perspective, starting from the pioneering works of Taylor [41] and Aris [42], later extended to various contexts [e.g., 43–46] including Taylor bubbles [47]. In fact, heat and mass transfer share similar governing equations, while the boundary conditions reflect different physical constraints across interfaces (i.e., a solid wall or other phases). So far, extensions of dispersion theory to heat transfer remain limited, mostly restricted to single-phase flows in insulated or radiant pipes [48, 49] and combustion processes [50]. In the context of two-phase flows, an effective model for two-phase forced convection valid for both gas-liquid and liquid-liquid core-annular flows was developed in Botticini *et al.* [51]. Although the core-annular pattern has proven to be a useful idealization of more complex flow regimes such as elongated bubbles [see 16, 52–54], a rigorous analytical description of heat transfer in the thin-film around a single elongated bubble is still lacking.

To address these limitations, the goal of this paper is to investigate the forced convection around a single elongated bubble in a horizontal capillary tube under uniform wall heat flux. We will focus on regimes where phase change is absent and inertial and gravitational effects are negligible. Starting from first principles, we generalize the perturbation scheme that characterizes the classical Taylor dispersion to the temperature field in the thin-film flow surrounding an elongated inviscid bubble. Specifically, the flow field and the shape of the bubble are the ones proposed by Bretherton [3] (i.e., the low capillary number regime), as typical of a broader class of coating problems [55, 56]. We aim to obtain a reduced-order effective description that explains the physical mechanisms behind the enhancement on the heat transfer coefficient.

The manuscript is structured as follows. We first review the thin-film flow around the elongated bubble (Sec. II A), present its energy balance (Sec. II B) and make the problem dimensionless (Sec. II C). By means of two-scale asymptotic expansion (Sec. III A), we derive a one-dimensional upscaled equation for the depth-averaged film temperature as function of space and time (Sec. III B), and specify its applicability conditions (Sec. III C). The resulting effective model is then solved numerically (Sec. III D) to study the evolution of the effective heat-transfer coefficients and the temperature field (Sec. IV A). Subsequently, we derive a closed-form expression for the local Nusselt number (Sec. IV B), quantifying the competition between convection and conduction in the liquid film. Our predictions

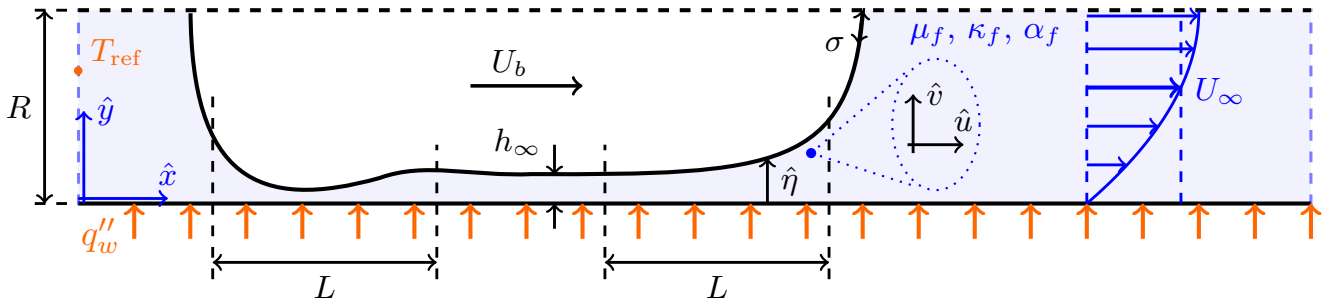

Figure 1. Sketch of the elongated bubble moving in a uniformly heated channel. The hat operator denotes the dimensional variables.

are compared with numerical results available in the literature (Sec. IV C), suggesting that our model may also hold beyond its rigorous applicability conditions. Finally, we analyze the heat transfer dynamics thorough the film in terms of the averaged Nusselt number (Sec. IV D). A summary discussion is presented in the concluding section (Sec. V).

II. PROBLEM FORMULATION

A. Flow in the thin-film of the elongated bubble

We consider a single inviscid elongated bubble that flows at speed U_b in an infinitely long channel of half-size R, see figure 1, in regimes where inertia and gravity can be neglected, namely the Reynolds and the Bond number are both small (i.e., $\mathrm{Re} = \rho_f U_b R/\mu_f \ll 1$ and $\mathrm{Bo} = \rho_f g R^2/\sigma \ll 1$ where ρ_f, μ_f, and σ are the fluid density, viscosity and surface tension, respectively). The motion is driven by a steady flow far behind the bubble with average speed U_∞ and the bubble is assumed to be sufficiently long so that there exists a region of uniform film thickness $h_\infty \ll R$ at the bubble center.

At the front and the rear of the bubble the meniscus is spherical, while, in the transition region in between, it follows the similarity profile typical of the Landau-Levich-Derjaguin-Bretherton problem [3, 56]. Specifically, in a reference frame attached to the bubble, the film thickness $\hat{\eta}(\hat{\xi}, \hat{t}) = \hat{\eta}(\hat{x} - U_b \hat{t}, \hat{t})$ is described by the following similarity equation [3]

$$\frac{\mathrm{d}^3\eta}{\mathrm{d}\xi^3} = \frac{\eta - 1}{\eta^3}, \tag{1}$$

with

$$\xi = \frac{\hat{\xi}}{h_\infty (3\,\mathrm{Ca})^{-1/3}}, \qquad \eta = \frac{\hat{\eta}}{h_\infty}, \quad \text{and} \quad \mathrm{Ca} = \frac{\mu_f U_b}{\sigma} \ll 1, \tag{2}$$

where ξ is is the dimensionless stretched axial coordinate, η is the dimensionless film thickness, and Ca is the capillary number. The Bretherton's similarity equation results from the lubrication theory and holds in the transition region of length L depicted in figure 1, whose order of magnitude is obtained balancing the pressure drop along the axial direction with the pressure jump generated by the curved meniscus as $L = h_\infty (3\,\mathrm{Ca})^{-1/3}$, see [3, 56, 57].

The bubble meniscus is obtained by integration of (1) starting from the uniform film where $\eta \approx 1$. Specifically, integrating (1) in the positive direction gives the front profile, which, for $\eta \gg 1$, joins a parabolic profile of constant curvature. There, the meniscus is matched to a spherical cap of radius R, giving the asymptotic relation for the film thickness

$$\frac{h_\infty}{R} = 0.643\,(3\,\mathrm{Ca})^{2/3}. \tag{3}$$

Note that, although Bretherton theory [3] builds on a planar geometry, in the small capillary number limit ($\mathrm{Ca} \ll 1$) the circular and planar geometries are asymptotically equivalent, as shown in appendix A. Integration of (1) towards the negative direction yields the rear profile, which exhibits the typical undulations, see figure 9. The integration in both the front and the rear is carried out numerically following the methodology outlined in Bretherton [3], Picchi *et al.* [57].

Interestingly, the elongated bubble always flows faster compared to the flow ahead, and mass conservation yields

$$\frac{U_b - U_\infty}{U_b} = (1+m)\,\frac{h_\infty}{R}, \qquad \text{where} \quad m = \begin{cases} 0 & \text{for planar channel,} \\ 1 & \text{for circular tube.} \end{cases} \tag{4}$$

B. Energy balance in the film

We study the forced convection in the thin liquid film around the elongated bubble subjected to a constant wall heat flux q''_w in the absence of phase change, as shown in figure 1. The internal energy balance in a reference frame attached to the bubble is given by

$$\rho_f\, c_p \left(\frac{\partial \hat{T}}{\partial \hat{t}} + (\hat{u} - U_b)\, \frac{\partial \hat{T}}{\partial \hat{\xi}} + \hat{v}\, \frac{\partial \hat{T}}{\partial \hat{y}} \right) = \kappa_f \left(\frac{\partial^2 \hat{T}}{\partial \hat{\xi}^2} + \frac{\partial^2 \hat{T}}{\partial \hat{y}^2} \right) + \hat{\Phi}, \tag{5}$$

where $\hat{T}(\hat{\xi},\, \hat{y},\, \hat{t})$, c_p, κ_f are the fluid temperature, the isobaric mass heat capacity and the thermal conductivity of the liquid, respectively, and $\hat{u}(\hat{\xi},\, \hat{y})$ and $\hat{v}(\hat{\xi},\, \hat{y})$ are the velocity profiles in the axial and traverse direction obtained via the lubrication approximation as in [3]; the thermal diffusivity is defined as $\alpha_f = \kappa_f / (\rho_f\, c_p)$. All the physical properties are assumed uniform and constant. The term $\hat{\Phi}$ is the rate of viscous dissipation of mechanical energy per unit mass and reads:

$$\hat{\Phi} = \mu_f \left[2 \left(\frac{\partial \hat{u}}{\partial \hat{\xi}} \right)^2 + 2 \left(\frac{\partial \hat{v}}{\partial \hat{y}} \right)^2 + \left(\frac{\partial \hat{u}}{\partial \hat{y}} + \frac{\partial \hat{v}}{\partial \hat{\xi}} \right)^2 \right]. \tag{6}$$

At the channel wall, $\hat{y} = 0$, we assume that a uniform heat flux is imposed [58], leading to

$$q''_w = -\kappa_f \left(\hat{\boldsymbol{\nabla}} \hat{T} \cdot \boldsymbol{n}_w \right)\Big|_{\hat{y}=0} = \kappa_f \left. \frac{\partial \hat{T}}{\partial \hat{y}} \right|_{\hat{y}=0}, \tag{7}$$

where the unit vector is given by $\boldsymbol{n}_w = (0;\, -1)$. At the film-bubble interface, $\hat{y} = \hat{\eta}$, we impose continuity of temperature and heat flux, while the entire domain is initialized with a temperature equal to T_{ref}.

C. Dimensionless formulation

In order to make the problem dimensionless, we identify its characteristic scales. Specifically, the relevant scale in the transverse direction is the uniform film thickness h_∞ while in the axial direction we use the length of the transition region L. This allow us to define a small scale parameter as

$$\varepsilon = \frac{h_\infty}{L} = (3\,\mathrm{Ca})^{1/3} \ll 1. \tag{8}$$

Among the different time scales of the thermal problem, namely the transversal, $\mathcal{T}_{d,\,h} = h_\infty^2/\alpha_f$, and longitudinal, $\mathcal{T}_{d,\,L} = L^2/\alpha_f$, heat diffusion time scales, and the advective time scale, $\mathcal{T}_a = L/U_b$, the time in the energy balance is made dimensionless according to the advective one by analogy with the Aris-Taylor dispersion [41, 42]. This means that we are interested in modeling a time window where traverse diffusion can be considered instantaneous, but longitudinal diffusion competes with advection.

Thus, we make the energy balance and its boundary conditions dimensionless by introducing the following dimensionless quantities:

$$\vartheta = \frac{\rho_f\, c_p\, (\hat{T} - T_{\mathrm{ref}})\, U_b\, h_\infty}{|q''_w|\, L}, \quad t = \frac{\hat{t}}{L/U_b}, \quad u = \frac{\hat{u}}{U_b}, \quad v = \frac{\hat{v}}{\varepsilon\, U_b}, \quad \Phi = \frac{\hat{\Phi}}{\mu_f\, U_b^2/h_\infty^2}. \tag{9}$$

The dimensionless temperature ϑ quantifies the energy convected within the film relative to that supplied through the wall, with the temperature deviation $\hat{T} - T_{\mathrm{ref}}$ serving as the main variable [59]. The axial and transverse coordinates

are made dimensionless based on L and h_∞, respectively, according to the Bretherton theory, i.e. $\xi = \hat{\xi}/L$ and $y = \hat{y}/h_\infty$, see (2). This leads to

$$\varepsilon^2 \,\mathrm{Pe}\left[\frac{\partial \vartheta}{\partial t} + (u-1)\,\frac{\partial \vartheta}{\partial \xi} + v\,\frac{\partial \vartheta}{\partial y}\right] = \varepsilon^2\,\frac{\partial^2 \vartheta}{\partial \xi^2} + \frac{\partial^2 \vartheta}{\partial y^2} + \varepsilon^2\,\mathrm{Pe}\,\mathrm{Br}\,\Phi, \tag{10}$$

where $y \in [0;\, \eta\,(\xi)]$ and the absolute components $(u,\, v)$ of the velocity field and the viscous dissipation function $\Phi\,(\eta,\, y)$ are given in appendix B. The Péclet number can be seen as the ratio between advection and thermal diffusion and is defined as

$$\mathrm{Pe} = \frac{L\,U_b}{\alpha_f}. \tag{11}$$

When $\mathrm{Pe} \ll 1$, diffusion dominates over advection, while for $\mathrm{Pe} \gg 1$, advection plays a major role with respect to diffusion. The Brinkman number accounts for the competition between the thermal power per unit mass produced by viscous dissipation and the one transferred from the solid walls, and is defined as

$$\mathrm{Br} = \frac{\mu_f\,U_b^2}{|q_w''|\;h_\infty}. \tag{12}$$

The uniform flux boundary condition imposed at the wall, $y = 0$, leads to

$$\left.\frac{\partial \vartheta}{\partial y}\right|_{y=0} = \nu\,\varepsilon^2\,\mathrm{Pe}, \qquad \text{with} \qquad \nu = \mathrm{sgn}\,(q_w''), \tag{13}$$

where $\nu = \pm 1$ denotes heat flux leaving or entering the tube, respectively. Typically, $\nu = -1$ in experimental setups where the tube is heated via external resistive elements [e.g., 60]. At the gas-liquid interface, $y = \eta$, the outward normal unit vector is

$$\boldsymbol{n}|_{y=\eta} = (n_\xi;\, n_y) = \left(\frac{-\varepsilon\,\mathrm{d}\eta/\mathrm{d}\xi}{\sqrt{1+\varepsilon^2\,(\mathrm{d}\eta/\mathrm{d}\xi)^2}};\; \frac{1}{\sqrt{1+\varepsilon^2\,(\mathrm{d}\eta/\mathrm{d}\xi)^2}}\right), \tag{14}$$

and the continuity of thermal fluxes, $\kappa_f\;(\boldsymbol{\nabla} T_f \cdot \boldsymbol{n})|_{y=\eta} = \kappa_b\;(\boldsymbol{\nabla} T_{\mathrm{gas}} \cdot \boldsymbol{n})|_{y=\eta}$, yields

$$\left(\frac{\partial \vartheta}{\partial y} - \mathcal{K}\,\frac{\partial \vartheta_{\mathrm{gas}}}{\partial y}\right)\bigg|_{y=\eta} - \varepsilon^2\,\frac{\partial \eta}{\partial \xi}\left(\frac{\partial \vartheta}{\partial \xi} - \mathcal{K}\,\frac{\partial \vartheta_{\mathrm{gas}}}{\partial \xi}\right)\bigg|_{y=\eta} = 0, \tag{15}$$

where the dimensionless bubble temperature is defined as $\vartheta_{\mathrm{gas}} = \rho_f\,c_p\,(\hat{T}_{\mathrm{gas}} - T_{\mathrm{ref}})\,U_b\,h_\infty/\,(|q_w''|\,L)$, and

$$\mathcal{K} = \frac{\kappa_b}{\kappa_f} \tag{16}$$

is the conductivity ratio. In this work, we are primarily interested in gas-liquid systems, where such ratio is typically of the order of $\mathcal{O}(\mathcal{K}) = 10^{-2}$, see table 1 in Botticini *et al.* [51]. We will show in the following that, when $\mathcal{K} \to 0$, the phases are thermally decoupled, reducing the boundary condition (15) to a one-sided model, and making the temperature continuity condition at the interface, namely $\vartheta|_{y=\eta} = \vartheta_{\mathrm{gas}}|_{y=\eta}$, unimportant for the purpose of our analysis. The problem is closed imposing the initial condition as a uniform temperature distribution for both phases in the absolute reference frame $(x,\, y,\, t)$:

$$\vartheta\,(0,\, y,\, 0) = \vartheta_{\mathrm{gas}}\,(0,\, y,\, 0) = 0, \tag{17}$$

and its reformulation in the moving reference frame $(\xi,\, y,\, t)$ will be discussed in Sec. III D.

III. THEORETICAL DERIVATION

In this section we derive the one-dimensional Advection-Diffusion-Heat-Transfer equation that describes the forced convection in the film region of an elongated bubble. First, we outline the mathematical procedure, and then, we apply it to the energy equation in the thin film.

A. Two-scale asymptotics of the energy equation

The main idea is to obtain a reduced-order model for the forced convection in the thin-film in terms of its averaged temperature. To do so, we use two-scale asymptotic expansions of the energy equation building on the work of [61]:

1. We start from the energy balance in dimensionless formulation, (10, 13, 15), where a small scale parameter $\varepsilon \ll 1$ has been identified to decouple axial and transverse heat transfer.

2. Each dimensionless group in the governing equations (11, 12, 16) is expressed in terms of integer powers of the scale parameter (or the capillary number, see (2)):

$$\mathrm{Pe} = \varepsilon^{-p}, \quad \mathrm{Br} = \varepsilon^{b}, \quad \mathcal{K} = \varepsilon^{k}, \tag{18}$$

   where the exponents p, b, k define the system behavior and can be selected independently. This is typical of perturbation methods (see e.g., 62, 63) and allows the different terms of the expanded energy balance to jump from one order to the other controlled by the order of magnitude of the dimensionless numbers.

3. The temperature $\vartheta(\xi,\, y,\, t)$ is, then, expanded in (10, 13, 15) into a power series as

$$\vartheta\,(\xi,\, y,\, t) = \vartheta^{(0)}\,(\xi,\, y,\, t) + \varepsilon^{2-p}\,\vartheta^{(1)}\,(\xi,\, y,\, t) + \varepsilon^{2(2-p)}\,\vartheta^{(2)}\,(\xi,\, y,\, t) + \ldots, \tag{19}$$

   where the perturbation parameter is the ratio of the competing characteristic time scales of thermal dispersion, i.e., $\mathcal{T}_{d,\,h}/\mathcal{T}_a = \varepsilon^{2-p}$. This choice helps in identifying the desired time window where the transverse diffusion can be considered instantaneous if compared to axial diffusion and advection.

4. Substituting the power-series expansion (19) into the governing equations and collecting terms by order yields a cascade of boundary-value problems for $\vartheta^{(n)}$ that are solved sequentially. The goal is to find an equation for the averaged temperature in the film defined as

$$\langle\vartheta\rangle \equiv \frac{1}{\eta}\int_0^{\eta} \vartheta(\xi,\, y,\, t)\ \mathrm{d}y. \tag{20}$$

   We will show in the next section that the zero-th order temperature $\vartheta^{(0)}$ is the averaged temperature in the film while the higher order terms, $\vartheta^{(n)}$ with $n \geq 1$, can be seen as fluctuations around the mean with zero mean [64].

5. The last step is to check that, at each order, the existence and uniqueness of the solution is guaranteed. This requirement – also known as Fredholm alternative [65] and compatibility or solvability condition – states that the boundary-value problem at each order has zero average over $[0;\, \eta]$. So far, several strategies have been proposed to ensure the compatibility condition [66]: adopting a moving reference frame with stretched length scales [41, 42, 51, 67]; expanding variables over multiple time coordinates [64, 68]; or adding and subtracting tailored advective terms [45, 47, 61, 69]. In this work, we follow the latter approach.

6. As a result of steps (i) - (iv), we obtain that, for certain combinations of the dimensionless parameters (Pe, Br, $\mathcal{K}$), it is possible to decouple the heat transfer between the axial and the transverse directions, and, therefore, an effective model can be formulated in terms of the averaged temperature. These conditions can be summarized in an applicability map (in terms of the exponents defined in (18)), which rigorously define conditions where the one dimensional description of forced convection in the film holds or not.

B. Derivation of the effective model

Following the procedure described in Sec. III A, we expand the variables in a power-series in ε^{2-p} as in (19) into the energy balance (10)

$$\begin{aligned}\varepsilon^{2-p}\,\partial_t\vartheta^{(0)} + \varepsilon^{2(2-p)}\,\partial_t\vartheta^{(1)} + \varepsilon^{2-p}\,(u-1)\,\partial_\xi\vartheta^{(0)} + \varepsilon^{2(2-p)}\,(u-1)\,\partial_\xi\vartheta^{(1)} + \\ + \varepsilon^{2-p}\,v\,\partial_y\vartheta^{(0)} + \varepsilon^{2(2-p)}\,v\,\partial_y\vartheta^{(1)} = \varepsilon^{2}\,\partial_{\xi\xi}\vartheta^{(0)} + \partial_{yy}\vartheta^{(0)} + \varepsilon^{2-p}\,\partial_{yy}\vartheta^{(1)} + \\ + \varepsilon^{2(2-p)}\,\partial_{yy}\vartheta^{(2)} + \varepsilon^{2-p+b}\,\Phi + \ldots,\end{aligned} \tag{21a}$$

and its boundary conditions (13, 15) at the channel wall

$$\partial_y\vartheta^{(0)}\Big|_{y=0} + \varepsilon^{2-p}\ \partial_y\vartheta^{(1)}\Big|_{y=0} + \varepsilon^{2(2-p)}\ \partial_y\vartheta^{(2)}\Big|_{y=0} + \ldots = \nu\,\varepsilon^{2-p}, \tag{21b}$$

and at the fluid-gas interface

$$\begin{aligned}&\partial_y\vartheta^{(0)}\Big|_{y=\eta}+\varepsilon^{2-p}\;\partial_y\vartheta^{(1)}\Big|_{y=\eta}+\varepsilon^{2(2-p)}\;\partial_y\vartheta^{(2)}\Big|_{y=\eta}-\varepsilon^{k}\;\partial_y\Theta|_{y=\eta}+\\&-\varepsilon^{2}\,\partial_\xi\eta\;\partial_\xi\vartheta^{(0)}\Big|_{y=\eta}-\varepsilon^{4-p}\,\partial_\xi\eta\;\partial_\xi\vartheta^{(1)}\Big|_{y=\eta}+\varepsilon^{k+2}\,\partial_\xi\eta\;\partial_\xi\Theta|_{y=\eta}+\ldots=0,\end{aligned}\tag{21c}$$

where the order of magnitude of the governing parameters (i.e., the exponents p, b, k) has been chosen to keep the maximum number of terms at each order [70–72]. Note that in this section we use a compact notation for time and spatial derivatives for the sake of brevity.

1. Leading order

At the leading order, the boundary value problem for $\vartheta^{(0)}$ is homogeneous

$$\begin{cases}\partial_{yy}\vartheta^{(0)}=0\,, & \text{(22a)}\\ \partial_y\vartheta^{(0)}=0 \quad \text{at} \quad y=0, & \text{(22b)}\\ \partial_y\vartheta^{(0)}=0 \quad \text{at} \quad y=\eta, & \text{(22c)}\end{cases}$$

ensuring that it admits a solution independent of y, namely $\vartheta^{(0)}(\xi,t)=\langle\vartheta\rangle(\xi,t)$. This means that the zero-th order temperature is the averaged temperature in the film, see (20). This is true as long as $0\leq p<2$ (or $1\leq \mathrm{Pe}\ll\varepsilon^{-2}$) and $b\geq 0$ (or $\mathrm{Br}\leq 1$), meaning that thermal transport has to take place within the dispersive time window, and viscous dissipation has to enter the problem as an $\mathcal{O}(\varepsilon^{2-p})$ contribution or lower.

By inspection of the expanded boundary condition (21c), we impose an additional constraint as $k>2(2-p)$, or $\mathcal{K}\ll(\varepsilon^2\mathrm{Pe})^2$, that reduces the model to a one-sided formulation. In other words, the gas-liquid interface is assumed to be adiabatic and the bubble temperature field ϑ_{gas} enters the problem only beyond the order $\mathcal{O}\left(\varepsilon^{2(2-p)}\right)$.

2. The next order

Since the leading-order problem is homogeneous, i.e., $\vartheta^{(0)}=\langle\vartheta\rangle(\xi,t)$, the term $\partial_y\vartheta^{(0)}$ in (21a) vanishes, and, at the next order $\mathcal{O}(\varepsilon^{2-p})$, we find the following equation for $\vartheta^{(1)}$

$$\begin{cases}\partial_t\vartheta^{(0)}+(u-1)\;\partial_\xi\vartheta^{(0)}=\;\partial_{yy}\vartheta^{(1)}+\varepsilon^{b}\,\Phi, & \text{(23a)}\\ \partial_y\vartheta^{(1)}=\nu \quad \text{at} \quad y=0, & \text{(23b)}\\ \partial_y\vartheta^{(1)}=\varepsilon^{p}\,\partial_\xi\eta\,\partial_\xi\vartheta^{(0)} \quad \text{at} \quad y=\eta. & \text{(23c)}\end{cases}$$

According to the solvability condition (see Sec. III A), a solution exists if and only if the partial differential equation (23a) has zero average over $[0;\eta]$. To satisfy this requirement, we follow the strategy from Rubinstein and Mauri [45], Mikelić *et al.* [69], decomposing the axial velocity as follows

$$u-1=\underbrace{u-\langle u\rangle}_{\text{(a)}}+\underbrace{\langle u\rangle-1}_{\text{(b)}},\tag{24}$$

to isolate its deviation around the mean, (a), which has zero average, from the remaining part, (b), which is uniform in y. After making such decomposition, by averaging (23a) over the film and applying the boundary conditions (23b, 23c), we obtain

$$\partial_t\vartheta^{(0)}+(\langle u\rangle-1)\,\partial_\xi\vartheta^{(0)}-\eta^{-1}\left(\varepsilon^{p}\,\partial_\xi\eta\,\partial_\xi\vartheta^{(0)}-\nu\right)-\varepsilon^{b}\;\langle\Phi\rangle=0.\tag{25}$$

Unfortunately, the solvability condition via the identity (25) is not satisfied because the boundary and initial data are incompatible [61]. Therefore, the strategy proposed by Rubinstein and Mauri [45] is to relax (25) by assuming that such equation is satisfied only up to $\mathcal{O}(\varepsilon^{(2-p)})$, namely

$$\underbrace{\partial_t\vartheta^{(0)}+(\langle u\rangle-1)\,\partial_\xi\vartheta^{(0)}}_{\mathcal{R}_{\mathrm{lhs}}}=\underbrace{\eta^{-1}\left(\varepsilon^{p}\,\partial_\xi\eta\,\partial_\xi\vartheta^{(0)}-\nu\right)+\varepsilon^{b}\;\langle\Phi\rangle}_{\mathcal{R}_{\mathrm{rhs}}}+\mathcal{O}(\varepsilon^{(2-p)}),\tag{26}$$

or, in other words, that the residual is small, $\mathcal{R} = \mathcal{R}_{\text{lhs}} - \mathcal{R}_{\text{rhs}} = \mathcal{O}(\varepsilon^{(2-p)})$, and jumps at the next order. Specifically, we make use of the solvability condition, first, isolating the second-order term in (23a) and using the velocity decomposition (24) as

$$\partial_{yy}\vartheta^{(1)} = \underbrace{\partial_t\vartheta^{(0)} + (\langle u\rangle - 1)\,\partial_\xi\vartheta^{(0)}}_{\mathcal{R}_{\text{lhs}}} + (u - \langle u\rangle)\,\partial_\xi\vartheta^{(0)} - \varepsilon^b\,\Phi, \tag{27}$$

and, then, replacing $\mathcal{R}_{\text{lhs}}$ with $\mathcal{R}_{\text{rhs}}$ in (27) using (26), leading to a regularized boundary boundary value problem

$$\partial_{yy}\vartheta^{(1)} = (u - \langle u\rangle)\,\partial_\xi\vartheta^{(0)} - \varepsilon^b\,(\Phi - \langle\Phi\rangle) + \eta^{-1}\left(\varepsilon^p\,\partial_\xi\eta\,\partial_\xi\vartheta^{(0)} - \nu\right) + \mathcal{O}(\varepsilon^{(2-p)}), \tag{28}$$

where the residual of the order of $\mathcal{O}(\varepsilon^{(2-p)})$ jumps at the next order.

The solution is finally obtained by integrating (28) twice and the two integration constants are found using either (23b) or (23c), together with the zero-average gauge condition, i.e., $\left\langle\vartheta^{(1)}\right\rangle = 0$. This gives the solution for the order one term of the asymptotic expansion as

$$\vartheta^{(1)}(\xi,\,y,\,t) = (\mathcal{M}_a + \varepsilon^p\,\partial_\xi\eta\,\mathcal{M}_\Gamma)\,\partial_\xi\vartheta^{(0)} + \varepsilon^b\,\mathcal{M}_\Phi + \nu\,\mathcal{M}_q, \tag{29}$$

where the following B-fields [named after 73]

$$\mathcal{M}_a = \frac{(\eta-1)\left(8\,\eta^4 - 60\,\eta^2\,y^2 + 60\,\eta\,y^3 - 15\,y^4\right)}{120\,\eta^3}, \qquad \mathcal{M}_\Gamma = \frac{3\,y^2 - \eta^2}{6\,\eta}, \tag{30a}$$

$$\mathcal{M}_\Phi = \frac{(\eta-1)^2\left(8\,\eta^4 - 60\,\eta^2\,y^2 + 60\,\eta\,y^3 - 15\,y^4\right)}{20\;\eta^6}, \qquad \mathcal{M}_q = -\frac{2\,\eta^2 - 6\,\eta\,y + 3\,y^2}{6\,\eta}, \tag{30b}$$

describe the effective contributions of advection ($\mathcal{M}_a$), film shape ($\mathcal{M}_\Gamma$), viscous dissipation ($\mathcal{M}_\Phi$), and wall heat flux ($\mathcal{M}_q$).

3. The next next order

At the next next order $\mathcal{O}\left(\varepsilon^{2(2-p)}\right)$, the boundary value problem for $\vartheta^{(2)}$ from (21a), plus the the residual $\mathcal{R}$ defined in (26) and resulting from the solvability condition of the previous order, is given by

$$\begin{cases} \partial_t\vartheta^{(1)} + (u-1)\,\partial_\xi\vartheta^{(1)} + v\,\partial_y\vartheta^{(1)} + \varepsilon^{p-2}\,\mathcal{R} = \partial_{yy}\vartheta^{(2)} + \varepsilon^{2p-2}\,\partial_{\xi\xi}\vartheta^{(0)}, & (31a)\\ \partial_y\vartheta^{(2)} = 0 \qquad \text{at} \quad y = 0, & (31b)\\ \partial_y\vartheta^{(2)} = \varepsilon^p\,\partial_\xi\eta\,\partial_\xi\vartheta^{(1)} \qquad \text{at} \quad y = \eta. & (31c) \end{cases}$$

Since we are interested only in deriving an effective equation for the averaged temperature, it not necessary to solve for $\vartheta^{(2)}$, but it is sufficient to enforce the solvability condition on (31). Specifically, we replace $\vartheta^{(1)}$ using the solution at the previous order (29), and, then, depth-average the equation (31a) using its boundary conditions (31b) and (31c). By doing so, the terms that are independent of y remain unchanged, while the average of the time derivative is zero since the film profile is a function of the axial coordinate only yielding $\left\langle\partial_t\vartheta^{(1)}\right\rangle = \partial_t\left\langle\vartheta^{(1)}\right\rangle = 0$.

The result of the average is an advection-diffusion-heat-transfer equation for the zero-th order temperature (or the averaged temperature)

$$\frac{\partial\vartheta^{(0)}}{\partial t} + (u^\star - 1)\,\frac{\partial\vartheta^{(0)}}{\partial\xi} = \varepsilon^p\,D^\star\,\frac{\partial^2\vartheta^{(0)}}{\partial\xi^2} + \varepsilon^b\,\Phi^\star - \nu\,q^\star, \tag{32}$$

where the effective coefficients for advection, diffusion, viscous heating, and the imposed flux are defined as

$$u^\star = u_0 + \varepsilon^2\sum_{i=1}^{8} u_i + u_9, \quad D^\star = 1 + \varepsilon^2\sum_{i=0}^{3} D_i, \quad \Phi^\star = \Phi_0 + \varepsilon^2\sum_{i=1}^{3}\Phi_i, \quad q^\star = q_0 + \varepsilon^2\sum_{i=1}^{3} q_i; \tag{33}$$

with the full expressions reported in table I.

$u^\star$	Mechanism	Shape	Type
u_0	$\langle u \rangle$	$\frac{\eta-1}{\eta}$	1
u_9	**	$-\frac{1}{\eta}$	$\partial_\xi \eta\, \mathrm{Pe}^{-1}$
u_1	$\langle u' \, \partial_\eta \mathcal{M}_a \rangle$	$-\frac{(\eta-1)(24\,\eta+41)}{840\,\eta}$	$\partial_\xi \eta\, \mathrm{Pe}$
u_2	$\langle v^\dagger \, \partial_y \mathcal{M}_a \rangle$	$\frac{(\eta-1)(19-8\,\eta)}{280\,\eta}$	$\partial_\xi \eta\, \mathrm{Pe}$
u_6	$\langle u' \, \mathcal{M}_\Gamma \rangle$	$\frac{7(\eta-1)}{120}$	$\partial_{\xi\xi} \eta$

$u^\star$	Mechanism	Shape	Type
u_3	$\langle u' \, \partial_\eta \mathcal{M}_\Gamma \rangle$	$\frac{47-7\,\eta}{120\,\eta}$	$\partial_\xi^2 \eta$
u_4	$\langle v^\dagger \, \partial_y \mathcal{M}_\Gamma \rangle$	$\frac{7\,\eta-18}{40\,\eta}$	$\partial_\xi^2 \eta$
u_5	$-\eta^{-1} \, \partial_\eta \mathcal{M}_a \vert_\eta$	$\frac{7(2\,\eta-1)}{120\,\eta}$	$\partial_\xi^2 \eta$
u_7	$-\eta^{-1} \, \partial_\eta \mathcal{M}_\Gamma \vert_\eta$	$\frac{2}{3\,\eta}$	$\partial_\xi^3 \eta\, \mathrm{Pe}^{-1}$
u_8	$-\eta^{-1} \, \mathcal{M}_\Gamma \vert_\eta$	$-\frac{1}{3}$	$\partial_\xi \eta \, \partial_{\xi\xi} \eta\, \mathrm{Pe}^{-1}$

$D^\star$	Mechanism	Shape
D_0	$-\langle u' \, \mathcal{M}_a \rangle$	$\frac{2(\eta-1)^2}{105}$
D_1	$-\langle u' \, \mathcal{M}_\Gamma \rangle$	$-\frac{7(\eta-1)}{120}$
D_2	$\eta^{-1} \mathcal{M}_a \vert_\eta$	$-\frac{7(\eta-1)}{120}$
D_3	$\eta^{-1} \mathcal{M}_\Gamma \vert_\eta$	$\frac{1}{3}$

$\Phi^\star$	Mechanism	Shape
Φ_0	$\langle \Phi \rangle$	$\frac{3\,(\eta-1)^2}{\eta^4}$
Φ_1	$-\langle u' \, \partial_\eta \mathcal{M}_\Phi \rangle$	$\frac{(\eta-1)^2(89-8\,\eta)}{140\,\eta^4}$
Φ_2	$-\langle v^\dagger \, \partial_y \mathcal{M}_\Phi \rangle$	$\frac{3(\eta-1)^2(8\,\eta-19)}{140\,\eta^4}$
Φ_3	$\eta^{-1} \partial_\eta \mathcal{M}_\Phi \vert_\eta$	$-\frac{7(\eta-1)}{10\,\eta^4}$

$q^\star$	Mechanism	Shape	Type
			Pe^2
q_0	*	$\frac{1}{\eta}$	1
q_1	$\langle u' \, \partial_\eta \mathcal{M}_q \rangle$	$\frac{7\,\eta+13}{120\,\eta}$	$\partial_\xi \eta\, \mathrm{Pe}$
q_2	$\langle v^\dagger \, \partial_y \mathcal{M}_q \rangle$	$\frac{3\,\eta-7}{40\,\eta}$	$\partial_\xi \eta\, \mathrm{Pe}$
q_3	$-\eta^{-1} \partial_\eta \mathcal{M}_q \vert_\eta$	$-\frac{1}{6\,\eta}$	$\partial_\xi^2 \eta$

Table I. Effective coefficients, according to (33). Each contribution u_i (top tables), D_i, Φ_i, q_i (bottom table) is expressed as the product of a 'Shape' and a 'Type' term. Specifically, 'Shape' is a function of the local film thickness only; 'Type' is the driving term that captures the effect of the Péclet number, the interface concavity ($\partial_{\xi\xi}\eta$) and slope ($\partial_\xi \eta$). To isolate the impact of the latter, the transverse velocity is written as $v \equiv v^\dagger \, \partial_\xi \eta$, see (B1); the film-relative velocity is indicated by prime notation, i.e., $u' \equiv u - 1$. The column 'Mechanism' identifies the physical origin of each term; mechanisms denoted with a single ($*$) or double ($**$) asterisk correspond to the regularizing boundary conditions (23b) and (23c), respectively.

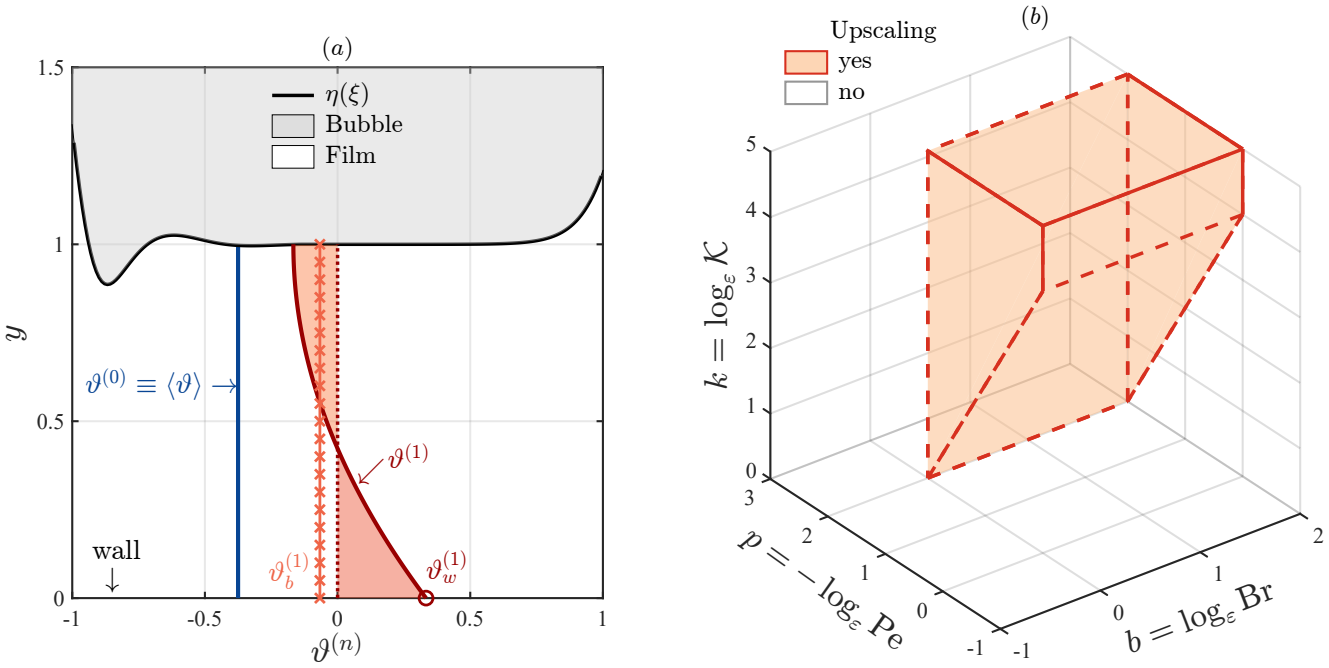

Figure 2. (a) Schematic of the upscaling technique, representing the temperature in the film domain $y \in [0;\, \eta(\xi)]$ as the sum of a uniform leading-order variable $\vartheta^{(0)} \equiv \langle \vartheta \rangle$ corrected by zero-mean higher-order fluctuations $\vartheta^{(n)}$. The first-order corrections ($n = 1$), the wall ('w') and the bulk temperature ('b') are plotted. (b) Applicability map showing the region of the parameter space (p, b, k) where the effective model (34) is valid, see (35) and (18): $0 \le p < 2$, $b \ge 0$, and $k > 2(2-p)$.

C. The 1D Advection-Diffusion-Heat-transfer equation and the applicability conditions

To sum up, the procedure, outlined schematically in figure 2 (a), yields a one-dimensional advection-diffusion-heat-transfer equation for the averaged temperature in the film:

$$\frac{\partial \langle \vartheta \rangle}{\partial t} + (u^\star - 1) \, \frac{\partial \langle \vartheta \rangle}{\partial \xi} = \frac{D^\star}{\mathrm{Pe}} \, \frac{\partial^2 \langle \vartheta \rangle}{\partial \xi^2} + \mathrm{Br} \, \Phi^\star - \nu \, q^\star, \tag{34}$$

where $u^\star$, $D^\star$, $\Phi^\star$ and $q^\star$ denote the effective advection, diffusivity, viscous dissipation, and heat flux coefficients, respectively. Their full expressions are provided in table I and (33).

As outlined in the derivation, (34) holds only for a specific range of the dimensionless groups, namely

$$\text{(a)}\ \ \varepsilon \ll 1, \qquad \text{(b)}\ \ 1 \leq \mathrm{Pe} \ll \varepsilon^{-2}, \qquad \text{(c)}\ \ \mathrm{Br} \leq 1, \qquad \text{(d)}\ \ \mathcal{K} \ll \left(\varepsilon^2\,\mathrm{Pe}\right)^2. \tag{35}$$

Such criteria provide sufficient conditions for the effective model to describe the averaged temperature field asymptotically, and the corresponding applicability map is shown in figure 2 (*b*). Specifically, (a) ensures the use of the lubrication approximation in the thin film; (b) bounds the Péclet number based on the dispersive time scale hierarchy, i.e., $\mathcal{T}_{d,\,h} \ll \mathcal{T}_a < \mathcal{T}_{d,\,L}$; (c) limits the shear heating; (d) ensures that the temperature field in the film is decoupled with respect to the one inside the bubble (i.e., the one-sided formulation) enforcing that the bubble temperature contributes only at higher orders (beyond $n = 2$, up to which model consistency is guaranteed).

D. Numerical solution and boundary conditions of the effective model

The numerical solution of (34) requires the evolution of the film profile, since it shapes its effective coefficients. Specifically, $\eta(\xi)$ is obtained solving (1) separately for the rear and front menisci, using MATLAB's Ordinary Differential Equation (ODE) solver `ode45` as outlined in [47, 57]. Setting the lengths of the transition regions at the front and rear to $\Delta l_{\mathrm{front}} = \Delta l_{\mathrm{rear}} = 15$, we get the entire film meniscus as shown in figure 1. This choice ensures that the second derivative of the interface profile converges to its asymptotic value, $\mathrm{d}^2\eta/\mathrm{d}\xi^2 \to 0.643$ when $\xi \sim \Delta l$, allowing the computed meniscus to match the fore and aft spherical caps. An additional region of uniform thickness (where $\eta = 1$) of length l can be artificially introduced between the front and the rear extending the studied domain of $l/2$ on either side of $\xi = 0$ to analyze the impact of the bubble length on the averaged Nusselt number as in § IV B. An example of the film profile obtained in this way is shown in figure 9.

Given the bubble shape, the equation (34) is solved numerically using MATLAB's built-in one-dimensional Partial Differential Equation (PDE) solver `pdepe`. Such solver employs a second-order accurate spatial discretization to convert the original problem into a system of ordinary differential equations (ODEs), and integrates them by dynamically adapting both the time step and the order of the scheme [74]. A uniform mesh with spacing $\Delta\xi \approx 0.089$ is used to resolve the film region, while the relative and absolute time-integration tolerances are set to 10^{-8} to ensure high accuracy. The boundary and initial conditions for the averaged temperature $\langle\vartheta\rangle$ are determined via the energy balance in the channel ahead and behind of the elongated bubble and is described in the next section. The error estimate is presented in appendix C, where we compare the numerical solution of (34) with the solution of the full two-dimensional problem (10).

1. *Initial and boundary condition for the averaged temperature*

To find the initial and the boundary conditions for the averaged temperature in the thin film, the idea is to match the film averaged temperature with the averaged temperature in the channel ahead and behind. To do so, we write the energy balance under thermally fully developed conditions in the liquid ahead of or behind the bubble [75] assuming that the portion of the channel considered is much greater than the channel half width. Specifically, we consider an infinitesimal slice of the channel in regimes where convection dominates over axial diffusion in the channel and viscous dissipation is neglected. Thus, the net heat transferred over an small portion of the channel $\delta\hat{x}$ with respect to the laboratory reference frame is given by

$$\delta q = \dot{m}\, c_p \left(\hat{T}_b\Big|_{\hat{x}+\delta\hat{x}} - \hat{T}_b\Big|_{\hat{x}} \right), \tag{36}$$

where $\dot{m}$ is the mass flow rate and $\hat{T}_b$ is the bulk temperature; the heat transferred from the wall to the fluid is given by $\delta q = -q''_w\, \mathcal{P}\, \delta\hat{x}$ with $\mathcal{P}$ the wetted perimeter of the channel cross-sectional area $\mathcal{A}$. Combining the definition of the mass flow rate, $\dot{m} = \rho_f\, \mathcal{A}\, U_\infty$ with that of the thermal diffusivity α_f, and taking the limit $\delta\hat{x} \to 0$, the energy balance (36) is recast in the differential form

$$\frac{\mathrm{d}\hat{T}_b}{\mathrm{d}\hat{x}} = -\frac{q''_w}{U_\infty}\,\frac{\mathcal{P}}{\mathcal{A}}\,\frac{\alpha_f}{\kappa_f}. \tag{37}$$

Under uniform heating conditions, the right-hand side of (37) is independent of $\hat{x}$, highlighting that the bulk temperature of the liquid varies linearly with the axial coordinate. The geometrical factor $\mathcal{P}/\mathcal{A}$ equals $1/R$ or $2/R$ for

a planar channel and a cylindrical tube, respectively, yielding $\mathcal{P}/\mathcal{A} = (1+m)/R$. Since the bulk and the averaged temperature differ by at most $\mathcal{O}(\varepsilon^2\,\mathrm{Pe})$, we assume that $\langle\vartheta\rangle \approx \vartheta_b$, see (41).

Then, introducing the dimensionless bulk temperature ϑ_b via (9) and the axial coordinate (in the laboratory reference frame) $x = \hat{x}/L$, and using relations (3, 4) the energy balance (37) reads

$$\frac{\mathrm{d}\langle\vartheta\rangle}{\mathrm{d}x} \approx \frac{\mathrm{d}\vartheta_b}{\mathrm{d}x} = -\frac{\nu\,(1+m)\,0.643\,\varepsilon^2}{1-(1+m)\,0.643\,\varepsilon^2}, \tag{38}$$

where we see that the slope of the bulk temperature is small and of the order of $\mathcal{O}(\varepsilon^2)$.

The initial and boundary conditions of the effective model are obtained by integrating (38), and setting the integration constant to zero, consistent with the initial condition (17) at $\langle\vartheta\rangle|_{x=0} = 0$. Specifically, we impose the following Dirichlet boundary conditions at the the right and left boundaries of the film domain

$$\langle\vartheta\rangle|_\xi = -\frac{\nu\,(1+m)\,0.643\,\varepsilon^2}{1-(1+m)\;0.643\,\varepsilon^2}\,(\xi+t)\,, \tag{39}$$

where we shift from the laboratory to the moving reference frame via $x = \xi + t$. Evaluating (39) at $t = 0$ yields the initial condition.

IV. RESULTS AND DISCUSSION

In this section, we discuss the ramifications of the effective model to understand why the presence of an elongated bubble enhances heat transfer under uniform heating conditions, identifying the key physical mechanisms and the scaling of the Nusselt number for this problem.

A. Effective heat-transfer coefficients and averaged temperature field

Figure 3 shows the impact of the Péclet number on the effective coefficients appearing in (34), ranging from $\mathrm{Pe} = \mathcal{O}(1)$ (diffusion-dominated regime) to the limiting case $\mathrm{Pe} = \mathcal{O}(\varepsilon^{-2})$ (advection-dominated). Those coefficients strongly depend on the shape of the meniscus, suggesting that different regions of the film (i.e., the uniform film, the front and the rear) may contribute differently to the overall heat transfer. Each of them originates from averaging the velocity profile and the Brenner's functions as summarized in table I: this means that it is possible to rigorously track back the physical mechanism responsible of an enhancement or a reduction of the effective coefficients.

The effective advection coefficient $u^\star$, shown in figure 3 (a), is the sum of the pure advection in the axial direction (u_0 in table I), the imposed heat-flux at the channel wall (u_9), advection in both axial and traverse directions via the Brenner's function (u_1, u_2 and u_5), the combined effect of axial and traverse advection and the Brenner's function due to the boundary conditions (u_3, u_4, u_6, u_7 and u_8). Interestingly, $u^\star$ is negligible only in the uniform film region, where the capillary driving force is negligible and the fluid is at rest, i.e., $\mathrm{d}^3\eta/\mathrm{d}\xi^3 = 0$ in (1) when $\eta = 1$. Instead, the shape oscillations at the bubble rear induce changes in its sign since the advective contributions to $u^\star$ (see u_1 and u_2 in table I) are proportional to the derivative of the bubble shape, $\propto -\eta\,\partial_\xi\eta\,\mathrm{Pe}$. As a result, the effective advection increases with the Péclet number at the bubble rear, while at the front it exhibits a non-monotonic behavior – particularly in the advection-dominated regime – due to the competition between advection and the imposed heat flux.

In the uniform film region the energy is transported purely by thermal diffusion, and the effective diffusion coefficient $D^\star$ equals unity, as shown in figure 3 (b). In the transition regions, instead, there is a net flow in the axial and transverse direction (see the streamlines in figure 9) that enhances the effective diffusion coefficient at sufficiently large Péclet numbers. The leading contribution to $D^\star$ (denoted as D_0 in table I) follows the scaling law typical of the Aris-Taylor dispersion – a quadratic dependence on the film-scale Péclet number – with a numerical prefactor equal to the theoretical limit for plane Poiseuille flow, 2/105. The evolution of the effective thermal diffusion coefficient is similar to the one obtained for the transport of a passive scalar in a thin film in Picchi and Poesio [47].

The effective coefficient accounting for viscous dissipation $\Phi^\star$, shown in figure 3 (c), is only weakly dependent on Pe. Specifically, the leading contribution to $\Phi^\star$ (denoted as Φ_0 in table I) takes the form of a quadratic expression $\propto (\eta-1)^2/\eta^4$, that can be seen as the product of the pressure gradient, $(\eta-1)/\eta^3$, and the averaged speed, $(\eta-1)/\eta$, in the thin film, obtained via the lubrication theory [3, 57]. This is the typical form of the viscous dissipation or the entropy production (when divided by the temperature) of a fluid flow in a confined geometry [76]. The viscous dissipation is maximal in the front (there is a region near the nose where the pressure gradient is maximal) and in

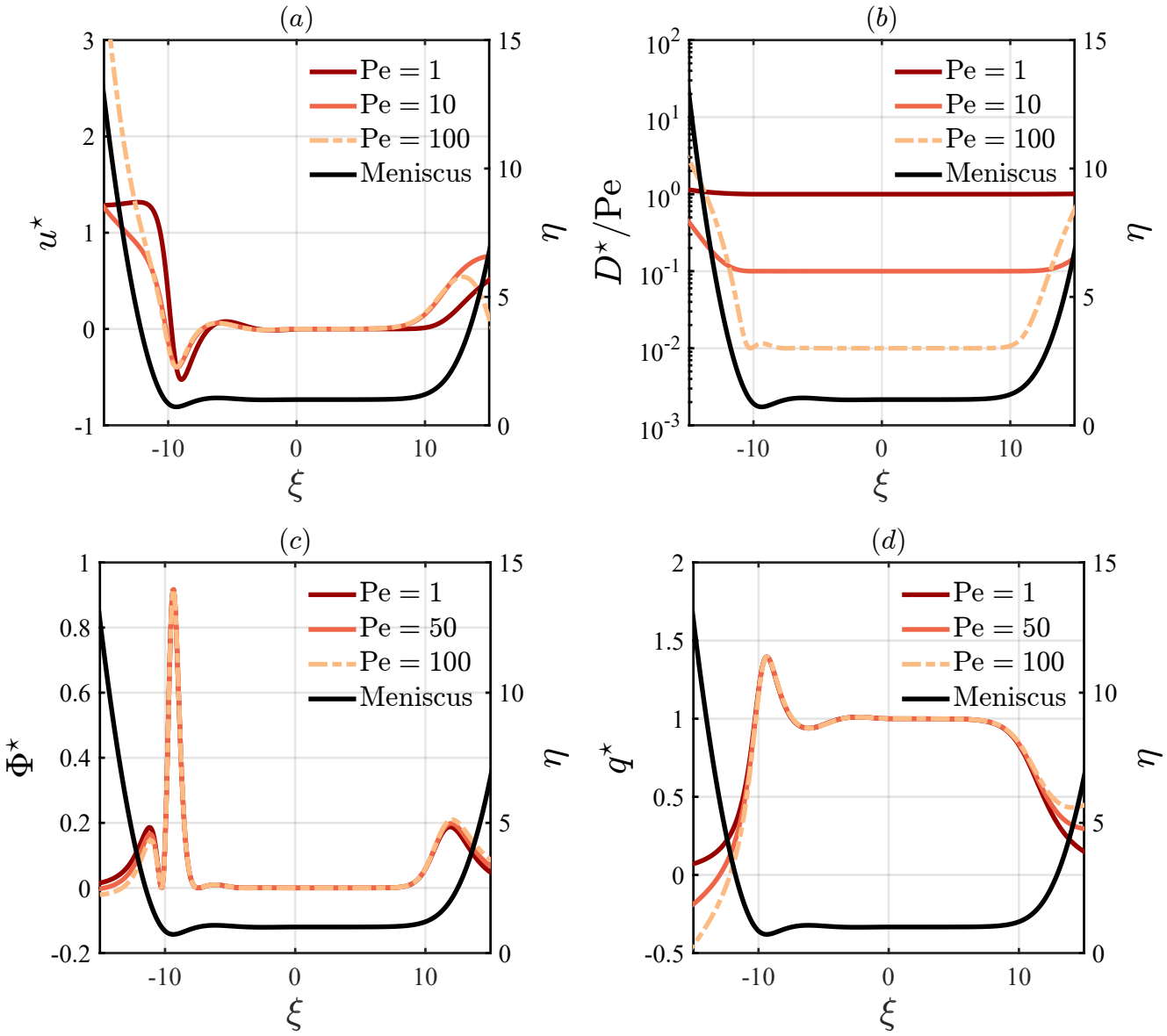

Figure 3. Impact of the Péclet (Pe) number on the model effective coefficients, see (33), for advection, diffusion, viscous dissipation, and heat flux as functions of the axial coordinate ξ: (*a*) $u^\star$, (*b*) $D^\star/\mathrm{Pe}$, (*c*) $\Phi^\star$, (*d*) $q^\star$; right, meniscus profile $\eta(\xi)$. The small-scale parameter is set to $\varepsilon = 0.1$, corresponding to $\mathrm{Ca} \approx 3.33 \times 10^{-4}$.

the rear corresponding to the meniscus undulations where local recirculation vortexes are present, see the streamlines in figure 9.

Similarly, the leading contribution to the effective heat source term $q^\star$ (denoted as q_0 in table I) scales as the inverse of the film thickness, $q_0 \sim \eta^{-1}$, suggesting that heat transfer is enhanced in regions where the fluid layer is smaller, namely the uniform film region and the bubble's rear, as shown in figure 3 (*d*). Higher Péclet numbers simultaneously increase $q^\star$ at the front and decrease it at the rear: when advection prevails, in fact, the velocity field tends to locally accumulate heat in the front, while removing it from the bubble's rear, see the streamlines in figure 8 (*b*).

Figure 4 shows the evolution of the averaged temperature field obtained solving numerically (34) as described in Sec. III D for the case of a cylindrical tube heated uniformly from the wall. The chosen time interval corresponds to the onset of thermally fully developed conditions in the reference frame attached to the bubble. At early times, the temperature increases almost uniformly along the central portion of the bubble, while, as time elapses, the temperature profile becomes almost linear in the thin film region. Under conditions of imposed uniform heat flux, a steady-state solution for the averaged temperature field in the moving reference frame cannot be achieved since the

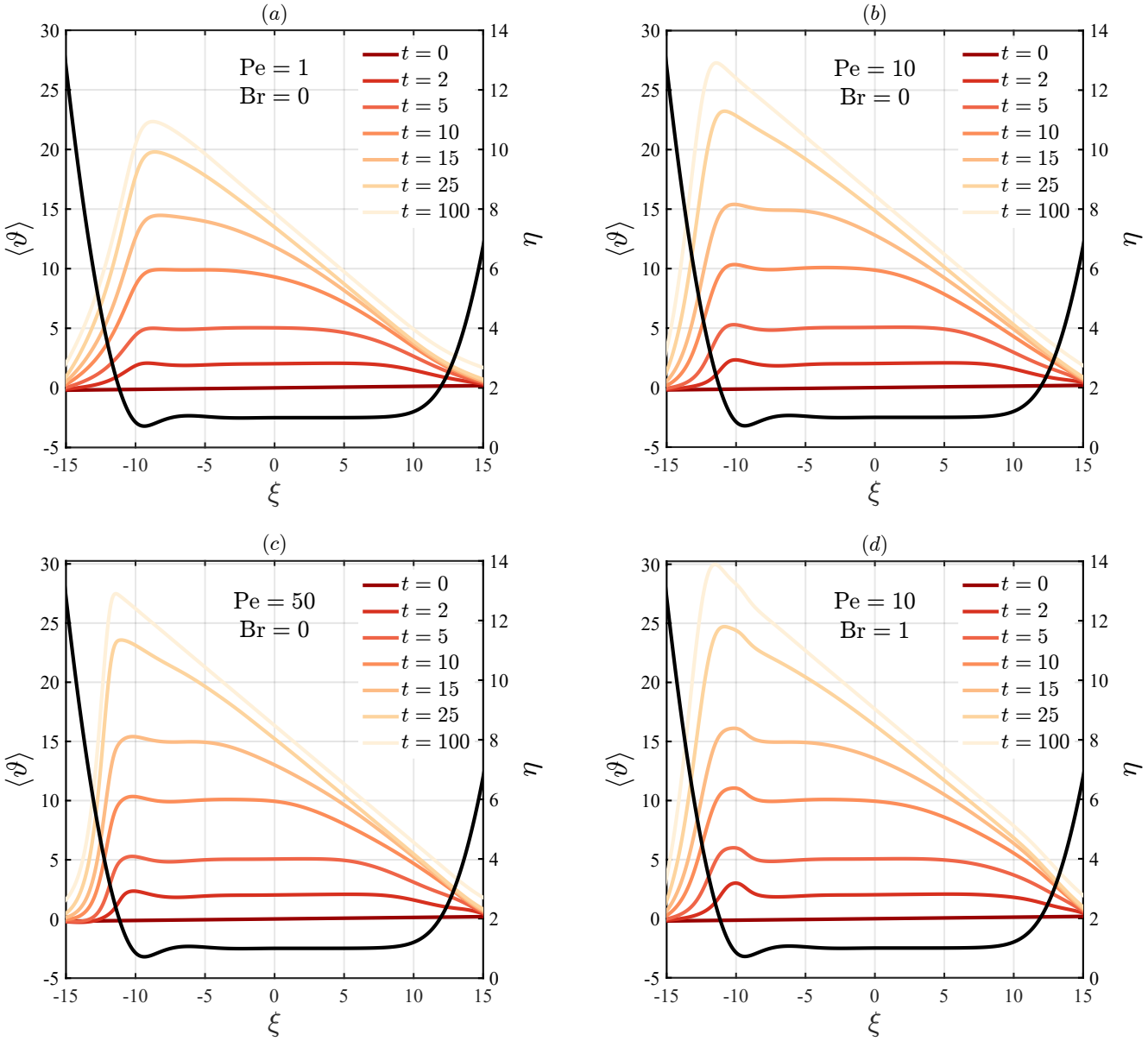

Figure 4. Impact of the Péclet (Pe) and Brinkman (Br) numbers on the mean film temperature $\langle\vartheta\rangle$ in a cylindrical tube ($m = 1$), under inward heat flux conditions ($\nu = -1$), as a function of the axial coordinate ξ, evaluated at fixed time instants t: (a) Pe = 1, (b) Pe = 10, and (c) Pe = 50, with Br = 0; in (d) Pe = 10 and Br = 1; right, meniscus profile $\eta(\xi)$. The small-scale parameter is set to $\varepsilon = 0.1$.

film is continuously heated from the solid boundary. However, a fully developed heat transfer coefficient is reached once the difference between the bulk and the wall temperatures becomes independent of the axial coordinate [75], as it will be discussed in detail in Sec. IV B.

As shown in panels (a) to (c) of figure 4, increasing the Péclet number leads to a sharper temperature gradient at the rear of the bubble and amplifies the peak located at the point of minimum film thickness. This is consistent with fluid recirculation in the bubble's rear (see figure 9), which increases the residence time of a fluid particle being continuously heated from the wall. A similar trend is observed in regimes where viscous dissipation plays a role: comparing panels (b) and (d), which differ only in the Brinkman number, we see that viscus heating amplifies both the height of the triangular profile and the magnitude and width of the peak, but, overall, the temperature profiles look qualitatively similar.

B. Local Nusselt number

The heat-transfer enhancement induced by an elongated bubble is quantified via the local convective heat transfer coefficient, defined as the ratio between the specific heat flux entering the fluid, q''_w, and the difference between the wall temperature and the bulk temperature [51, 58, 75, 77], that, in terms of the dimensionless variables defined in Sec. II C, yields

$$h = -\nu \, \frac{\kappa_f \, U_b \, h_\infty}{\alpha_f \, L \, (\vartheta_w - \vartheta_b)}, \tag{40}$$

where $\vartheta_w \equiv \vartheta|_{y=0}$ is the dimensionless wall temperature and ϑ_b is the dimensionless bulk temperature. The latter is defined as an enthalpy-weighted average relative to the laboratory reference frame and differs from the mean film temperature $\langle\vartheta\rangle$ due to higher-order corrections:

$$\vartheta_b \equiv \frac{\int_0^\eta u \, \vartheta \, \mathrm{d}y}{\int_0^\eta u \, \mathrm{d}y} = \langle\vartheta\rangle + \varepsilon^{2-p} \, \vartheta_b^{(1)} + \mathcal{O}\big(\varepsilon^{2(2-p)}\big), \quad \text{with} \quad \vartheta_b^{(1)} \equiv \frac{\int_0^\eta u \, \vartheta^{(1)} \, \mathrm{d}y}{\int_0^\eta u \, \mathrm{d}y}. \tag{41}$$

Such average is taken over the liquid film thickness, given its dominant heat capacity relative to the one of the gas [78]. Expanding the wall temperature, $\vartheta_w = \langle\vartheta\rangle + \varepsilon^{2-p} \, \vartheta_w^{(1)} + \mathcal{O}\big(\varepsilon^{2(2-p)}\big)$, and combining (40, 41) we obtain a closed-form solution for the local Nusselt number based on the uniform film thickness

$$\mathrm{Nu}_x^{h_\infty} = \frac{h \, h_\infty}{\kappa_f} = -\frac{\nu}{\vartheta_w^{(1)} - \vartheta_b^{(1)}}. \tag{42}$$

This formulation of the local Nusselt number is based on the uniform film thickness as the relevant length scale for the forced convection around an elongated bubble. However, the local Nusselt number for Taylor flows is conventionally formulated using the hydraulic diameter, namely $2\,(2-m)\,R$, instead of the uniform film thickness [see, e.g., 29, 30, 34]. Thus, rescaling (42) with $2\,(2-m)\,R/h_\infty$ via (3), we get the local Nusselt number based on the hydraulic diameter as

$$\mathrm{Nu}_x = -\frac{2\,(2-m)}{0.643\,(3\,\mathrm{Ca})^{2/3}} \, \frac{\nu}{\vartheta_w^{(1)} - \vartheta_b^{(1)}}. \tag{43}$$

Using (29, 30) and the velocity profile (B1), the first-order corrections to the wall and bulk temperature are given by

$$\vartheta_w^{(1)}(\xi,\, t) = \eta \left(\frac{\eta - 1}{15} - \frac{1}{6\,\mathrm{Pe}} \frac{\mathrm{d}\eta}{\mathrm{d}\xi} \right) \frac{\partial\langle\vartheta\rangle}{\partial\xi} + \frac{2\,\mathrm{Br}}{5} \left(\frac{\eta - 1}{\eta} \right)^2 - \nu \, \frac{\eta}{3}, \tag{44a}$$

$$\vartheta_b^{(1)}(\xi,\, t) = \eta \left(-\frac{2\,(\eta - 1)}{105} + \frac{7}{120\,\mathrm{Pe}} \frac{\mathrm{d}\eta}{\mathrm{d}\xi} \right) \frac{\partial\langle\vartheta\rangle}{\partial\xi} - \frac{4\,\mathrm{Br}}{35} \left(\frac{\eta - 1}{\eta} \right)^2 + \nu \, \frac{\eta}{15}, \tag{44b}$$

and these are, then, substituted into (43), yielding

$$\mathrm{Nu}_x = \frac{\mathrm{Nu}_0}{\eta\,(1 - \nu\,\Gamma)}, \quad \text{with} \quad \mathrm{Nu}_0 = \frac{5\,(2-m)}{0.643\,(3\,\mathrm{Ca})^{2/3}}, \tag{45}$$

where Nu_0 is the Nusselt number in the uniform film region and Γ accounts for the contribution of advection and viscous dissipation as

$$\Gamma\,(\xi,\, t;\, \mathrm{Pe},\, \mathrm{Br}) = \left(\frac{3\,(\eta - 1)}{14} - \frac{9}{16\,\mathrm{Pe}} \frac{\mathrm{d}\eta}{\mathrm{d}\xi} \right) \frac{\partial\langle\vartheta\rangle}{\partial\xi} + \frac{9\,\mathrm{Br}}{7} \frac{(\eta - 1)^2}{\eta^3}. \tag{46}$$

To sum up, the local Nusselt number in the thin-film region surrounding an elongated, inviscid Bretherton's bubble (i.e., negligible inertial and gravitational effects) under uniform heat flux conditions depends on space and time through the film thickness, its slope, and the temperature gradient. This dependence is governed by a set of dimensionless groups – namely the Péclet, Brinkman and capillary numbers – as well as the cross-sectional geometry and the orientation of the thermal flux, namely $\mathrm{Nu}_x = \mathrm{Nu}_x\,(\eta,\, \mathrm{d}\eta/\mathrm{d}\xi,\, \partial\langle\vartheta\rangle/\partial\xi;\, \mathrm{Pe},\, \mathrm{Br},\, \mathrm{Ca};\, \nu,\, m)$. Formulated as in (45), we see that the dependence on the capillary number enters only via Nu_0, while the Nusselt number scales as the inverse

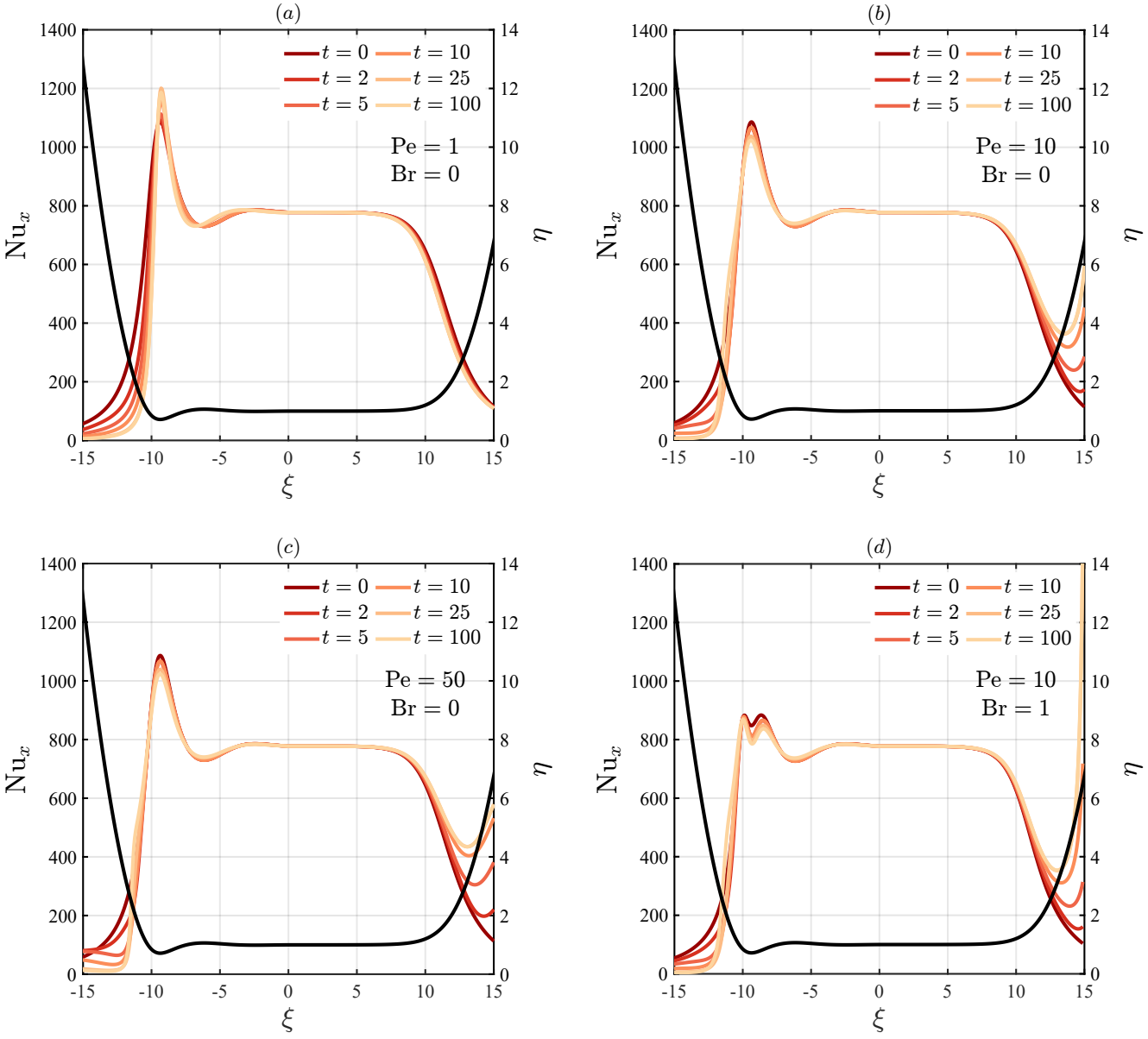

Figure 5. Impact of the Péclet (Pe) and Brinkman (Br) numbers on the local Nusselt number Nu_x for the cases shown in figure 4; right, meniscus profile $\eta(\xi)$.

of the film thickness, $\mathrm{Nu}_x \sim \eta^{-1}$, similarly to what observed for core-annular flows in Botticini *et al.* [51]. The Péclet and the Brinkman numbers only affect the term $(1 - \nu\,\Gamma)$ and have a small effect on the Nusselt number.

In the uniform film region, where $\eta = 1$, $\mathrm{d}\eta/\mathrm{d}\xi = 0$, and $\Gamma = 0$, Nu_x depends only on the capillary number and the geometry of the cross-section, i.e., $\mathrm{Nu}_x = \mathrm{Nu}_0\,(\mathrm{Ca},\, m)$, simplifying to $\mathrm{Nu}_x \equiv \mathrm{Nu}_0 \approx 3.7383\,\mathrm{Ca}^{-2/3}$ for a cylindrical tube ($m = 1$). Therefore, viscous dissipation and temperature gradient do not affect the heat transfer coefficient in the uniform film region of the elongated bubble. There, in fact, the fluid is at rest and the thermal problem is dominated by thermal diffusion.

Outside the flat-film region, the evolution of the local Nusselt number is highly sensitive to both the shape of the interface and time, as shown in figure 5. In general, the local Nusselt number decreases over time in the rear of the bubble and increases in the front. Specifically, at low Péclet numbers – panel (a) – diffusion dominates over advection and the decay of the local Nusselt number in the rear is smooth and monotonic, while no significant temporal variation is observed in the front. As advection becomes more relevant – panel (b) – the increase of Nu_x in the front becomes more pronounced with time, suggesting the onset of convective enhancement in that region. In the strongly advection-

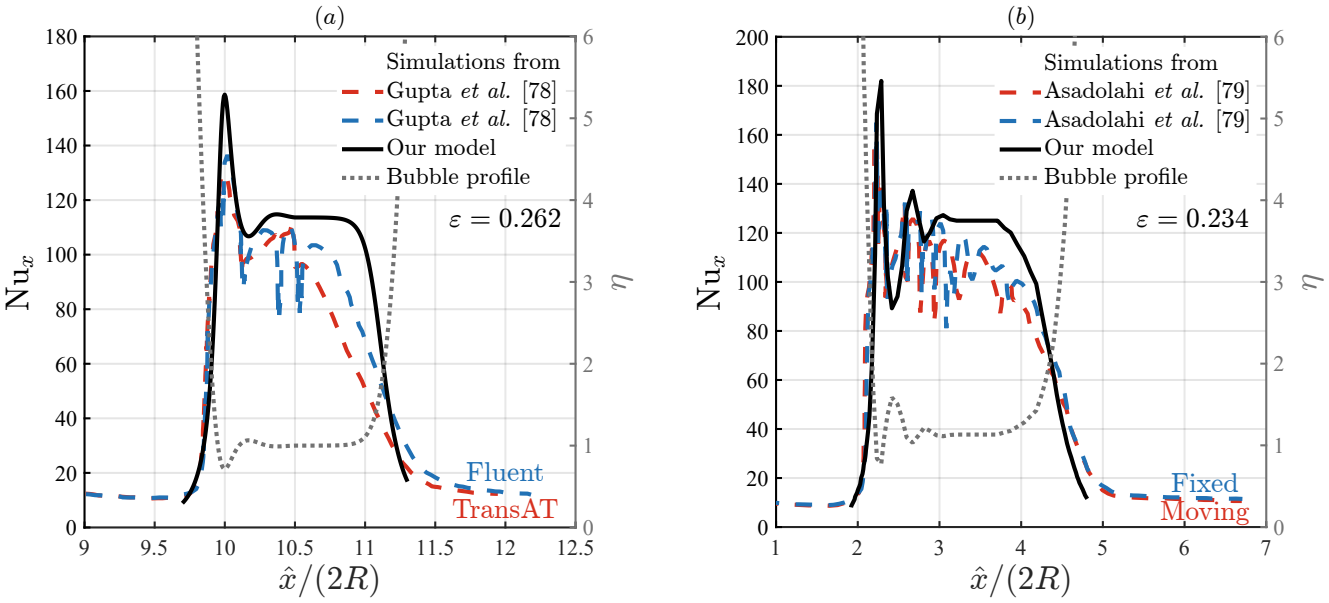

Figure 6. Comparison between the spatial evolution of the local Nusselt number Nu_x predicted by the upscaled model (with $m = 1$) in the limit $\Gamma \to 0$ (continuous black line) – see (45, 46) – and available results from numerical simulations of an elongated bubble in a horizontal capillary under iso-flux boundary conditions: (*a*) Gupta *et al.* [78], (*b*) Asadolahi *et al.* [79] (blue and red dashed lines); right, meniscus profile $\eta(\xi)$ (dotted grey line). Here, $\hat{x}$ denotes the dimensional axial coordinate relative to the laboratory reference frame, consistent with the cited works.

dominated regime – panel (*c*) – the Nu_x profile in the rear shows a local minimum that progressively shifts towards the tip of the bubble with time, accompanied by a steepening near the point of minimum film thickness (at $\xi \approx -10$). Interestingly, in the front, the local Nusselt number increases significantly with time far from the uniform film due to the predominant advection (the effect of the transverse velocity is significant there). However, it is worth mentioning that, when $\eta \gg 1$, the profile matches the spherical cap and the thin-film approximation does not hold anymore.

Viscous heating reduces the peak in the local Nusselt number in the bubble's rear compared to the case with $\mathrm{Br} = 0$, see figure 5 (*d*). This indicates a lower heat-transfer efficiency since part of the thermal energy is internally generated and is not exchanged with the solid wall.

C. Validation with existing literature

In figure 6, we assess the validity of the effective model (34) by comparing the local Nusselt number predicted by the scaling law (45) with two numerical studies from the literature, detailed in table II. Unfortunately, we were not able to find experiments or numerical data within the applicability region of the model expressed by (35). In both cases, the governing dimensionless parameters lies just beyond the applicability conditions: in both cases, $\mathrm{Ca} \ll 1$ but the Reynolds number Re is finite, meaning a weak effect of inertia (that is neglected by Bretherton's theory). Also the Péclet numbers slightly exceed the theoretical bound expressed by (35), implying that, since the inequalities given by (35) are not met, the rigorous thermal decoupling between the transverse and the axial scales cannot be guaranteed [80]. Nevertheless, it is worth recalling that those constraints provide only sufficient but not necessary conditions, and are, in some, cases even too restrictive [63, 81, 82]. Therefore, we compare the numerical data of Gupta *et al.* [78] and Asadolahi *et al.* [79] with the local Nusselt number obtained with our model neglecting (i) the viscous dissipation, since the Brinkman number is of order $< 10^{-3}$, see table II; and (ii) the contribution of the axial temperature gradient, that is not given in those two works. This corresponds to the limit $\lim_{\Gamma \to 0} \mathrm{Nu}_x$ (with $m = 1$), see (45, 46).

Figure 6 (*a*) shows the comparison with Gupta *et al.* [78] where the elongated bubble is investigated using both the level-set and volume-of-fluid implemented through the *TransAT* (dashed red line) and *ANSYS Fluent* (dashed blue

Parameter [unit of measurement]	**Symbol**	**Gupta *et al.* [78]**	**Asadolahi *et al.* [79]**
Reference frame		fixed	fixed & co-moving
Tube radius [m]	R	$2.5 \cdot 10^{-4}$	$1 \cdot 10^{-3}$
Specific wall heat flux $\left[\mathrm{W\,m^{-2}}\right]$	$\lvert q''_w \rvert$	$3.20 \cdot 10^{4}$	$3.20 \cdot 10^{4}$
Gas/liquid		air/water	nitrogen/water
Liquid dynamic viscosity [Pa s]	μ_f	$8.90 \cdot 10^{-4}$	$8.90 \cdot 10^{-4}$
Liquid thermal conductivity $\left[\mathrm{W\,m^{-1}\,K^{-1}}\right]$	κ_f	0.6	0.6
Liquid density $\left[\mathrm{kg\,m^{-3}}\right]$	ρ_f	997	997
Surface tension $\left[\mathrm{N\,m^{-1}}\right]$	σ	0.072	0.072
Gas-to-liquid viscosity ratio		$2.06 \cdot 10^{-2}$	$2.36 \cdot 10^{-2}$
Gas-to-liquid thermal conductivity ratio	$\mathcal{K}$	$4.03 \cdot 10^{-2}$	$4.03 \cdot 10^{-2}$
Uniform film thickness [m]	h_∞	$1.10 \cdot 10^{-5}$	$4.10 \cdot 10^{-5}$
Scale parameter	ε	0.262	0.234
Bubble mean velocity $\left[\mathrm{m\,s^{-1}}\right]$	U_b	0.483	0.348
Interfacial length [m]	L	$4.21 \cdot 10^{-5}$	$1.75 \cdot 10^{-4}$
Capillary number	$\mathrm{Ca} = \mu_f\, U_b / \sigma$	$5.97 \cdot 10^{-3}$	$4.30 \cdot 10^{-3}$
Reynolds number	$\mathrm{Re} = \rho_f\, U_b\, R / \mu_f$	135	390
Weber number	$\mathrm{We} = \mathrm{Ca}\,\mathrm{Re}$	0.80	1.67
Bond number	$\mathrm{Bo} = \rho_f\, g\, R^2 / \sigma$	$8.50 \cdot 10^{-3}$	$1.36 \cdot 10^{-1}$
Péclet number	$\mathrm{Pe} = L\, U_b / \alpha_f$	141	422
Brinkman number	$\mathrm{Br} = \dfrac{\mu_f\, U_b^2}{\lvert q''_w \rvert\, h_\infty}$	$5.89 \cdot 10^{-4}$	$8.19 \cdot 10^{-5}$
$-\log_\varepsilon \mathrm{Pe}$	p	3.69	4.17
$+\log_\varepsilon \mathrm{Br}$	b	5.55	6.49
$+\log_\varepsilon \mathcal{K}$	k	2.39	2.21

Table II. Summary of simulation parameters adopted in two numerical studies on heat transfer in non-boiling gas-liquid Taylor flow within horizontal circular ($m = 1$) micro-channels subject to iso-flux heating ($\nu = -1$) boundary condition at the wall, see figure 6.

line) codes, respectively. Note that the discrepancies between these two numerical models are caused by differences in the description of the curvature of the meniscus, which is reconstructed in one case and explicitly tracked in the other. Since the gas-liquid interface is not reported in figure 7 of Gupta *et al.* [78], we reproduce the bubble profile (right ordinate) using the Bretherton equation (1), adjusting its length, and translating it along the axial coordinate to fit with the simulated bubble. Overall, our model exhibits good qualitative and quantitative agreement with both the numerical simulations, except for the undulating evolution of the Nusselt number in the bubble's rear. Those inertia-driven undulations are typical of high-Reynolds-number regimes [83], and are not captured by Bretherton similarity equation.

Panel (*b*) shows the local Nusselt number data from Asadolahi *et al.* [79] obtained using *ANSYS Fluent* for a unit cell moving with the bubble speed (dashed red line) and with respect to the laboratory reference frame (dashed blue line). Since figure 12 of Asadolahi *et al.* [79] reports the computed bubble profile (right ordinate), we use that profile to compute Nu_x instead of that derived from Bretherton equation (1). Also in this case, the agreement between the scaling law (45) and the simulations is quite satisfactory, considering also that the model is used slightly outside its range of applicability. Our analysis seems to confirm that the main parameter that affects the evolution of the local Nusselt number is the film thickness, similarly to observations reported in earlier works on core-annular flows Botticini *et al.* [51].

Thanks to its capability of accounting for the bubble shape, we believe that the scaling law (45) has the potential of being integrated in widely used mechanistic models for trains of elongated bubbles [9, 16, 17, 37, 84].

D. Averaged Nusselt number

A more complete characterization of forced convection in the film of an elongated bubble is given by the averaged Nusselt number, computed via integration of the local Nusselt number over the axial direction [see, e.g., 27, 58]. Alternative averaging approaches are discussed in appendix D.

In the following, we investigate the effect of the bubble length on the averaged Nusselt number distinguishing between the three sub-regions, namely the rear, the uniform film, and the front. Thus, we introduce the average

Nusselt numbers for the rear and the front as

$$\overline{\mathrm{Nu}}_{\mathrm{front}} = \frac{1}{\Delta l_{\mathrm{front}}} \int_{\mathrm{front}} \mathrm{Nu}_x(\xi)\, \mathrm{d}\xi, \qquad \overline{\mathrm{Nu}}_{\mathrm{rear}} = \frac{1}{\Delta l_{\mathrm{rear}}} \int_{\mathrm{rear}} \mathrm{Nu}_x(\xi)\, \mathrm{d}\xi, \tag{47}$$

while the Nusselt number in the uniform-film region is independent of its length l, i.e., $\overline{\mathrm{Nu}}_0 = \mathrm{Nu}_0$. Therefore, we can define the averaged Nusselt number for the entire bubble as

$$\overline{\mathrm{Nu}}\,(t,\, \mathrm{Pe},\, \mathrm{Br},\, \varepsilon) = \frac{\Delta l_{\mathrm{rear}}\, \overline{\mathrm{Nu}}_{\mathrm{rear}} + l\, \mathrm{Nu}_0 + \Delta l_{\mathrm{front}}\, \overline{\mathrm{Nu}}_{\mathrm{front}}}{\Delta l_{\mathrm{rear}} + l + \Delta l_{\mathrm{front}}}. \tag{48}$$

In figure 7, we examine the impact of the Péclet and Brinkman numbers at a fixed capillary number ($\varepsilon = 0.1$) on the time evolution of $\overline{\mathrm{Nu}}$ in the front and in the rear of the bubble. Typically, the averaged Nusselt number increases with time and exhibits an S-shaped evolution at the front, whereas a reversed trend in the rear, see figure 7 (a). An exception occurs for $\mathrm{Pe} = 1$, where diffusion competes with advection, resulting in a monotonically decreasing profile of the averaged Nusselt number at the front. When the problem is thermally fully developed, $t \gg 0$, in the front, the final $\overline{\mathrm{Nu}}_{\mathrm{front},\, t\to\infty}$ increases with the Péclet number and saturates to a common asymptotic value for $\mathrm{Pe} = 50$ and $\mathrm{Pe} = 90$. At the rear, instead, $\overline{\mathrm{Nu}}_{\mathrm{rear},\, t\to\infty}$ follows a non-monotonic trend increasing in the following order $\mathrm{Pe} = (1,\, 2,\, 90,\, 50,\, 10)$. Interestingly, at high Péclet numbers ($\mathrm{Pe} > 10$), the average Nusselt number in the rear exhibits an undershoot followed by damped oscillations, reflecting the emergence of transient thermal instabilities before reaching thermally developed conditions. The effect of viscous dissipation ($\mathrm{Br} = 1$) yields a similar overall trend, as shown in figure 7 (b). The only difference is that the long-time value in the front increase according to the sequence $\mathrm{Pe} = (1,\, 2,\, 10,\, 90,\, 50)$ rather than monotonically with the Péclet number due to the competing effects of advection and viscous heating.

In panel (c) we show the impact of a uniform film of 10 dimensionless units in length. The overall behavior is similar to that described in (a) for the case $l = 0$, except for the fact that increasing its length leads to more intense and irregular fluctuations in the averaged Nusselt number in the bubble rear in regimes where advection is dominant. The uniform film length has the strongest impact on the final $\overline{\mathrm{Nu}}_{t\to\infty}$ taken over the entire bubble: as l increases, it converges toward the uniform-film value Nu_0 due to its growing relative weight in the spatial average (48), see figure 7 (d).

To better understand the time evolution of the average Nusselt number, we try to illustrate the underlying physical mechanisms in figure 8 choosing $\mathrm{Pe} = 50$, where the time oscillations in the bubble rear are present. Specifically, in the front, the time required for the Nusselt number to reach its final value is of the order of the time required for a fluid particle initially in contact with the wall to reach the channel centerline and return. This time interval can be estimated as the time required for the bubble to travel a distance equal to the channel diameter, equal to $t^* \sim (2\,R/U_b)\,(U_b/L) = 2\,(0.643\,\varepsilon)^{-1}$ in dimensionless terms, see figure 8 (a). In fact, in the front, clockwise vortices entrain hot fluid into the computational domain, enhancing forced convection and increasing the averaged Nusselt number over time (see the streamlines in a reference frame attached to the bubble in panel (b)). Conversely, at the rear, the vortices advect hot fluid away from the film, leading to a reduction of heat transfer.

The oscillatory behavior of the averaged Nusselt number at the bubble rear – also identified in previous studies (e.g., 34, 85, 86) – is linked to the coupling between the interface geometry and the development of flow recirculation in the rear, resulting in intermittent heating and cooling flow patterns [40, 87]. To show this, we identify six characteristic time instants ('A' to 'F') in figure 8 (a). Specifically, the temporal fluctuations originate from the flow constriction at the point of minimum film thickness, where a heat pulse forms and remains trapped in the recirculation zone. At the location of the bubble undulations in the rear the effective advection coefficient $u^\star$ changes sign, see figure 3 (a), and the hotspot is advected back and forth. This alters the temperature distribution, progressively reducing the maximum of the local Nusselt number at $\xi \approx -9.5$ and distorting its profile near $\xi \approx -11.5$ (see figure 3 (c)). The interplay between peak suppression and hump formation modifies the area under the local Nusselt number, namely the average Nusselt number. Over time, diffusion and the heat entering from the wall smooth out the hotspot, as illustrated in the supplementary Movie.

V. CONCLUSIONS

In this paper, we developed an asymptotic one-dimensional model to describe forced convection in the liquid film surrounding a single elongated bubble within a horizontal channel subjected to a uniform heat flux (extended Graetz-type problem). In the visco-capillary regime – characterized by negligible gravitational and inertial effects – and in the limit of an inviscid, non-conductive gas phase, the mathematical description of the system reduces to a single advection–diffusion-heat-transfer equation, where the dominant thermal transport mechanisms, namely transverse

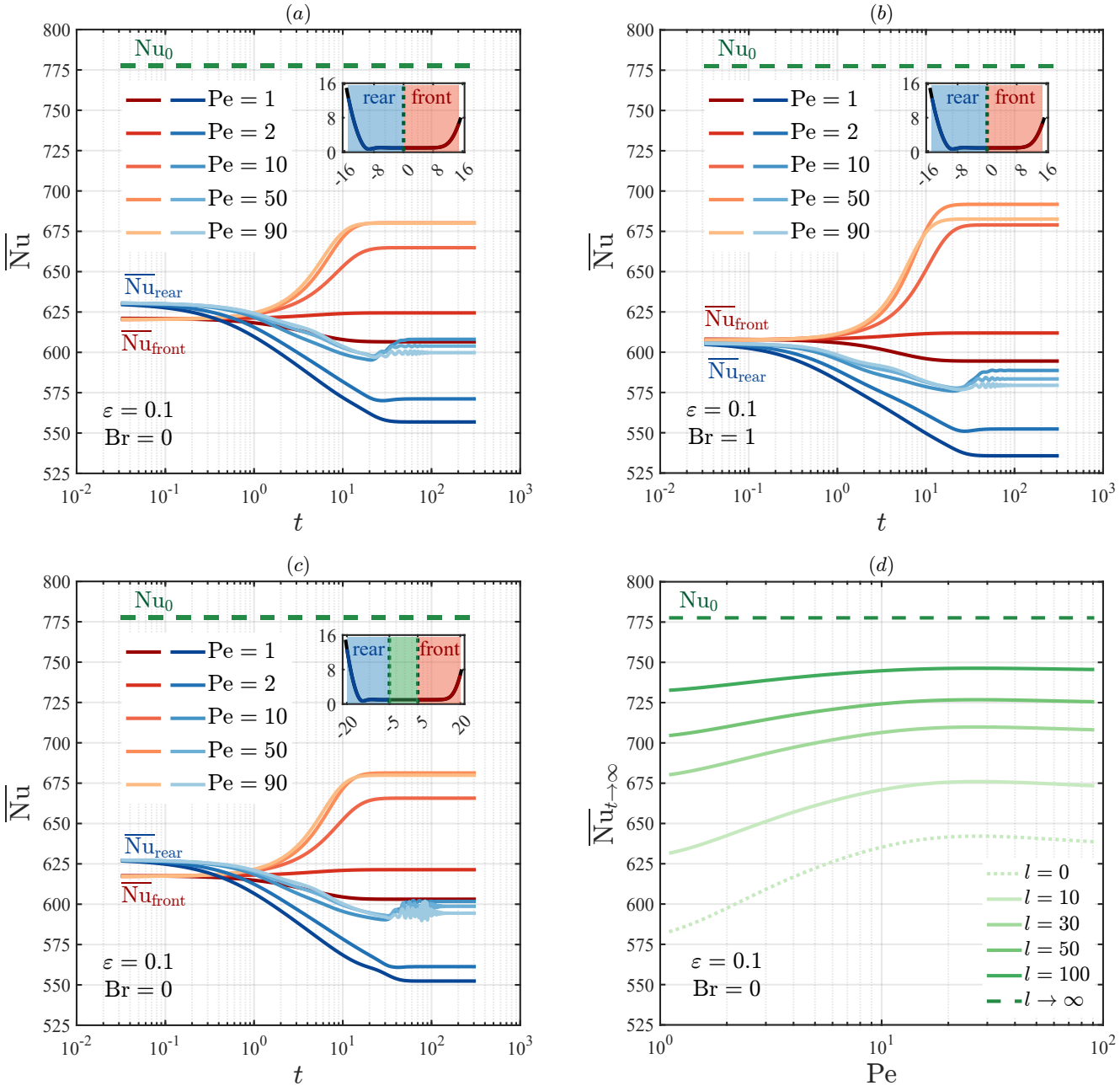

Figure 7. Impact of the Péclet (Pe) and Brinkman (Br) numbers on the averaged Nusselt numbers for the front ($\overline{\mathrm{Nu}}_{\mathrm{front}}$), rear ($\overline{\mathrm{Nu}}_{\mathrm{rear}}$), and uniform-film ($\mathrm{Nu}_0$) regions, see (47) and (45). Time-dependent evolution of the averaged Nusselt numbers at different Péclet numbers for fixed values of flat-film length l and Brinkman number: (*a*) $l = 0$ and $\mathrm{Br} = 0$, (*b*) $l = 0$ and $\mathrm{Br} = 1$, (*c*) $l = 10$ and $\mathrm{Br} = 0$. (*d*) Influence of l on the overall averaged Nusselt number $\overline{\mathrm{Nu}}$, given in (48), under thermally fully developed conditions. Small-scale parameter: $\varepsilon = 0.1$.

diffusion and axial advection, are modeled through effective coefficients that depend exclusively on the Péclet and Brinkman numbers, as well as on the geometry of the gas–liquid interface. Interestingly, the resulting diffusion coefficient generalizes the classical Taylor-Aris dispersion to thermal dispersion in a thin film.

We derived a closed-form expression for the Nusselt number, elucidating how film-driven flow confinement enhances heat transfer compared to the single-phase regime. In the uniform-film region, the local Nusselt number remains uniform and scales inversely with the capillary number following a 2/3 power-law, highlighting the impact of phase topology on heat removal efficiency. Additionally, we clarified the role of recirculation patterns emerging at the front

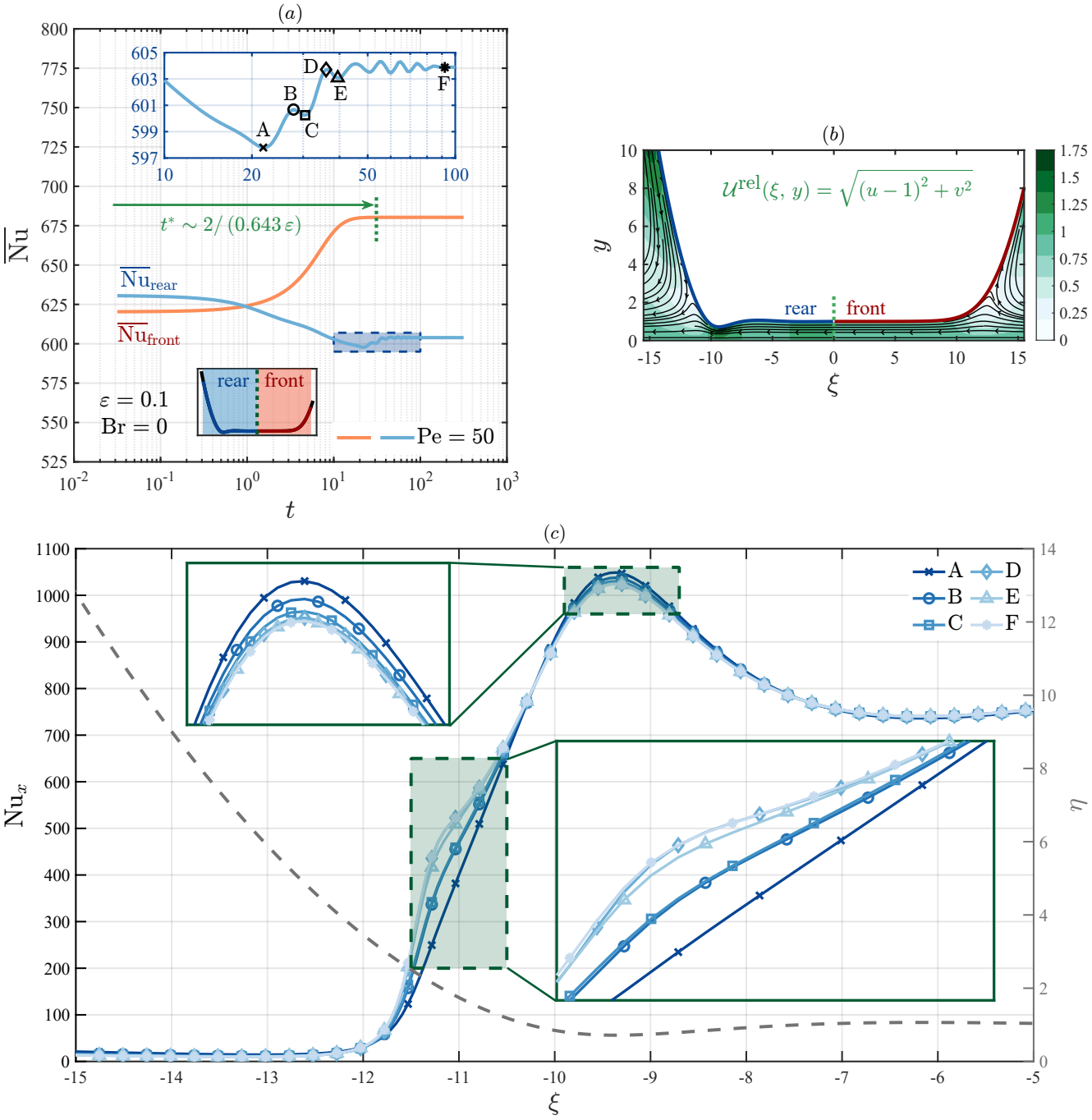

Figure 8. (*a*) Temporal evolution of the average Nusselt number at the front and rear of the bubble, highlighting six reference points (labeled 'A' to 'F') illustrating the oscillatory dynamics. (*b*) Streamlines in the moving reference frame and contours of the relative velocity magnitude $\mathcal{U}^{\mathrm{rel}}$, see (B1). For the selected time instants, spatial evolution along the rear interface of (*c*) the local Nusselt number. Small-scale parameter: $\varepsilon = 0.1$.

and rear menisci in shaping the overall thermal response of the film under advection-dominated conditions. We demonstrated that the formation of hotspots at the point of minimum film thickness – resulting from the interplay between purely diffusive transport in the uniform-film region and the flow constriction in the bubble rear – gives rise to an oscillatory thermal dynamics of the averaged Nusselt number. Our analysis is complemented by the identification of the model's applicability region, where upscaling remains a physically consistent approach. Comparison with numerical simulations available in the literature reveals that the formal constraints on the Péclet number can be

relaxed, extending the predictive capabilities of the model to a broader region of the parametric space.

Future work may explore the extension of this framework to regimes with larger capillary numbers and with fluid evaporation/condensation. This would enable the investigation of thermal interactions between consecutive slugs in bubble-train flows, shedding light on more complex flow patterns and their influence on the overall heat-transfer performance in heat-transfer applications.

Funding. This study has received funding from the European Union 'NextGenerationEU', Ministero dell'Università e della Ricerca (MUR) 'Italiadomani' Piano Nazionale di Ripresa e Resilienza (PNRR), Mission 4, Research Project PRIN 2022 'Predictive forecasting and risk assessment for CO_2 transport in pipelines', MUR code: 20229JPN53; CUP Master code: J53D23002000006; CUP code: D53D23003250006.

Declaration of interests. The authors report no conflict of interest.

Supplementary material and movies. A supplementary movie is available.

Appendix A: Equivalence of the planar and radial coordinates in the low Ca limit

In this section we show that, in the $\mathrm{Ca} \ll 1$ limit, the planar and the axisymmetric configurations are asymptotically equivalent as in [3]. Specifically, recalling that the transverse and the radial coordinates are related via $\hat{y} = R - \hat{r}$ (see figure 1) and using (3) we obtain

$$\frac{\hat{y}}{h_\infty} = \frac{1 - \hat{r}/R}{0.643\,(3\,\mathrm{Ca})^{2/3}}, \tag{A1}$$

that maps the thin layer onto an $\mathcal{O}(1)$ interval [88, 89]. Then, applying the chain rule we see that the the differential operators in cylindrical coordinates reduce to their planar counterparts up to higher–order corrections ($y = \hat{y}/h_\infty$ and $r = \hat{r}/R$)

$$\frac{1}{r}\,\partial_r\,(r\,\star) = -\frac{\partial_y \star}{0.643\,(3\,\mathrm{Ca})^{2/3}} + \frac{\star}{1 - 0.643\,(3\,\mathrm{Ca})^{2/3}\,y} \approx -\frac{\partial_y \star}{0.643\,(3\,\mathrm{Ca})^{2/3}}, \tag{A2a}$$

$$\frac{1}{r}\,\partial_r\,(r\,\partial_r\,\star) = \frac{1}{0.643^2\,(3\,\mathrm{Ca})^{4/3}}\left(\partial_{yy}\,\star - \frac{0.643\,(3\,\mathrm{Ca})^{2/3}}{1 - 0.643\,(3\,\mathrm{Ca})^{2/3}\,y}\,\partial_y \star\right) \approx \frac{\partial_{yy}\star}{0.643^2\,(3\,\mathrm{Ca})^{4/3}}. \tag{A2b}$$

Appendix B: Velocity profile in the thin film

The velocity profile in the thin film is obtained following the classical Landau-Levich-Derjaguin-Bretherton theory, by means of the lubrication approximation, as shown in [3]. Specifically, the axial velocity u follows from the incompressible Stokes equation for a Newtonian free-surface film, while the transverse component v is obtained via the continuity equation [47], yielding the following dimensionless velocity components

$$u\,(\eta,\,y) = \frac{3\,y\,(\eta-1)\,(2\,\eta - y)}{2\,\eta^3}, \quad v\,(\eta,\,y) = \frac{y^2\,[(3-2\,\eta)\,y - 3\,\eta\,(2-\eta)]}{2\,\eta^4}\,\frac{\mathrm{d}\eta}{\mathrm{d}\xi}. \tag{B1}$$

These expressions fix a typo with respect to equations (A7) and (A8) in Picchi and Poesio [47], where a prefactor 3 (consistent with the axial stretching embedded in the definition of the small-scale parameter (2)) is missing. Figure 9 provides the streamline representation of the velocity field in the laboratory reference frame. Given the velocity profiles, the viscous dissipation function is computed analytically as

$$\Phi\,(\eta,\,y) = 2\,\varepsilon^2\left[\left(\frac{\partial\,u}{\partial\xi}\right)^2 + \left(\frac{\partial\,v}{\partial y}\right)^2\right] + \left(\frac{\partial\,u}{\partial y} + \varepsilon^2\frac{\partial\,v}{\partial\xi}\right)^2 = \left[\frac{3\,(\eta-1)\,(\eta-y)}{\eta^3}\right]^2 + \mathcal{O}(\varepsilon^2). \tag{B2}$$

Appendix C: Accuracy of the effective model

The one-dimensional effective model (34) is validated with the depth-averaged temperature (through the operator (20)) of the two-dimensional solution $\theta_{2\mathrm{D}}$ of the full energy balance equation (10). The latter is computed using

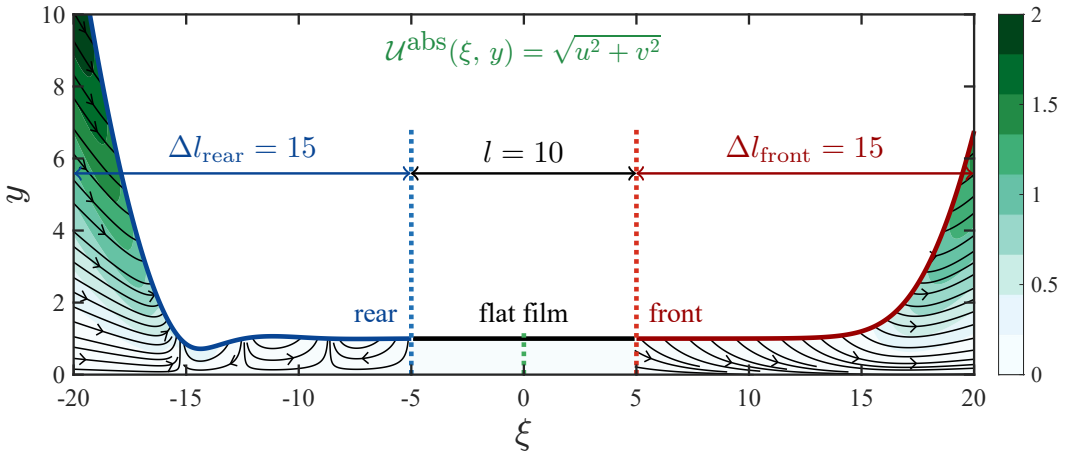

Figure 9. Streamlines in the laboratory reference frame and contours of the absolute velocity magnitude $\mathcal{U}^{\mathrm{abs}}$, see (B1).

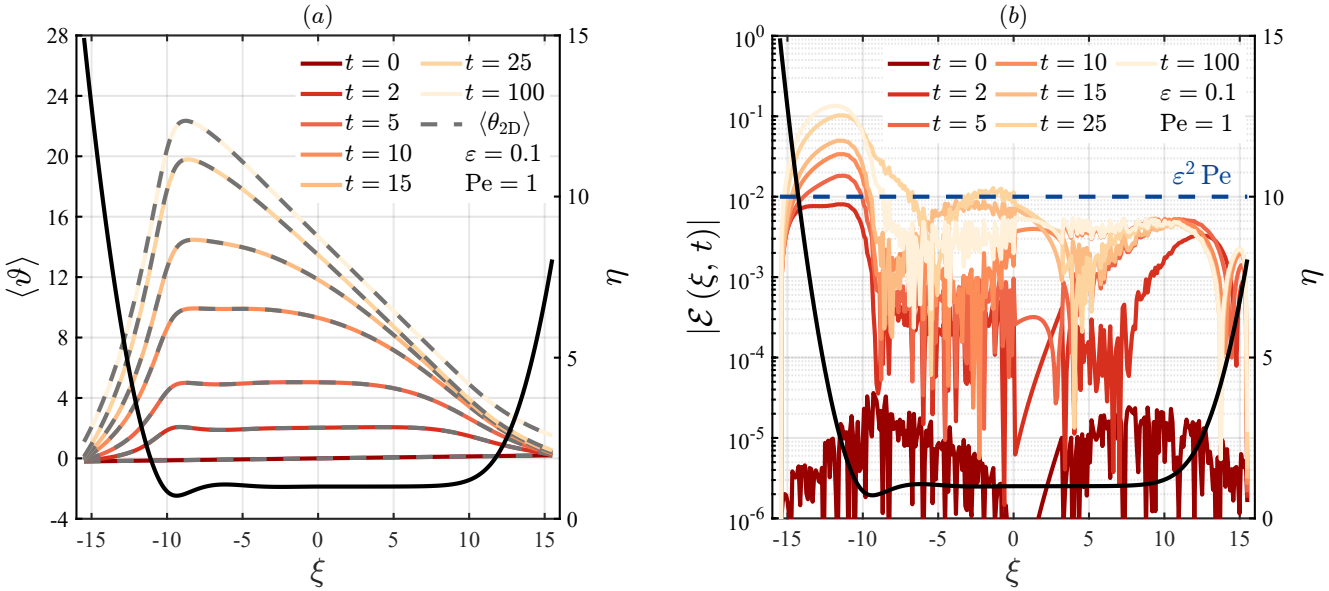

Figure 10. (a) Time evolution of the average film temperature $\langle\vartheta\rangle$ along a cylindrical tube ($m = 1$) under uniform heating ($\nu = -1$), obtained from the effective model (34) (solid lines) and the 2D full problem (10) (dashed grey lines: $\theta_{2\mathrm{D}}$) for $\mathrm{Pe} = 1$ and $\mathrm{Br} = 0$. (b) Absolute error $|\mathcal{E}(\xi, t)| = |\langle\theta_{2\mathrm{D}}\rangle - \langle\vartheta\rangle|$ corresponding to each pair of temperature profiles. The dashed horizontal blue line represents the theoretical error bound prescribed by homogenization with $\varepsilon = 0.1$. Right, meniscus profile $\eta(\xi)$ with $l = 0$.

the Finite Element Method (FEM) discretization scheme, implemented via MATLAB's built-in Partial Differential Equation Toolbox, `pdetool` [90]. The computational domain is delimited by four sides: the Dirichlet-type conditions (39) are imposed on the left and right boundaries; the Neumann condition (13) prescribing a uniform heat flux is applied at the bottom wall; and the adiabatic condition – corresponding to (15) in the limit of $\mathcal{K} \to 0$ – is enforced on each mesh element of the bubble fluid interface obtained solving (1) and discretizing it according to the mesh elements. The initial temperature field ($t \to 0$) is set to the linear profile (39), while the problem is solved in a reference frame attached to the bubble. The liquid film is represented using an adaptive triangular mesh composed of quadratic elements – with nodes at corners and edge centers – characterized by a maximum element height of 0.025 and a growth rate of 2, ensuring adequate resolution near the interface. A polygonal approximation is used to reconstruct the front and rear film domains, based on 301 uniformly spaced points along the longitudinal direction. To interpolate data from mesh nodes onto a rectangular Cartesian grid and perform transverse averaging, a uniform spatial resolution of $\Delta y \approx 2.5 \times 10^{-4}$ is used over the interval $[0; \max_\xi \eta]$. Consistent with our analysis in Sec. IV, the numerical simulations are performed at a fixed capillary number (i.e., $\varepsilon = 0.1$) and they are stopped when the

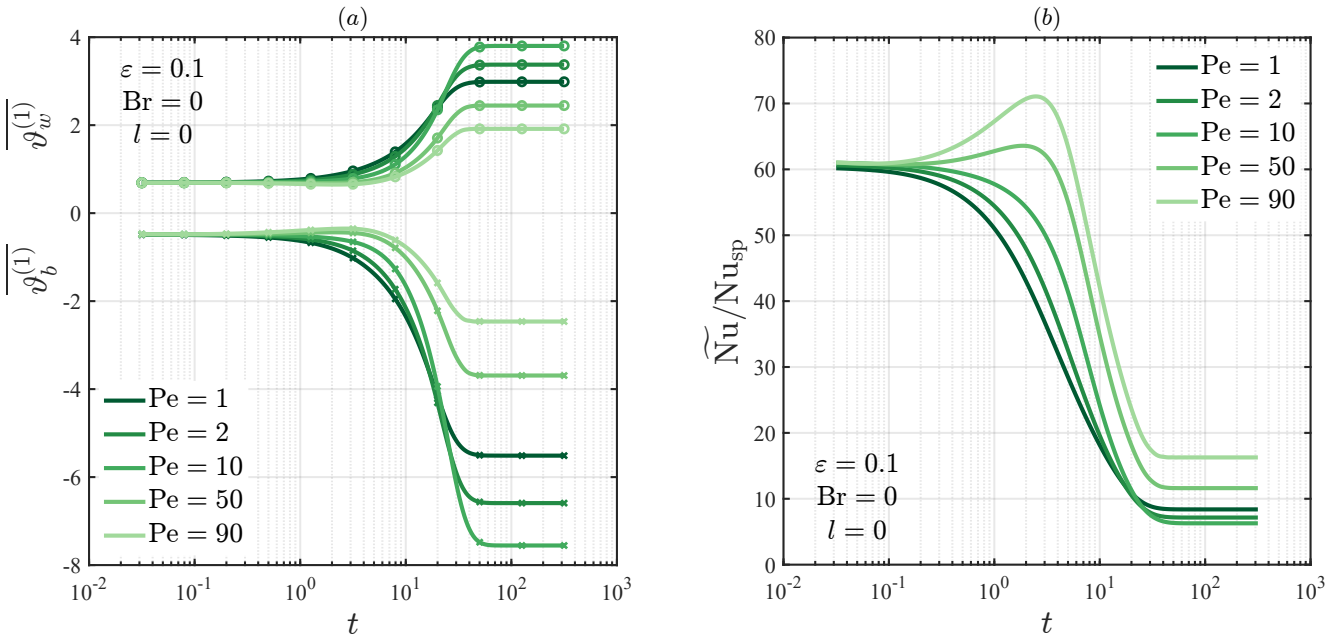

Figure 11. (a) Time evolution of the domain-averaged first-order corrections to the wall ('w') and bulk ('b') temperatures, and (b) averaged Nusselt number $\widetilde{\mathrm{Nu}}$ – see (D1) – relative to the single-phase value $\mathrm{Nu}_{\mathrm{sp}} = 48/11$ in a cylindrical tube ($m = 1$) under uniform flux heating ($\nu = -1$), for different values of the Péclet number Pe, neglecting the impact of viscous dissipation (Br $= 0$). The domain-average is performed over a distance $\ell = \Delta l_{\mathrm{front}} + \Delta l_{\mathrm{rear}} = 30$, with a negligible uniform film region ($l = 0$). Small-scale parameter: $\varepsilon = 0.1$.

temperature field reaches fully thermal development conditions, corresponding to a dimensionless time $t \sim 100$.

To evaluate the accuracy of the effective model, we introduce the absolute error $\mathcal{E}(\xi, t) \equiv \langle \theta_{2\mathrm{D}} \rangle - \langle \vartheta \rangle$ between the averaged fully resolved solution and its approximation obtained via the asymptotics. This metric is widely adopted to estimate the error introduced by the asymptotic expansions and unresolved high order terms [67, 91].

Figure 10 (a) compares the spatial evolution of the averaged fully resolved solution and its approximation obtained via two-scale expansions at fixed time instants choosing the lowest admissible Péclet number, Pe $= 1$, which gives the most stringent tolerance criteria. In fact, the upscaled solution is predictive of the small-scale behavior only if the absolute error remains bounded by the expansion parameter, i.e., $|\mathcal{E}| \lesssim \varepsilon^2\,\mathrm{Pe}$. As shown in panel ($a$), the averaged temperature profiles overlap at each time considered, indicating an excellent agreement between the full and the approximated solution. In panel (b), we analyze the spatial distribution of the absolute error along the bubble profile. The error remains bounded by $\varepsilon^2\,\mathrm{Pe}$ over most of the domain except for a small region in the bubble's rear where, at sufficiently high times, it locally exceeds this theoretical threshold ($-15 \lesssim \xi \lesssim -10$). This is attributed to a localized steepening of the temperature profile that makes the first derivative of the averaged temperature greater than the unity, i.e., $|\partial\langle\vartheta\rangle/\partial\xi| \gtrsim \mathcal{O}(1)$, amplifying the contribution of higher-order corrections in (29). We recall that an underlying hypothesis of methods based on two-scale asymptotics is that, after normalization, the derivatives remain of order one, but, as in this case, there may exist regions of the domain where this condition is not met. Despite this, the absolute error remains small, confirming the robustness and reliability of the approach, as shown in figure 10 (a).

Appendix D: Other definitions of the average Nusselt number

Since its definition is not unique, here, we discuss other definitions of the averaged Nusselt number that differ from the one obtained by averaging the local Nusselt number given in (48). Although, according to Newton's law of cooling, the local convective heat transfer coefficient at a solid boundary is defined as the ratio between the heat flux per unit area and a reference temperature difference, its spatial average varies from case to case.

For example, in the case of external flows (e.g., laminar and incompressible thermal boundary layer over a flat plate), such temperature difference is typically taken between the wall and the free-stream temperature. Then, the average heat transfer coefficient is defined as the mean flux normalized by the fixed temperature difference (in the

case of isothermal wall), or as the flux normalized by the mean temperature difference (in the uniform-flux case). In both cases, the averaged Nusselt number is not obtained by averaging the local Nusselt number [77, 92].

In contrast, in internal convection problems, the reference temperature difference is not uniquely defined and varies across experimental and numerical studies [93]. This ambiguity leads to different definitions of the Nusselt number, particularly in problems with non-isothermal boundaries [94]. The most common approach is to use the temperature difference between the tube wall and a the enthalpy-weighted average temperature, commonly known as the bulk or mixing-cup temperature [75, 95], see (41). Other definitions of temperature difference (e.g., wall-to-bulk, wall-to-inlet, mean wall-to-inlet, etc.) are usually guided by the application and the imposed boundary condition [29]. For example, in single-phase channel flow under uniform flux conditions the local Nusselt number varies only in the thermal entrance region, making the definition of the averaged Nusselt number as the integral of the local one not relevant outside the entrance region. In this case, in fact, an alternative formulation of the mean Nusselt number based on a domain-averaged temperature difference is usually adopted. In other words, instead of averaging the local Nusselt number over the spatial domain as in (48), the strategy is to divide the flux by the difference between the domain-averaged wall temperature and the domain-averaged bulk temperature.

This idea has been borrowed from many works in the context of slug and Taylor flows, where researchers have been using averaged wall and bulk temperatures [96, 97], to define the averaged Nusselt number over a representative unit cell (e.g., 40, 78, 79, 87). Specifically, the Nusselt number obtained from the averaged temperature difference reads

$$\widetilde{\mathrm{Nu}} = -\frac{2\,(2-m)}{0.643\,(3\,\mathrm{Ca})^{2/3}}\,\frac{\nu}{\overline{\vartheta_w^{(1)}}-\overline{\vartheta_b^{(1)}}}, \quad \text{with} \quad \begin{cases} \overline{\vartheta_w^{(1)}} \equiv \dfrac{1}{\ell}\displaystyle\int_\ell \vartheta_w^{(1)}\,\mathrm{d}\xi, \\ \overline{\vartheta_b^{(1)}} \equiv \dfrac{\int_\ell \int_0^\eta u\,\vartheta_b^{(1)}\mathrm{d}y\,\mathrm{d}\xi}{\int_\ell \int_0^\eta u\,\mathrm{d}y\,\mathrm{d}\xi}, \end{cases} \tag{D1}$$

where, in analogy with (47), the overline denotes a domain average performed over a longitudinal distance $\ell = \Delta l_{\mathrm{rear}} + l + \Delta l_{\mathrm{front}}$. The domain-averaged first-order corrections to the wall and bulk temperatures are shown in figure 11 (a) and their final values vary non-monotonically with the Péclet number, increasing for the bulk and decreasing for the wall in the sequence $\mathrm{Pe} = (10,\ 2,\ 1,\ 50,\ 90)$. Accordingly, the $\widetilde{\mathrm{Nu}}$ normalized by the single-phase reference value for a cylindrical tube $\mathrm{Nu_{sp}} = 48/11 \approx 4.36$ is shown in figure 11 (b). The Nusselt number decreases monotonically in the diffusion-dominated regimes, while for $\mathrm{Pe} > 50$ it displays a non-monotonic trend with an intermediate maximum before reaching thermally fully developed conditions. Specifically, the final value indicates a heat-transfer enhancement ranging from 6 to 16 times with respect to single-phase flow.

An alternative formulation has been proposed by [98] as a time-averaged local Nusselt number based on wall and bulk temperatures averaged over the recirculation period, motivated by the periodicity of Taylor flow in a reference frame attached to the bubble. This definition has been reported to facilitate the comparison between numerical simulations and experimental data since it is easier to measure averaged quantities along a channel segment than knowing the local wall temperature field [99]. It is worth mentioning that the detailed analysis of these alternative formulations of the Nusselt number falls outside the scope of our work.

[1] P. Angeli and A. Gavriilidis, Hydrodynamics of Taylor flow in small channels: A review, Proceedings of the Institution of Mechanical Engineers, Part C: Journal of Mechanical Engineering Science **222**, 737–751 (2008).

[2] G. I. Taylor, Deposition of a viscous fluid on the wall of a tube, Journal of Fluid Mechanics **10**, 161 (1961).

[3] F. P. Bretherton, The motion of long bubbles in tubes, Journal of Fluid Mechanics **10**, 166 (1961).

[4] P. Griffith and G. B. Wallis, Two-phase slug flow, Journal of Heat Transfer **83**, 307 (1961).

[5] R. A. S. Brown, The mechanics of large gas bubbles in tubes: I. Bubble velocities in stagnant liquids, The Canadian Journal of Chemical Engineering **43**, 217 (1965).

[6] R. M. Davies and G. I. Taylor, The mechanics of large bubbles rising through extended liquids and through liquids in tubes, Proceedings of the Royal Society of London. Series A. Mathematical and Physical Sciences **200**, 375 (1950).

[7] R. Gupta, S. S. Y. Leung, R. Manica, D. F. Fletcher, and B. S. Haynes, Hydrodynamics of liquid-liquid Taylor flow in microchannels, Chemical Engineering Science **92**, 180 (2013).

[8] R. Abiev, Analysis of hydrodynamics and mass transfer of gas-liquid and liquid-liquid taylor flows in microchannels: Theoretical approach and experimental proofs, in *Process Analysis, Design, and Intensification in Microfluidics and Chemical Engineering* (IGI Global, 2019) p. 1–49.

[9] X. Zhang and V. S. Nikolayev, Physics and modeling of liquid films in pulsating heat pipes, Physical Review Fluids **8**, 084002 (2023).

[10] M. Abela, M. Mameli, S. Filippeschi, and V. S. Nikolayev, Experimental and numerical studies of the pulsating heat pipe stopover regime, International Journal of Heat and Mass Transfer **247**, 127102 (2025).

[11] S. S. Mehendale, A. M. Jacobi, and R. K. Shah, Fluid flow and heat transfer at micro- and meso-scales with application to heat exchanger design, Applied Mechanics Reviews **53**, 175 (2000).

[12] J. R. Thome, Boiling in microchannels: a review of experiment and theory, International Journal of Heat and Fluid Flow **25**, 128–139 (2004).

[13] M. B. Darshan, M. Magnini, and O. K. Matar, Numerical modelling of flow boiling inside microchannels: A critical review of methods and applications, Applied Thermal Engineering **257**, 124464 (2024).

[14] I. Mudawar and M. B. Bowers, Ultra-high critical heat flux (CHF) for subcooled water flow boiling - i: CHF data and parametric effects for small diameter tubes, International Journal of Heat and Mass Transfer **42**, 1405 (1999).

[15] G. Wang, P. Cheng, and A. E. Bergles, Effects of inlet/outlet configurations on flow boiling instability in parallel microchannels, International Journal of Heat and Mass Transfer **51**, 2267 (2008).

[16] J. R. Thome, V. Dupont, and A. M. Jacobi, Heat transfer model for evaporation in microchannels. Part i: presentation of the model, International Journal of Heat and Mass Transfer **47**, 3375–3385 (2004).

[17] V. Dupont, J. R. Thome, and A. M. Jacobi, Heat transfer model for evaporation in microchannels. Part ii: comparison with the database, International Journal of Heat and Mass Transfer **47**, 3387–3401 (2004).

[18] S. Szczukiewicz, M. Magnini, and J. R. Thome, Proposed models, ongoing experiments, and latest numerical simulations of microchannel two-phase flow boiling, International Journal of Multiphase Flow **59**, 84 (2014).

[19] M. Magnini, B. Pulvirenti, and J. R. Thome, Numerical investigation of hydrodynamics and heat transfer of elongated bubbles during flow boiling in a microchannel, International Journal of Heat and Mass Transfer **59**, 451 (2013).

[20] F. Municchi, I. El Mellas, O. K. Matar, and M. Magnini, Conjugate heat transfer effects on flow boiling in microchannels, International Journal of Heat and Mass Transfer **195**, 123166 (2022).

[21] X. Zhang and V. S. Nikolayev, Dewetting acceleration by evaporation, Journal of Fluid Mechanics **948**, A49 (2022).

[22] C. Tecchio, X. Zhang, B. Cariteau, G. Zalczer, P. Roca i Cabarrocas, P. Bulkin, J. Charliac, S. Vassant, and V. S. Nikolayev, Microlayer in nucleate boiling seen as landau–levich film with dewetting and evaporation, Journal of Fluid Mechanics **989**, A4 (2024).

[23] X. Zhang, I. El Mellas, and M. Magnini, Predicting initial microlayer thickness in nucleate boiling using landau–levich theory, Journal of Fluid Mechanics **997**, A44 (2024).

[24] X. Zhang, I. El Mellas, N. Andreini, and M. Magnini, The microlayer and force balance of bubbles growing on solid in nucleate boiling, International Journal of Multiphase Flow **183**, 105049 (2025).

[25] X. Zhang, I. El Mellas, N. Andreini, and M. Magnini, The microlayer and force balance of bubbles growing on solid in nucleate boiling, International Journal of Multiphase Flow **183**, 105049 (2025).

[26] A. Bar-Cohen, M. Arik, and M. Ohadi, Direct liquid cooling of high flux micro and nano electronic components, Proceedings of the IEEE **94**, 1549 (2006).

[27] T. Bandara, N.-T. Nguyen, and G. Rosengarten, Slug flow heat transfer without phase change in microchannels: A review, Chemical Engineering Science **126**, 283–295 (2015).

[28] R. Gupta, D. F. Fletcher, and B. S. Haynes, Taylor flow in microchannels: A review of experimental and computational work, The Journal of Computational Multiphase Flows **2**, 1 (2010).

[29] Y. S. Muzychka, E. J. Walsh, and P. Walsh, Heat transfer enhancement using laminar gas-liquid segmented plug flows, Journal of Heat Transfer **133**, 10.1115/1.4002807 (2011).

[30] V. Talimi, Y. S. Muzychka, and S. Kocabiyik, Numerical simulation of the pressure drop and heat transfer of two phase slug flows in microtubes using moving frame of reference technique, International Journal of Heat and Mass Transfer **55**, 6463–6472 (2012).

[31] A. Etminan and Y. S. Muzychka, Effects of flow characteristics on the heat transfer mechanism in Taylor flow, International Journal of Heat and Mass Transfer **219**, 124917 (2024).

[32] D. R. Oliver and S. J. Wright, Pressure drop and heat transfer in gas-liquid slug flow in horizontal tubes, British Chemical Engineering **9**, 590 (1964).

[33] G. A. Hughmark, Holdup and heat transfer in horizontal slug gas-liquid flow, Chemical Engineering Science **20**, 1007 (1965).

[34] P. A. Walsh, E. J. Walsh, and Y. S. Muzychka, Heat transfer model for gas–liquid slug flows under constant flux, International Journal of Heat and Mass Transfer **53**, 3193–3201 (2010).

[35] S. S. Y. Leung, Y. Liu, D. F. Fletcher, and B. S. Haynes, Heat transfer in well-characterised Taylor flow, Chemical Engineering Science **65**, 6379–6388 (2010).

[36] M. T. Kreutzer, P. Du, J. J. Heiszwolf, F. Kapteijn, and J. A. Moulijn, Mass transfer characteristics of three-phase monolith reactors, Chemical Engineering Science **56**, 6015 (2001).

[37] Z. Dai, Z. Guo, D. F. Fletcher, and B. S. Haynes, Taylor flow heat transfer in microchannels - Unification of liquid–liquid and gas–liquid results, Chemical Engineering Science **138**, 140–152 (2015).

[38] L. Graetz, Ueber die Wärmeleitungsfähigkeit von Flüssigkeiten (On the thermal conductivity of liquids), Annalen der Physik **254**, 79–94 (1882).

[39] A. Lévêque, *Les Lois de la transmission de chaleur par convection* (Dunod, 1928) p. 193.

[40] Z. Che, T. N. Wong, and N.-T. Nguyen, Heat transfer in plug flow in cylindrical microcapillaries with constant surface heat flux, International Journal of Thermal Sciences **64**, 204 (2013).

[41] G. I. Taylor, Dispersion of soluble matter in solvent flowing slowly through a tube, Proceedings of the Royal Society of London. Series A. Mathematical and Physical Sciences **219**, 186 (1953).

[42] R. Aris, On the dispersion of a solute in a fluid flowing through a tube, Proceedings of the Royal Society of London. Series A. Mathematical and Physical Sciences **235**, 67 (1956).

[43] D. G. Levitt, Capillary-tissue exchange kinetics: An analysis of the Krogh cylinder model, Journal of Theoretical Biology **34**, 103–124 (1972).

[44] H. Brenner and K. Stewartson, Dispersion resulting from flow through spatially periodic porous media, Philosophical Transactions of the Royal Society of London. Series A, Mathematical and Physical Sciences **297**, 81 (1980).

[45] J. Rubinstein and R. Mauri, Dispersion and convection in periodic porous media, SIAM Journal on Applied Mathematics **46**, 1018 (1986).

[46] J.-L. Auriault and J. Lewandowska, Diffusion/adsorption/advection macrotransport in soils, European Journal of Mechanics A-solids **15**, 681 (1996).

[47] D. Picchi and P. Poesio, Dispersion of a passive scalar around a Taylor bubble, Journal of Fluid Mechanics **951**, A22 (2022).

[48] R. P. Batycky, D. A. Edwards, and H. Brenner, Thermal Taylor dispersion in an insulated circular cylinder - i. Theory, International Journal of Heat and Mass Transfer **36**, 4317 (1993).

[49] R. P. Batycky, D. A. Edwards, and H. Brenner, Thermal Taylor dispersion phenomena in nondiabatic systems, Chemical Engineering Communications **130**, 53–104 (1994).

[50] A. Liñán, P. Rajamanickam, A. D. Weiss, and A. L. Sánchez, Taylor-diffusion-controlled combustion in ducts, Combustion Theory and Modelling **24**, 1054–1069 (2020).

[51] P. Botticini, D. Picchi, and P. Poesio, Forced convection in two-phase core-annular flows, Journal of Fluid Mechanics **1011**, A41 (2025).

[52] J. G. Collier and J. R. Thome, *Convective Boiling and Condensation* (Oxford University Press, 1994).

[53] D. Picchi and I. Battiato, The impact of pore-scale flow regimes on upscaling of immiscible two-phase flow in porous media, Water Resources Research **54**, 6683 (2018).

[54] D. Picchi, A. Ullmann, and N. Brauner, Modeling of core-annular and plug flows of Newtonian/non-Newtonian shear-thinning fluids in pipes and capillary tubes, International Journal of Multiphase Flow **103**, 43–60 (2018).

[55] P.-G. de Gennes, F. Brochard-Wyart, and D. Quéré, *Capillarity and Wetting Phenomena: Drops, Bubbles, Pearls, Waves* (Springer New York, 2003).

[56] H. A. Stone, Interfaces: in fluid mechanics and across disciplines, Journal of Fluid Mechanics **645**, 1–25 (2010).

[57] D. Picchi, A. Ullmann, N. Brauner, and P. Poesio, Motion of a confined bubble in a shear-thinning liquid, Journal of Fluid Mechanics **918**, A7 (2021).

[58] R. K. Shah and A. L. London, *Laminar Flow Forced Convection in Ducts* (Elsevier BV, 1978).

[59] K. Chen, R. M. Cotta, C. P. Naveira-Cotta, and P. C. Pontes, Heat transfer analysis of compressible laminar flow in a parallel-plates channel via integral transforms, International Communications in Heat and Mass Transfer **138**, 106368 (2022).

[60] P. J. Murphy, S. Alimohammadi, and S. M. O'Shaughnessy, Experimental investigation of dual jet flow past a heated surface: Effect of Reynolds number, International Journal of Heat and Mass Transfer **218**, 124786 (2024).

[61] C. J. van Duijn, A. Mikelić, I. S. Pop, and C. Rosier, Effective dispersion equations for reactive flows with dominant Péclet and Damköhler numbers, in *Advances in Chemical Engineering*, Advances in Chemical Engineering, Vol. 34, edited by G. B. Marin, D. West, and G. S. Yablonsky (Academic Press, 2008) pp. 1–45.

[62] I. Battiato and D. M. Tartakovsky, Applicability regimes for macroscopic models of reactive transport in porous media, J. Contam. Hydrol. **120-121**, 18 (2011).

[63] B. Ling, A. M. Tartakovsky, and I. Battiato, Dispersion controlled by permeable surfaces: surface properties and scaling, Journal of Fluid Mechanics **801**, 13–42 (2016).

[64] R. Mauri, Heat and mass transport in random velocity fields with application to dispersion in porous media, Journal of Engineering Mathematics **29**, 77–89 (1995).

[65] J. Wloka, *Partial Differential Equations* (Cambridge University Press, 1987).

[66] R. Mauri, Heat and mass transport in nonhomogeneous random velocity fields, Phys. Rev. E **68**, 066306 (2003).

[67] R. Mauri, Dispersion, convection, and reaction in porous media, Physics of Fluids A: Fluid Dynamics **3**, 743–756 (1991).

[68] C. C. Mei and B. Vernescu, *Homogenization Methods for Multiscale Mechanics* (World Scientific, 2010).

[69] A. Mikelić, V. Devigne, and C. J. van Duijn, Rigorous upscaling of the reactive flow through a pore, under dominant Péclet and Damköhler numbers, SIAM Journal on Mathematical Analysis **38**, 1262 (2006).

[70] M. Van Dyke, *Perturbation Methods in Fluid Mechanics*, Applied mathematics and mechanics, Vol. 8 (Academic Press, 1964).

[71] F. Feuillebois and A. Lasek, Computer aided application of the principle of least degeneracy, Zeitschrift für angewandte Mathematik und Physik ZAMP **28**, 1141–1146 (1977).

[72] G. L. Richard, C. Ruyer-Quil, and J. P. Vila, A three-equation model for thin films down an inclined plane, Journal of Fluid Mechanics **804**, 162–200 (2016).

[73] H. Brenner and D. A. Edwards, *Macrotransport processes* (Butterworth-Heinemann, 1993).

[74] R. D. Skeel and M. Berzins, A method for the spatial discretization of parabolic equations in one space variable, SIAM Journal on Scientific and Statistical Computing **11**, 1 (1990).

[75] F. P. Incropera, *Fundamentals of Heat and Mass Transfer* (Wiley, 2007).

[76] S. Kjelstrup, D. Bedeaux, E. Johannessen, and J. Gross, *Non-equilibrium Thermodynamics for Engineers*, 2nd ed. (World Scientific, 2017).

[77] A. Bejan, *Heat Transfer* (John Wiley and Sons, New York, 1993) p. 704.

[78] R. Gupta, D. F. Fletcher, and B. S. Haynes, CFD modelling of flow and heat transfer in the Taylor flow regime, Chemical Engineering Science **65**, 2094 (2010).

[79] A. N. Asadolahi, R. Gupta, D. F. Fletcher, and B. S. Haynes, CFD approaches for the simulation of hydrodynamics and heat transfer in Taylor flow, Chemical Engineering Science **66**, 5575–5584 (2011).
[80] F. Boso and I. Battiato, Homogenizability conditions for multicomponent reactive transport, Advances in Water Resources **62**, 254 (2013).
[81] B. Ling, M. Oostrom, A. M. Tartakovsky, and I. Battiato, Hydrodynamic dispersion in thin channels with micro-structured porous walls, Physics of Fluids **30**, 076601 (2018).
[82] B. Ling, C. B. Rizzo, I. Battiato, and F. P. J. de Barros, Macroscale transport in channel-matrix systems via integral transforms, Physical Review Fluids **6**, 044501 (2021).
[83] M. Magnini and M. A. Herrada, Two-dimensional global stability analysis of elongated bubbles moving in a horizontal tube, Phys. Rev. Fluids **10**, 053603 (2025).
[84] M. Magnini and J. R. Thome, An updated three-zone heat transfer model for slug flow boiling in microchannels, International Journal of Multiphase Flow **91**, 296–314 (2017).
[85] E. Baird and K. Mohseni, Digitized heat transfer: A new paradigm for thermal management of compact micro systems, IEEE Transactions on Components and Packaging Technologies **31**, 143 (2008).
[86] A. Fershtman, L. Shemer, and D. Barnea, Instantaneous heat transfer rate around consecutive Taylor bubbles, International Journal of Heat and Mass Transfer **95**, 865 (2016).
[87] Z. Che, T. N. Wong, and N.-T. Nguyen, Heat transfer enhancement by recirculating flow within liquid plugs in microchannels, International Journal of Heat and Mass Transfer **55**, 1947 (2012).
[88] H. Schlichting, *Boundary Layer Theory* (Pergamon Press, London, 1955).
[89] C. M. Bender and S. A. Orszag, *Advanced Mathematical Methods for Scientists and Engineers I: Asymptotic Methods and Perturbation Theory* (Springer, New York, 1999).
[90] The MathWorks, Inc., *Partial Differential Equation Toolbox™ User's Guide*, The MathWorks, Inc., Natick, MA, USA (2025).
[91] Y. Z. Ma, Introduction to model upscaling, validation and history match, in *Quantitative Geosciences: Data Analytics, Geostatistics, Reservoir Characterization and Modeling* (Springer International Publishing, Cham, 2019) pp. 565–591.
[92] J. H. I. Lienhard and J. H. V. Lienhard, *A Heat Transfer Textbook*, 5th ed. (Phlogiston Press, Cambridge, Massachusetts, 2019).
[93] A. Vangeffelen, G. Buckinx, C. De Servi, M. R. Vetrano, and M. Baelmans, Nusselt number for steady periodically developed heat transfer in micro- and mini-channels with arrays of offset strip fins subject to a uniform heat flux, International Journal of Heat and Mass Transfer **195**, 123145 (2022).
[94] M. Bhattacharya and T. Basak, On the definition of Nusselt number for convection within enclosures involving isothermal and non-isothermal walls, International Communications in Heat and Mass Transfer **169**, 109416 (2025).
[95] W. M. Deen, *Analysis of Transport Phenomena* (OUP USA, New York, 1998) p. 618.
[96] K. Fukagata, N. Kasagi, P. Ua-arayaporn, and T. Himeno, Numerical simulation of gas–liquid two-phase flow and convective heat transfer in a micro tube, International Journal of Heat and Fluid Flow **28**, 72–82 (2007).
[97] Q. He, Y. Hasegawa, and N. Kasagi, Heat transfer modelling of gas–liquid slug flow without phase change in a micro tube, International Journal of Heat and Fluid Flow **31**, 126 (2010).
[98] S. Kumari, N. Kumar, and R. Gupta, Flow and heat transfer in slug flow in microchannels: Effect of bubble volume, International Journal of Heat and Mass Transfer **129**, 812 (2019).
[99] A. Mehdizadeh, S. A. Sherif, and W. E. Lear, Numerical simulation of thermofluid characteristics of two-phase slug flow in microchannels, International Journal of Heat and Mass Transfer **54**, 3457 (2011).

Paper III

P. Botticini, D. Picchi, S. Sinha and A. Hansen, *Origin of pressure-flow non-linearity in two-phase intermittent flow in porous media*, submitted to *Physical Review Fluids*, Oct. 2025. arXiv: 2510.12588 [physics.flu-dyn]

In the previous paper, the heat transfer analysis was built around the classical scaling law that relates the characteristic film thickness to the capillary number with a two-thirds power dependence. In the present study, we turn to a different nonlinearity governed by the same exponent: the relationship between the tip-to-tip pressure drop across an elongated bubble and the capillary number. Our investigation demonstrates how bubble-induced pressure losses shape the effective rheological response of a segmented flow characterised by wetting liquid films. Through coalescence, this configuration can evolve towards the core–annular limit examined in the first work. When embedded in a heterogeneous porous domain, the resulting ganglia dynamics extend the reduced-order modelling framework beyond thermal transport, encompassing multiphase flow behaviour in porous media.

Origin of pressure-flow non-linearity in two-phase intermittent flow in porous media

Paolo Botticini,[1,2,*] Davide Picchi,[2] Santanu Sinha,[1] and Alex Hansen[1]

[1] *PoreLab, Department of Physics, Norwegian University of Science and Technology NTNU, N-7491 Trondheim, Norway*
[2] *Department of Mechanical and Industrial Engineering, Università degli Studi di Brescia, Brescia 25123, Italy*

(Dated: October 15, 2025)

This study presents a first-principles model to predict the two-phase pressure drop in gas–liquid intermittent flow through round capillaries, which serve as the simplest analogous of a porous medium. We derive a model for a train of elongated bubbles, and rigorously quantify its validity in terms of the dimensionless parameters of the problem (capillary number, number of bubbles, gas volume fraction, and channel length-to-diameter ratio). Our model is built upon the classical theory by Bretherton, with the extensions of Aussillous and Quéré and Balestra *et al.*, to account for film-induced lubrication effects, the interplay between viscous and capillary forces in the thin-film, and the jump in viscous normal stresses.

The total two-phase pressure drop is found to be non-linear with respect to the mean liquid slug velocity, varying in discrete steps due to its explicit dependence on the number of bubbles, and also influenced by the motion of both phases. Moreover, formulating the model in dimensionless terms reveals key scaling laws that govern the two-phase flow rheology. Perturbation theory shows that a single bubble induces an excess pressure drop in a liquid-filled slender channel, enabling the introduction of a pressure-dependent effective viscosity to describe the system.

Finally, our analytical framework is extended from a single capillary to a bundle of cylindrical tubes. In nearly homogeneous bundles, inviscid bubble trains exhibit a smooth transition from a Bretherton-like regime with an apparent flow exponent of 2/3 at low pressure drops to weaker sub-linear regimes (with exponents between 2/3 and 1) as the pressure drop increases. Introducing the smallest pores disrupts the monotonic scaling of the flow exponent, reflecting a more complex rheological response. Deviations in two-phase flow behavior from the Darcy law are examined across the model parameter space and in relation to geometrical heterogeneity, offering new insights into pore-scale multiphase transport.

* Contact author: p.botticini@studenti.unibs.it

CONTENTS

I. INTRODUCTION

Two-phase transport processes in porous materials are central to numerous areas of science [1, 2], including hydrogeology and oil recovery, reservoir and biomechanical engineering, design of fuel cells and other industrial devices [3]. For example, suspensions of air bubbles in water have been used to enhance bioremediation by introducing oxygen into groundwater [4], as well as to remove volatile organic compounds from contaminated soils [5]. In these systems, the dispersed gas phase alters the flow within individual pores, thereby influencing macroscopic transport properties such as hydraulic conductivity.

In capillaries, gas–liquid mixtures preferentially adopt a plug-train configuration, referred to as Taylor (or segmented, intermittent) flow, where elongated bullet-shaped bubbles are separated by liquid slugs and surrounded by a thin lubricating film [6, 7]. This flow pattern is largely controlled by the dominance of surface tension over viscous effects (i.e., low capillary numbers), which inhibits alternative regimes typical of larger channels, such as bubbly or stratified flows [8]. Under these conditions, commonly encountered in most microfluidic applications, the pressure drop over a bubble is significant compared to the continuous phase [9], and well-established theoretical frameworks for predicting the two-phase pressure drop – such as the Lockhart-Martinelli-Chisholm correlation [10–12] and the homogeneous-type approach [13–15] – prove inadequate.

Such inaccuracy stems primarily from neglecting essential physical mechanisms, namely surface tension phenomena and the complex hydrodynamic features of Taylor flow, such as phase and velocity distributions [16]. In fact, the incomplete displacement of the wetting phase by the non-wetting discontinuous phase [17] results in a thin lubricating film around the bubble which makes the pressure drop analysis more challenging.

Research into bubble formation in a continuous phases traces back to Rayleigh's analysis of jet breakup [18] and Taylor's subsequent studies on the stability of fluid interfaces [19]. Taylor [20] later postulated that the key hydrodynamic features of capillary slug flow was the emergence of internal recirculation within the slugs. In the same years, Bretherton [21] investigated the motion of a long inviscid bubble displacing a viscous liquid in a capillary tube in absence of inertial and gravitational forces, using lubrication theory to describe the flow near the menisci. Specifically, between the hemispherical bubble caps, the thin film is governed by the interplay of viscous and capillary forces, and, through asymptotic matching, Bretherton [21] obtained an estimate for the film thickness. He also derived an expression for the pressure drop across the thin film and the additional jumps at the front and rear menisci, ultimately yielding the total pressure drop across the bubble. Although Bretherton's theory [21] agrees satisfactorily with the experimental data of Taylor [20] only in the limit of low capillary numbers, its range of validity has been extended up to capillary numbers of order unity by Aussillous and Quéré [22], who proposed an *ad hoc* polynomial ratio with a fitting parameter to model the film thickness.

Later on, Bretherton's framework [21] has been extended to describe bubble train in smooth capillaries and bead packs [23, 24]. These models assume joint motion of the gas, the separating liquid slugs, and the wetting films at a common velocity, enabling a pseudohomogeneous single-phase representation of the mixture – as a chain of bubbles separated by liquid lamellae – treated as a Darcy flow driven by an applied pressure gradient [25]. A critical limitation of this oversimplified picture is its lack of consideration for the velocity mismatch between the gas bubbles and the surrounding liquid. In reality, bubbles advance slightly faster than the wetting phase, as revealed by a simple mass balance, see Refs. [7, 26] for instance. As the film becomes thinner, the velocity difference between the phases diminishes; however, in most practical cases, this speed discrepancy remains non-negligible. Given the significantly higher viscosity of the liquid phase relative to the gas, even small differences in phase velocities can result in appreciable changes in the apparent gas viscosity [25].

Despite its foundational value, Bretherton's work [21] is rarely mentioned in studies of gas–liquid pressure drop in small channels (see, for example, Sec. 7 in Etminan *et al.* [27], for an exhaustive review). An exception is the semi-empirical model by Kreutzer *et al.* [28], which decomposes the total pressure drop in Taylor flow into two main contributions: (i) frictional losses in the liquid slugs, and (ii) the capillary pressure jumps near the bubble caps, based on Bretherton's result for an isolated gas bubble [21]. This model treats Taylor flow as a perturbation of fully developed Hagen–Poiseuille flow within the slugs, where the presence of gas bubbles induces an excess pressure drop. However, its dependence on Bretherton's analysis [21] restricts its validity to very thin liquid films (or equivalently vanishing capillary numbers).

To address these limitations, Warnier *et al.* [16] introduced three key improvements building on Kreutzer *et al.*'s model [28]: (i) combining Bretherton's asymptotic results [21] with the scaling analysis of Aussillous and Quéré [22], (ii) basing the computations on the actual gas bubble velocity, and (iii) accounting for a more detailed description of the bubble volume. However, the authors proposed an empirical adaptation of the capillary pressure drop correlation – based on the film thickness saturation mechanism described by Aussillous and Quéré [22] – which is not supported by theoretical justification. In addition, since their analysis is formulated in dimensional form, the identification of relevant scaling laws remains an open question in the community, representing a limitation especially critical in the context of porous media.

The motion of bubbles in straight tubes is frequently used as a proxy for understanding two-phase transport processes at the pore-scale [29]. Although this idealized geometry is a clear oversimplification of real porous structures, it still offers valuable insights into the fundamental hydrodynamic mechanisms at play [30]. Building on this idea, Stark and Manga [31] numerically investigated the motion of discrete non-wetting bubbles through a network of parallel straight tubes under an imposed flow rate, aiming to evaluate the effective permeability and the mean residence time of the bubbles. Bretherton's theory [21] was incorporated to account for both the capillary pressure drop and the velocity difference between phases. However, their simulations suffer from several limitations. First, the analytical treatment is restricted to low gas volume fractions and presumes a uniform bubble size distribution. Moreover, instead of explicitly adopting a non-linear pressure–flow rate law, the authors retain the formalism of a linear relationship by introducing a pressure-dependent conductivity matrix. As a result, the authors preserve the electrical analogy of the network [32] by employing a modified Kirchhoff law, which requires iterative solution algorithms and introduces numerical challenges, such as convergence issues and constraints on the network size.

The evolution of phase topology, governed by flow conditions, plays a central role in immiscible displacement within porous media. Specifically, as the capillary number increases, a threefold transition in flow connectivity is observed: from quasi-static disconnected pathways, to ganglion mobilization, and ultimately to viscous-dominated connected pathways [33, 34]. To overcome the challenges of formal upscaling in systems with convoluted phase topology [35], Picchi and Battiato [36] mapped the observed configurations onto idealized flow patterns: from capillary bundles at low capillary numbers to core-annular structures at high capillary numbers. This conceptual framework has been extended to scenarios typical of geothermal reservoirs [37], where it captures the scaling of relative permeabilities with flow conditions and is consistent with experimental observations. However, while the authors bridge the intermediate regime between these two limiting cases with a heuristic model for relative permeability, a physically grounded framework that robustly captures the transitional behavior of the flow has yet to be established [38]. In porous media, the combined flow of two immiscible Newtonian fluids under steady-state conditions may be described via a power-law relationship between the applied pressure drop (net of a possible threshold pressure) and the resulting volumetric flow rate [39], i.e., $\Delta p - \Delta p_t \propto Q^{\zeta}$ where $\zeta \in (0; 1)$ is an exponent reflecting the gradual mobilization of fluid interfaces at intermediate flow rates (see Sec. IV B). The value of ζ quantifies the transition from standard linear Darcy behavior ($\zeta = 1$) [40], which corresponds to simultaneous percolation of both phases, to a non-linear regime emerging at moderate capillary numbers due to evolving flow topology [41]. Although numerous studies have addressed this issue, as outlined in Tab. I, a comprehensive quantification of ζ is still lacking, and a clear physical interpretation of its dependence on flow conditions remains elusive.

Authors	**Method**	**Wetting & nonwetting phase**	**Threshold**	**Power-law exponent**
Tallakstad *et al.* [42, 43]	E	glycerin/water & air	no	0.54 ± 0.08
Rassi *et al.* [44, 45]	E	water & air	no	$0.3 - 0.45$
Sinha and Hansen [46]	T, N	-	yes	0.5
Yiotis *et al.* [47]	N (†)	water & NAPLs	yes	0.5
Aursjø *et al.* [48]	E	glycerin/water & rapeseed oil	no	0.67 ± 0.05, 0.74 ± 0.05
Chevalier *et al.* [49]	E	water & n-heptane	no	0.65 ± 0.1
Sinha *et al.* [50]	E, N	water & air	yes	$0.46 \pm 0.05 - 0.54 \pm 0.03$
Roy *et al.* [51]	T, N	-	yes	1/2 or 2/3
Yiotis *et al.* [52]	N (†)	water & oil	yes	2/3
Gao *et al.* [41]	E	water & oil	no	0.60 ± 0.01
Fyhn *et al.* [53]	T, N	-	yes	1/2 or 2/3
Roy *et al.* [54]	T, N	-	yes	1/2 or 2/3
Zhang *et al.* [55]	E	KI brine & n-decane	yes	$0.44 \pm 0.02 - 0.74 \pm 0.02$
Zhang *et al.* [56]	E	KI brine & n-decane	yes	$0.50 \pm 0.01 - 0.58 \pm 0.01$
Fyhn *et al.* [57]	N	-	both	$0.39 - 0.45$
Anastasiou *et al.* [58]	E	water & n-heptane	no	$0.714 - 1$

Table I. Summary of theoretical (T), numerical (N), and experimental (E) studies on the effective rheology of Newtonian two-phase flow in porous media. The pairs of wetting and non-wetting fluids are reported, along with an indication of whether a capillary threshold pressure Δp_t is included in the model (yes/no/both), and the corresponding values of the non-linear apparent flow exponent ζ, as described in § IV B – see Eq. (47). The symbol (†) indicates studies where flow is driven by a constant body force, with the Bond number (representing the ratio of gravitational to capillary forces) used as the control parameter instead of the capillary number (ratio of viscous to surface tension-related stresses).

Motivated by these shortcomings, in this study we investigate the steady-state effective rheology of a two-phase

gas–liquid Taylor flow consisting of immiscible Newtonian fluids in a smooth capillary tube and in a bundle of parallel tubes with non-uniform radii. Building on the analysis of Roy *et al.* [54], our analytical model introduces several key developments: the inclusion of film flow, velocity mismatch and jump in viscous normal stresses across the phases, and a dimensionless formulation that enables the identification of universal scaling laws for the problem.

Accordingly, the rest of the manuscript is structured as follows. We begin by presenting the theoretical formulation for the decomposition of pressure drop in a liquid-filled tube containing a single gas bubble, reviewing existing correlations (Sec. II A). We then reformulate the problem in dimensionless terms and extend the analysis to arbitrary bubble trains (Sec. II B), which allows us to identify the dominant parameters governing the total pressure drop at the single-tube level (Sec. II C). Next, we analyze how the pressure drop in intermittent gas-liquid Taylor flow evolves across the parameter space (Sec. III A), and we complement this analysis with a rigorous assessment of the theoretical bounds of model applicability (Sec. III B). In the slender-channel limit, we employ perturbation analysis to establish how a single gas bubble perturbs the system dynamics (Sec. III C), leading to deviations from Darcian behavior and enabling the derivation of a closed-form expression for the effective viscosity of the gas-liquid flow. We then extend this framework to a capillary bundle by introducing a statistical distribution of pore sizes. A dimensionless formulation of the problem allows us to derive an exact expression for the effective permeability of the bundle under single-phase flow conditions (Sec. IV A). Finally, we review existing models that describe the non-linear effective rheology of two-phase flow in porous media (Sec. IV B), and show how our model captures the observed power-law relationship between flow rate and pressure drop (Sec. IV C), ultimately clarifying the combined influence of structural disorder and bubble distribution in determining the bulk flow behavior of two-phase systems in porous media. A summary discussion is provided in the concluding section (Sec. V).

II. SINGLE-TUBE MODEL

A. Pressure drop decomposition for an elongated bubble

We first examine the case of a single bubble moving in a capillary tube, focusing on regimes where surface tension competes solely with viscous forces. In Sec. II B, this theoretical framework is extended to account for multiple bubbles within the channel.

We consider the motion of a single elongated bubble of length L_B and negligible viscosity displacing a fluid with dynamical viscosity μ along a horizontal smooth capillary tube of radius r and length L. This is illustrated in Fig. 1. The flow is driven by an imposed pressure drop $\Delta p = p_{\rm in} - p_{\rm out} > 0$ between the inlet and the outlet of the tube. We assume full wetting of the channel walls by the continuous phase, which allows us to neglect contact line dynamics. Bubble coalescence and break-up are also not considered. The axial pressure drop over the channel length L is decomposed as follows [16, 28, 59–69]:

$$\Delta p = \Delta p_r + \Delta p_{\rm B} + \Delta p_f, \tag{1}$$

where the first and third term indicate the viscous pressure drop of the liquid slugs respectively at the rear ('r') and at the front ('f') of the bubble, and the second term is the pressure drop over the bubble ('B'), as shown in Fig. 1. Equation (1) should also account for the frictional losses in the thin liquid that separates the body of the bullet-shaped bubble from the channel wall. However, when gravity and inertial effects are neglected, and the bubble is treated as inviscid, the film is almost stagnant and does not contribute to the pressure calculation [16, 61, 70]. Specifically, in the region of constant film thickness, the pressure at the wall is almost constant, whereas large pressure oscillations can form at the rear of the bubble due to typical meniscus oscillations at the gas-liquid interface [28, 65]. The pressure drop due to frictional losses in the gas bubble is not taken into account, due to the low viscosity of the gas phase compared to that of the liquid [16, 28].

The flow established along the slug regions of length L_r and L_f, located respectively at the rear and at the front of the bubble, is assumed to be laminar and fully-developed. Under these approximations [65], whose validity is discussed in Sec. III B, the Hagen-Poiseuille equation [71, 72] linearly relates the volumetric flow rate of the liquid Q to the local pressure drop due to friction:

$$Q = \frac{\pi\, r^4}{8\, L_j\, \mu}\, \Delta p_j\,, \qquad j = \{r,\, f\}\,. \tag{2}$$

Thus, the local pressure drop can be expressed in terms of the average speed of the liquid slugs v, i.e. $Q = \pi\, r^2\, v$, as:

$$\Delta p_j = \frac{8\, L_j\, \mu}{r^2}\, v\,, \qquad j = \{r,\, f\}\,. \tag{3}$$

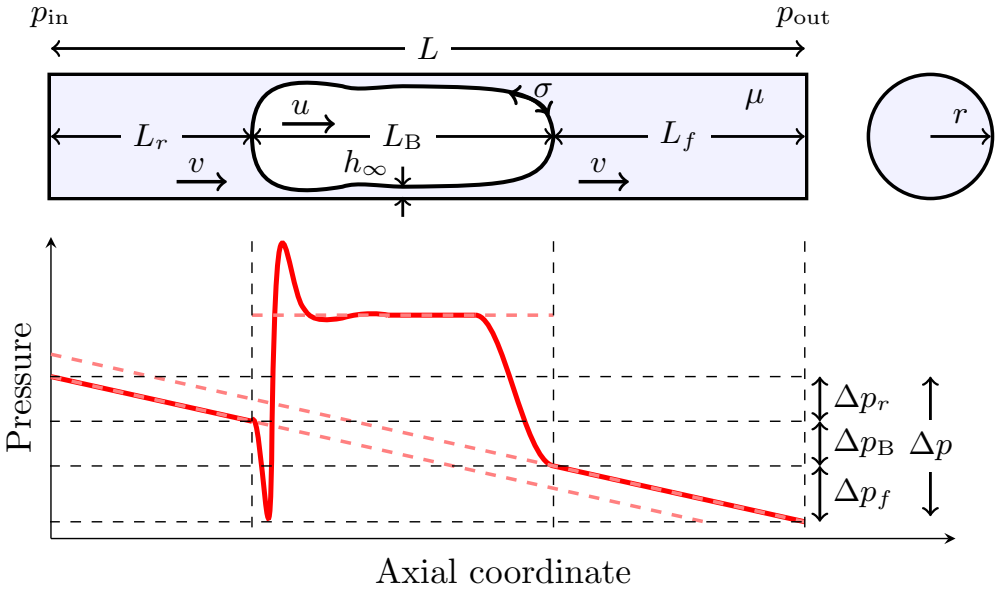

Figure 1. Two-dimensional sketch of the physical problem, and qualitative plot of the wall pressure distribution along the axial direction.

The injection of a gas bubble into the continuous phase causes an excess pressure drop Δp_{B}, perturbing the liquid flow and ultimately leading to a non-linear relation between the pressure differential and the velocity [16, 27]. The key parameter governing the dynamics of a bubble advancing through a viscous fluid in a round capillary at constant speed u is the capillary number:

$$\text{Ca} = \frac{\mu\, u}{\sigma}, \tag{4}$$

which expresses the competition between viscous stresses and those associated with the surface tension σ. Given that in a circular tube the average velocity of the wetting fluid is lower than the bubble velocity, i.e., $v < u$, a capillary number based on the average liquid velocity can be introduced as

$$\text{Ca}_l = \frac{\mu\, v}{\sigma}, \tag{5}$$

which will be used later, see Sec. III A and Sec. IV, in deriving an expression for the effective flow rate, while its relationship with Eq. (4) is examined in Sec. II C 1. Bretherton's foundational analysis [21] of bubble motion identifies the scaling laws for: (i) the uniform film thickness normalized by the tube radius, (ii) the relative velocity of the bubble with respect to the surrounding fluid, and (iii) the mean curvature of the front and rear static menisci. For clarity of exposition, in the following, we review the main theoretical developments.

1. *Characteristic film thickness and velocity ratio*

In Fig. 2 (*a*) we review widely used correlations for estimating the uniform film thickness normalized by the tube radius. Many of the these can be summarized in the following form [61, 73]:

$$\frac{h_\infty}{r} = \frac{A\ (3\,\text{Ca})^{2/3}}{1 + \alpha\, A\ (3\,\text{Ca})^{2/3}}, \quad \text{with} \quad A = 0.643. \tag{6}$$

The pioneering lubrication approach developed by Bretherton [21] enabled the derivation of the theoretical expression for the uniform film thickness in the limit of vanishing capillary numbers, $\text{Ca} \lesssim 0.005$, which corresponds to a formulation where $\text{Ca} \to 0$ in Eq. (6). To improve the agreement with Taylor's experiments [20], Aussillous and Quéré [22] introduced a saturation term in the denominator of Bretherton's original law and fitted the empirical constant to $\alpha = 2.5$, extending the validity of Eq. (6) up to $\text{Ca} \lesssim 2$. The detailed numerical investigation by Balestra *et al.* [74] extended the analysis to viscous drops, yielding $\alpha = 2.483$ in the limit of inviscid bubbles. Still, the theoretical analysis

by Klaseboer *et al.* [75] demonstrates that the actual value of this fitting constant follows from a "tube fit" condition, and is influenced by the (arbitrary) choice of the point where the bubble front meniscus is matched to a parabolic profile, leading to $\alpha = 2.79$ when the asymptotic argument originally employed by Bretherton is adopted. Further extensions to expression Eq. (6) are available in the literature, accounting for inertial effects [76], buoyancy [77], and extending the analysis to non-circular cross-sections [78, 79].

The bubble travels faster than the surrounding liquid due to the presence of the wetting film, yielding the relation

$$\frac{v}{u} = 1 - w, \tag{7}$$

where w is termed the relative *drift* (or *excess*) velocity, see Refs. [73, 80]. Assuming the liquid film remains perfectly stagnant – a condition that holds exactly only within the region of constant film thickness for an inviscid bubble – the expression for w can be derived from a mass balance in a reference frame attached to the bubble, see Refs. [26, 73, 74, 81], namely $(v-u)\,\pi\,r^2 = -\,u\,\pi\left[r^2 - (r-h_\infty)^2\right]$, which simplifies to:

$$w = 1 - \left(1 - \frac{h_\infty}{r}\right)^2. \tag{8}$$

Thus, equation Eq. (8) relates the bubble excess velocity to the *wetting fraction*, which instead quantifies the cross-sectional area occupied by the liquid film.

2. *Pressure drop over the bubble*

An outline of the main correlations for the overall pressure drop across a bubble moving in an axisymmetric capillary, in regimes where inertia and buoyancy are negligible, is given in Fig. 2 (*b*). In the limit of vanishing capillary number, the pressure drop across each interface (front and rear) is governed by the mean curvature via Young-Laplace's law, resulting in a non-zero net pressure jump over the bubble – in principle, these two contributions would compensate if the bubble were symmetric, but this symmetry is disrupted by the bubble motion [62]. Bretherton [21] derived the following law

$$\Delta p_\mathrm{B} = \beta\,\frac{\sigma}{r}\,(3\,\mathrm{Ca})^{2/3}, \tag{9}$$

assuming that the asymptotic plane curvature of the bubble nose approaches the inverse of the channel radius. Although frequently misquoted [73, 75], the constant coefficient $\beta = \beta_f + \beta_r$ in Eq. (9) accounts for both the pressure jumps across the front and the rear menisci of the bubble. Specifically, Bretherton [21] estimated the overall *dynamic* pressure drops as $\beta \approx 2\,[1.79 - (-0.46)] \approx 4.52$. Using rigorous matched asymptotics, Suresh and Grotberg [82] have shown that in a plane channel the scaling behavior indicated by Eq. (9), i.e. $\Delta p_\mathrm{B} \sim \mathrm{Ca}^{2/3}$, is preserved only when the effects of gravity are small and surface tension prevails over viscous forces. Nevertheless, Cherukumudi *et al.* [83] have argued that the validity of Eq. (9) could be expected to hold for much larger Ca. Besides, the authors corrected the numerical factor to a value $\beta \approx 2\,[1.286 - (-0.464)] \approx 3.50$ to account for the actual difference in nose curvatures at the front and the rear of the bubble in case of thicker films.

These classical models predict the capillary pressure drop solely based on the interface's mean curvature, namely $\Delta p_\mathrm{B} \approx \Delta p_{\mathrm{B},\,c}$. However, Balestra *et al.* [74] demonstrated that this assumption yields an incomplete description, as the jump in the normal viscous stress, i.e., $\Delta p_{\mathrm{B},\,n}$, should not be neglected for $\mathrm{Ca} \gtrsim 10^{-3}$. An improved estimate for the total pressure jump across the bubble is thus obtained by summing these two terms:

$$\Delta p_\mathrm{B} = \Delta p_{\mathrm{B},\,c} + \Delta p_{\mathrm{B},\,n}, \tag{10a}$$

$$\Delta p_{\mathrm{B},\,c} = \frac{2\,\sigma}{r}\left(\frac{1 + T_f\,(3\,\mathrm{Ca})^{2/3}}{1 + Z_f\,(3\,\mathrm{Ca})^{2/3}} - \frac{1 + T_r\,(3\,\mathrm{Ca})^{2/3}}{1 + Z_r\,(3\,\mathrm{Ca})^{2/3}}\right), \tag{10b}$$

$$\Delta p_{\mathrm{B},\,n} = \frac{\sigma}{r}\left(\frac{M_f\,(3\,\mathrm{Ca}) + N_f\,(3\,\mathrm{Ca})^{4/3}}{1 + O_f\,(3\,\mathrm{Ca})} - \frac{M_r\,(3\,\mathrm{Ca}) + N_r\,(3\,\mathrm{Ca})^{4/3}}{1 + O_r\,(3\,\mathrm{Ca})}\right), \tag{10c}$$

each derived via numerical fitting. The values of the front ('f') and rear ('r') coefficients, in the limit of inviscid bubble for an axisymmetric channel, are listed in Table II for ease of reference. Consistently, the asymptotic series of the rational function model (10), namely

$$\Delta p_\mathrm{B} \sim \frac{2\,\sigma}{r}\left[(T_f - Z_f) - (T_r - Z_r)\right](3\,\mathrm{Ca})^{2/3}, \tag{11}$$

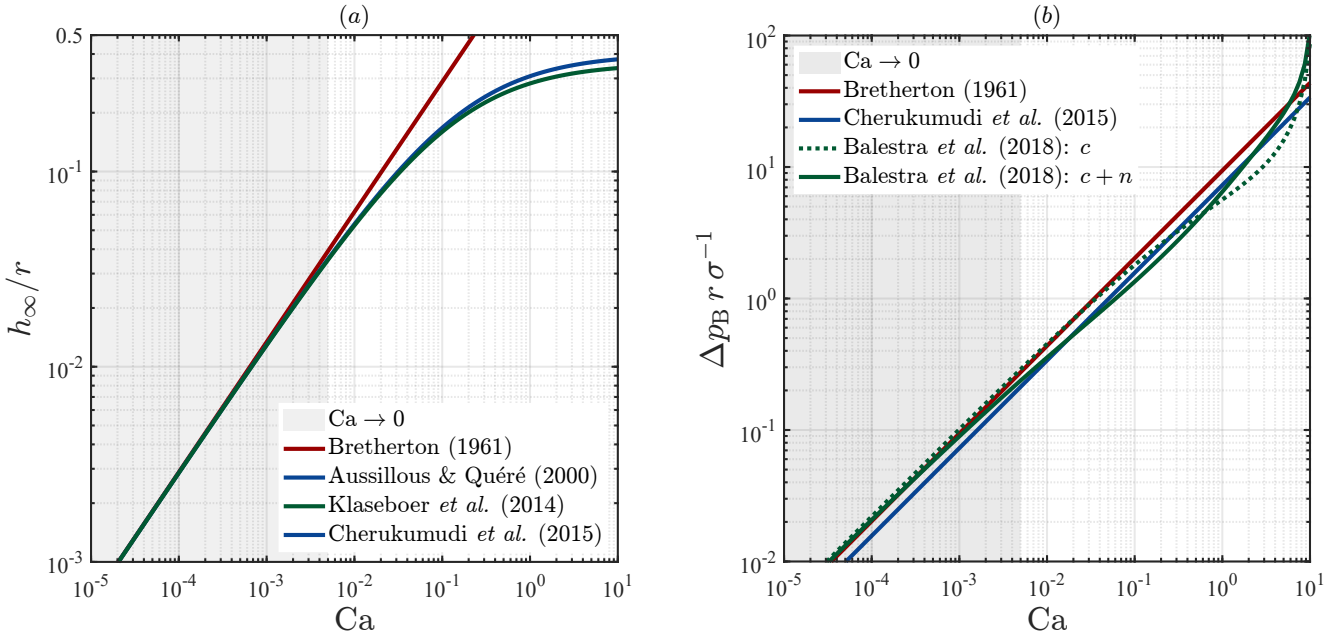

Figure 2. Comparison of the main available correlations for the dimensionless (a) uniform thin-film thickness and (b) tip-to-tip bubble pressure drop in an axisymmetric capillary of radius r, neglecting inertia and buoyancy effects, in the limit of inviscid bubble. For the correlation proposed by Balestra *et al.* [74], see Eq. (10), both the curvature-induced component alone ('c') and the combined contribution including the jump in normal viscous stresses ('$c+n$') are displayed for comparison. The abscissa represents the capillary number, given in Eq. (4), being σ the surface tension at the interface between the bubble and the surrounding fluid. The region of vanishing capillary numbers ($\mathrm{Ca} \lesssim 0.005$), where Bretherton's model is valid, is highlighted by the grey area.

is in line with the scaling law proposed by Bretherton [21] in the low-Ca regime, i.e. $\Delta p_\mathrm{B} \sim \mathrm{Ca}^{2/3}$.

Constant	T	Z	M	N	O
front: 'f'	2.725	0.646	−2.011	1.669	0.167
rear: 'r'	−0.473	−0.094	2.381	−1.744	2.732

Table II. Front and rear coefficients in the inviscid-bubble limit in an axisymmetric channel, used in the pressure drop correlation of Balestra *et al.* [74] given by Eq. (10).

B. Dimensionless formulation

To quantify the competition between viscous and capillary phenomena, we normalize Eqs. (1, 3, 10) using the capillary pressure scale, $\mathcal{P} = \sigma/L$, which includes exclusively parameters related to the system geometry and the physical properties of the fluids at the interface. Instead, using the viscous scale – e.g., $\mu\, v/r$ or $\mu\, u/r$, as commonly adopted in other works [28, 60] – is not possible *a priori* at this stage of the analysis, as it depends on the velocity of one of the phases. Additionally, choosing $\mathcal{P}$ as the reference scale for pressure is consistent with our focus on regimes characterized by low-to-moderate capillary numbers, where surface tension is expected to prevail over viscous losses, see Eq. (4). We denote the resulting dimensionless quantities by the asterisk, i.e., $\Delta p^* = \Delta p\, \mathcal{P}^{-1}$, and introduce the reduced capillary number

$$z = (3\,\mathrm{Ca})^{1/3}\,, \tag{12}$$

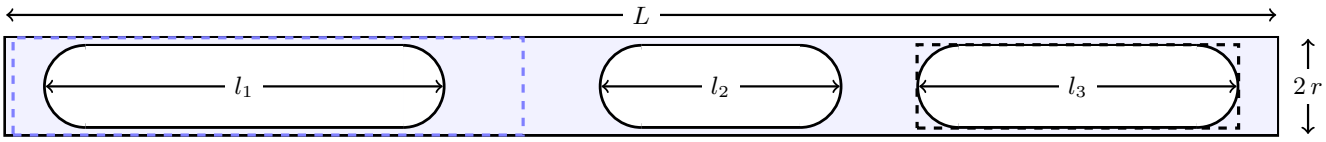

Figure 3. Schematic of Taylor flow with $N = 3$ gas bubbles separated by liquid slug domains in a capillary tube. The front and rear menisci of each bubble are idealized as hemispherical caps, as highlighted by the black dashed rectangle enclosing the last bubble. The blue dashed rectangle denotes a representative unit cell – shown separately in Fig. 1 – which forms the repeating element (of varying length) of the two-phase flow [28, 65].

to lighten notation. This procedure yields the following expressions for the dimensionless pressure jumps within the liquid slug and over the bubble:

$$\Delta p^*_{\mathrm{S}} = \Delta p^*_r + \Delta p^*_f = \frac{8}{3}\, z^3\, \frac{v}{u}\, \left(\frac{L}{r}\right)^2\, \frac{L_r + L_f}{L}, \tag{13a}$$

$$\Delta p^*_{\mathrm{B}} = \Delta p^*_{\mathrm{B},\,c} + \Delta p^*_{\mathrm{B},\,n} = \frac{L}{r}\, \beta(z), \tag{13b}$$

where the following functions

$$\beta(z) = 2\, \beta_c(z) + \beta_n(z), \tag{14a}$$

$$\beta_c = \frac{1 + T_f\, z^2}{1 + Z_f\, z^2} - \frac{1 + T_r\, z^2}{1 + Z_r\, z^2}, \qquad \beta_n = \frac{M_f\, z^3 + N_f\, z^4}{1 + O_f\, z^3} - \frac{M_r\, z^3 + N_r\, z^4}{1 + O_r\, z^3}, \tag{14b}$$

describe how the bubble-related pressure drop evolves with the reduced capillary number z, building on the comprehensive analysis by Balestra *et al.* [74].

Assuming that both the phases are incompressible, we express the bubble length as the difference between the total channel length and the sum of the lengths of the rear and front slugs, yielding the relation $L_r + L_f = L - L_{\mathrm{B}}$. We extend this identity to a train of N bubbles of individual lengths l_i, as shown in Fig. 3, by replacing L_{B} with the total length occupied by the gas phase, $\sum_{i \le N} l_i$, and incorporating the resulting expression into Eq. (13a). Moreover, since each bubble introduces a front and rear menisci and each pair of interfaces contributes a pressure drop that is independent of the bubble length, we account for the total gas-related contribution by multiplying the term in Eq. (13b) by the number of bubbles N. In view of Eqs. (6, 7, 8), this procedure leads to

$$\Delta p^* = \Delta p^*_{\mathrm{S}} + \Delta p^*_{\mathrm{B}}, \tag{15a}$$

$$\Delta p^*_{\mathrm{S}} = \frac{8}{3}\, z^3 \left(1 - \frac{A\, z^2}{1 + \alpha\, A\, z^2}\right)^2 \left(\frac{L}{r}\right)^2\, \frac{L - \sum_{i \le N} l_i}{L}, \tag{15b}$$

$$\Delta p^*_{\mathrm{B}} = N\, \frac{L}{r}\, \beta(z), \tag{15c}$$

revealing that the bubble-induced pressure drop evolves in discrete steps with the number of bubble N, while within the liquid phase the governing parameter is the total slug length relative to the channel length. Accordingly, we introduce the bubble length fraction as

$$\varphi = \frac{\sum_{i \le N} l_i}{L}. \tag{16}$$

Finally, we make the tube length in Eqs. (15b, 15c) dimensionless using the channel radius as the reference length scale, i.e. $L^* = L/r$, yielding the pressure drop model:

$$\Delta p^* = \frac{8}{3}\, z^3 \left(1 - \frac{A\, z^2}{1 + \alpha\, A\, z^2}\right)^2 (L^*)^2\, (1 - \varphi) + N\, L^*\, \beta(z). \tag{17}$$

C. Analysis of the parameter space

To delineate the bounds of validity for the flow description given by Eq. (17) and elucidate the dominant scaling laws governing the system, we introduce geometrical constraints and analyze an equivalent reparameterization of the model that improves its physical understanding.

1. Bubble length and capillary number

The assumption of an infinitely long bubble is practically addressed by enforcing a minimum bubble length requirement. Klaseboer *et al.* [75] proposed a criterion based on a transition region of approximately $\lambda \sim 10$ dimensionless units, ensuring that the front and rear interfaces do not overlap and can be treated independently. By accounting for the presence of front and rear spherical caps, Cherukumudi *et al.* [83] refined this condition (Eq. 42 there) as:

$$\frac{l_i}{r} \geq \frac{b}{r} \equiv b^*, \qquad b^* = 2\left[1 + \lambda \frac{h_\infty}{r} \left(3\,\mathrm{Ca}\right)^{-1/3}\right] = 2\left(1 + \lambda \frac{A\,z}{1 + A\,\alpha\,z^2}\right), \tag{18}$$

where the last equality follows from Eq. (6). As shown in Fig. 4 (*a*), the above expression highlights that the minimum length of a Taylor bubble corresponds to the channel diameter and is achieved in the limit of vanishing capillary numbers ($z \to 0$). Ultimately, the minimum bubble length normalized by the tube radius is expressed by a rational function in the reduced capillary number which exhibits a global maximum at $z = 1/\sqrt{\alpha\,A}$ – corresponding to $\mathrm{Ca} \approx 0.164$ for $\alpha = 2.5$ – where it reaches a value equal to $2 + \lambda\,A/\sqrt{\alpha\,A}$ (approximately 7.071 choosing $\lambda = 10$). Our analysis reveals that this non-monotonic behavior stems from a competing interplay between two physical mechanisms: while the numerator captures the elongation of the dynamic meniscus with increasing capillary number, the denominator reflects a saturating effect associated with the thickening of the lubricating film.

To facilitate comparison between the two-phase flow behavior and the single-phase (all-liquid) limit, we examine the relationship between the capillary numbers based on the average liquid slug and bubble velocities, as defined in Eqs. (4, 5):

$$\mathrm{Ca}_l = \frac{\mu\,v}{\sigma} = \frac{\mu\,u}{\sigma}\frac{v}{u} = \mathrm{Ca}\left[\frac{1 + (\alpha - 1)\,A\,\left(3\,\mathrm{Ca}\right)^{2/3}}{1 + \alpha\,A\,\left(3\,\mathrm{Ca}\right)^{2/3}}\right]^2, \tag{19}$$

which follows directly from Eq. (7). The scaling behavior derived in the low Ca-limit remains valid under this new parametrization, as a result of the asymptotic relationship $\mathrm{Ca}_l \sim \mathrm{Ca} - 2 \cdot 3^{2/3} A\,\mathrm{Ca}^{5/3} + \mathcal{O}(\mathrm{Ca}^{7/3})$. In contrast, for thicker films (typically $\mathrm{Ca} \gtrsim 10^{-2}$), Ca_l drops below Ca, indicating the bubble's non-linear influence on the flow, as shown in Fig. 4 (*a*).

2. Bubble fraction

To improve the physical interpretation, we formulate our model in terms of the *volumetric* gas fraction (or *saturation*), defined as

$$\Phi = \frac{\sum_{i \leq N} V_i}{V}, \tag{20}$$

where V_i is the volume of the i-th bubble and V is the total channel volume. This quantity can be related to the linear gas fraction φ defined in Eq. (16) based solely on geometrical considerations. In this work, we adopt the approach proposed by Warnier *et al.* [16], which offers a suitable compromise between accuracy and simplicity. Estimating each bubble volume as the product of the cap-to-cap length l_i and the cross-sectional area in the region of uniform film thickness, namely $\pi\,r_b^2$, with $r_b = r - h_\infty$, tends to overestimate the actual gas volume. This is because bubbles in confined channels are not perfectly cylindrical, but rather exhibit a bullet-shaped profile, with rounded fore-and-aft menisci that contain liquid instead of gas. To account for this geometric discrepancy, a corrective length δ can be introduced, reducing the effective gas length accordingly. For hemispherical caps, it can be shown that $\delta = 2/3\,r_b$. This leads to a more accurate relationship between the gas saturation Φ and the geometric parameters introduced previously:

$$\varphi = \frac{\Phi}{\left(1 - \dfrac{h_\infty}{r}\right)^2} + \frac{2}{3}\,N\,\frac{r}{L}\left(1 - \frac{h_\infty}{r}\right). \tag{21}$$

The effective range of variation of both linear and volumetric gas fractions lies within a sub-interval of [0; 1], governed by the problem's parameter space – namely the bubble number N, the dimensionless channel length L^* and film thickness h_∞/r, the latter being ultimately controlled by the bubble capillary number Ca as described by Eq. (6).

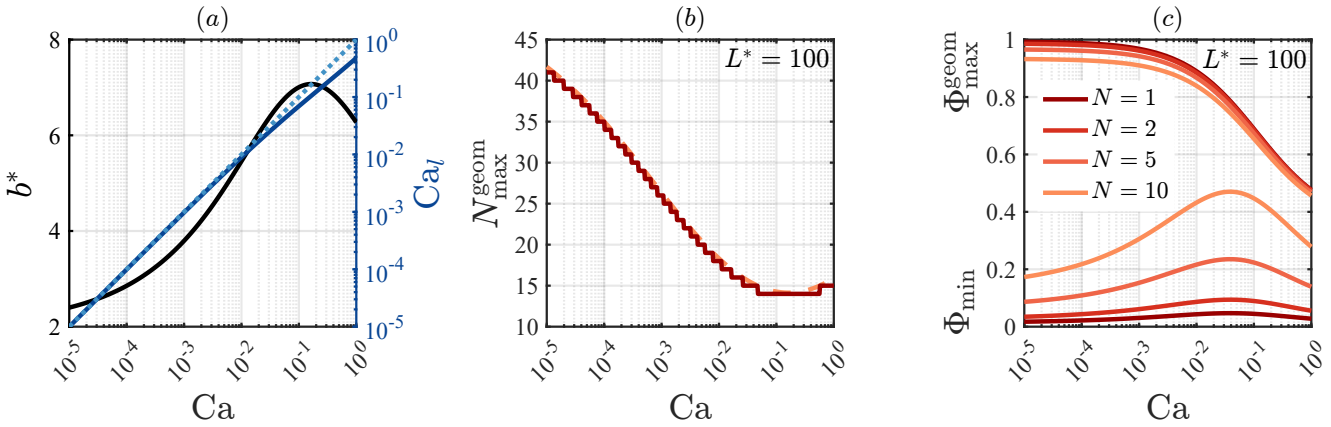

Figure 4. (*a*) Validity constraint imposed by (18) on the dimensionless mean bubble length b^* (left ordinate axis) and relationship between the capillary numbers based on the bubble and liquid slug velocities (right ordinate axis), as given by Eq. (19). (*b*) Variation of the maximum bubble number $N_{\max}^{\mathrm{geom}}$ with the capillary number based on the bubble velocity, see Eq. (22): the dashed line represents the continuous trend of the ratio L^*/b^*, for a channel of slenderness $L^* = 100$, while the superimposed staircase-like profile visualizes the effect of the floor operator, highlighting discrete changes in the bubble number. (*c*) Geometric range of variation of the volumetric gas fraction Φ with the capillary number based on the bubble velocity, showing both the lower ($\Phi_{\min}$) and upper ($\Phi_{\max}^{\mathrm{geom}}$) bounds – see Eqs. (23, 24) – for $L^* = 100$ and a varying number $N < N_{\max}^{\mathrm{geom}}$ of bubbles composing the train.

The lower bound for the admissible bubble number N under two-phase flow conditions corresponds to the single-bubble case ($N = 1$); conversely, the upper bound ($N = N_{\max}$) is not uniquely defined. From a simplified geometrical perspective, the corresponding limiting configuration is associated with the foam-like regime, in which the channel is entirely filled with densely packed least-elongated bubbles. The long-bubble requirement expressed by Eq. (18) leads to the following geometrical constraint:

$$N_{\max}^{\mathrm{geom}} = \min_{\mathrm{Ca}} \left\lfloor \frac{L}{b} \right\rfloor = \min_{\mathrm{Ca}} \left\lfloor \frac{L^*}{b^*} \right\rfloor = \left\lfloor \frac{L^*}{2 + \lambda\, A/\sqrt{\alpha\, A}} \right\rfloor , \tag{22}$$

where the floor function ensures that the maximum bubble number remains an integer, and the minimization over the range of capillary numbers based on the bubble speed selects the flow condition yielding the longest bubble consistent with the channel-level constraint. This geometrical estimate, shown in Fig. 4 (*b*), assumes ideal packing and does not account for hydrodynamic limitations. Accordingly, the criterion used to constrain the maximum number of bubble will be refined in Sec. III B, leading to a more restrictive condition, i.e., $N_{\max} = N_{\max}^{\mathrm{flow}} < N_{\max}^{\mathrm{geom}}$. Fig. 4 (*c*) shows the evolution of the upper and lower geometrical limits of the saturation versus the capillary number based on bubble speed, for different numbers of bubbles composing the train. The bubble volume fraction spans an interval whose lower bound corresponds to the case of N bubbles with the smallest admissible length; this configuration yields a linear gas fraction equal to $\varphi = N\, b/L$, for which equation (21) gives:

$$\Phi_{\min} = \frac{N}{L^*} \left[b^* - \frac{2}{3} \left(1 - \frac{h_\infty}{r} \right) \right] \left(1 - \frac{h_\infty}{r} \right)^2 , \qquad \text{with} \quad N \in [0;\, N_{\max}] , \tag{23}$$

recovering the single-phase (all-liquid) limit when $N = 0$. In contrast, the upper bound for the gas saturation ($\Phi = \Phi_{\max}$) lacks a unique characterization. The previously established tube-fitting condition, i.e., $\varphi = 1$, describing the packing of N bubbles along the entire channel length, leads to the following geometric constraint:

$$\Phi_{\max}^{\mathrm{geom}} = \left[1 - \frac{2}{3} \frac{N}{L^*} \left(1 - \frac{h_\infty}{r} \right) \right] \left(1 - \frac{h_\infty}{r} \right)^2 , \qquad \text{with} \quad N \in [1;\, N_{\max}] . \tag{24}$$

To preserve the validity of this description, we will further restrict the upper bound for the gas saturation in Sec. III B based on the physics of intermittent two-phase flows, yielding a refined estimate, i.e., $\Phi_{\max} = \Phi_{\max}^{\mathrm{flow}} < \Phi_{\max}^{\mathrm{geom}}$.

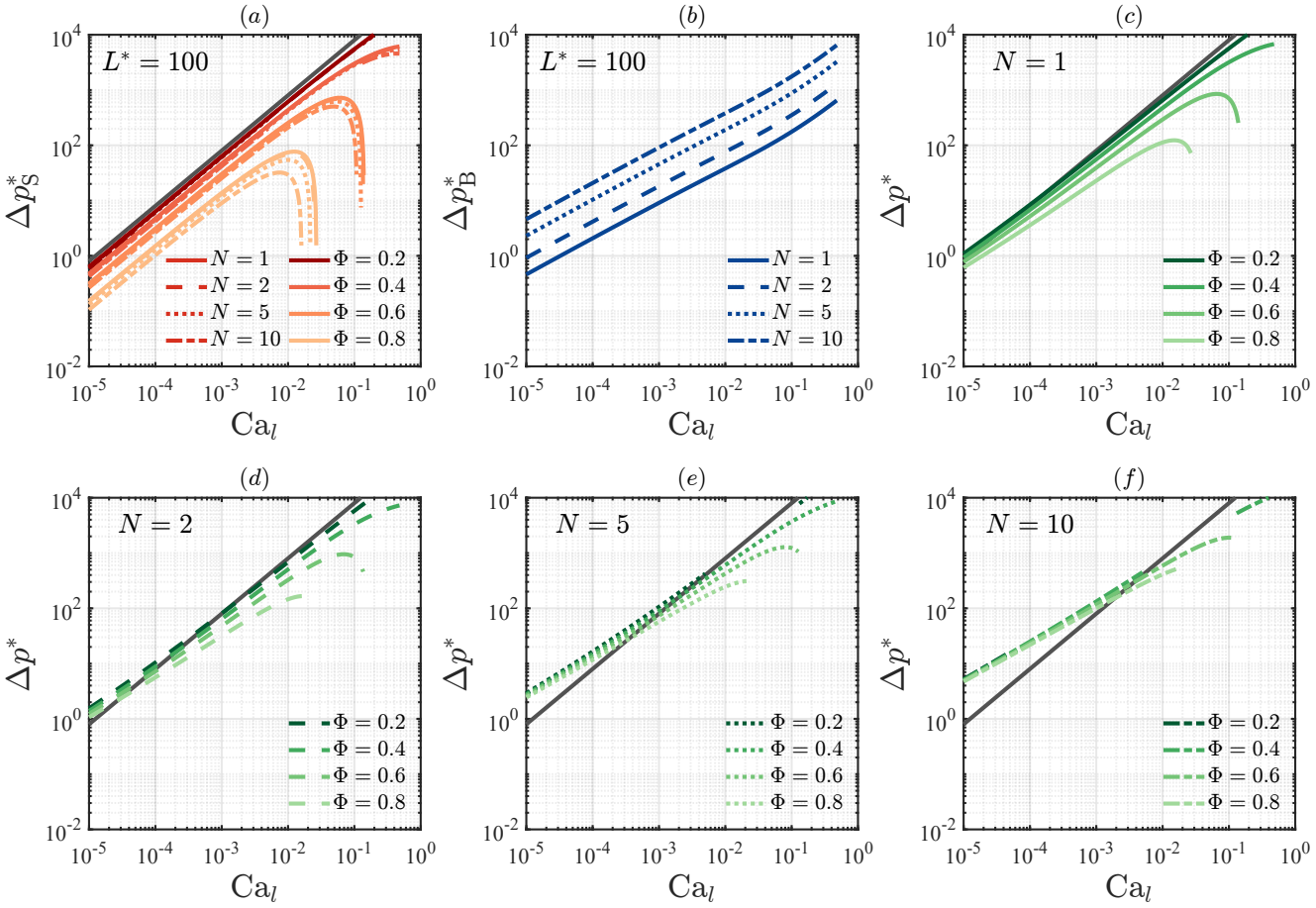

Figure 5. Dimensionless pressure drops plotted against the capillary number based on the liquid velocity for a channel of slenderness $L^* = 100$. Panels (a) and (b) show the slug- and bubble-related contributions, respectively, for varying gas saturation Φ and bubble number N. Panels (c) to (f) display the total pressure drop for fixed bubble numbers and varying volumetric gas fractions; for reference, the single-phase limit is shown as a continuous grey line.

III. RESULTS AND DISCUSSION

A. Pressure-flow curves

The final expression for the overall dimensionless pressure drop in gas–liquid Taylor flow is given by Eq. (17), where the gas linear fraction φ is expressed in terms of its volumetric counterpart Φ using Eq. (21). To isolate the effects of viscous and capillary pressure drops, we initially plot these contributions separately – panels (a) and (b) – and subsequently sum them to obtain the total pressure jump – panels (c) to (f) – in Fig. 5. To facilitate comparison with the single-phase (all-liquid) limit ($\Phi \to 0$), governed by the Darcy law, we present these results in terms of the capillary number based on the liquid velocity, rather than the bubble velocity, using the transformation given in Eq. (19).

The liquid pressure drop contribution depends on both the bubble number and the saturation, whereas the gas contribution depends solely on the bubble number. In panel (a), we observe four families of curves corresponding to increasing saturations, each distinguished by a different color. On the other hand, the linestyle indicates the bubble number, selected to ensure that the geometrical constraint expressed by Eq. (22) is satisfied for a fixed length-to-radius ratio. This choice reflects the fact that, at the system level, the same saturation can be attained by using a larger number of shorter bubbles. For reference, the single-phase limit is shown as a continuous grey line, exhibiting a linear trend with the capillary number based on the mean liquid velocity, consistent with the Darcy-type behavior. At low gas volume fractions, this linearity is only slightly perturbed. However, as saturation increases, the curves begin to deviate at moderate to high capillary numbers, displaying a non-monotonic trend: the pressure drop initially increases, reaches a maximum, then declines rapidly, and ultimately becomes negative – signaling an apparent flow reversal. The

mathematical origin of this inconsistent behavior arises from the unbounded growth of the term $\Phi/(1-h_\infty/r)^2$, driven by film thickening and embedded in the expression for the linear gas fraction φ given in Eq. (21), thereby revealing a physical limitation of the model. In this regard, previous studies [62, 84] have suggested that the breakdown of simplified bubble transport models for intermittent flow at high capillary numbers may stem from the neglect of dissipation near the bubble end caps, where recirculation patterns dominate. Nevertheless, since the present work considers bubble transfer dynamics primarily as a proxy for investigating the non-linear effective rheology of two-phase flows in porous media – where the relevant capillary numbers are typically small – this limitation does not compromise the validity of our description. Accordingly, we retain a broad range of capillary numbers in Fig. 5 – extending up to $\mathcal{O}(1)$ values – in order to illustrate the model's behavior beyond its expected range of validity, and present a rigorous discussion of the model's applicability in Sec. III B.

In Fig. 5, panel (b), we observe four curves corresponding to increasing bubble numbers, distinguished by different linestyles. These curves share the same shape, as the bubble number N acts merely as a multiplicative factor in the pressure drop expression. At low values of the liquid-phase capillary number Ca_l, the slope corresponds to the theoretical prediction of 2/3 from Bretherton's analysis of curvature-induced pressure drops across long bubbles. Minor deviations appearing at higher capillary numbers stem from the model's inclusion of the additional pressure jump component arising from the difference in normal stress across the interface, given by Eq. (10).

In Fig. 5, panels (c) to (f) present the overall pressure drop for fixed bubble numbers across varying saturations. This choice facilitates direct comparison and interpretation of the data; in fact, the gas-phase contribution to the pressure drop – depending exclusively on the bubble number – remains constant, as it is unaffected by changes in saturation. In the case of a single bubble (panel c), the pressure drop at the system level remains below the single-phase benchmark across all saturations over the chosen range of capillary numbers. This outcome reflects the interplay between two effects: the introduction of a bubble generates an interfacial pressure jump, but simultaneously removes a liquid segment from the system, effectively reducing viscous resistance. As the bubble number increases, the number of liquid–gas interfaces – and corresponding interfacial jumps – increases. At low capillary numbers, this leads to a total pressure drop that exceeds that of the single-phase liquid flow. However, the rate of increase of the gas-related pressure drop with respect to the capillary number Ca_l is lower than that of the liquid phase. In this framework, the intersection between the overall pressure drop curves and the single-phase reference line indicates a regime transition, characterized by a shift in the dominant pressure drop mechanism. At this point, for a given dimensionless tube length (e.g., $L^* = 100$), the reduction in viscous losses due to bubble addition is counterbalanced by an equivalent increase in interface-related contributions, resulting in an unchanged total pressure drop. Notably, this intersection shifts toward higher capillary numbers as the bubble number increases, and for larger values of N the intersection points corresponding to varying saturations tend to converge. In fact, at high bubble numbers, the system enters a surface tension-dominated regime where saturation-induced variations in viscous resistance play a diminished role – yielding a reduced spread in transition points across different saturation conditions. At low to moderate gas saturations, some of the curves exhibit discontinuities with respect to the capillary number. This behavior arises from the non-monotonic nature of the minimum saturation threshold $\Phi_{\min}$ – see Fig. 4 (c) – which is determined by the long-bubble constraint given by Eq. (18). Specifically, in an intermediate range of capillary numbers where Φ falls below $\Phi_{\min}$, the flow configuration becomes inadmissible, and the corresponding pressure–flow rate relationship is interrupted, see Sec. III B.

B. Applicability region of the model

As anticipated, the non-monotonic trend in the pressure–flow rate relationship within the liquid slugs may arise from an underestimation of the local pressure drop, due to the simplified assumption that flow is strictly axial. At higher capillary numbers, non-parallel flow effects – such as stagnation and loss of streamwise invariance – become increasingly significant, particularly near the bubble caps [62, 74], even in the case of inviscid bubbles. To ensure physical consistency, we require that the dimensionless pressure drop within the slug, Δp^*_{S}, remains an increasing function of the capillary number, imposing the constraint

$$\frac{\partial\, \Delta p^*_{\mathrm{S}}}{\partial z} > 0. \tag{25}$$

Developing this condition analytically from Eq. (15b) yields an additional upper bound $\Phi^{\mathrm{flow}}_{\max}$ on the admissible gas saturation, which is found to be more restrictive than the previous geometrical limit, given by Eq. (24), over the entire range of capillary numbers:

$$\Phi_{\max} = \min_{\mathrm{Ca}_l} \left\{ \Phi^{\mathrm{geom}}_{\max},\, \Phi^{\mathrm{flow}}_{\max} \right\} = \Phi^{\mathrm{flow}}_{\max}. \tag{26}$$

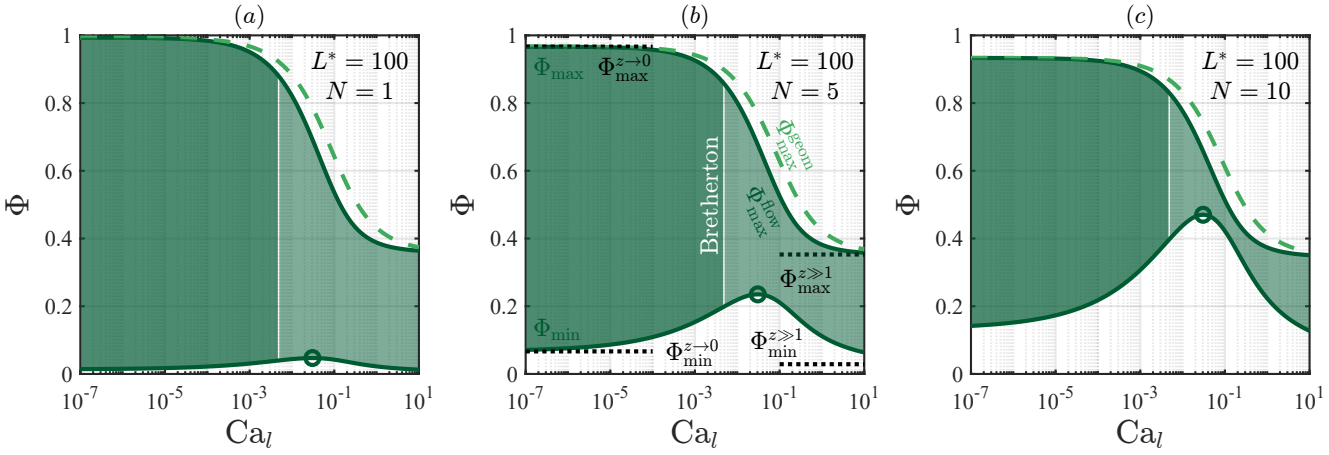

Figure 6. Applicability map of the pressure drop model given by (15) for intermittent gas-liquid flows in a channel with fixed slenderness $L^* = 100$, for different numbers of bubbles composing the train: (*a*) $N = 1$ (single-bubble case), (*b*) $N = 5$, and (*c*) $N = 10$. The regions (Ca_l; Φ) in the plane of capillary number (based on the mean velocity of the liquid slugs) and gas volume fraction that are shaded in green indicate the parameter space where the model is valid. The dark green subregion corresponds to the limit of vanishing capillary numbers ($\text{Ca} \lesssim 0.005$), where Bretherton's theory also applies. The curves associated with the maximum gas saturation $\Phi_{\max}^{\text{flow}}$ due to the monotonicity constraint – see Eq. (25) – and the minimum gas saturation $\Phi_{\min}$ – see Eq. (23) – are shown as dark green continuous lines. The global maximum of the latter is highlighted with a green circle. The upper bound imposed by geometry $\Phi_{\max}^{\text{geom}}$ – see Eq. (24) – is represented by a dashed light green line. In panel (*b*), the two pairs of horizontal asymptotes – see Eqs. (27, 28) – are shown as black dotted lines and labeled for reference.

As a consequence, the maximum number of bubbles that can be effectively accommodated within the channel is lower than the maximum value allowed by the purely geometrical condition given by Eq. (22), i.e., $N_{\max} < N_{\max}^{\text{geom}}$. The value of $N_{\max}$ must be determined numerically by ensuring that the inequality $\Phi_{\min} < \Phi < \Phi_{\max}$ is satisfied across a prescribed range of capillary numbers. Fig. 6 shows how the model's applicability region, defined by the admissible volumetric gas fractions, varies with the capillary number based on the slug-mean velocity, for a fixed dimensionless channel length L^* and varying numbers N of bubbles composing the train. Interestingly, the functions $\Phi_{\max}$ expressing the upper bounds for the gas saturation exhibit reverse S-shaped profiles, approaching the same pair of horizontal asymptotes in the limits $z \to 0$ and $z \gg 1$:

$$\Phi_{\max}^{z\to 0} = 1 - \frac{2}{3}\frac{N}{L^*}, \qquad \Phi_{\max}^{z\gg 1} = \left[1 - \frac{2}{3}\left(\frac{\alpha-1}{\alpha}\right)\frac{N}{L^*}\right]\left(\frac{\alpha-1}{\alpha}\right)^2. \tag{27}$$

Similarly, the function expressing the lowest admissible gas saturation is asymptotically bounded between the following limits:

$$\Phi_{\min}^{z\to 0} = \frac{4}{3}\frac{N}{L^*}, \qquad \Phi_{\min}^{z\gg 1} = \frac{2}{3}\left(\frac{2\,\alpha+1}{\alpha}\right)\frac{N}{L^*}\left(\frac{\alpha-1}{\alpha}\right)^2. \tag{28}$$

Unlike $\Phi_{\max}$, $\Phi_{\min}$ exhibits a non-monotonic trend. The position of its maximum can be evaluated numerically: specifically, its location depends only on the constants A, α and λ (with $\text{Ca} \approx 0.0385$ for $\alpha = 2.5$ and $\lambda = 10$), while its corresponding value is found to be approximately $4.70\,N/L^*$. We note that the ratio N/L^* represents the linear bubble density within the channel, i.e., the number of bubbles per unit channel length (normalized using the channel radius). Notably, in the limiting case of an infinitely slender channel, $L^* \to \infty$, the volumetric correction term associated with the sphericity of bubble menisci asymptotically approaches zero, reflecting a simplified geometrical representation of bubbles as cylindrical segments.

C. Perturbation analysis

To investigate how the introduction of a bubble leads the flow to deviate from the Darcy-type response, we analyze the system's departure from the single-phase limit using asymptotics. Therefore, we consider the case of a slender channel, whose geometry is characterized by the small-scale parameter

$$\varepsilon = \frac{r}{L} \ll 1, \tag{29}$$

defined here, for notational convenience, as the reciprocal of the dimensionless channel length introduced earlier ($\varepsilon \equiv 1/L^*$). We then examine the effect of inserting a single bubble into the channel. To determine the relative magnitude of each term in the governing equations (1, 3, 10), we follow a dominant balance approach [85, 86]. Specifically, introducing a tunable length to characterize the capillary pressure scale leads to the following reference quantity used for normalization: $\mathcal{P}_\gamma = \sigma/\left(\varepsilon^\gamma L\right)$, where γ is an exponent tailored to reflect the dominant physical mechanism. Introducing the reduced capillary number as per Eq. (12), and denoting the resulting dimensionless quantities by the star decoration, i.e., $\Delta p^\star = \Delta p\, \mathcal{P}_\gamma^{-1}$, yields the bubble-induced pressure drop:

$$\Delta p^\star_{\mathrm{B}} = \varepsilon^{\gamma-1}\, \beta(z), \tag{30}$$

evolving with the capillary number according to Eq. (14). On the other hand, the dimensionless pressure drop associated with the slug, namely

$$\Delta p^\star_{\mathrm{S}} = \Delta p^\star_r + \Delta p^\star_f = \frac{8}{3}\, z^3 \frac{v}{u}\, \varepsilon^{\gamma-2}\, (1-\varphi)\,, \tag{31}$$

is directly proportional to the liquid fraction of the channel, $1-\varphi$, as defined in Eq. (16). Thus, the least perturbative configuration corresponds to reducing the bubble linear fraction to its minimum value compatible with the theoretical framework of long-bubble theory, expressed by Eq. (18):

$$\varphi \geq \frac{b}{L} = \frac{r}{L}\,\frac{b}{r} = 2\,\varepsilon \left(1 + \frac{\lambda}{z}\,\frac{h_\infty}{r}\right), \tag{32}$$

where $\lambda \sim 10$, see Sec. II C 1. Using Eqs. (6, 7, 8) leads to the final expression for the dimensionless pressure drop associated with the slug:

$$\Delta p^*_{\mathrm{S}} = \left[\frac{1 + A\,(\alpha-1)\, z^2}{1 + A\,\alpha\, z^2}\right]^2 \left[\frac{8}{3}\, z^3\, \varepsilon^{\gamma-2} - \frac{16}{3}\, z^3\, \varepsilon^{\gamma-1} \left(1 + \frac{\lambda\, A\, z}{1 + A\,\alpha\, z^2}\right)\right]. \tag{33}$$

By inspection of Eqs. (30, 33), we select $\gamma = 2$ to ensure that the bubble-related contributions appear as $\mathcal{O}(\varepsilon)$ corrections to the slug-related pressure drop. The corresponding terms are shown in Fig. 7 $(a)-(c)$.

We now focus on the surface-tension-dominated regime ($z \ll 1$), which is particularly relevant to porous media applications. Neglecting all the contributions lower than the dominant term, i.e., smaller than $\varepsilon\, z^3$, the dimensionless pressure jumps simplifies as

$$\Delta p^\star = \Delta p^\star_{\mathrm{S}} + \Delta p^\star_{\mathrm{B}}, \tag{34a}$$

$$\Delta p^\star_{\mathrm{S}} \sim \frac{8}{3} z^3 - \frac{16}{3} \varepsilon\, z^3, \tag{34b}$$

$$\Delta p^\star_{\mathrm{B}} \sim 2\,\varepsilon\, [(T_f - Z_f) - (T_r - Z_r)]\, z^2 + \varepsilon\, (M_f - M_r)\, z^3, \tag{34c}$$

reducing the system description to the following cubic equation in z, where the coefficients a_2 and a_3 capture geometric and dynamic asymmetries between the front and rear menisci:

$$\left(\frac{8}{3} + \varepsilon\, a_3\right) z^3 + 2\,\varepsilon\, a_2\, z^2 - \Delta p^\star = 0, \tag{35a}$$

$$a_3 = M_f - M_r - \frac{16}{3}, \qquad a_2 = (T_f - Z_f) - (T_r - Z_r)\,. \tag{35b}$$

In the case of large scale separation ($\varepsilon \to 0$), the full solution to the cubic equation (35) – derived via Cardano's method but omitted here for brevity – can be accurately approximated by the initial terms Λ_i ($i = \{1, 2\}$) of its power-series expansion:

$$\mathrm{Ca} \sim \frac{\Delta p^\star}{8} \left[1 - \varepsilon\, \Lambda_1 + \varepsilon^2\, \Lambda_2 + \mathcal{O}(\varepsilon^3)\right], \tag{36a}$$

$$\Lambda_1 = \frac{3\, a_3}{8} + \frac{3^{2/3}\, a_2}{2\,(\Delta p^\star)^{1/3}}, \qquad \Lambda_2 = \frac{9\, a_3^2}{64} + \frac{3^{1/3}\, a_2^2}{2\,(\Delta p^\star)^{2/3}} + 5\,\frac{3^{2/3}\, a_2\, a_3}{16\,(\Delta p^\star)^{1/3}}, \tag{36b}$$

which already reflect the system's non-linear behavior and highlight how the bubble-related coefficients a_2 and a_3 drive deviations from the Darcy-like single-phase description. However, as the scale separation diminishes, this

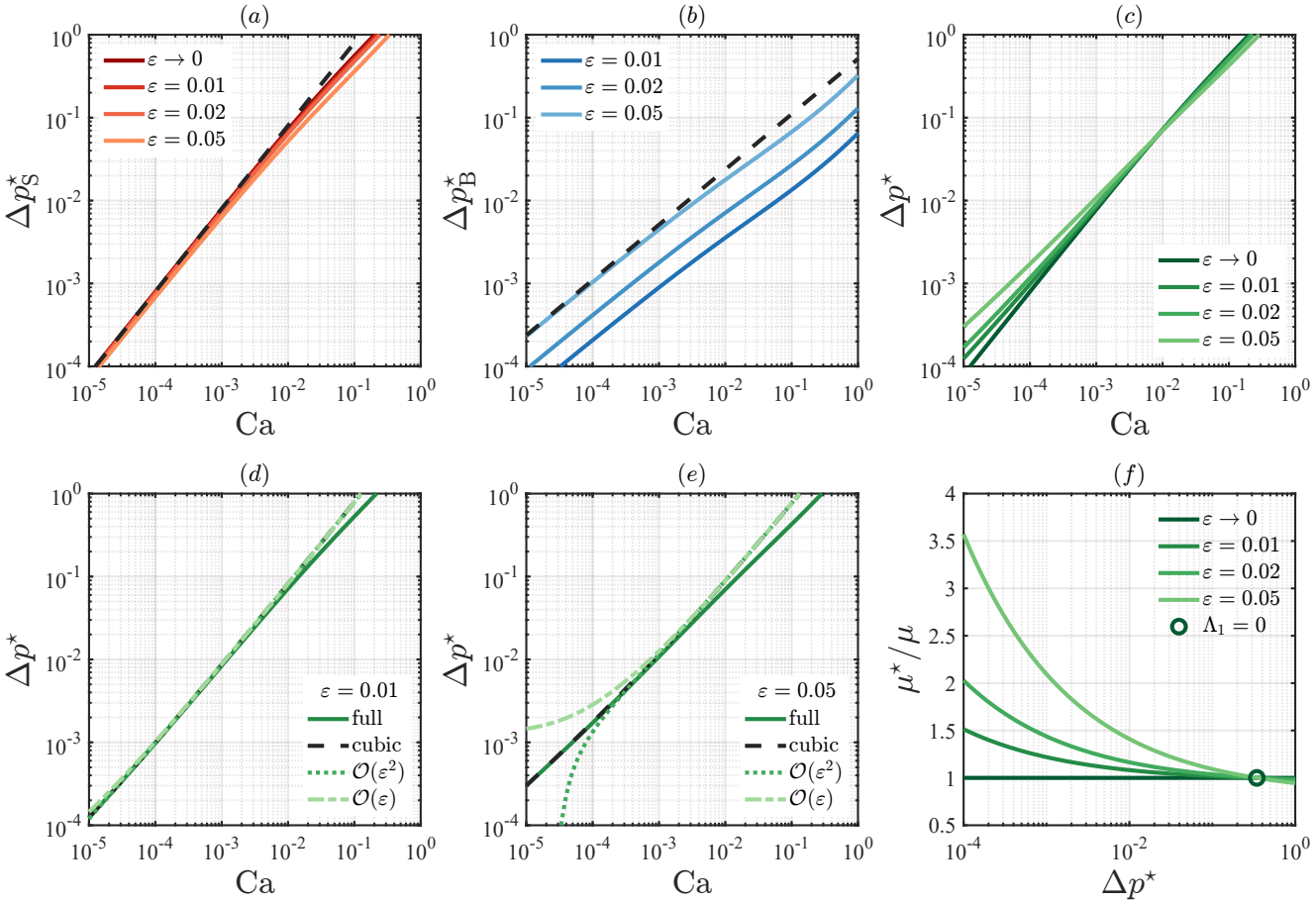

Figure 7. Dimensionless pressure drops as functions of the capillary number for different values of the channel slenderness ε, see Eqs. (30, 33), with $\gamma = 2$: (*a*) slug-related $\Delta p^\star_{\rm S}$, (*b*) bubble-related $\Delta p^\star_{\rm B}$, and (*c*) combined $\Delta p^\star$ contributions. Panels (*d*) - (*e*) compare the full-form solution with the solution of the cubic equation (35) describing the two-phase pressure evolution in the low-capillary-number regime, along with its asymptotic expansion, Eq. (36), including terms up to $\mathcal{O}(\varepsilon^2)$ and $\mathcal{O}(\varepsilon)$, for different values of the perturbation parameter: (*d*) $\varepsilon = 0.01$ and (*e*) $\varepsilon = 0.05$. Panel (*f*) shows the dimensionless effective viscosity of the two-phase system $\mu^\star/\mu$ given by Eq. (38) as a function of the dimensionless pressure drop $\Delta p^\star$ for different values of ε.

approximation is no more accurate due to the unbounded growth of higher-order contributions in the expansion for small values of the dimensionless pressure drop $\Delta p^\star$, and a larger number of terms is required to ensure the convergence of the series to the full solution to the cubic equation, see Fig. 7 (*d*) and (*e*). An appealing feature of the two-phase constitutive law (36) is that its lowest order approximation ($\varepsilon \ll 1$) admits to be recast in a Darcy-like fashion, see Eq. (2). Specifically, reverting to dimensional variables via Eq. (29) yields the relation

$$Q \sim \frac{\pi\, r^4\, \Delta p}{8\, \mu^\star\, L}, \tag{37}$$

whose non-linear character – see panel (*f*) – is embedded in the pressure-dependent effective viscosity

$$\mu^\star(\Delta p) = \mu \left[1 + \frac{r}{L}\, \Lambda_1(\Delta p)\right]. \tag{38}$$

IV. CAPILLARY BUNDLE MODEL

In this section, we adopt a capillary fiber bundle model [87–99], consisting of an array of parallel, disconnected capillary tubes of equal length, each carrying independent trains of bubbles that flow under the action of a shared external pressure drop. This model is widely used to analyze the non-linearity in the effective rheology of two-

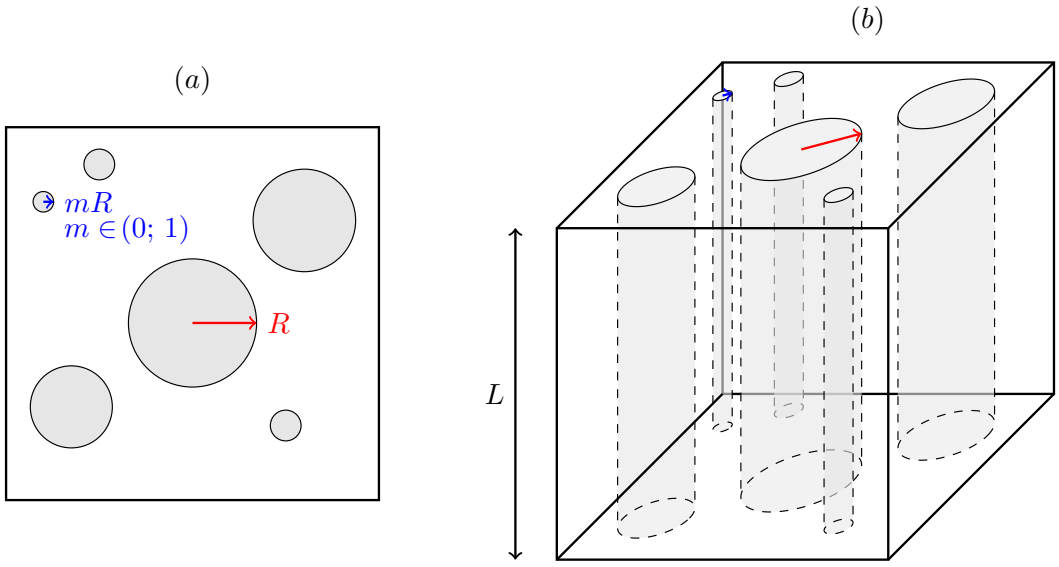

Figure 8. Schematic representation of a capillary bundle of length L, consisting of $M = 6$ tubes with radii varying from a minimum value $m\,R$ to a maximum value R. (a) Top view. (b) 3D view.

phase flow in porous media; it serves as a minimal yet insightful prototype for mimicking structural disorder through variations in properties such as capillary threshold pressures [51], wetting angles [53] or pore sizes [54].

Here, we aim to capture the influence of film dynamics in disordered porous structures by incorporating the single-capillary description of intermittent flow (as discussed in the previous sections) into the capillary bundle framework, with a focus on the effects of pore-size variability. To this end, we consider a bundle of M tubes whose average radii are sampled from a prescribed probability density function $\rho(r)$. We assume the pore radii vary from a minimum value $m\,R$ to a maximum value R (with $0 < m < 1$), as shown in Fig. 8. Under this assumption, the steady-state effective flow rate per tube, Q_M, averaged over the bundle, is given by:

$$Q_M = \int_{mR}^{R} q(r)\,\rho(r)\,\mathrm{d}r, \tag{39}$$

where $q(r)$ denotes the single-tube flow rate as a function of radius, computed as the average liquid-phase velocity times the cross-sectional area, i.e., $q(r) = \pi\,r^2\,v(r)$, with $v(r) = \dfrac{\sigma}{\mu}\,\mathrm{Ca}_l(r)$. The integral thus represents the effective contribution of a two-phase fluid mixture, averaged across the heterogeneous bundle. We consider a power-law distribution where radii are chosen with different probabilities depending on a scaling exponent γ:

$$\rho(r;\,R,\,m,\,\gamma \neq 1) = \begin{cases} \dfrac{1-\gamma}{R^{1-\gamma}\,(1-m^{1-\gamma})}\,r^{-\gamma} & \text{if} \quad mR \leq r \leq R, \\ 0 & \text{otherwise,} \end{cases} \tag{40}$$

indicating that the probability associated with the random variable r exhibits a polynomial decay. Specifically, the parameter m sets the lower cut-off of the distribution, avoiding the singularity at $r = 0$. The exponent γ controls the weight of the distribution tails, favoring smaller or larger radii for positive or negative values, respectively. As shown in the insets of Figs. 10, 11 and 12, the uniform distribution arises as a special case of (40) when $\gamma = 0$. In contrast, when the scaling exponent equals 1, Eq. (40) becomes degenerate; the case $\gamma = 1$ corresponds to the so-defined reciprocal (or log-uniform) distribution:

$$\rho(r;\,R,\,m,\,1) = \begin{cases} -\dfrac{1}{\ln m}\,r^{-1} & \text{if} \quad mR \leq r \leq R, \\ 0 & \text{otherwise.} \end{cases} \tag{41}$$

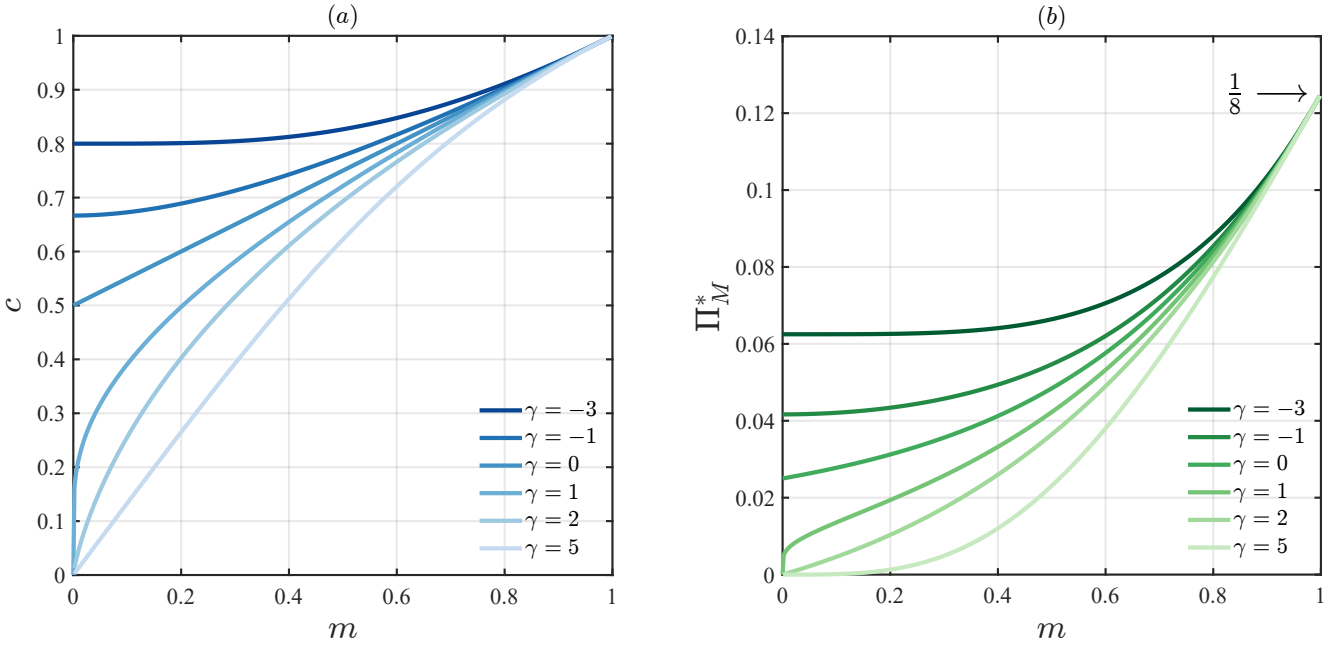

Figure 9. Variation of (a) the constant c defining the average pore radius relative to the largest pore – see Eq. (42) – and (b) the single-phase dimensionless permeability Π^*_M – see Eq. (46) – as functions of the lower cutoff m, for different values of the scaling exponent γ, based on the power-law pore-size distribution, given in Eq. (43), associated with the capillary bundle model.

A. Dimensionless formulation

A critical aspect of gas–liquid intermittent flow, often neglected in conventional capillary bundle models, is the ability of bubbles to move past the carrier fluid. To investigate the impact of film-induced dynamics on the effective rheology, we develop a dimensionless formulation of the capillary bundle model building on our single-channel description. To this end, starting from Eqs. (40, 41), we compute the average radius of the distribution $\bar{r}$ by integrating the product $\rho\, r$ over the interval $[m\, R;\, R]$, yielding

$$\bar{r} = c\, R, \quad \text{where} \quad c\,(\gamma,\, m) = \begin{cases} \dfrac{m-1}{\ln m} & \text{if} \quad \gamma = 1, \\ \dfrac{m\,\ln m}{m-1} & \text{if} \quad \gamma = 2, \\ \dfrac{1-\gamma}{2-\gamma}\,\dfrac{1-m^{2-\gamma}}{1-m^{1-\gamma}} & \text{otherwise.} \end{cases} \tag{42}$$

Figure 9 (a) shows the dependence of the constant c on the parameters γ and m. The channel radius is then made dimensionless as $r^* = r/\bar{r}$, while the dimensionless probability distribution is obtained as $\rho^* = \bar{r}\,\rho$. In view of Eq. (42), its expression over the dimensionless range of bundle radii, $r^* \in [m/c;\, 1/c]$, reads as follows:

$$\rho^*(r^*) = \begin{cases} -\dfrac{1}{\ln m}\,(r^*)^{-1} & \text{if} \quad \gamma = 1, \\ \dfrac{c^{1-\gamma}\,(1-\gamma)}{1-m^{1-\gamma}}\,(r^*)^{-\gamma} & \text{otherwise.} \end{cases} \tag{43}$$

The effective flow rate given in Eq. (39) can therefore be expressed in dimensionless form as:

$$Q_M = \frac{\pi\,\sigma}{\mu}\,R^2\,Q^*_M, \quad \text{with} \quad Q^*_M = c^2 \int_{m/c}^{1/c} (r^*)^2\ \mathrm{Ca}_l(r^*)\,\rho^*(r^*)\,\mathrm{d}r^*. \tag{44}$$

In dimensionless term, each tube in the bundle is subjected to a pressure drop Δp^*, as defined in Sec. II B. Thus, the capillary number of the liquid slugs flowing through an individual pore, Ca_l, is computed by first solving Eq. (17) numerically for the reduced capillary number z, and then applying the transformation given in Eq. (19). However, to

adapt this framework to the capillary bundle model – where the channel radius r is no longer constant but instead sampled from the probability distribution given by (43) – a fixed representative length scale must be introduced to express the tube length L in dimensionless form. Selecting the maximum pore radius R as the reference length scale enables the definition of the slenderness $L^{**} = L/R$ at the bundle level. This quantity is independent of the distribution parameters m and γ, and reflects the most restrictive scenario in terms of model applicability. In fact, smaller pores yield higher slenderness values, extending the region of the parametric space where the model remains valid for a given number of bubbles (see Sec. III B), while using R provides a conservative estimate. Using the relation $L^* = L^{**}/(c\,r^*)$ – along with Eq. (14) and the joint substitution of Eq. (21) and Eq. (6) – allows recasting Eq. (17) in terms of the dimensionless radius r^*:

$$\Delta p^* = \frac{8}{3}\,z^3\left(1-\frac{A\,z^2}{1+\alpha\,A\,z^2}\right)^2\frac{(L^{**})^2}{(c\,r^*)^2}\Bigg[1-\Phi\left(1-\frac{A\,z^2}{1+\alpha\,A\,z^2}\right)^{-2}+ \\ -\frac{2}{3}N\frac{c\,r^*}{L^{**}}\left(1-\frac{A\,z^2}{1+\alpha\,A\,z^2}\right)\Bigg]+N\,\frac{L^{**}}{c\,r^*}\Bigg[2\left(\frac{1+T_f\,z^2}{1+Z_f\,z^2}-\frac{1+T_r\,z^2}{1+Z_r\,z^2}\right)+ \\ +\left(\frac{M_f\,z^3+N_f\,z^4}{1+O_f\,z^3}-\frac{M_r\,z^3+N_r\,z^4}{1+O_r\,z^3}\right)\Bigg]. \tag{45}$$

We begin by analyzing the single-phase flow condition: the case where the flow consists entirely of liquid corresponds to setting $\Phi \equiv 0$ and $N \equiv 0$ in Eq. (45). In this limit, the dimensionless flow rate can be computed analytically from Eq. (44), yielding a closed-form expression for the dimensionless permeability Π_M^* of the bundle that depends solely on the pore-scale statistical descriptors γ and m:

$$\Pi_M^* = \frac{Q_M^*\,L^{**}}{\Delta p^*/L^{**}} = \begin{cases} \dfrac{m^4-1}{32\,\ln m} & \text{if} \quad \gamma = 1, \\ \dfrac{1}{2}\,\dfrac{m^4\,\ln m}{m^4-1} & \text{if} \quad \gamma = 5, \\ \dfrac{1}{8}\,\dfrac{1-\gamma}{5-\gamma}\,\dfrac{1-m^{5-\gamma}}{1-m^{1-\gamma}} & \text{otherwise.} \end{cases} \tag{46}$$

For values of $m \to 1$, the power-law probability density function of pore radii becomes increasingly narrow and tends toward a Dirac delta function (unit impulse), collapsing the distribution to a single pore size. In this limit, the bundle model becomes homogeneous, and – as highlighted in Fig. 9 (*b*) – its dimensionless permeability converges to 1/8. This value reflects the permeability of a single circular tube (as given by Poiseuille flow) and defines the geometric factor that links microscale flow to macroscale permeability in the Darcy law. Compared to the homogeneous limit, any heterogeneous power-law distribution of pore sizes yields a lower permeability, and Π_M^* is found to be a strictly increasing function of m for any given γ. Moreover, two distinct classes of distributions emerge as $m \to 0$, corresponding to the inclusion of infinitesimally small pores. For the reciprocal distribution ($\gamma = 1$) or those heavy-tailed toward small radii ($\gamma > 1$), the dimensionless permeability approaches zero, indicating a blockage of flow due to the dominance of near-zero pore sizes. In contrast, for distributions strongly weighted toward larger pores ($\gamma < 1$), the permeability remains finite for vanishing m and is given by $\Pi_M^* \to \dfrac{1}{8}\,\dfrac{1-\gamma}{5-\gamma}$. This analytical expression captures the interplay between local heterogeneity and bulk flow resistance, highlighting the non-trivial role of pore-size distribution in determining the effective permeability of the bundle, even under single-phase flow conditions.

B. Modeling of non-Darcian two-phase flows

Immiscible two-phase flow of Newtonian fluids in porous media exhibits complex and non-linear dynamics. In such systems, the Darcy law – which assumes a linear relationship between flow rate and pressure drop, valid for a single-phase laminar flow – breaks down [39]. This deviation arises from the dependence of permeability on the capillary number, which captures the evolving ganglion structure of the phases, ultimately affecting flow resistance. Two distinct flow patterns are typically observed, governed by the visco-capillary balance: simultaneous percolation of both phases and intermittent flow characterized by alternating phase invasion. As summarized in Table I, an extensive body of research has been devoted to modeling the transition between these regimes – driven by an increase in the capillary number – and leading to the development of generalized non-linear Darcy-type equations. These empirical scaling laws often take the form of power-law relationships between the imposed pressure drop Δp and the

total steady-state volumetric flow rate Q_M, expressed as:

$$\Delta p \propto Q_M^{\zeta} \quad \text{or} \quad \Delta p - \Delta p_t \propto Q_M^{\zeta}, \tag{47}$$

where Δp_t denotes a threshold pressure governing the crossover between flow regimes – for example, a depinning pressure marking the onset of flow [100] – and ζ (with $0 < \zeta < 1$) is a characteristic exponent reflecting the progressive mobilization of interfaces as the flow rate increases. The variability of the flow exponent ζ observed in the literature motivates a comparison with predictions from our capillary bundle model, which incorporates the film dynamics typical of intermittent gas–liquid flow. These results are presented and discussed in Sec. IV C.

Before addressing two-phase flow behavior, we summarize our key modeling assumptions. For computational simplicity, uniform gas saturation and bubble number are assumed across all tubes. Although larger pores are more readily invaded by the gas phase due to lower capillary entry thresholds – implying that Φ and N should increase with pore radius – our simplification preserves the dominant bulk flow characteristics and is commonly used to retain analytical tractability [51, 54]. Moreover, we focus on small capillary numbers, where interfacial tension and pore-scale geometry govern the displacement dynamics. This choice is motivated by the typical capillary number range encountered in porous media, $10^{-7} \lesssim \mathrm{Ca} \lesssim 10^{-4}$. In contrast, at higher capillary numbers ($10^{-3} \lesssim \mathrm{Ca} \lesssim 1$) – more characteristic of micro-fluidic flows [101] – viscous forces become dominant, leading to stripping of trapped phases and the subsequent formation of interconnected flow pathways [102, 103]. It is also worth noting that the evolution of the effective dimensionless pressure drop is studied as a function of the capillary number based on the mean velocity of the liquid slugs, Ca_l. This approach facilitates a direct comparison between the physics of two-phase intermittent flow and the single-phase (all-liquid) limit. Alternatively, the capillary number can be formulated at the bundle level using the Darcy velocity, which corresponds to the effective volumetric flow rate normalized by the total cross-sectional area of the porous medium, incorporating both the solid matrix and the pore spaces [104]. Still, this formulation requires the porosity of the medium to be introduced as an additional parameter, reflecting the volumetric fraction of the medium actually available for fluid flow.

C. Two-phase effective flow

We characterize the bulk behavior of the capillary bundle under varying pressure conditions and examine how different pore-size distributions influence the system. The procedure required to generate the effective flow rate-pressure curve $Q_M^*(\Delta p^*)$ involves the following computational steps.

1. *Initialization of statistical properties*: select the distribution parameter m and γ, and compute the corresponding value of the constant c, which defines the average pore radius related to the largest, according to Eq. (42).

2. *Channel configuration*: select the slenderness L^{**} of the largest capillary within the bundle, and choose an appropriate number of bubbles N and gas saturation Φ, ensuring compatibility with the applicability domain of the single-tube model described in Sec. III B.

3. *Capillary number mapping*: for each value of dimensionless pressure drop $\Delta\tilde{p}^*$ within a prescribed interval, iterate over the relevant range of dimensionless radii $r^* \in [m/c;\, 1/c]$, numerically solve Eq. (45), and obtain the corresponding solution $z(r^*)|_{\Delta\tilde{p}^*}$ expressing how the reduced capillary number varies with the dimensionless radius under a fixed pressure drop.

4. *Capillary number conversion*: transform the resulting function $z(r^*)|_{\Delta\tilde{p}^*}$ into the corresponding capillary number based on the mean slug velocity $\mathrm{Ca}_l(r^*)|_{\Delta\tilde{p}^*}$, via the analytical relation defined in Eq. (19).

5. *Flow rate computation*: evaluate numerically the integral expression for the dimensionless flow rate Q_M^*, as defined in Eq. (44).

6. *Iteration over pressure drops*: repeat steps (3) - (5) for increasing values of the dimensionless pressure drop Δp^*, avoiding flow regimes with moderate to high capillary numbers (indicatively $\mathrm{Ca} \gtrsim 10^{-2}$) where model breakdown is expected, see Sec. III B.

The obtained data are post-processed by computing the local logarithmic derivative of the pressure–flow rate curve

$$\zeta(Q_M^*) = \frac{\mathrm{d}\log \Delta p^*}{\mathrm{d}\log Q_M^*}, \tag{48}$$

providing a point-wise characterization of the scaling behavior. A finite difference approximation is used to implement Eq. (48), with central differences applied at interior points of the domain, and forward or backward differences at the endpoints.

We now analyze the evolution of the volumetric flow rate and the apparent flow exponent as a function of increasing pressure drop, for different pore-size probability distributions. In our simulations, the length of the bundle relative to its largest pore is fixed at $L^* = 100$. The results presented in Figs. 10, 11, and 12 differ in the lower cut-off of the power-law pore-size distribution, set to $m = 0.01$, $m = 0.5$ and $m = 0.9$, respectively. Varying this parameter allows us to investigate the impact of including smaller pores in the distribution, with values closer to unity indicating a more homogeneous bundle in terms of pore size. Each figure consists of a 3×3 panel grid: rows correspond to the scaling exponents $\gamma = -3$, 0 and 3, representing distributions with tails favoring larger pores, uniform distributions, and those favoring smaller pores, respectively, as illustrated in each inset plot and displayed in the first column. Columns indicate increasing bubble number per tube: $N = 1$ (single-bubble case), $N = 5$, and $N = 10$. In each plot, curves with different linestyles represent different values of gas saturation, selected within the admissible range defined in Sec. III B, as specified in the central column of each figure. The results are presented in dimensionless form as $\Delta p^*(Q_M^*)$ (left ordinate axis), accompanied by the corresponding logarithmic derivative $\zeta(Q_M^*)$, as defined in Eq. (48) (right ordinate axis), with the benchmark value predicted by Bretherton's theory ($\zeta = 2/3$) highlighted by a light red dashed line.

To facilitate the analysis, we begin by examining the effective rheology of intermittent flow in cases where the pore-size distributions are moderately or highly narrow and centered around larger radii. A comparison between Figs. 11 and 12 reveals similar trends and values for corresponding power-law exponents and bubble numbers. This indicates the primary role of largest pores in governing the flow behavior – although, as will be shown later, smaller pores also have a non-negligible influence. Furthermore, the similarity across rows suggests that when the pore radii are confined to a sufficiently narrow range, the direction in which the distribution tails are weighted (i.e., toward smaller or larger pores) has a limited influence on the overall flow characteristics. For these probability distributions, the apparent flow exponent is a strictly increasing function of the dimensionless flow rate, starting from a baseline value of $\zeta = 2/3$, characteristic of the Bretherton regime. Comparing the columns, we observe that increasing the bubble number leads to families of curves that are more tightly clustered and progressively flatter, approaching the limiting value of 2/3. Similarly, increasing the gas saturation reduces the extent of the transition toward regimes with higher apparent flow exponents. This behavior can be attributed to the enhanced influence of bubbles on the flow: as saturation increases, more viscous liquid segments are replaced by inviscid gas, diminishing the overall slug-related contribution and thus dampening the rheological response of the system.

Finally, we turn our attention to porous systems that include the smallest radii, which display the richest and most complex rheological behavior, see Fig. 10. Unlike earlier scenarios, in this case the scaling exponent γ is a key factor, as evident from the differences in the magnitude of the dimensionless flow rate: when the distribution favors the smallest pores (third row of subplots), the flow rate is up to three orders of magnitude lower than in the cases where the distribution is uniform (second row) or favors larger pores (first row), under the same range of pressure drops. A distinctive feature of these systems is the emergence of a non-trivial rheological response, due to the inclusion of very small pores. Specifically, in most regimes, the trend of the apparent flow exponent becomes non-monotonic with increasing flow rate: it initially rises from values close to Bretherton's limit, reaches a peak, and then decreases – sometimes even falling below $\zeta = 2/3$. When only a single short bubble per tube is present, this peak tends to be close to one, indicating that the bubble acts as a minor perturbation to the single-phase (all-liquid) flow – a behavior confirmed at the single-tube level by the asymptotic analysis presented in Sec. III C. As saturation increases, the peak diminishes and shifts toward lower flow rates. Increasing the number of bubbles causes the curves to flatten progressively, until reaching a regime where the pressure drop becomes bubble-dominated. In this limit – characterized by high gas saturation and a large number of bubbles – see subplots (c) and (f) for $\Phi = 0.8$ – the rheological response exhibits a decreasing trend in the apparent flow exponent, with an extended initial regime where the exponent remains constant at $\zeta = 2/3$. The observed behavior results from the competing impact of viscous and interfacial resistance within narrow pores, giving rise to a broad range of non-linear rheological responses influenced by both pore-scale structural disorder and bubble configuration.

In general, the values of the characteristic exponent predicted by our capillary bundle model fall within the range $0.5 < \zeta < 1$, consistent with those reported in the literature (see Table I). However, direct comparisons with experimental studies should be made cautiously, as those typically adopt fractional and total flow rate as control parameters, rather than the imposed pressure gradient. Among theoretical and numerical works, our findings closely align with those of Roy *et al.* [51], particularly in regimes characterized by sufficiently narrow pore-size distributions and bubble-dominated pressure drops (e.g., at high gas saturation or bubble number). In these regimes, our model reproduces their analytical prediction of an exponent equal to 3/2 – noting that they express flow non-linearity through the inverse exponent, i.e., $1/\zeta$ – once the pressure drop is sufficient to activate the flow. Our results complement their analysis by also capturing the transition toward alternative non-linear regimes driven by increasing flow rate and the

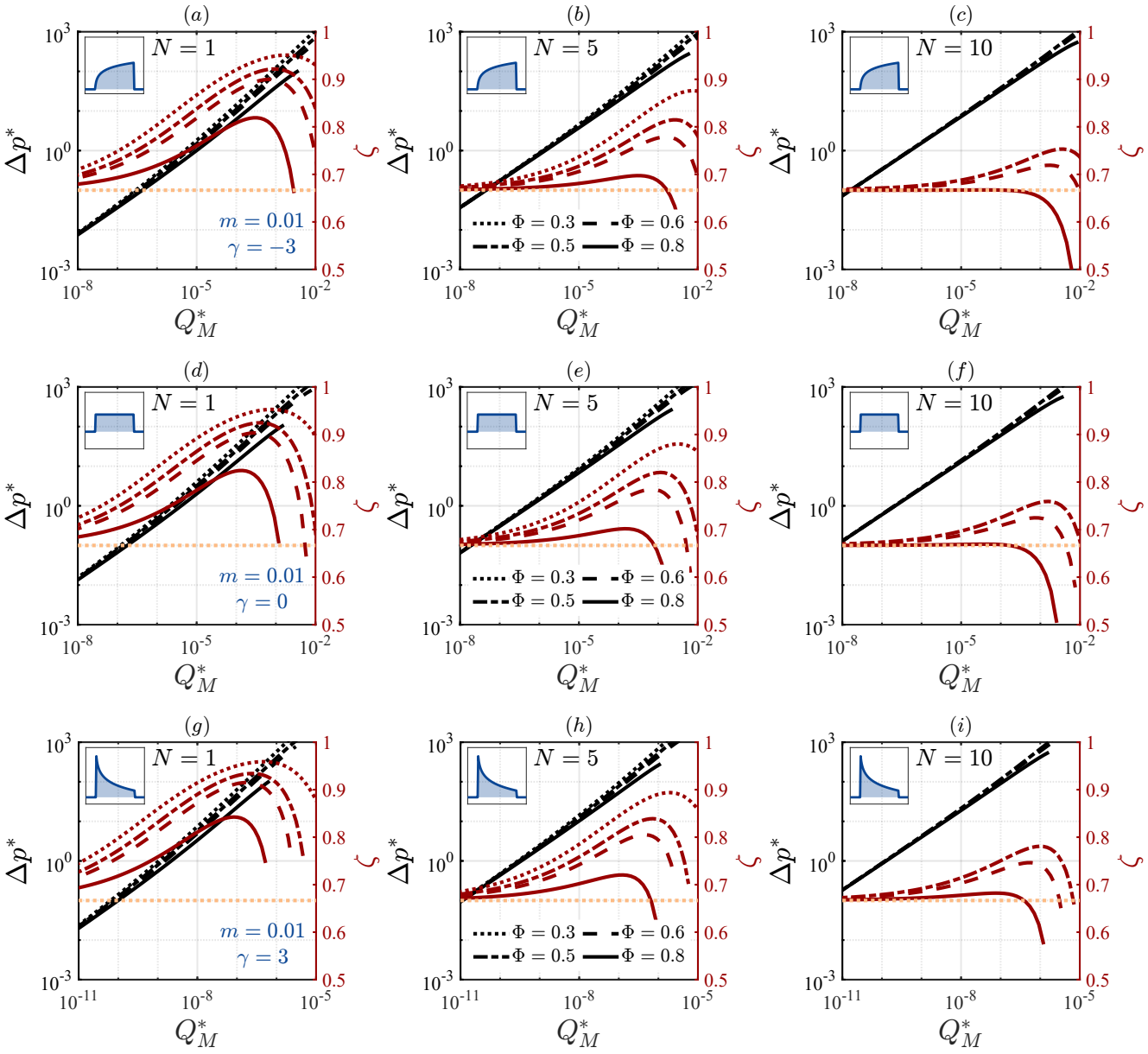

Figure 10. Evolution of the dimensionless pressure drop, Δp^* (left axis), and apparent flow exponent, ζ (right axis), versus the dimensionless flow rate, Q_M^*. Each row corresponds to a pore-radii distribution exponent γ, each column to a bubble number N, and linestyles denote the gas saturation Φ. Each subplot includes an inset illustrating the corresponding pore-size probability distribution. Results shown here are for a capillary bundle model with slenderness $L^* = 100$ and lower cut-off $m = 0.01$.

inclusion of the smallest pores.

V. CONCLUSIONS

Understanding the flow of two immiscible phases in porous media has significant implications for both subsurface and biological systems. In this work, we have explored the non-trivial rheological response of two-phase intermittent flow in porous media under steady-state conditions, focusing on the impact of structural disorder on flow behavior. Motivated by the rich and subtle physics underlying the effective rheology of bubbles in confined geometries [105], we developed an analytical framework to predict the pressure drop, based on the superposition of viscous losses in liquid slugs and interfacial contributions from gas bubbles. We extended this model to a porous medium idealized as

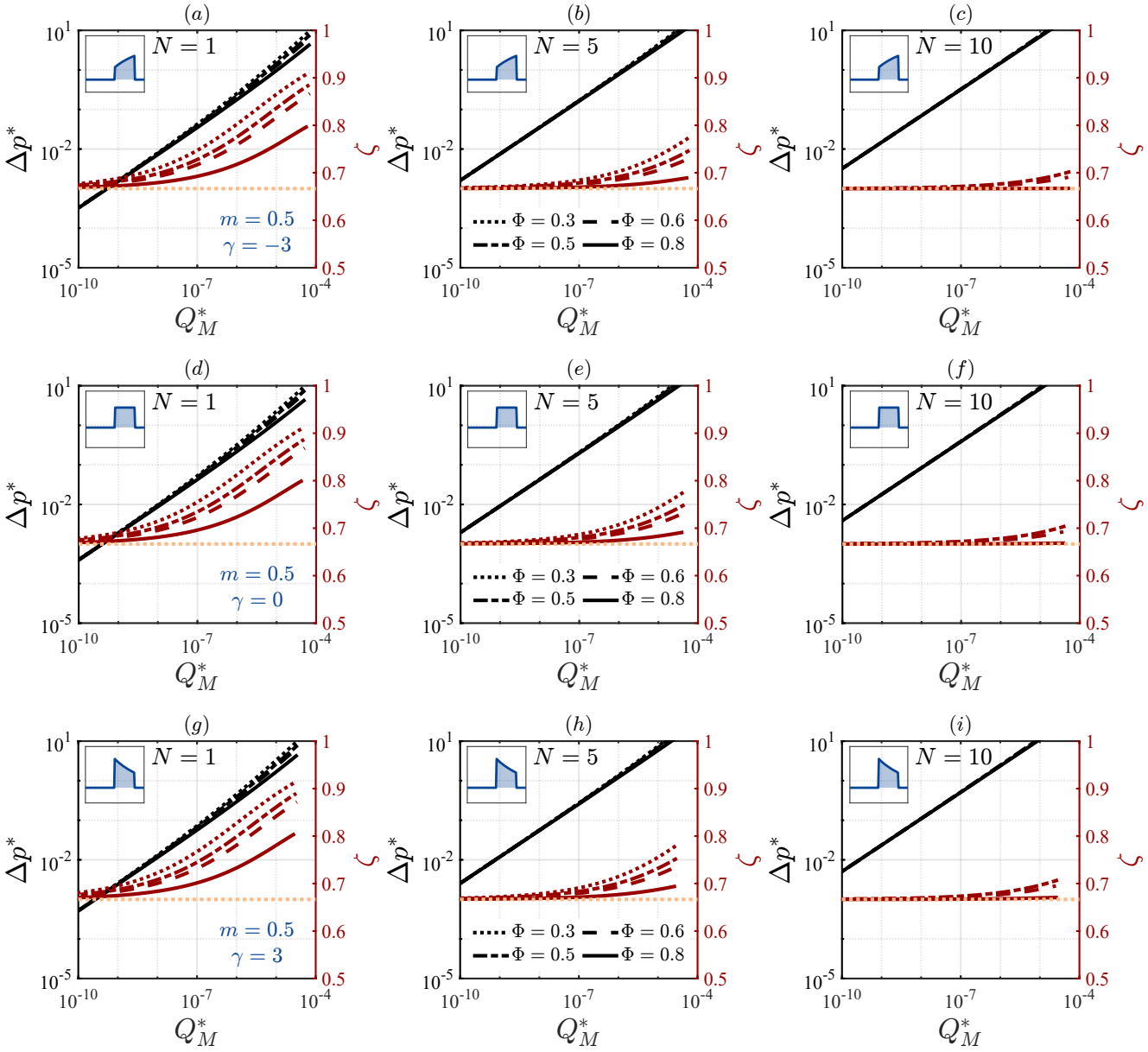

Figure 11. Evolution of the dimensionless pressure drop, Δp^* (left axis), and apparent flow exponent, ζ (right axis), versus the dimensionless flow rate, Q_M^*. Each row corresponds to a pore-radii distribution exponent γ, each column to a bubble number N, and linestyles denote the gas saturation Φ. Each subplot includes an inset illustrating the corresponding pore-size probability distribution. Results shown here are for a capillary bundle model with slenderness $L^* = 100$ and lower cut-off $m = 0.5$.

a capillary bundle, thereby incorporating film-induced lubrication dynamics. By varying the shape and width of the pore-size distribution through two control parameters, we characterized the non-linear flow regime as a function of gas saturation, bubble number, and structural heterogeneity.

Numerical results reveal that largest pore dictate the magnitude of the total flow rate. Moderately and extremely narrow distributions centered around the largest radii are largely insensitive to asymmetries in the distribution tails. In such nearly homogeneous bundles, a train of inviscid bubbles displays a smooth crossover from a Bretherton-like regime (with scaling exponent $\zeta = 2/3$) at low pressure drops to a regime with weaker sub-linearity ($2/3 < \zeta < 1$) as the imposed pressure drop increases. Conversely, the inclusion of smaller pores often introduces a non-monotonic rheological response, marked by a peak in the apparent flow exponent. At higher pressures, the activation of these smaller pores dampens the system's overall response – due to their higher hydraulic and interfacial resistance – leading to flow regimes possibly characterized by exponents even below the canonical 2/3 threshold. This complex

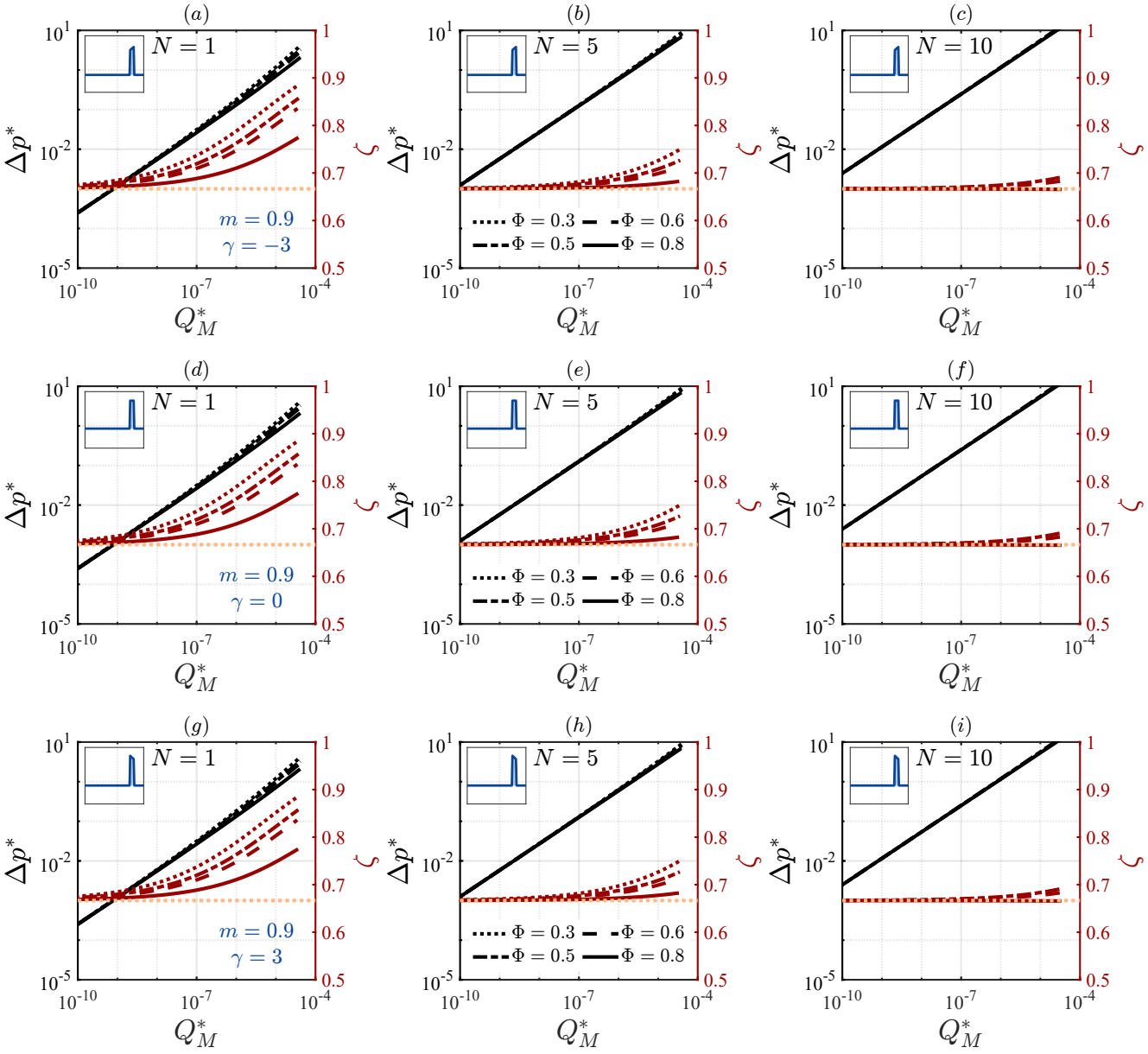

Figure 12. Evolution of the dimensionless pressure drop, Δp^* (left axis), and apparent flow exponent, ζ (right axis), versus the dimensionless flow rate, Q_M^*. Each row corresponds to a pore-radii distribution exponent γ, each column to a bubble number N, and linestyles denote the gas saturation Φ. Each subplot includes an inset illustrating the corresponding pore-size probability distribution. Results shown here are for a capillary bundle model with slenderness $L^* = 100$ and lower cut-off $m = 0.9$.

behavior can be qualitatively interpreted by viewing the total flow rate as superposition of contributions from distinct conductive pathways [106]: liquid slugs that follow linear scaling with velocity ($\zeta = 1$), and gas bubbles obeying the sub-linear Bretherton scaling ($\zeta = 2/3$). As a result, the effective two-phase rheology emerges from the interplay between pore-scale geometrical disorder and the spatial configuration of the gas phase within individual pores.

The proposed analytical approach, grounded in first principles, offers a promising route to predicting transport properties directly from the geometrical characteristics of the medium and the spatial phase distribution. In the present study, we simplified the analysis under the hypotheses of inviscid bubbles, no recirculation effects, and fixed values of bubble number and saturation per tube. Future work should investigate how relaxing these assumptions may affect the effective rheology of two-phase flow in disordered porous systems. While capillary bundle models without lateral interconnections offer a simplified representation of multiphase imbibition dynamics, they fail to capture cross-flow and mixing phenomena that arise in realistic porous structures. To improve predictive capabilities, interacting

capillary bundle models – starting from those pioneered by Dong *et al.* [107] – have been proposed. However, these frameworks introduce new challenges related to mixing and flow partitioning at the nodes, where phase redistribution significantly affects the local effective rheology [108, 109].

ACKNOWLEDGMENTS

This work was partly supported by the Research Council of Norway through its Centers of Excellence funding scheme, project number 262644, and the INTPART program, project number 309139. We furthermore acknowledge funding from the European Research Council (Grant Agreement 101141323 AGIPORE). Prof. Picchi acknowledges funding from the European Union 'NextGenerationEU', Ministero dell'Università e della Ricerca (MUR) 'Italiadomani' Piano Nazionale di Ripresa e Resilienza (PNRR), Mission 4, Research Project PRIN 2022 'Predictive forecasting and risk assessment for CO_2 transport in pipelines', MUR code: 20229JPN53; CUP Master code: J53D23002000006; CUP code: D53D23003250006.

[1] J. Bear, *Dynamics of Fluids in Porous Media* (Dover Publications, Mineola, New York, 1988).
[2] F. A. L. Dullien, *Porous Media: Fluid Transport and Pore Structure*, 2nd ed. (Academic Press, San Diego, California, 1992).
[3] V. Joekar-Niasar, S. M. Hassanizadeh, and H. K. Dahle, Non-equilibrium effects in capillarity and interfacial area in two-phase flow: dynamic pore-network modelling, Journal of Fluid Mechanics **655**, 38 (2010).
[4] V. A. Fry, J. S. Selker, and S. M. Gorelick, Experimental investigations for trapping oxygen gas in saturated porous media for in situ bioremediation, Water Resources Research **33**, 2687 (1997).
[5] U. Böhler, J. Brauns, H. Hötzl, and M. Nahold, Air injection and soil air extraction as a combined method for cleaning contaminated sites — observations from test sites in sediments and solid rocks, in *Contaminated Soil '90: Third International KfK/TNO Conference on Contaminated Soil, 10–14 December 1990, Karlsruhe, Federal Republic of Germany*, edited by F. Arendt, M. Hinsenveld, and W. J. Van Den Brink (Springer Netherlands, Dordrecht, 1990) pp. 1039–1044.
[6] M. Suo and P. Griffith, Two-phase flow in capillary tubes, Journal of Basic Engineering **86**, 576–582 (1964).
[7] M. Wörner, A correlation for the characteristic velocity ratio to predict hydrodynamics of capillary gas–liquid taylor flow, Theoretical Foundations of Chemical Engineering **54**, 3 (2020).
[8] E. Vasserman, Pressure waves in capillaries containing liquid plugs: numerical simulation, in *Poromechanics II: Proceedings of the Second Biot Conference on Poromechanics, Grenoble, France, 26-28 August 2002*, edited by J.-L. Auriault, C. Geindreau, P. Royer, and J.-F. Bloch (CRC Press, London, 2002) pp. 845–849, ebook published 2020.
[9] A. Günther and M. T. Kreutzer, Multiphase flow, in *Micro Process Engineering* (John Wiley & Sons, Ltd, 2009) Chap. 1, pp. 1–40.
[10] R. W. Lockhart and R. C. Martinelli, Proposed correlation of data for isothermal two-phase, two-component flow in pipes, Chemical Engineering Progress **45**, 39 (1949).
[11] D. Chisholm, A theoretical basis for the lockhart-martinelli correlation for two-phase flow, International Journal of Heat and Mass Transfer **10**, 1767 (1967).
[12] Y. Taitel and A. E. Dukler, A model for predicting flow regime transitions in horizontal and near horizontal gas-liquid flow, AIChE Journal **22**, 47 (1976).
[13] D. Beattie and P. Whalley, A simple two-phase frictional pressure drop calculation method, International Journal of Multiphase Flow **8**, 83 (1982).
[14] K. Triplett, S. Ghiaasiaan, S. Abdel-Khalik, A. LeMouel, and B. McCord, Gas–liquid two-phase flow in microchannels: Part ii: void fraction and pressure drop, International Journal of Multiphase Flow **25**, 395 (1999).
[15] A. Kawahara, P.-Y. Chung, and M. Kawaji, Investigation of two-phase flow pattern, void fraction and pressure drop in a microchannel, International Journal of Multiphase Flow **28**, 1411 (2002).
[16] M. J. F. Warnier, M. H. J. M. de Croon, E. V. Rebrov, and J. C. Schouten, Pressure drop of gas–liquid taylor flow in round micro-capillaries for low to intermediate reynolds numbers, Microfluidics and Nanofluidics **8**, 33 (2010).
[17] A. C. Payatakes and M. M. Dias, Immiscible microdisplacement and ganglion dynamics in porous media, Reviews in Chemical Engineering **2**, 85 (1984).
[18] L. Rayleigh, On the capillary phenomena of jets, Proceedings of the Royal Society of London **29**, 71 (1879).
[19] G. I. Taylor, The formation of emulsions in definable fields of flow, Proceedings of the Royal Society of London A, **146**, 501 (1934).
[20] G. I. Taylor, Deposition of a viscous fluid on the wall of a tube, Journal of Fluid Mechanics **10**, 161–165 (1961).
[21] F. P. Bretherton, The motion of long bubbles in tubes, Journal of Fluid Mechanics **10**, 166 (1961).
[22] P. Aussillous and D. Quéré, Quick deposition of a fluid on the wall of a tube, Physics of Fluids **12**, 2367 (2000).
[23] G. J. Hirasaki and J. B. Lawson, Mechanisms of foam flow in porous media: Apparent viscosity in smooth capillaries, Society of Petroleum Engineers Journal **25**, 176 (1985).

[24] J. Ratulowski and H.-C. Chang, Transport of gas bubbles in capillaries, Physics of Fluids A: Fluid Dynamics **1**, 1642–1655 (1989).

[25] K. G. Kornev, A. V. Neimark, and A. N. Rozhkov, Foam in porous media: thermodynamic and hydrodynamic peculiarities, Advances in Colloid and Interface Science **82**, 127 (1999).

[26] H. A. Stone, Interfaces: in fluid mechanics and across disciplines, Journal of Fluid Mechanics **645**, 1–25 (2010).

[27] A. Etminan, Y. S. Muzychka, and K. Pope, A review on the hydrodynamics of taylor flow in microchannels: Experimental and computational studies, Processes **9**, 870 (2021).

[28] M. T. Kreutzer, F. Kapteijn, J. A. Moulijn, C. R. Kleijn, and J. J. Heiszwolf, Inertial and interfacial effects on pressure drop of taylor flow in capillaries, AIChE Journal **51**, 2428 (2005).

[29] W. L. Olbricht, Pore-scale prototypes of multiphase flow in porous media, Annual Review of Fluid Mechanics **28**, 187 (1996).

[30] A. G. Hunt and M. Manga, Effects of bubbles on the hydraulic conductivity of porous materials – theoretical results, Transport in Porous Media **52**, 51 (2003).

[31] J. Stark and M. Manga, The motion of long bubbles in a network of tubes, Transport in Porous Media **40**, 201–218 (2000).

[32] J. Koplik and T. J. Lasseter, Two-phase flow in random network models of porous media, Society of Petroleum Engineers Journal **25**, 89–100 (1985).

[33] S. Schlüter, S. Berg, M. Rücker, R. T. Armstrong, H. Vogel, R. Hilfer, and D. Wildenschild, Pore-scale displacement mechanisms as a source of hysteresis for two-phase flow in porous media, Water Resources Research **52**, 2194–2205 (2016).

[34] R. T. Armstrong, J. E. McClure, M. A. Berrill, M. Rücker, S. Schlüter, and S. Berg, Beyond darcy's law: The role of phase topology and ganglion dynamics for two-fluid flow, Phys. Rev. E **94**, 043113 (2016).

[35] D. Picchi and I. Battiato, The impact of pore-scale flow regimes on upscaling of immiscible two-phase flow in porous media, Water Resources Research **54**, 6683 (2018).

[36] D. Picchi and I. Battiato, Relative permeability scaling from pore-scale flow regimes, Water Resources Research **55**, 3215–3233 (2019).

[37] D. Picchi and I. Battiato, Scaling of two-phase water-steam relative permeability and thermal fluxes in porous media, International Journal of Multiphase Flow **129**, 103257 (2020).

[38] D. Picchi, A. Ullmann, and N. Brauner, Modeling of core-annular and plug flows of newtonian/non-newtonian shear-thinning fluids in pipes and capillary tubes, International Journal of Multiphase Flow **103**, 43 (2018).

[39] S. Roy, S. Sinha, and A. Hansen, Immiscible two-phase flow in porous media: Effective rheology in the continuum limit, Transport in Porous Media **151**, 1295–1311 (2024).

[40] H. Darcy, *Les fontaines publiques de la ville de Dijon* (Victor Dalmont, Paris, 1856) p. 647.

[41] Y. Gao, Q. Lin, B. Bijeljic, and M. J. Blunt, Pore-scale dynamics and the multiphase darcy law, Phys. Rev. Fluids **5**, 013801 (2020).

[42] K. T. Tallakstad, H. A. Knudsen, T. Ramstad, G. Løvoll, K. J. Måløy, R. Toussaint, and E. G. Flekkøy, Steady-state two-phase flow in porous media: Statistics and transport properties, Physical Review Letters **102**, 074502 (2009).

[43] K. T. Tallakstad, G. Løvoll, H. A. Knudsen, T. Ramstad, E. G. Flekkøy, and K. J. Måløy, Steady-state, simultaneous two-phase flow in porous media: An experimental study, Physical Review E **80**, 036308 (2009).

[44] E. M. Rassi, S. L. Codd, and J. D. Seymour, Nuclear magnetic resonance characterization of the stationary dynamics of partially saturated media during steady-state infiltration flow, New Journal of Physics **13**, 015007 (2011).

[45] E. M. Rassi, S. L. Codd, and J. D. Seymour, Corrigendum: Nuclear magnetic resonance characterization of the stationary dynamics of partially saturated media during steady-state infiltration flow (2011 new j. phys. 13 015007), New Journal of Physics **16**, 039501 (2014).

[46] S. Sinha and A. Hansen, Effective rheology of immiscible two-phase flow in porous media, EPL (Europhysics Letters) **99**, 44004 (2012).

[47] A. G. Yiotis, L. Talon, and D. Salin, Blob population dynamics during immiscible two-phase flows in reconstructed porous media, Physical Review E **87**, 033001 (2013).

[48] O. Aursjø, M. Erpelding, K. T. Tallakstad, E. G. Flekkøy, A. Hansen, and K. J. Måløy, Film flow dominated simultaneous flow of two viscous incompressible fluids through a porous medium, Frontiers in Physics **2**, 63 (2014).

[49] T. Chevalier, D. Salin, L. Talon, and A. G. Yiotis, History effects on nonwetting fluid residuals during desaturation flow through disordered porous media, Physical Review E **91**, 043015 (2015).

[50] S. Sinha, A. T. Bender, M. Danczyk, K. Keepseagle, C. A. Prather, J. M. Bray, L. W. Thrane, J. D. Seymour, S. L. Codd, and A. Hansen, Effective rheology of two-phase flow in three-dimensional porous media: Experiment and simulation, Transport in Porous Media **119**, 77–94 (2017).

[51] S. Roy, A. Hansen, and S. Sinha, Effective rheology of two-phase flow in a capillary fiber bundle model, Frontiers in Physics **7**, 92 (2019).

[52] A. G. Yiotis, A. Dollari, M. E. Kainourgiakis, D. Salin, and L. Talon, Nonlinear darcy flow dynamics during ganglia stranding and mobilization in heterogeneous porous domains, Physical Review Fluids **4**, 114302 (2019).

[53] H. Fyhn, S. Sinha, S. Roy, and A. Hansen, Rheology of immiscible two-phase flow in mixed wet porous media: Dynamic pore network model and capillary fiber bundle model results, Transport in Porous Media **139**, 491–512 (2021).

[54] S. Roy, S. Sinha, and A. Hansen, Role of pore-size distribution on effective rheology of two-phase flow in porous media, Frontiers in Water **3**, 709833 (2021).

[55] Y. Zhang, B. Bijeljic, Y. Gao, Q. Lin, and M. J. Blunt, Quantification of nonlinear multiphase flow in porous media,

Geophysical Research Letters **48**, e2020GL090477 (2021).
[56] Y. Zhang, B. Bijeljic, and M. J. Blunt, Nonlinear multiphase flow in hydrophobic porous media, Journal of Fluid Mechanics **934**, R3 (2022).
[57] H. Fyhn, S. Sinha, and A. Hansen, Effective rheology of immiscible two-phase flow in porous media consisting of random mixtures of grains having two types of wetting properties, Frontiers in Physics **11**, 1175426 (2023).
[58] A. Anastasiou, I. Zarikos, A. Yiotis, L. Talon, and D. Salin, Steady-state dynamics of ganglia populations during immiscible two-phase flows in porous micromodels: Effects of the capillary number and flow ratio on effective rheology and size distributions, Transport in Porous Media **151**, 469–493 (2024).
[59] P.-Y. Chung and M. Kawaji, The effect of channel diameter on adiabatic two-phase flow characteristics in microchannels, International Journal of Multiphase Flow **30**, 735–761 (2004).
[60] E. Walsh, Y. Muzychka, P. Walsh, V. Egan, and J. Punch, Pressure drop in two phase slug/bubble flows in mini scale capillaries, International Journal of Multiphase Flow **35**, 879–884 (2009).
[61] R. Gupta, D. Fletcher, and B. Haynes, Taylor flow in microchannels: A review of experimental and computational work, The Journal of Computational Multiphase Flows **2**, 1 (2010).
[62] C. N. Baroud, F. Gallaire, and R. Dangla, Dynamics of microfluidic droplets, Lab on a Chip **10**, 2032 (2010).
[63] H. Minagawa, H. Asama, and T. Yasuda, Void fraction and frictional pressure drop of gas-liquid slug flow in a microtube, Transactions of the Japan Society of Mechanical Engineers, Series B **79**, 1500 (2013).
[64] M. Mac Giolla Eain, V. Egan, J. Howard, P. Walsh, E. Walsh, and J. Punch, Review and extension of pressure drop models applied to taylor flow regimes, International Journal of Multiphase Flow **68**, 1 (2015).
[65] D. Ni, F. Hong, P. Cheng, and G. Chen, Numerical study of liquid-gas and liquid-liquid taylor flows using a two-phase flow model based on arbitrary-lagrangian–eulerian (ale) formulation, International Communications in Heat and Mass Transfer **88**, 37–47 (2017).
[66] A. Kawahara, Y. Yonemoto, and Y. Arakaki, Pressure drop for gas and polymer aqueous solution two-phase flows in horizontal circular microchannel, Flow, Turbulence and Combustion **105**, 1325–1344 (2020).
[67] R. Kurimoto, K. Nakazawa, H. Minagawa, and T. Yasuda, Prediction models of void fraction and pressure drop for gas-liquid slug flow in microchannels, Experimental Thermal and Fluid Science **88**, 124 (2017).
[68] R. Kurimoto, H. Tsubouchi, H. Minagawa, and T. Yasuda, Pressure drop of gas–liquid taylor flow in square microchannels, Microfluidics and Nanofluidics **24**, 5 (2019).
[69] R. Kurimoto, K. Hayashi, and A. Tomiyama, Pressure drop and bubble velocity in taylor flow through square microchannel, Microfluidics and Nanofluidics **28**, 58 (2024).
[70] T. Fouilland, D. Fletcher, and B. Haynes, Film and slug behaviour in intermittent slug–annular microchannel flows, Chemical Engineering Science **65**, 5344–5355 (2010).
[71] G. Hagen, Ueber die bewegung des wassers in engen cylindrischen röhren, Annalen der Physik **122**, 423–442 (1839).
[72] J. L. M. Poiseuille, Recherches expérimentales sur le mouvement des liquides dans les tubes de très petits diamètres, Mémoires présentés par divers savants à l'Académie Royale des Sciences de l'Institut de France **9**, 433 (1846).
[73] D. Langewisch and J. Buongiorno, Prediction of film thickness, bubble velocity, and pressure drop for capillary slug flow using a cfd-generated database, International Journal of Heat and Fluid Flow **54**, 250 (2015).
[74] G. Balestra, L. Zhu, and F. Gallaire, Viscous taylor droplets in axisymmetric and planar tubes: from bretherton's theory to empirical models, Microfluid Nanofluid **22**, 67 (2018).
[75] E. Klaseboer, R. Gupta, and R. Manica, An extended bretherton model for long taylor bubbles at moderate capillary numbers, Physics of Fluids **26**, 032107 (2014).
[76] Y. Han and N. Shikazono, Measurement of the liquid film thickness in micro tube slug flow, International Journal of Heat and Fluid Flow **30**, 842–853 (2009).
[77] H. Moran, M. Magnini, C. Markides, and O. Matar, Inertial and buoyancy effects on the flow of elongated bubbles in horizontal channels, International Journal of Multiphase Flow **135**, 103468 (2021).
[78] H. Wong, C. J. Radke, and S. Morris, The motion of long bubbles in polygonal capillaries. part 1. thin films, Journal of Fluid Mechanics **292**, 71–94 (1995).
[79] A. De Lózar, A. Juel, and A. L. Hazel, The steady propagation of an air finger into a rectangular tube, Journal of Fluid Mechanics **614**, 173–195 (2008).
[80] R. S. Abiev, Simulation of the slug flow of a gas-liquid system in capillaries, Theoretical Foundations of Chemical Engineering **42**, 105–117 (2008).
[81] D. Picchi, A. Ullmann, N. Brauner, and P. Poesio, Motion of a confined bubble in a shear-thinning liquid, Journal of Fluid Mechanics **918**, A7 (2021).
[82] V. Suresh and J. B. Grotberg, The effect of gravity on liquid plug propagation in a two-dimensional channel, Physics of Fluids **17**, 031507 (2005).
[83] A. Cherukumudi, E. Klaseboer, S. A. Khan, and R. Manica, Prediction of the shape and pressure drop of taylor bubbles in circular tubes, Microfluidics and Nanofluidics **19**, 1221–1233 (2015).
[84] S. A. Vanapalli, A. G. Banpurkar, D. van den Ende, M. H. G. Duits, and F. Mugele, Hydrodynamic resistance of single confined moving drops in rectangular microchannels, Lab Chip **9**, 982–990 (2009).
[85] E. J. Hinch, *Perturbation Methods* (Cambridge University Press, Cambridge, England, 1991).
[86] C. M. Bender and S. A. Orszag, *Advanced Mathematical Methods for Scientists and Engineers I: Asymptotic Methods and Perturbation Theory* (Springer, New York, 1999).
[87] A. E. Scheidegger, Theoretical models of porous matter, Producers Monthly **17**, 17 (1953).
[88] A. E. Scheidegger, *The Physics of Flow Through Porous Media* (University of Toronto Press, Toronto, ON, 1974).

[89] G. C. Vradis and A. L. Protopapas, Macroscopic conductivities for flow of bingham plastics in porous media, Journal of Hydraulic Engineering **119**, 95–108 (1993).

[90] J. T. Bartley and D. W. Ruth, Relative permeability analysis of tube bundle models, Transport in Porous Media **36**, 161–188 (1999).

[91] J. Bartley and D. Ruth, Relative permeability analysis of tube bundle models, including capillary pressure, Transport in Porous Media **45**, 445–478 (2001).

[92] H. K. Dahle, M. A. Celia, and S. Majid Hassanizadeh, Bundle-of-tubes model for calculating dynamic effects in the capillary-pressure- saturation relationship, Transport in Porous Media **58**, 5–22 (2005).

[93] D. Yang, R. P. Currier, and D. Z. Zhang, Ensemble phase averaged equations for multiphase flows in porous media. part 1: The bundle-of-tubes model, International Journal of Multiphase Flow **35**, 628–639 (2009).

[94] F. Civan, Effective correlation of apparent gas permeability in tight porous media, Transport in Porous Media **82**, 375–384 (2009).

[95] A. Hansen, P. Hemmer, and S. Pradhan, *The Fiber Bundle Model: Modeling Failure in Materials*, Statistical Physics of Fracture and Breakdown (Wiley, 2015).

[96] R. Liu, Y. Jiang, B. Li, and L. Yu, Estimating permeability of porous media based on modified hagen–poiseuille flow in tortuous capillaries with variable lengths, Microfluidics and Nanofluidics **20**, 120 (2016).

[97] Y. Xiong, J. Yu, H. Sun, J. Yuan, Z. Huang, and Y.-s. Wu, A new non-darcy flow model for low-velocity multiphase flow in tight reservoirs, Transport in Porous Media **117**, 367–383 (2017).

[98] L. Zhao, H. Jiang, H. Wang, H. Yang, F. Sun, and J. Li, Representation of a new physics-based non-darcy equation for low-velocity flow in tight reservoirs, Journal of Petroleum Science and Engineering **184**, 106518 (2020).

[99] F. Lanza, A. Rosso, L. Talon, and A. Hansen, Non-newtonian rheology in a capillary tube with varying radius, Transport in Porous Media **145**, 245–269 (2022).

[100] X. Xu and X. Wang, Non-darcy behavior of two-phase channel flow, Physical Review E **90**, 023010 (2014).

[101] F. Jousse, G. Lian, R. Janes, and J. Melrose, Compact model for multi-phase liquid–liquid flows in micro-fluidic devices, Lab Chip **5**, 646 (2005).

[102] I. Chatzis and N. R. Morrow, Correlation of capillary number relationships for sandstone, Society of Petroleum Engineers Journal **24**, 555–562 (1984).

[103] H. Guo, K. Song, and R. Hilfer, A brief review of capillary number and its use in capillary desaturation curves, Transport in Porous Media **144**, 3–31 (2022).

[104] D. Nield and A. Bejan, *Convection in Porous Media* (Springer, 2006).

[105] S. Sinha, A. Hansen, D. Bedeaux, and S. Kjelstrup, Effective rheology of bubbles moving in a capillary tube, Physical Review E **87**, 025001 (2013).

[106] S. Roux and H. J. Herrmann, Disorder-induced nonlinear conductivity, Europhysics Letters (EPL) **4**, 1227–1231 (1987).

[107] M. Dong, F. a. L. Dullien, and J. Zhou, Characterization of waterflood saturation profile histories by the 'complete' capillary number, Transport in Porous Media **31**, 213–237 (1998).

[108] S. Ashraf, Y. Méheust, and J. Phirani, Spontaneous imbibition dynamics in two-dimensional porous media: A generalized interacting multi-capillary model, Physics of Fluids **35**, 012005 (2023).

[109] W.-Q. Deng, T.-B. Liang, W.-Z. Wang, H. Liu, J.-L. Wu, and F.-J. Zhou, A new interacting capillary bundle model on the multiphase flow in micropores of tight rocks, Petroleum Science **21**, 1099–1112 (2024).

Paper IV

P. Botticini, G. Lavalle, D. Picchi and P. Poesio, 'Compressibility-induced destabilisation of falling liquid films: An integral approach', *International Journal of Multiphase Flow*, vol. 171, p. 104 667, 2024, ISSN: 0301-9322. DOI: 10.1016/j.ijmultiphaseflow.2023.104667

Beyond bubble-mediated nonlinear dynamics, reduced-order modelling proves equally effective in addressing instabilities in continuous gravity-driven liquid films. These films are widely employed owing to their low thermal resistance and large contact area, with wavy dynamics acting as an additional mechanism for transport enhancement. By incorporating compressibility effects, this study demonstrates how hydrostatic pressure distribution and depth-averaged density are modulated by the local film thickness, yielding dispersive properties consistent with the linear theory of compressible flow in the long-wave limit. This final contribution further broadens the scope of the thesis, demonstrating how reduced-order approaches can unify diverse thin-film phenomena within a coherent multiscale framework.

International Journal of Multiphase Flow 171 (2024) 104667

Contents lists available at ScienceDirect

International Journal of Multiphase Flow

journal homepage: www.elsevier.com/locate/ijmulflow

Compressibility-induced destabilisation of falling liquid films: an integral approach

P. Botticini [a,b], G. Lavalle [a,*], D. Picchi [b], P. Poesio [b]

[a] Mines Saint-Etienne, Univ. Lyon, CNRS, UMR 5307 LGF, Centre SPIN, F-42023, Saint-Etienne, France
[b] Dipartimento di Ingegneria Meccanica e Industriale, Università di Brescia, Via Branze 38, 25123, Brescia, Italy

ARTICLE INFO

MSC:
76E17
76E19
76M45

Keywords:
Falling liquid films
Interfacial instability
Low-dimensional models

ABSTRACT

We revisit the classical 2D problem of a gravity-driven liquid layer down an inclined plate (Kapitza, 1948), relaxing the usual assumption of homogeneous fluid. We set out to answer three major issues. When the fluid density is allowed to vary, (i) how does this feature structurally affect the formulation of a low-dimensional depth-averaged model? (ii) To what extent and (iii) by virtue of which physical mechanism does compressibility participate in the long-wave interfacial instability? To provide the relevant answers, (i) we first make use of a second-order asymptotic expansion in the shallowness parameter to develop a weakly-compressible boundary-layer system: starting from a two-equation momentum-integrated model, an additional barotropic equation of state is required for closure purposes. In this respect, (ii) a temporal linear stability analysis is performed: it is revealed that compressibility plays a destabilising role whose magnitude is enhanced at intermediately tilted configurations, and the more the Reynolds number approaches the critical threshold in the incompressible limit. (iii) We finally interpret the ensuing dispersion relation under the convenient framework of two-wave hierarchy, initiated by Whitham (1974): the primary instability gets promoted by the flow compressibility as it contributes to deceleration of dynamic waves most significantly in the low-inertia regime. Indeed, compressibility locally acts as a further boost to the inertia-based mechanism of Kapitza instability by amplifying flow-rate variations within the liquid film.

1. Introduction

Liquid layers sliding down an incline are routinely encountered in nature and represent a cross-disciplinary and highly topical object of study. Starting with the pioneer studies of Kapitza father–son team (Kapitza, 1948; Kapitza and Kapitza, 1949), visual observations have revealed the development of a wide variety of intriguing patterns along the fluid interface, from simple sinusoidal perturbations to strongly non-periodic three-dimensional solitons (Chang, 1994; Alekseenko et al., 1994).

This issue is also of practical relevance in many biological and industrial processes (Craster and Matar, 2009). Cooling towers, distillation units, multi-phase heat exchangers, fluid-phase separators, jet–film devices, power station condenser tubes, absorption columns, electrolytic cells, scrubbers for pollution abatement, injection systems for enhanced oil recovery, *etc*. all benefit from the strong effect of superficial waves on the underlying processes of heat and mass transfer. For instance, according to data reported by Frisk and Davis (1972), the heat transfer intensification by waves forming along a water film in presence of a co-current air flow attains more than 100% with respect to the flat-film scenario. On the other hand, for some applications such as coating operations, a uniform flow thickness is required and instabilities should be prevented (Weinstein and Ruschak, 2004).

So far, the majority of works on wavy falling films is performed assuming flow incompressibility, *i.e.* the density of a fluid element remains uniform and constant. However, in many fields of science and engineering, this assumption may constitute an oversimplification of the physical problem, possibly leading to inaccurate conclusions. One example is the transport of carbon dioxide in pipelines from the energy plants to the injection sites for CCUS applications. When supercritical carbon dioxide is employed as solvent or carrier, in fact, density turns out to be an essential parameter in determining the performance of such a technological process. In this context, avoiding the unbounded growth of superficial disturbances, which can result in the emergence of slugs or even structural damages (Lu et al., 2020), is necessary for the safety of the transport infrastructure.

Although the convective long-wave interfacial mode known as Kapitza instability (Kapitza, 1948) constitutes a long-standing knowledge in case of a tilted or vertical plate, a deep understanding of how

* Corresponding author.
E-mail address: gianluca.lavalle@emse.fr (G. Lavalle).

https://doi.org/10.1016/j.ijmultiphaseflow.2023.104667
Received 17 August 2023; Received in revised form 24 October 2023; Accepted 8 November 2023
Available online 10 November 2023

density variations enter this paradigm is still lacking in the literature. Thus, the link between the compressibility and the occurrence of the Kapitza instability needs to be clarified and has prompted us to address the following question: which are the main implications of density inhomogeneities on the onset of Kapitza instability in inclined falling liquid films?

Recently, the relevance of wavy film flows has led to a number of attempts to achieve models for the evolution of the film thickness and its mean velocity (or flow rate) and to find a compromise between the accuracy and the computational effort. In most cases, the flow description is not too far from its wavy-less configuration, designed as Nusselt state (Nusselt, 1916). This makes the long-wave asymptotic expansion a feasible approach, which forms the cornerstone of many models derived after the influential paper of Benney (1966), who developed an evolution equation for the film height by introducing a small-scale parameter. However, Benney's equation suffers of finite-time blow-up of the time-dependent solution. This problem was addressed by Shkadov (1967) assuming that streamwise variations are small as compared with those developing in the crosswise direction, and through pressure removal boundary layer equations (BLEs) ensue. These are then averaged over the fluid depth to capture the main physical features of the flow by means of integral variables. Nonetheless, Shkadov's system of equations fails in capturing the correct long-wave instability threshold. This issues was addressed by Ruyer-Quil and Manneville (1998, 2000), who introduced the weighted residual integral boundary-layer model (WRIBL) and assured model consistency by formulating a closure law for the wall shear stress.

In this paper, our purpose is to deal with a weakly inhomogeneous medium to investigate whether and how the action of a low compressibility enhances or mitigates the onset of long-wave interfacial instability. We therefore start by applying Benney's modelling strategy to a barotropic flow in a weakly-compressible scenario. We globally characterise it in terms of compressibility by means of the Mach number and formulate a coupled system of two evolution equations by making use of the depth-wise averaging method based on the classical long-wave expansion as in Lavalle et al. (2015, 2017), *i.e.* by integration of the momentum balance (momentum integral method or MIM). The resulting model is comprehensive of second-order viscous diffusion effects, which allow us to achieve good agreement in the incompressible limit in terms of the cut-off wavenumber with the Orr–Sommerfeld solution (Kalliadasis et al., 2013).

Our study focuses on the influence of compressibility on the development of linear surface waves on a liquid film falling down an inclined wall under a shear-free atmosphere (Fig. 1). For this, we consider the primary instability of the weakly-compressible uniform base flow and solve the temporal stability problem based on the long-wave model equations. By doing this, we answer two additional questions: (i) how does compressibility affect the formulation of depth-integrated equations? (ii) Which physical mechanism does the compressibility trigger in the long-wave interfacial instability?

Behind the usual incompressible way of modelling falling liquid layers, it is assumed that the speed of sound, when compared to the convective velocity scale, is sufficiently high to be considered infinite. Therefore, (i) a unique velocity scale appears in the problem and (ii) the fluid density is uniform and constant. On the contrary, when a finite speed of sound is taken into account, the scenario significantly changes. (i) Convective transport and pressure wave propagation occur at disproportional rates, thereby requiring a proper incorporation of an additional dimensionless group in the problem. In this regard, the Sarrau–Mach number can be used to express the magnitude of the fluid speed as compared to the sound speed within the same medium. In addition, (ii) the fact that density field is allowed to vary in space and time demands the introduction of an Equation of State (EoS) among the governing equations.

Unfortunately, very little attention, to the best of our knowledge, has been up to now devoted to the assessment of the impact of compressibility on the film long-wave instability. In fact, only a few works tried to tackle this issue.

An extension of long-wave models to weakly-compressible barotropic flows is first proposed by Richard (2021). Compressibility-related effects are captured by means of a dedicated Mach number, defined by means of the incompressible surface waves celerity, and, in the limit where the sound speed goes to infinity, the incompressible version of the model is correctly recovered. However, the system of four Favre-averaged equations derived by Richard (2021) is intended for simulation of coastal waves and the author frames his argumentation around the ultimate goal of correctly predicting tsunamis' arrival time. Although the long-wave assumption still holds for a tidal wave in a deep ocean, the relevant spatial scales involved widely differs from the ones we are interested in. Moreover, in Richard (2021), the wave propagation is studied within an inviscid medium, neglecting viscous effects.

Such friction terms have also been neglected in the work of Bresch et al. (2020), who developed an augmented skew-symmetric system of depth-integral equations with capillarity. Their work aims at ensuring the stability of numerical schemes in presence of large gradients of fluid height or fluid density.

In the context of flows within a narrow interstice formed between two surfaces, Almqvist et al. (2019) consider a class of iso-viscous fluids obeying a constitutive power–law density–pressure relationship. Lubrication theory, scaling and asymptotic analysis are extensively used in that work to show that the degree of compressibility for a thin film flow determines whether the terms governing inertia may or may not be neglected. Notwithstanding the rigorousness of their procedure, the study of a capillary flow is not at all comparable to a free-surface gravity-driven liquid film.

We conclude by recalling the fundamental results regarding the linear stability problem of a falling liquid film in a passive gas or shear–free atmosphere, which is the configuration studied in this work. Benjamin (1957) and Yih (1963) solved the temporal linear stability problem formulated by Orr (1907) and Sommerfeld (1908) in the context of a gravity-driven incompressible film flow. In particular, they detected the long-wave instability threshold in terms of a critical Reynolds number $Re_{cr} = 5/6 \cot \beta$, where β identifies the inclination angle, being the Reynolds number based on the mean film flow velocity. Their analysis reveals that inertia destabilises long waves and the related mechanism has been explained either through the shift between the vorticity perturbation and the perturbed interface (Kelly et al., 1989; Kalliadasis et al., 2013; Smith, 1990), or via the time lag at which flow rate adapts to its inertialess target value (Dietze, 2016). With the aim to investigate the role of compressibility on the long-wave instability, we follow the latter approach by considering the effect of compressibility on the inertialess flow rate, similarly to Lavalle et al. (2019), who applied the same methodology to explain the confinement-induced stabilisation of falling liquid films. Finally, we complement this analysis by studying the role of compressibility via the two-wave competition theory formulated by Whitham (1974), and employed by Samanta et al. (2011) and Samanta (2014) for liquid films down a slippery inclined plane or for shear-imposed falling films.

Accordingly, the structure of our paper is as follows. Section Section 2 contains the basic governing equations, the boundary conditions of the problem, and the definition of the principal dimensionless groups, together with the long-wave scaling. Then, the low-dimensional modelling is discussed in Section 3, from the specification of the EoS to the derivation of the weakly-compressible integral model. This will serve in the second part of the manuscript, devoted to the linear temporal stability eigen-problem, whose compatibility yields the dispersion relation outlined in Section 4. To follow, Section 5 presents our main findings in terms of critical threshold and parametric study of celerity branches. The mechanism governing the influence of compressibility on the film stability is finally elucidated in Section 6. Concluding remarks are summarised in Section 7, while some details of the analysis that were not included in the main body of the text are given in the appendix for completeness.

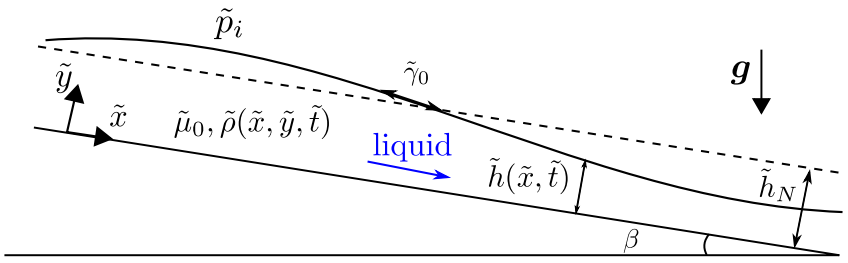

Fig. 1. Schematic diagram of the 2D slightly compressible flow of a wavy gravity-driven liquid film with uniform and constant viscosity $\tilde{\mu}_0$ and surface tension $\tilde{\gamma}_0$, exhibiting a non-uniform and variable density $\tilde{\rho}(\tilde{x}, \tilde{y}, \tilde{t})$. The coordinate system is defined by $\langle \tilde{x}, \tilde{y} \rangle$. The fluid layer, of variable thickness $\tilde{h}(\tilde{x}, \tilde{t})$, flows under the action of gravity $\boldsymbol{g}$ along a plate having an inclination angle β with respect to the horizontal direction. $\tilde{h}_N$ refers to Nusselt solution (Nusselt, 1916) and denotes the waveless film thickness. An interfacial constant and uniform normal pressure $\tilde{p}_i$ is present.

2. Flow configuration and theoretical formulation

Herein we consider the two-dimensional compressible flow of a gravity-driven iso-viscous liquid film, falling along a tilted wall within a shear-free atmosphere, as sketched in Fig. 1. The liquid film is Newtonian. $\beta \in]0, \frac{\pi}{2}]$ refers to the angle of inclination formed between the wall and the horizontal direction. The Cartesian coordinate axes $\tilde{x}$ and $\tilde{y}$ are placed along the streamwise and crosswise flow directions, respectively, being the origin of the spatial reference frame located at the wall; $\tilde{t} \in \mathbb{R}_0^+$ specifies the time coordinate. Assume that, with the exception of density $\tilde{\rho} \in \mathbb{R}^+$, the physical properties of the liquid, such as dynamic viscosity $\tilde{\mu}_0 \in \mathbb{R}^+$ and surface tension $\tilde{\gamma}_0 \in \mathbb{R}^+$, are uniform within the physical fluid domain $\tilde{\mathcal{V}}$, defined as

$$\tilde{\mathcal{V}}(\tilde{t}) = \left\{ (\tilde{x}, \tilde{y}) \in \tilde{\mathbb{R}}^2 \mid 0 \leq \tilde{y} \leq \tilde{h}(\tilde{x}, \tilde{t}) \right\}, \tag{1}$$

where $\tilde{h}$ is a dimensional function tracing the spatial and temporal evolution of the wavy film free surface.

2.1. Governing equations

At the continuum level, the dimensional form of the governing equations of motion enforcing the conservation of mass and momentum for the compressible flow of the Newtonian falling film reads:

$$\partial_{\tilde{t}} \tilde{\rho} + \tilde{\nabla} \cdot (\tilde{\rho}\, \tilde{\mathbf{v}}) = 0 \tag{2a}$$

$$\tilde{\rho} \left(\partial_{\tilde{t}} \tilde{\mathbf{v}} + (\tilde{\mathbf{v}} \cdot \tilde{\nabla})\, \tilde{\mathbf{v}} \right) = -\tilde{\nabla} \tilde{p} + \tilde{\rho}\, \boldsymbol{g} + \tilde{\mu}_0 \left(\tilde{\nabla}^2 \tilde{\mathbf{v}} + \left(\frac{1}{3} + \vartheta \right) \tilde{\nabla} (\tilde{\nabla} \cdot \tilde{\mathbf{v}}) \right), \tag{2b}$$

where $\tilde{\mathbf{v}} = (\tilde{u}, \tilde{v})$ and $\tilde{p}$ denote, respectively, the film velocity vector and the thermodynamic pressure, whereas $\boldsymbol{g} = (g \sin\beta, -g \cos\beta)$ is the gravitational acceleration. The parameter labelled by $\vartheta = \tilde{\zeta}_0 / \tilde{\mu}_0$ expresses the ratio between the expansion viscosity $\tilde{\zeta}_0 \in \mathbb{R}$ and the dynamic viscosity $\tilde{\mu}_0$. Although ϑ is conventionally set to zero invoking Stokes' hypothesis ($\tilde{\zeta}_0 \equiv 0$) (Batchelor, 2000), we will not assume any particular value in order to preserve the widest possible generality throughout the paper. As will be demonstrated in Section 3.2, this choice has no consequences in the ultimate formulation of the reduced model (25a).

The flow system is subject to the following boundary conditions. At the rigid bottom $\tilde{y} = 0$, the no-slip and no-penetration conditions lead to

$$\tilde{\mathbf{v}}|_0 = \mathbf{0}. \tag{3}$$

At the free surface $\tilde{y} = \tilde{h}(\tilde{x}, \tilde{t})$, the balance of normal and tangential stress components for the shear–free film yields the dynamic coupling conditions

$$\left[\tilde{\mathbf{n}}^T \cdot \tilde{\mathbf{T}}^{(\tilde{\mathbf{n}})} \right] = \tilde{\gamma}_0\, \tilde{\boldsymbol{\nabla}} \cdot \tilde{\mathbf{n}} \tag{4a}$$

$$\left[\tilde{\mathbf{t}}^T \cdot \tilde{\mathbf{T}}^{(\tilde{\mathbf{n}})} \right] = 0, \tag{4b}$$

where $\tilde{\gamma}_0$ is the surface tension and $\tilde{\mathbf{T}}^{(\tilde{\mathbf{n}})}$ is the fluid stress vector at the interface, whose orientation is determined by

$$\tilde{\mathbf{n}} = \left\{ -\partial_{\tilde{x}} \tilde{h},\ 1 \right\}^T \Big/ \sqrt{1 + \left(\partial_{\tilde{x}} \tilde{h} \right)^2} \tag{5a}$$

$$\tilde{\mathbf{t}} = \left\{ 1,\ \partial_{\tilde{x}} \tilde{h} \right\}^T \Big/ \sqrt{1 + \left(\partial_{\tilde{x}} \tilde{h} \right)^2} \tag{5b}$$

as normal and tangential unit column vector, respectively. Square brackets are used in (4a) to designate the jump in any quantity of interest across the interface. Lastly, being the substantial derivative symbolised by $D(\star)/D\tilde{t} = \partial_{\tilde{t}}(\star) + \tilde{\mathbf{v}} \cdot (\tilde{\boldsymbol{\nabla}} \star)$, an additional kinematic condition for the gas–liquid interface is introduced as follows

$$\frac{D}{D\tilde{t}} \left(\tilde{y} - \tilde{h}\left(\tilde{x}, \tilde{t} \right) \right) = 0. \tag{6}$$

2.2. Scaling and dimensionless formulation

To make the problem dimensionless, we choose the value of the density at the gas–fluid interface as the reference scale for density $\tilde{\rho}_0$ in line with Richard (2021). This scale is convenient since at $\tilde{y} = \tilde{h}$ the hydrostatic contribution on pressure and density fields is depth-independent. The Nusselt film thickness $\tilde{h}_N$ (Nusselt, 1916) is chosen as the relevant length scale (Fig. 1), while we adopt the longitudinal characteristic speed as scale for the velocity $\tilde{U}_N = \tilde{q}_N / \tilde{h}_N = \tilde{\rho}_0\, g\, \sin\beta\, \tilde{h}_N^2 / 3\, \tilde{\mu}_0$, where $\tilde{q}_N$ is the flow rate per unit of channel length:

$$\tilde{q}_N = \int_0^{\tilde{h}_N} \tilde{u}_N(\tilde{y})\, d\tilde{y}, \tag{7}$$

being $\tilde{u}_N(\tilde{y})$ the well-known Nusselt parabolic velocity profile (Nusselt, 1916). The average velocity $\tilde{U}_N$ is indeed defined from the balance of the viscous friction force, $\propto \tilde{\mu}_0 \tilde{U}_N / \tilde{h}_N^2$, and the streamwise gravity force, $\propto \tilde{\rho}_0\, g\, \sin\beta$. The time and pressure scales are chosen as $\tilde{h}_N / \tilde{U}_N$ and $\tilde{\rho}_0 \tilde{U}_N^2$, respectively (Lavalle et al., 2015).

As a customary practice in the study of the wavy film dynamics, we will adopt a shallow water approximation. Denoting by $\tilde{\mathcal{L}}$ a typical lengthwise distance characterising superficial corrugations, we define the following film aspect ratio

$$\varepsilon = \frac{\tilde{h}_N}{\tilde{\mathcal{L}}} \ll 1, \tag{8}$$

as the scale parameter of the problem. Specifically, $\varepsilon \sim \partial_{x,t}(\star)$ accounts for the slowly-varying downstream modulations of the free surface with respect to space and time.

Thus, the governing Eqs. (2a) are rewritten in dimensionless terms:

$$\partial_t \rho + \partial_x (\rho u) + \partial_y (\rho v) = 0 \tag{9a}$$

$$\rho\, \varepsilon \left(\partial_t u + u \partial_x u + v \partial_y u \right) = -\varepsilon\, \partial_x p + \frac{\rho}{Fr} \sin\beta + \frac{1}{Re} \left[\partial_{yy} u + \varepsilon^2 \partial_{xx} u + \varepsilon^2 \left(\frac{1}{3} + \vartheta \right) \partial_x \left(\partial_x u + \partial_y v \right) \right] \tag{9b}$$

$$\rho\, \varepsilon^2 \left(\partial_t v + u \partial_x v + v \partial_y v \right) = -\partial_y p - \frac{\rho}{Fr} \cos\beta + \frac{\varepsilon}{Re} \left[\varepsilon^2 \partial_{xx} v + \partial_{yy} v + \left(\frac{1}{3} + \vartheta \right) \partial_y \left(\partial_x u + \partial_y v \right) \right], \tag{9c}$$

being $Re = \tilde{\rho}_0 \tilde{U}_N \tilde{h}_N / \tilde{\mu}_0$ and $Fr = \tilde{U}_N^2 / g \tilde{h}_N$ the Reynolds number and the Froude number, respectively, with $(x, y, t) \in \mathbb{R} \times [0, h] \times [0, +\infty[$.

The system (9a) is coupled with the following set of dimensionless boundary conditions:

$$u|_0 = v|_0 = 0 \tag{10a}$$

$$Re\left(1+\varepsilon^2\partial_x^2 h\right)\left(p|_h - p_i\right) + \varepsilon\left(\frac{2}{3}-\vartheta\right)\left(1+\varepsilon^2\partial_x^2 h\right)\left(\partial_x u|_h + \partial_y v\big|_h\right) + \tag{10b}$$

$$-2\,\varepsilon\left(\partial_y v\big|_h + \varepsilon^2\partial_x^2 h\;\partial_x u|_h\right) + 2\,\varepsilon\,\partial_x h\left(\partial_y u\big|_h + \varepsilon^2\partial_x v\big|_h\right) = -\frac{Re}{We}\frac{\varepsilon^2\partial_{xx}h}{\sqrt{1+\varepsilon^2\partial_x^2 h}}$$

$$2\,\varepsilon^2\partial_x h\left(\partial_y v\big|_h - \partial_x u|_h\right) + \left(1-\varepsilon^2\partial_x^2 h\right)\left(\partial_y u\big|_h + \varepsilon^2\partial_x v\big|_h\right) = 0 \tag{10c}$$

$$\partial_t h + u|_h\,\partial_x h = v|_h\,, \tag{10d}$$

where p_i is the dimensionless atmospheric pressure exerted at the film interface and $We = \tilde{\rho}_0\,\tilde{h}_N\,\tilde{U}_N^2/\tilde{\gamma}_0$ is the Weber number.

3. Low-dimensional modelling

Here, the free-surface flow problem is tackled adopting an asymptotic approximation of the continuity and the Navier–Stokes equations based on the film aspect ratio $\varepsilon \ll 1$ introduced in Section 2.2. A great simplification can be accomplished by means of a boundary layer approach together with a depth-averaging technique. Such a procedure leads to the determination of a reduced coupled system of two equations, having the film thickness $h(x,t)$ and the flow rate per unit of channel width $q(x,t)$ as local dimensionless unknowns. We propose a two-equation momentum-integral model (MIM) that is accurate up to and including order $O(\varepsilon^2)$ both in inertial and in viscous diffusion terms. Based on this approximation, the problem expressed by ((9a), (10a)) will be consistently simplified accounting for the higher magnitude of surface tension, $We = O(\varepsilon^2)$, compared to inertia-related phenomena, $Re \sim Fr = O(1)$.

Following the classical Polhausen–von Kármán momentum-integral analysis, the y–momentum equation (9c) and related boundary condition (10b) serve to eliminate the streamwise pressure gradient term $\partial_x p$ in the x–momentum equation (9b). Being this term of $O(\varepsilon)$, it is sufficient to retain (9c) and (10b) up to $O(\varepsilon)$. Differently from the incompressible scenario, in this work, a supplementary constitutive relation is required to describe completely the fluid system due to the presence of a density term $\rho = \tilde{\rho}/\tilde{\rho}_0 = O(1)$ as an additional unknown (Richard, 2021).

3.1. Barotropic equation of state

Since it is difficult to encounter large variations in density in gravity-driven falling films, we make use of the following linearised Equation of State (EoS)

$$\tilde{\rho}\left(\tilde{p},\tilde{T},\tilde{S}\right) = \tilde{\rho}|_{\tilde{h}} + \left(\frac{\partial\tilde{\rho}}{\partial\tilde{p}}\right)_{\tilde{T},\tilde{S}}\left(\tilde{p}-\tilde{p}|_{\tilde{h}}\right) + \left(\frac{\partial\tilde{\rho}}{\partial\tilde{T}}\right)_{\tilde{p},\tilde{S}}\left(\tilde{T}-\tilde{T}|_{\tilde{h}}\right) + \left(\frac{\partial\tilde{\rho}}{\partial\tilde{S}}\right)_{\tilde{p},\tilde{T}}\left(\tilde{S}-\tilde{S}|_{\tilde{h}}\right), \tag{11}$$

in the form of a first-order truncated Taylor series expansion as in Batchelor (2000), Colinet et al. (2001). The validity of (11) is intended to be restricted to a neighbourhood of the reference state, *i.e.* $\tilde{\rho} - \tilde{\rho}|_{\tilde{h}} \ll 1$. Specifically, besides pressure $\tilde{p}$, the parameters that characterise such a functional dependence are the fluid temperature $\tilde{T}$ and its entropy $\tilde{S}$ for a fixed vector of amounts of constituents.

At the present stage, density-affecting thermal effects – which would have required an energy equation coupling – will be ignored, so as to confine our current inquiry to a two-equation MIM pattern. Moreover, although the flow is not itself homentropic, the propagation of small-amplitude long-wave perturbations is shown to be scarcely affected by acoustic attenuation and dispersion phenomena (Van Dael, 1968; Kinsler et al., 2000). We postpone a more rigorous proof of this statement to Section 6.1, where we deal with the notion of wave hierarchy.

Therefore, the EoS (11) is reduced to a *barotropic* formulation where density variations with pressure support the propagation of sound waves:

$$\tilde{\rho}\left(\tilde{p}\right) = \tilde{\rho}_0 + \left(\frac{\partial\tilde{\rho}}{\partial\tilde{p}}\right)_{\tilde{S}}\left(\tilde{p}-\tilde{p}|_{\tilde{h}}\right). \tag{12}$$

Notably, one can refer to the thermodynamic definition of isentropic speed of sound (Shapiro, 1953)

$$\tilde{a}_0 = \sqrt{\left(\frac{\partial\tilde{p}}{\partial\tilde{\rho}}\right)_{\tilde{S}}}, \tag{13}$$

whose magnitude $\tilde{a}_0$ is supposed to be uniform and constant within $\tilde{\Psi}$, in order to achieve the dimensionless version of (11), which ultimately reads

$$\rho\left(p\right) = 1 + Ma^2\left(p - p|_h\right). \tag{14}$$

In (14) an overall Sarrau–Mach number

$$Ma = \frac{\tilde{U}_N}{\tilde{a}_0} \in \mathbb{R}^+, \tag{15}$$

expressing the magnitude of inertial forces with respect to elastic ones, has been introduced as dimensionless group to capture the influence of compressibility on the film flow. As it can be inferred from (14), the classical incompressible limit is recovered as a limiting case when the acoustic propagation is modelled as an instantaneous phenomenon, *i.e.* $\tilde{a}_0 \to +\infty \iff Ma \to 0^+$.

3.1.1. Pressure distribution

Replacement of (14) into the $O(\varepsilon)$ estimate of (9c) leads to the following first-order linear non-homogeneous Ordinary Differential Equation (ODE) with respect to the crosswise coordinate y for the film pressure $p(x,y,t)$:

$$\partial_y p + \frac{\cos\beta}{Fr}Ma^2\,p = \frac{\cos\beta}{Fr}\left(Ma^2\;p|_h - 1\right) + \frac{\varepsilon}{Re}\,\partial_y\mathcal{W} + O(\varepsilon^2), \tag{16}$$

in which the function $\mathcal{W}(u,v;\vartheta) = \partial_y v + \left(\frac{1}{3}+\vartheta\right)\left(\partial_x u + \partial_y v\right)$ implicitly depends on y through the dimensionless velocity field. The solution of (16), in which the dimensionless interfacial pressure $p|_h$ has been evaluated using the normal stress boundary condition (10b), is determined as summation of the particular solution of (16) and the solution of the corresponding homogeneous ODE. The latter is obtained via the method of separation of variables, whereas the former through the technique of variation of parameters (sometimes referred to as Duhamel's principle). As a result, the proper solution of (16) reads:

$$p(x,y,t;\vartheta) = p_i + \overbrace{\frac{\exp\left[\frac{\cos\beta}{Fr}Ma^2\left(h-y\right)\right]-1}{Ma^2}}^{\blacklozenge} - \frac{\varepsilon^2}{We}\partial_{xx}h + \frac{\varepsilon}{Re}\left(\mathcal{W} - \left(\partial_x u\right)\big|_h\right) + \underbrace{O(\varepsilon\,Ma^2)}_{\clubsuit}, \tag{17}$$

being its full-form given in Appendix A. As expected, as the Mach number approaches zero, (17) reduces to the pressure distribution obtained by Ruyer-Quil and Manneville (1998) in the context of a perfectly incompressible free-surface flow, by virtue of the exponential limit $\left(e^{m\star}-1\right)/\star \to m$ for vanishing $\star$ (with $m \in \mathbb{R}\backslash\{0\}$), along with the incompressible continuity identity $\partial_y v = -\partial_x u$.

Based on the above considerations, the barotropic EoS (14) can be recast as

$$\rho\left(x,y,t;\vartheta\right) = \underbrace{\exp\left[\frac{\cos\beta}{Fr}Ma^2\left(h-y\right)\right]}_{\blacklozenge} + \underbrace{O(\varepsilon\,Ma^2)}_{\clubsuit}. \tag{18}$$

3.1.2. Weak compressibility hypothesis

Although the flow compressibility is taken into account in this model, thin descending liquid films usually show a weakly compressible behaviour and, therefore, the expression (18) can be simplified. To do so, the magnitude of the Mach number can be estimated with respect to ε and, taking inspiration from Richard (2021), we can write

$$Ma = M\,\varepsilon^{\alpha}, \tag{19}$$

where α controls the compressibility behaviour and $M = O(1) \in \mathbb{R}_0^+$. As a consequence, the accuracy of the model is retained only if $\alpha \geq 1$ since the residual term ♣ in (18) is of $O(2\alpha + 1)$. In our model, the Mach number enters into the governing equations only through the barotropic EoS (14) and, since $Ma^2 = O(\varepsilon^{2\alpha})$, the different orders in terms of integer power of the Mach number can be classified as $\alpha = \{1,\ 3/2,\ 2,\ 5/2,\ \ldots\}$.

An estimation of the order of magnitude of the exponential term ♦ in ((17), (18)) within the low–Ma limit requires one to take the Maclaurin series expansion $e^{\star} = \sum_{n=0}^{\infty}(\star^n/n!)$, that, together with the preliminary guess about the order of magnitude of $Fr = O(1)$, yields to:

$$\underbrace{\exp\left[\frac{\cos\beta}{Fr}Ma^2\,(h-y)\right]}_{\blacklozenge} \approx 1 + \underbrace{\frac{\cos\beta}{Fr}Ma^2\,(h-y)}_{\blacklozenge_1} + \frac{1}{2}\underbrace{\left[\frac{\cos\beta}{Fr}Ma^2\,(h-y)\right]^2}_{\blacklozenge_2}, \tag{20}$$

implying that $\blacklozenge_1 = O(\varepsilon^{2\alpha})$ and $\blacklozenge_2 = O(\varepsilon^{4\alpha})$. Depending on the value of α, a twofold level of compressibility can be consequently addressed in view of the prescribed $O(\varepsilon^2)$ accuracy criterion:

$$\rho(x,y,t;\vartheta) = \begin{cases} 1 + O(\varepsilon^3), & \alpha \geq \frac{3}{2} \\ 1 + \frac{\cos\beta}{Fr}Ma^2\,(h-y) + O(\varepsilon^3), & \alpha = 1. \end{cases} \tag{21}$$

Thus, when $\alpha \geq 3/2$ the analysis is formally identical to the incompressible scenario, since a relation of asymptotic equivalence holds between $\tilde{\rho}(x,y,t)$ and $\tilde{\rho}_0$. In other words, the relation (19) provides a rule-of-thumb criterion for the film flow to be considered as weakly-compressible in asymptotic terms. For example, if we assume $\varepsilon = 0.01$ as long-wave parameter (jointly with a unitary-valued M), we find the threshold for incompressibility as $Ma \lesssim 0.001$.

3.2. Boundary layer equations

In this paper we focus on the weakly–compressible regime corresponding to $\alpha = 1$. In this scenario, the derivative of the pressure distribution (17) is computed using the expression (21) with $\alpha = 1$, leading to

$$\partial_x p(x,y,t;\vartheta) = \frac{\cos\beta}{Fr}\partial_x h - \frac{\varepsilon^2}{We}\partial_{xxx}h + \\ + \frac{\varepsilon}{Re}\left[\partial_{xy}v + \left(\frac{1}{3} + \vartheta\right)\partial_x\left(\partial_x u + \partial_y v\right) - \partial_x\left(\left(\partial_x u\right)|_h\right)\right] + O(\varepsilon^2). \tag{22}$$

As mentioned above, (22) is now substituted in lieu of $\partial_x p$ in (9b), showing that ϑ–dependent contributions mutually cancel themselves out.

Then, the replacement of ρ and $\partial_x p$ jointly permits obtaining the second-order set of weakly compressible Boundary Layer Equations (BLEs), which finally reads:

$$\partial_x u + \partial_y v + \frac{\cos\beta}{Fr}\,Ma^2\,\left(\partial_t h + u\partial_x h - v\right) = 0 \tag{23a}$$

$$\varepsilon\,\left(\partial_t u + u\partial_x u + v\partial_y u\right) = \frac{\partial_{yy}u}{Re} + \frac{\varepsilon^3}{We}\partial_{xxx}h - \varepsilon\,\frac{\cos\beta}{Fr}\partial_x h + \\ + \frac{\sin\beta}{Fr}\left(1 + \frac{\cos\beta}{Fr}Ma^2\,(h-y)\right) + \frac{\varepsilon^2}{Re}\left[\partial_{xx}u - \partial_{xy}v + \partial_x\left(\left(\partial_x u\right)|_h\right)\right]. \tag{23b}$$

By resorting to Leibniz's integral rule, BLEs (23a) are integrated over the depth $\int_0^h(\star)\,dy$ to reduce the space dimensionality of the problem. The basic idea behind this modelling strategy is the elimination of the cross-stream flow dependency (Ruyer-Quil and Manneville, 2000).

Unfortunately, the resulting BLEs fail to be entirely expressed in terms of the local film thickness $h(x,t)$ and the local flow rate $q(x,t) = \int_0^h u(y)\,dy$. Thus, closure laws are needed in (23b) for the following terms: the so-called shape factor $\int_0^h u^2\,dy$, the difference between interfacial and wall shear stresses $\left(\left(\partial_y u\right)|_h - \left(\partial_y u\right)|_0\right)$, and the antiderivative of other second-order terms within square brackets ($\propto \varepsilon^2/Re$). Moreover, since the compressibility introduces a novel second-order contribution, related to the crosswise component of velocity, *viz.* $\int_0^h v\,dy$, in (23a) an additional closure is required. Such closures can be obtained via the explicit expression for the unknown velocity field $u(x,y,t)$, $v(x,y,t)$.

3.2.1. Long-wave approximation

In this work, we adopt a long wave approach following the classical Benney's closure technique (Benney, 1966; Gjevik, 1970; Lin, 1974; Chang, 1986). Accordingly, each variable $\mathcal{V} = \{u,\ v,\ p,\ \rho\}$ appearing in the primitive problem is decomposed as a formal power-series regular perturbation expansion, having ε as basis:

$$\mathcal{V}^{(\varepsilon)} = \mathcal{V}^{(0)} + \varepsilon\,\mathcal{V}^{(1)} + \varepsilon^2\,\mathcal{V}^{(2)} + \cdots. \tag{24}$$

The right-hand side of (24) is ideal for assessing the effect of a small perturbation in ε about zero, provided that proper accuracy constraints are met (Simmonds and Mann Jr., 1998). Specifically, mathematical convergence of the infinite series (24) is not necessary (Jeffreys, 1926; Van Dyke and Rosenblat, 1975). On the other hand, it is required that – once truncated – $\mathcal{V}^{(\varepsilon)}$ rapidly approaches $\mathcal{V}$ in the limit of vanishing ε. This is equivalent to enforce that the approximation error $\left|\mathcal{V} - \mathcal{V}^{(\varepsilon)}\right|$ scales as the first neglected term of the series (24). By assuming this residue to be $\sim \varepsilon^3$, the $O(\varepsilon^2)$ truncation of the previous ansatz (24) can be then substituted in ((9a), (10a), (14)), allowing the corresponding equations to be broken up into different orders and sequentially solved. Specifically, the $O(\varepsilon^0,\ \varepsilon^1)$ restrictions of the problem coincide with their respective incompressible versions, due to the fact that Ma–related influence intervenes only at $O(\varepsilon^2)$ when $\alpha = 1$, through the equality $\rho^{(2)} = M^2\left(p^{(0)} - p^{(0)}\big|_h\right)$ by (14). Also, the terms including the expansion viscosity appear to be irrelevant, due to the fact that the $O(\varepsilon^0,\ \varepsilon^1)$ velocity fields are solenoidal. Hence, a comparison between the compressible second-order profiles and their incompressible analogues will be helpful to understand the impact of a varying density on flow-related quantities; this aspect will be discussed in Section 6.2.

3.3. Depth-averaged model

Upon substitution, we now take advantage of the expressions for the asymptotic expansions determined beforehand. These are confined to Appendix B only for the sake of brevity.

In order to derive the depth-integral model, three steps need to be performed: (i) replace higher-order time derivatives of h by virtue of a consistent estimate of the kinematic boundary condition (10d), (ii) replace space derivatives of q – except for the diffusive term $\partial_{xx}q$ – by the corresponding consistent asymptotic expansions, and (iii) add to the r.h.s. of (23b) the higher–order residue $+3\left(q^{(0)} + \varepsilon q^{(1)} + \varepsilon^2 q^{(2)} - q\right)/Re\,h^2 = O(\varepsilon^3)$, so to preclude algebraic cancellation of linear source terms – see (26) – as part of the model quasi-linear reformulation (Lavalle et al., 2015). After these manipulations, the following depth-averaged closed set of two evolution equations is obtained:

$$\partial_t h + \partial_x q - \frac{\Lambda\cos\beta\,h^3\,\left(\partial_x h\right)}{2\,Fr}\,Ma^2 = 0 \tag{25a}$$

$$\frac{h\,\left(\partial_x h\right)\cos\beta\,\varepsilon}{Fr} + \frac{3\,h^4\,\left(\partial_x h\right)\,\Lambda^2\,\varepsilon}{5} + \varepsilon\,\left(\partial_t q\right) = \frac{h\,\left(\partial_{xxx}h\right)\,\varepsilon^3}{We} + \\ - \frac{4\,Re\,h^5\,\left(\partial_{xxxx}h\right)\,\Lambda\,\varepsilon^4}{21\,We} - \frac{2\,Re\,h^4\,\left(\partial_x h\right)\,\left(\partial_{xxx}h\right)\,\Lambda\,\varepsilon^4}{3\,We} + \tag{25b}$$

$$+\frac{2\,Re\,h^4\left(\partial_{xx}h\right)^2\Lambda\,\varepsilon^4}{5\,We}+\frac{4\,Re\,h^3\left(\partial_x h\right)^2\left(\partial_{xx}h\right)\Lambda\,\varepsilon^4}{5\,We}+$$
$$+\frac{4\,Re\,h^5\left(\partial_{xx}h\right)\Lambda\cos\beta\,\varepsilon^2}{21\,Fr}+\frac{16\,Re\,h^4\left(\partial_x h\right)^2\Lambda\cos\beta\,\varepsilon^2}{15\,Fr}+$$
$$+\frac{3\,Ma^2\,h^2\,\Lambda\cos\beta}{8\,Fr\,Re}-\frac{8\,Re\,h^8\left(\partial_{xx}h\right)\Lambda^3\,\varepsilon^2}{105}-\frac{23\,Re\,h^7\left(\partial_x h\right)^2\Lambda^3\,\varepsilon^2}{35}+$$
$$+\frac{h^2\left(\partial_{xx}h\right)\Lambda\,\varepsilon^2}{Re}+\frac{3\,h\left(\partial_x h\right)^2\Lambda\,\varepsilon^2}{Re}+\frac{2\left(\partial_{xx}q\right)\varepsilon^2}{Re}+\frac{h\,\Lambda}{Re}-\frac{3\,q}{Re\,h^2},$$

where the dimensionless number Λ is defined as $Re/Fr\,\sin\beta$. Here, by using the definitions of $\tilde{U}_N$, Re and Fr, we get that $\Lambda = 3$. In other contexts, this parameter may assume different values, such as when a different characteristic speed is used instead of Nusselt integral velocity $\tilde{U}_N$, in case of a fluid exhibiting a non-Newtonian constitutive behaviour (Noble and Vila, 2013), or in presence of a variable or uneven interfacial pressure p_i; it has been decided not to replace Λ by any numerical value (Richard et al., 2019) only to prevent loss of generality.

With reference to Eq. (25b), it is worth pointing out two additional facts. (i) Higher-order and non-linear capillary terms have been explicitly and fully retained, unlike what customarily developed (Ruyer-Quil and Manneville, 1998; Richard et al., 2016, 2019). In fact, their contribution could be equally gathered on the l.h.s. within the canonical convective term proportional to $\varepsilon\,\partial_x\left(q^2/h\right)$, leading to an equivalent model in terms of consistency. (ii) Inertial terms have been maintained up to $O(\varepsilon^2)$, dissimilarly from the well-established practice of relying on a simplified model (Ruyer-Quil and Manneville, 2002). In fact, we are interested in comparing the whole second-order expansions with their incompressible analogues.

The derived shallow-water system (25a) constitutes a second-order reduced model describing the weakly-compressible free–surface flow of a wavy gravity-driven Newtonian falling film. In the scenario where the temperature field within the liquid film yields density variations, the EoS (12) should be modified accordingly to take into account density-affecting thermal effects. In addition, the model (25a) should be coupled to an integral form of the energy equation to characterise the interplay between hydrodynamics, compressibility and heat transfer. For this, reduced models for non-isothermal (incompressible) falling films have been successful in solving the heat transfer across the liquid film (Trevelyan et al., 2007; Thompson et al., 2019; Cellier and Ruyer-Quil, 2020).

4. Temporal linear stability

A temporal stability analysis relies on the existence of a steady solution about which perturbations are superimposed. Let $\mathbf{Q}(x,\,t) = \{h(x,t),\,q(x,t)\}^T$ represent the column vector containing the two unknown integral variables describing the film descent. Indeed, the weakly-compressible shallow-water Eqs. (25a) possibly admit to be recast as

$$\partial_t\,\mathbf{Q} + \partial_x\,\boldsymbol{\mathcal{F}}\left(\mathbf{Q}\right) = \boldsymbol{\mathcal{S}}\left(\mathbf{Q}\right), \tag{26}$$

where $\boldsymbol{\mathcal{F}}$ is the associated flux vector whereas $\boldsymbol{\mathcal{S}}$ gathers source terms together (Noble and Vila, 2014).

4.1. Normal mode analysis

The linear stability problem of the low-dimensional weakly-compressible model (25a) is approached through normal mode decomposition, according to which a harmonic infinitesimal disturbance $\mathbf{Q}_p$, having $\|\hat{\mathbf{Q}}\| \ll 1$ as amplitude, is added to the Nusselt base state. The latter is explained in terms of the dimensionless uniform parallel solution $\mathbf{Q}_0 = \left\{h_0,\,q_0\right\}^T$, in which $h_0 = \tilde{h}_0/\tilde{h}_N \equiv 1$ by definition, whereas the novel expression for the compressible primary discharge q_0 will be disclosed as part of the linearisation process. Accordingly, it is written

$$\mathbf{Q}(x,t) = \mathbf{Q}_0 + \mathbf{Q}_p(x,t) \tag{27a}$$
$$\mathbf{Q}_p(x,t) = \hat{\mathbf{Q}}\,\exp\left[\,i\,k\,(x - c\,t)\right], \tag{27b}$$

where it remains understood that $k = 2\pi\,\tilde{h}_N/\tilde{\mathcal{L}} \in \mathbb{R}^+$ and $c = c_r + i\,c_i \in \mathbb{C}$ are, respectively, the dimensionless real wave-number and the complex wave celerity of the propagating sine-type pulse. In particular, c_r accounts for its phase velocity, whereas $k\,c_i$ determines its degree of amplification or damping, depending on its sign: with reference to (27b), instability of the mean flow evidently sets in on the condition that $k\,c_i > 0$.

4.1.1. Base flow calculation

Quasi-linear conservation form (26) actually stipulates a formal relation between differential operators (Meliga et al., 2010) in such a way that

$$\boldsymbol{\mathcal{S}}\left(\mathbf{Q}_0\right) = 0 \tag{28}$$

restores the equilibrium condition constraining the dimensionless compressible base flow rate $q_0\,(Re,\,\beta,\,Ma)$ to the dimensionless waveless thickness h_0. Solving (28) we find:

$$q_0 = \frac{\Lambda\,h_0^3}{3}\left(1 + \overbrace{\frac{3}{8}\,\frac{Ma^2\,\Lambda\,\cot\beta\,h_0}{Re}}^{\Delta\,q^{(2)}_{0,\mathrm{rel}}}\right), \tag{29}$$

which explicitly shows that compressibility entails a relative increase in the equilibrium flow rate q_0, according to the over-bracketed second-order contribution denoted as $\Delta\,q^{(2)}_{0,\mathrm{rel}}$, with respect to its incompressible limit $q_0^{Ma\to 0^+} = \Lambda\,h_0^3/3$. Expression (29) likewise coincides with the stationary waveless solution associated to system (23a) in the case of unidirectional flow. Compressible effects are kept at the base flow level $\mathbf{Q}_0$, on which linear disturbances $\mathbf{Q}_p$ develop, by means of a small additive contribution to the incompressible ground-state flow rate $q_0^{Ma\to 0^+}$. Such a correction $(q_0^{Ma\to 0^+}\,\Delta\,q^{(2)}_{0,\mathrm{rel}})$ appears to be of $O(\varepsilon^2)$ since, choosing $\alpha = 1$, we assumed Ma to be of order $O(\varepsilon)$.

4.1.2. Model dispersion relation

Dropping higher-order perturbations and plugging (27a) into (25a) yields the following matrix-form differential system:

$$\partial_t\,\mathbf{Q}_p + \begin{bmatrix} a_{11} & 1 \\ a_{21} & 0 \end{bmatrix}\partial_x\,\mathbf{Q}_p = \begin{bmatrix} 0 & 0 \\ b_{21} & b_{22} \end{bmatrix}\mathbf{Q}_p +$$
$$+\begin{bmatrix} 0 & 0 \\ c_{21} & c_{22} \end{bmatrix}\partial_{xx}\,\mathbf{Q}_p + \begin{bmatrix} 0 & 0 \\ s_{21} & 0 \end{bmatrix}\partial_{xxx}\,\mathbf{Q}_p + \begin{bmatrix} 0 & 0 \\ d_{21} & 0 \end{bmatrix}\partial_{xxxx}\,\mathbf{Q}_p, \tag{30}$$

where

$$a_{11} = -\frac{Ma^2\,h_0^3\,\Lambda^2\,\cot\beta}{2\,Re} \qquad b_{21} = \frac{3\,\Lambda}{Re} + \frac{3}{2}\,\frac{Ma^2\,h_0\,\Lambda^2\,\cot\beta}{Re^2} \tag{31a}$$
$$a_{21} = \frac{3}{5}\,h_0^4\,\Lambda^2 + \frac{h_0\,\Lambda\,\cot\beta}{Re} \qquad b_{22} = -\frac{3}{Re\,h_0^2} \qquad c_{22} = \frac{2}{Re} \qquad s_{21} = \frac{h_0}{We} \tag{31b}$$
$$c_{21} = \frac{4}{21}\,h_0^5\,\Lambda^2\,\cot\beta - \frac{8}{105}\,Re\,h_0^8\,\Lambda^3 + \frac{h_0^2\,\Lambda}{Re} \qquad d_{21} = -\frac{4}{21}\,\frac{Re\,h_0^5\,\Lambda}{We}. \tag{31c}$$

Expressions (31b)–(31c) do not incorporate the Mach number, thus ε has been legitimately replaced there by a unitary value (Richard et al., 2019). Such assignment is based on the fact that pertinent orders of magnitude have been already accounted for in the integral model (25a).

Eq. (30) accounts for the normal mode evolution (27b) under the form of a generalised algebraic eigenvalue problem for c and $\hat{\mathbf{Q}}$, having $\langle k;\ Re,\ \beta,\ We,\ Ma\rangle$ as independent set of relevant parameters. Seeking a non-trivial solution, one has to impose that the matrix associated to

the linearised system is degenerate. This leads to a quadratic polynomial dispersion relation over the complex field in the phase speed c with complex k–dependent coefficients, written as

$$-k\,c^2+\left[a_{11}\,k+i\,\left(b_{22}-k^2\,c_{22}\right)\right]\,c+ \\ +\;k^3\,s_{21}+k\,a_{21}+i\,\left[d_{21}\,k^4+\left(a_{11}\,c_{22}-c_{21}\right)\,k^2+\left(b_{21}-a_{11}\,b_{22}\right)\right]\;=0. \tag{32}$$

4.2. Celerity long-wave expansion

Following Yih (1963), we consider the temporal stability problem in terms of an asymptotic expansion of the wave celerity $c(k)$ into successive powers of the wavenumber k:

$$c=c^{(0)}+k\,c^{(1)}+k^2\,c^{(2)}+k^3\,c^{(3)}+\cdots, \tag{33}$$

within the limit provided by the long-wave approximation ($k\ll 1$) assumed in this work. In analogy with the closure algorithm illustrated in Section 3.2.1, the expansion (33) is substituted into the dispersion relation (32). Ensuring that each order in k satisfies (32), we get a cascade of equations from which the higher-order celerities $c^{(n)}(k)$ ($n=0,1,2,\ldots$) are obtained. Although evolution Eqs. (25a) are consistent up to $O(\varepsilon^2)$, we intentionally take the expansion (33) for the celerity $c(k)$ up to its successive order in terms of k, that is until $O(k^3)$. In this way, we can test the accuracy of the present model (25a) in its incompressible limit $Ma\to 0^+$, by setting the benchmark against the Orr–Sommerfeld stability problem (Orr, 1907; Sommerfeld, 1908) at the corresponding order. Such a comparative approach constitutes a well-trodden path among the falling-film community (Ruyer-Quil and Manneville, 1998; Samanta et al., 2011; Samanta, 2014; Richard et al., 2016). Specifically, we obtain:

$$c^{(0)}=3 \tag{34a}$$

$$c^{(1)}=3\,i\left(\frac{2}{5}\,Re-\frac{1}{3}\,\cot\beta+\Gamma_2^{(1)}\,Ma^2\,\cot\beta\right) \tag{34b}$$

$$c^{(2)}=3\left(-1+\frac{10}{21}\,Re\,\cot\beta-\frac{4}{7}\,Re^2+\Gamma_2^{(2)}\,Ma^2\,\cot\beta+\Gamma_4^{(2)}\,Ma^4\,\cot^2\beta\right) \tag{34c}$$

$$c^{(3)}=3\,i\left(-\frac{1}{9}\,Re\,\cot^2\beta+\frac{128}{105}\,Re^2\,\cot\beta+\frac{2}{9}\,\cot\beta-\frac{Re}{9\,We}-\frac{228}{175}\,Re^3+ \right. \\ \left. -\frac{34}{15}\,Re+\Gamma_2^{(3)}\,Ma^2\,\cot\beta+\Gamma_4^{(3)}\,Ma^4\,\cot^2\beta+\Gamma_6^{(3)}\,Ma^6\,\cot^3\beta\right), \tag{34d}$$

in which we use the equality $\Lambda=3$ and the identity $h_0\equiv 1$. Those expressions for the wave celerities have been written to highlight the effect of the compressibility. In fact, the expansions (34a) are impacted by compressibility from $n=1$ onwards ($n=1,2,\ldots$) through additive contributions that take the form $\Gamma_{2j}^{(n)}\,Ma^{2j}\cot^j\beta$, with $1\le j\le n$. These are found to be:

$$\Gamma_2^{(1)}=\frac{3}{2}\qquad \Gamma_2^{(2)}=\frac{1}{2}\,\cot\beta-\frac{18}{5}\,Re-\frac{1}{Re} \tag{35a}$$

$$\Gamma_4^{(2)}=-\frac{9}{4}\qquad \Gamma_2^{(3)}=\frac{19}{7}\,Re\,\cot\beta-\frac{324}{35}\,Re^2-\frac{9}{2} \tag{35b}$$

$$\Gamma_4^{(3)}=\frac{3}{4}\,\cot\beta-\frac{243}{20}\,Re-\frac{3}{2\,Re}\qquad \Gamma_6^{(3)}=-\frac{27}{8}. \tag{35c}$$

In accordance with the adopted standard of accuracy, the current model is consistent with the asymptotic expansions of solutions to Orr–Sommerfeld boundary-value problem, reported in Ruyer-Quil and Manneville (1998), in the limit of $Ma\to 0^+$: (25a) is able to correctly recover $c^{(0)}$, $c^{(1)}\big|_{Ma\to 0^+}$ and $c^{(2)}\big|_{Ma\to 0^+}$, but it manifests disagreements on successive orders. For more in-depth reflection on such validation the reader is referred to Appendix C, being the primary focus of sections Sections 4, 5 upon the influence of a weak compressibility on the linear stability.

5. Results and discussion

In this section we examine the relations (34a) in the light of the well-known results from Kapitza (1948) and Benjamin (1957). The $O(k^0)$ celerity (34a) immediately captures the classical phase speed of free-surface waves, which travel three times faster than the averaged flat film, regardless of its compressible behaviour. Due to the nature of (14) as EoS, the compressibility terms controlled by the Mach number affect only even powers Ma^{2j} throughout $O(k^n)$ expansions (34b)–(34d), for $1\le j\le n$.

Secondly, as evidenced by the relations (31a) and (34a), a vertical liquid film is not affected by the compressibility since $\cot\left(\frac{\pi}{2}\right)=0$ in (25a). On the other hand, when the plate is horizontal, $\beta=0$ and no gravity–driven drainage is possible.

5.1. Impact of compressibility on the wave celerity

Differently from the incompressible Navier–Stokes equations, whose temporal stability analysis is pursued through numerical solution of the Orr–Sommerfeld fourth-order differential problem in the cross-stream coordinate, in this case the dispersion relation (32) is a quadratic polynomial equation in $c(k)$, which is easily solvable numerically.

Initially, we consider a falling liquid film whose incompressible flow is marginally stable. This case will be shown to be the most favourable to discern compressibility-related effects on the film flow stability within the investigated weakly-compressible regime. The plate is angled at $\beta=4.6°$. As an aside, this choice enables us to compare the wave celerity and growth rate (see Appendix C) between the results presented here within the incompressible limit $Ma\to 0^+$ (dark red line in Fig. 2) and those determined by Brevdo et al. (1999) for a perfectly incompressible falling film in a passive atmosphere. The effects of compressibility on the hydraulic branch solving (32) both in its real and imaginary parts are displayed in Fig. 2*a*, *b* respectively, for sufficiently small values of the Mach number $Ma=O(\varepsilon)$. Specifically, the evolution of the phase speed $c_r(k)$ bends downwards as the Mach number increases. Nonetheless, the same long-wave limit $c^{(0)}$ is recovered, as established by (34a). The delaying effect of compressibility on the phase velocity of linear waves (Richard et al., 2019) finds confirmation in our study. The growth rate $k\,c_i(k)$ shown in Fig. 2*b* deviates upwards and towards increasing cut-off wavenumber k_c for growing Ma. Thus, compressibility plays a destabilising role on linear free-surface waves.

Even more distinctly, we observe this feature in Fig. 3, which shows the curve of marginal stability obtained for different values of the Mach number in the $(Re,\,k_c)$ plane for $\beta=1.5°$. Above the marginal stability curve, perturbations of wavenumber k decay in time, whereas they are amplified below. Here, the unstable region systematically undergoes a non-linear enlargement up to a smaller critical Reynolds number Re_{cr} due to the compressibility.

In order to quantify this shift into the stability threshold, we can examine the first-order expansion of the wave celerity $c^{(1)}$, which for $Ma\ll 1$ yields the following relation

$$Re_{cr}=\frac{5}{6}\left(1-\frac{9}{2}\,Ma^2\right)\cot\beta, \tag{36}$$

obtained by making Re explicit from (34b) when the neutral stability condition $k\,c_i\left(k_c\right)=0\iff c^{(1)}\big|_{Re_{cr}}=0$ is imposed. In the limit of null Mach number, equation (36) reduces to the result of Benjamin (1957) and Yih (1963), *i.e.*, $Re_{cr}^{Ma\to 0^+}=5/6\,\cot\beta$. Conversely, we observe that for $Ma=O(\varepsilon)>0$ the compressibility lowers the critical Reynolds number Re_{cr} by a factor equal to

$$\frac{Re_{cr}\,(Ma)}{Re_{cr}^{Ma\to 0^+}}=1-\frac{9}{2}\,Ma^2<1, \tag{37}$$

anticipating the flow primary instability. This effect tends to asymptotically vanish in highly inertial regimes, within which compressible

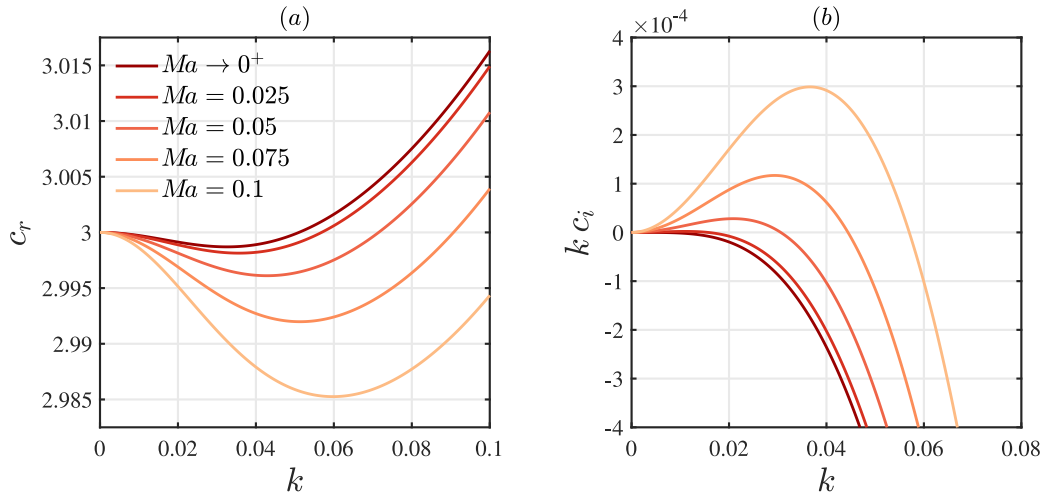

Fig. 2. Impact of compressibility on the graphical representation of solutions to the dispersion relation (32) for the second-order integral model (25a), in terms of (*a*) phase speed c_r and (*b*) growth rate $k\,c_i$ as a function of the dimensionless wavenumber k, for different small values of the Mach number Ma, displayed in the legend. The axes are dimensionless. The data used are taken from Brevdo et al. (1999) and correspond to the following set of values: $g = 9.81$ m s^{-2}, $\beta = 4.6°$, $Re = 5/6\,\cot\beta = 10.357$, $\tilde{\rho}_0 = 1130$ kg m^{-3}, $\tilde{\mu}_0 = 5.673\,10^{-3}$ Pa s, $\tilde{\gamma}_0 = 69.0\,10^{-3}$ N m^{-1}. Comparison with Brevdo et al. (1999) is shown in Appendix C for the incompressible scenario.

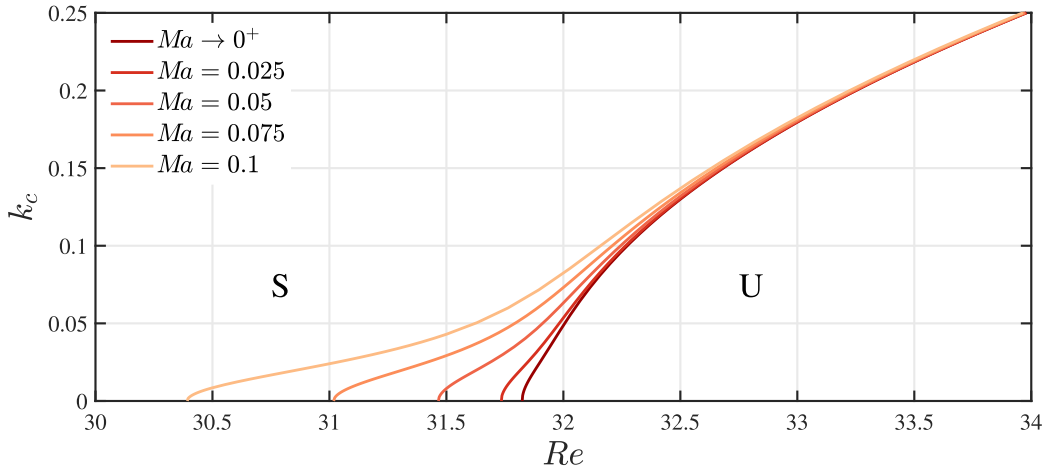

Fig. 3. Impact of compressibility on the neutral stability diagram displaying the dimensionless cut-off wavenumber k_c as a function of the Reynolds number Re, for different small values of the Mach number Ma, shown in the legend. Parameter values: $g = 9.81$ m s^{-2}, $\beta = 1.5°$. Fluid physical properties – related to a falling film consisting of a water–glycerin mixture – are taken from Liu and Gollub (1994): $\tilde{\rho}_0 = 1070$ kg m^{-3}, $\tilde{\mu}_0 = 6.72\,10^{-3}$ Pa s, $\tilde{\gamma}_0 = 67.0\,10^{-3}$ N m^{-1}. The *stable* and *unstable* domain in the (Ma, Re) plane corresponds to areas labelled, respectively, "S" and "U".

curves visibly become rapidly convergent towards the incompressible marginal stability plot (right-most line in Fig. 3). This finding is consistent as both the two compressible coefficients (31a) of the eigenproblem (30) are inversely proportional to the Reynolds number or its square power. Interestingly, we remark that the ratio expressed by (37) is independent of the plate inclination β.

5.2. Parametric analysis

Aiming at understanding the basic effects of compressibility on the film destabilisation, we investigate how the growth rate of disturbances $k\,c_i$ evolves as the parameter space, namely $\langle Re,\ \beta,\ We,\ Ma\rangle$, is explored. This will enable us to understand the fundamental physical mechanism through which compressibility acts, which we examine more in depth in Section 6.

We start by providing a variety of numerical solutions to the linear stability problem (30) within the plane $(k,\ k\,c_i)$, for different values of the Reynolds number Re and angle of inclination β. Eqs. (34a) suggest that a polynomial-type dependence is established by the novel Ma^{2j}–related contributions, namely $\Gamma_{2j}^{(n)}\cot^j\beta$. Unfortunately, the coefficients $\Gamma_{2j}^{(n)}$ display a fairly cumbersome functional dependence on $\cot\beta$ (as well as on Re) – apart from when $j = n$. For this reason, notwithstanding that the compressibility has no impact on a vertical falling film, it is not possible to determine *a priori* whether its effects varies with the inclination. Therefore, we will extensively cover the full range of variability in β, starting by focusing on mildly tilted configurations.

In Fig. 4 we initially consider four cases, denoted with letters (*a*–*d*), which differ from each other in terms of slope. To draw an appropriate comparison among these scenarios between each compressible curve ($Ma = 0.1$ – dashed lines) and its incompressible counterpart (solid lines), the so-defined Reynolds critical ratio RCR

$$\mathrm{RCR} \overset{\mathrm{def}}{=} \frac{Re}{Re_{cr}^{Ma\to 0^+}} \tag{38}$$

is introduced as an inertia-based parameter. Four growing values of RCR are considered in each of the panels of Fig. 4, starting from a value

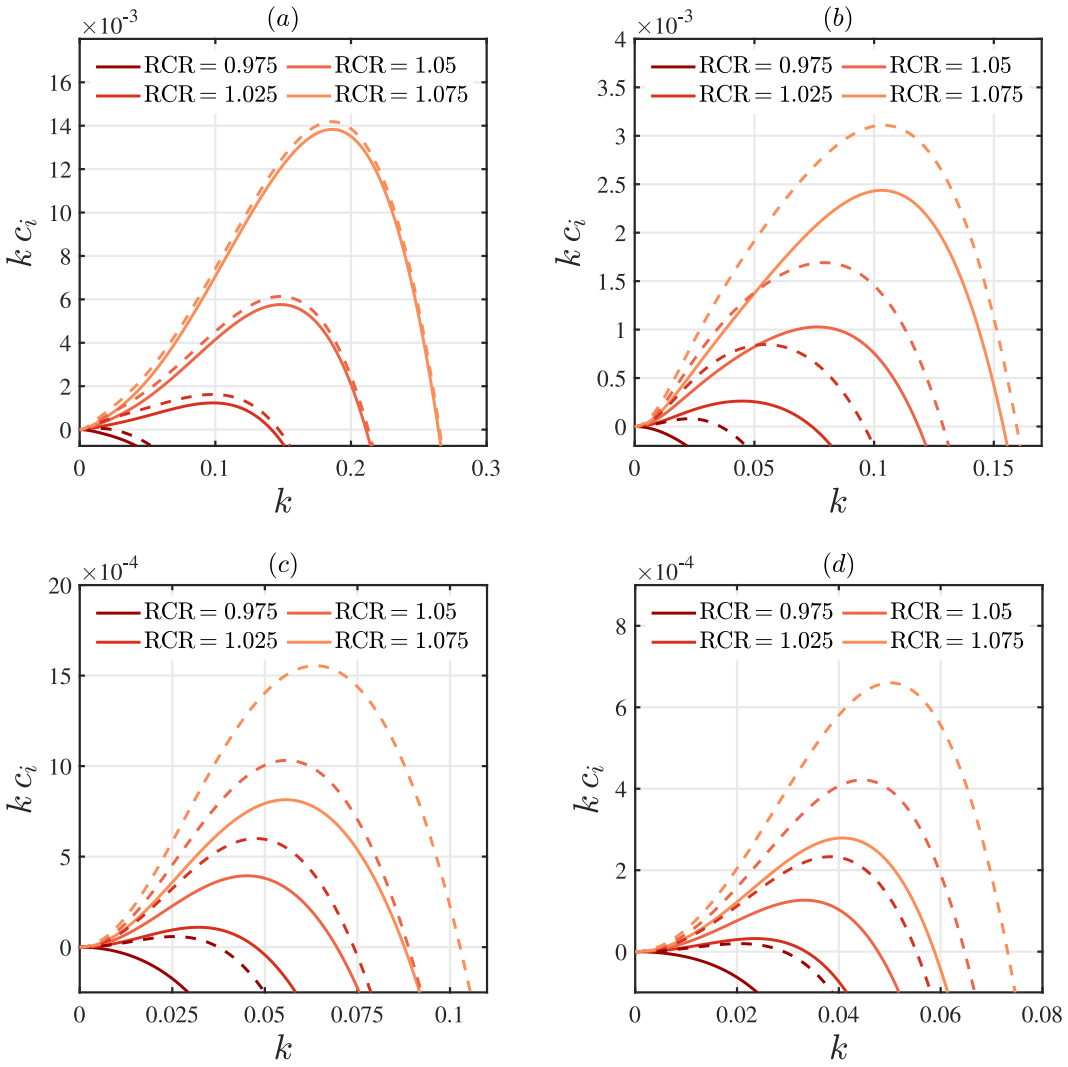

Fig. 4. Effect of the Reynolds critical ratio RCR (38) (shown in the legend) on the graphical representation of the solution to the dispersion relation (32) for the derived weakly-compressible second-order model (25a), in terms of the dimensionless imaginary growth rate $k\,c_i$ as a function of the dimensionless wavenumber k, for flow configurations which differ from each other in the value of the inclination angle β: (*a*) $\beta = 1.5°$, (*b*) $\beta = 3.0°$, (*c*) $\beta = 6.0°$, (*d*) $\beta = 12.0°$. The axes are dimensionless. Solid lines: $Ma \to 0^+$ (incompressible case), dashed lines: $Ma = 0.1$. Apart from the tilt angle β, other parameter values and fluid physical properties employed here are those of Fig. 3.

which is numerically less than unity – which indicates a stable situation for a perfectly incompressible falling film flow – before moving to values of Re which progressively exceed the critical incompressible threshold.

As expected, the augmentation of RCR is associated with the extension of the instability region $c_i(k) > 0$. When we switch from each incompressible plot to its compressible analogue, the rightwards shift of the cut-off wavenumber k_c is reduced as the RCR is raised. This is in accordance with what previously shown in Fig. 3. As the incline of the plate becomes steeper, provided that moderately low-angle configurations are explored, the compressibility plays an increasingly important effect in relative terms in terms of a rightward shift of the dispersion curves.

In order to better appreciate this phenomenon, we represent in Fig. 5 the contours of the cut-off wavenumber related to its incompressible limit $k_c/k_c^{Ma\to 0^+}$ as a function of the Mach number Ma and of the inclination angle β for two different values of Reynolds critical ratio RCR beyond the stability threshold, corresponding to (*a*) RCR = 1.025 and (*b*) RCR = 1.05, respectively. In both scenarios we identify two distinct regions of the (Ma, β) plane: (i) a low-angle region ($1.5° \lesssim \beta \lesssim 12°$) where compressibility-induced destabilisation is not fully-developed in terms of rightward shift of the cut-off wavenumber and (ii) a region that covers moderately to highly tilted configurations ($12° \lesssim \beta \lesssim 80°$), where the same effects are independent of the value of inclination angle β. From a graphical point of view, the isolines rapidly tend to become vertical, indicating a fast saturation of $k_c/k_c^{Ma\to 0^+}$ with respect to slope.

Within area (ii), at $Ma = 0.1$ – the highest level of weak compressibility investigated – the cut-off wavenumber is increased by up to roughly 60% when RCR = 1.025 and 35% when RCR = 1.05 in comparison with the incompressible case. As it will soon become clear, there exists a third upper region (iii) – for $80° \lesssim \beta \leq 90°$ – which is difficult to explore by employing the parameter RCR since, there, a vertically falling film flow is always unstable to linear perturbations (Benjamin, 1957; Yih, 1963).

A similar behaviour is shown by the most unstable wavenumber and the maximum growth rate of linear disturbances related to their incompressible limit, *viz.* $k_{\max}/k_{\max}^{Ma\to 0^+}$ and $\omega_{i,\max}/\omega_{i\,\max}^{Ma\to 0^+}$ respectively, which are displayed in Fig. 6*a,b* as a function of the Mach number Ma and the inclination angle β in the case of a Reynolds critical

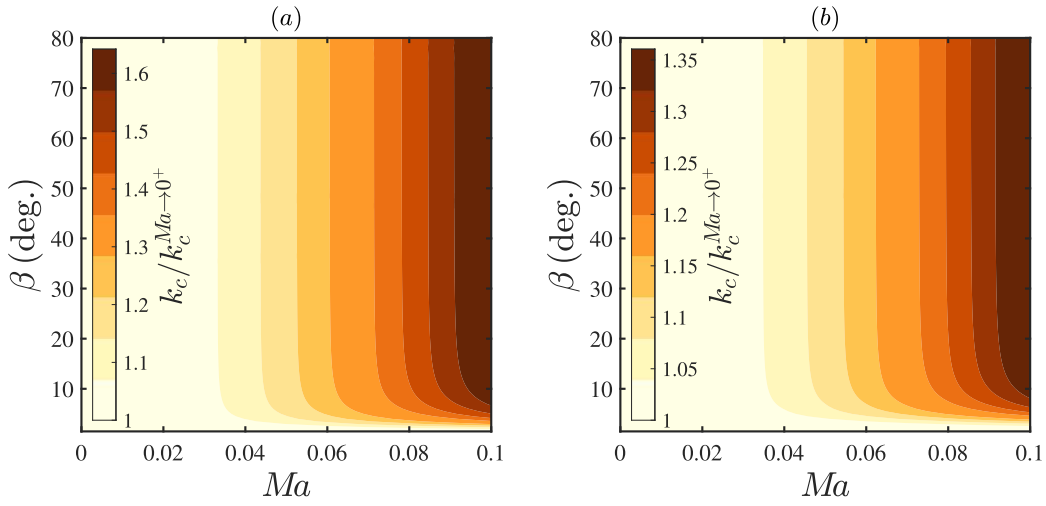

Fig. 5. Effect of the Mach number $Ma = O(\epsilon)$ and of the angle of inclination β on the stability of a falling water–glycerin film in terms of deviation of the cut-off wavenumber k_c from its incompressible limit $k_c^{Ma\to 0^+}$ with reference to the temporal growth rate of linear disturbances $k\, c_i(k)$, for two different fixed values of the Reynolds critical ratio (38), corresponding to (*a*) RCR = 1.025 and (*b*) RCR = 1.05. In overall terms, darker regions correspond to a greater destabilisation. The set of parameter values and fluid physical properties is the same specified for Fig. 3.

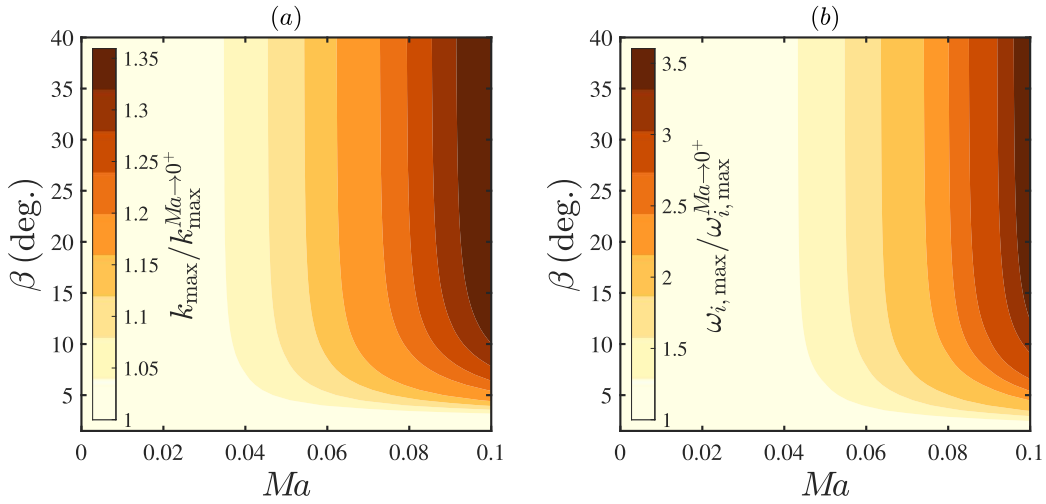

Fig. 6. Effect of the Mach number $Ma = O(\epsilon)$ and of the angle of inclination β on the stability of a falling water–glycerin film. Deviation of (*a*) the most unstable wavenumber $k_{\max}$ from its incompressible limit $k_{\max}^{Ma\to 0^+}$, (*b*) the maximum growth rate $\omega_{i,\max}$ from its incompressible limit $\omega_{i,\max}^{Ma\to 0^+}$ for a value of Reynolds critical ratio (38) equal to RCR = 1.05. In overall terms, darker regions correspond to a greater destabilisation. The set of parameter values and fluid physical properties is the same specified for Fig. 3.

ratio equal to RCR = 1.05. The results are shown up to $\beta = 40°$, as the isocontour does not change in the region $40° < \beta < 80°$, as discussed before. The most unstable wavenumber increases up to 35% compared with its incompressible analogue. Also, the compressibility induces a similar increase of $k_c/k_c^{Ma\to 0^+}$ and $k_{\max}/k_{\max}^{Ma\to 0^+}$, as shown in Figs. 6*a* and 5*b*, indicating that the destabilisation involves both long and relatively short waves. Meanwhile, the maximum growth rate $\omega_{i,\max}$ can reach values up to about three and a half times higher than the incompressible one.

A method to explore the role of compressibility at highly-tilted configurations consists in predetermining an adequate value of Re. For such a selection, we chose to cover a reasonably broad spectrum of slopes (with special attention to the steepest ones), without dropping the shallowness assumption.

Fig. 7 displays the contours of the normalised cut-off wavenumber as a function of the Mach number and of the inclination angle for two different fixed values of the Reynolds number, corresponding to (*a*) $Re = 1$ (with β ranging between 60° and 90°) and (*b*) $Re = 3$ (with $20° \leq \beta \leq 60°$). These combination of (Re, β) is such as to determine the onset of interfacial instability. From panels *a*–*b*, one may erroneously infer that, as β increases, $k_c/k_c^{Ma\to 0^+}$ exhibits a diminishing trend in contrast with previous results. However, this evolution is fully justifiable in the following terms: keeping Re fixed while the solid substrate steepens is tantamount to moving further away from the critical threshold, which corresponds to a progressive augmentation of the Reynolds critical ratio RCR, that is a situation where the compressibility-related effects on the destabilisation are less significant. As a consequence, Fig. 7 is consistent with what displayed in Figs. 3, 5 and, besides, helps in extending our analysis to the case of a vertical falling film flow.

As final part of the parametric study our sole aim is to investigate the influence of the Weber number We – and thus of the surface tension – on the compressibility – induced destabilising mechanism. To do so, we conclude by presenting numerical results for three different fluids: (i) water, (ii) aqueous solution of dimethylsulfoxide (DMSO), and (iii) aqueous solution of glycerin. As summarised in Table 1, these fluids display different physical properties in terms of density, kinematic viscosity and surface tension, notwithstanding that the adopted barotropic EoS (14) remains unaltered among them. As regards the other variables belonging to the parameter space, the angle of inclination and the Reynolds critical ratio have been kept fixed and equal to $\beta = 15°$ and

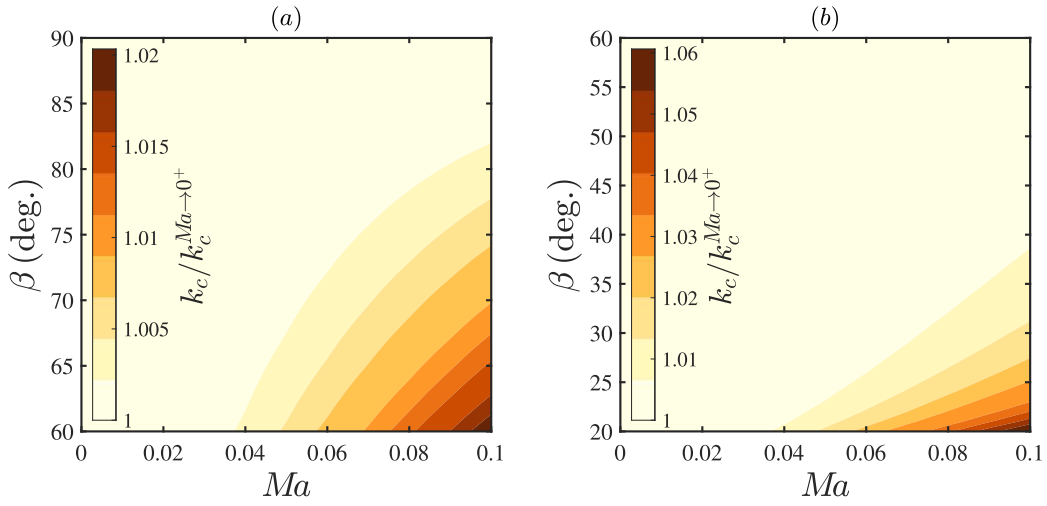

Fig. 7. Effect of the Mach number $Ma = O(\epsilon)$ and of the angle of inclination β on the stability of a falling water–glycerin film in terms of deviation of the cut-off wavenumber k_c from its incompressible limit $k_c^{Ma\to 0^+}$ with reference to the temporal growth rate of linear disturbances $k\, c_i(k)$, for two different fixed values of the Reynolds number, corresponding to (*a*) $Re = 1$ and (*b*) $Re = 3$. In overall terms, darker regions correspond to a greater destabilisation. The set of parameter values and fluid physical properties is the same specified for Fig. 3.

Table 1
Physical properties of fluids considered in the numerical stability calculations. The working liquids are the same as in Lavalle et al. (2019) (table 3 there): water, an aqueous solution of DMSO at 83.11% by weight, and an aqueous solution of glycerin at 50% by weight. The Kapitza number Ka is defined as $Ka = \tilde{\gamma}_0 \left(\tilde{\rho}_0\, g^{1/3}\, \tilde{\nu}_0^{4/3}\right)^{-1}$, being $\tilde{\nu}_0 = \tilde{\mu}_0/\tilde{\rho}_0$ the kinematic viscosity of the fluid under consideration.

Fluid	$\tilde{\rho}_0$ $(\mathrm{kg\,m^{-3}})$	$\tilde{\nu}_0$ $(10^{-6}\,\mathrm{m^2\,s^{-1}})$	$\tilde{\gamma}_0$ $(10^{-3}\,\mathrm{N\,m^{-1}})$	Ka
Water	1000.0	1.00	76.9	3592
DMSO (83.11%)	1098.3	2.85	48.4	509.5
Glycerin (50%)	1130.0	5.02	69.0	331.8

RCR = 1.05, respectively. Such a choice corresponds to the following set of values for the Weber number: (i) $We = 8.841\ 10^{-4}$, (ii) $We = 6.234\ 10^{-3}$, (iii) $We = 1.156\ 10^{-2}$. We have represented in Fig. 8 the cut-off wavenumber (a) and the maximum growth rate (b) as a function of the Mach number Ma for the three liquids considered. As before, in both panels the quantities shown are related to their analogues in the limit of a perfectly incompressible flow. Within the present weakly compressible scenario, we see that the onset of the long-wave instability is dimly affected by surface tension and the destabilising effect of compressibility is felt earlier at low Weber numbers.

6. Physical basis for the destabilising effect of compressibility

This section aims at clarifying the underlying physics behind the compressibility effect on the onset of the flow primary instability.

6.1. Whitham wave hierarchy

The hydrodynamic stability of a shallow-water flow is linked to the propagation of interfacial waves (Whitham, 1974; Alekseenko et al., 1985, 1994; Ooshida, 1999; Kalliadasis et al., 2013). In this respect, Whitham's theory of two-wave competition serves as a framework to interpret the linear stability properties of the depth-averaged weakly-compressible model (25a). To do so, we can make use of the dispersion relation (32) to study the mechanism at the base of the compressible-induced destabilisation. Specifically, we formally recast (32) into the canonical form

$$i\,(c - c_k) + \Omega\, k\,(c - c_{d^+})\,(c - c_{d^-}) = 0, \tag{39}$$

where $c_k\left(k^2; Re, \beta, We, Ma\right)$, $c_{d^\pm}\left(k^2; Re, \beta, We, Ma\right)$ and $\Omega\left(k^2; Re\right)$ are defined as follows

$$c_k = \frac{3}{2\,k^2+3}\left[3 + k^2\left(-1 - \frac{4}{7}\,Re\cot\beta + \frac{24}{35}\,Re^2 - \frac{3}{Re}\,Ma^2\cot\beta\right) - \frac{4}{21}\,\frac{Re^2}{We}\,k^4\right] \tag{40a}$$

$$c_{d^\pm} = -\frac{9\,Ma^2\,\cot\beta}{4\,Re} \pm \frac{1}{2}\sqrt{\frac{4\,k^2}{We} + \frac{12\,\cot\beta}{Re} + \frac{108}{5} + \frac{81\,Ma^4\,\cot^2\beta}{4\,Re^2}} \tag{40b}$$

$$\Omega = \frac{Re}{2\,k^2+3}. \tag{40c}$$

Since the dispersion relation (39) recalls a two-wave structure, our reduced model (25a) can be systematically reinterpreted as a second-order wave equation

$$\underbrace{\left(\partial_t + c_k\,\partial_x\right)h}_{\text{(i)}} + \Omega\,\underbrace{\left(\partial_t + c_{d^-}\,\partial_x\right)\left(\partial_t + c_{d^+}\,\partial_x\right)h}_{\text{(ii)}} = 0, \tag{41}$$

which consists of two levels (i) (ii) of linear hyperbolic wave equations. The lower-order solutions to (i) are the *kinematic* waves since they origin from the mass conservation (25a). These fast waves travel at a speed equal to c_k and they are dominant at long time and in the inertialess limit $\Omega(Re) \to 0^+$. Conversely, the higher-order *dynamic* waves of the second kind (ii) arise from the film response, governed by the stress continuity condition (10b)–(10c) or – equivalently – by the momentum balance (25b), to variations in momentum, hydrostatic pressure and surface tension. They correspond to the limit $\Omega(Re) \to +\infty$. In their early stage, wavefronts located at the leading front and at the trailing edge of a produced wave packet begin to travel at a speed equal to c_{d^+} and c_{d^-}, respectively.

Interestingly, the dependence of $\Omega(k)$ on the wavenumber k is a mere consequence of the non-hyperbolicity of the evolution equation appertaining to the integral model (25a), since terms whose order of spatial derivation exceeds the second would be ultimately included in it (Ruyer-Quil, 2012; Kalliadasis et al., 2013). Physically, this means that surface wave dispersion is modified by the streamwise viscous diffusion as early as the instability onset (Sharma and Dandapat, 2006). Anyway, $\Omega(k^2)$ is not appreciably affected by the squared wavenumber k^2. In fact, by inspection of (40c), the denominator $2\,k^2 + 3 \approx 3$ within the long-wave limit ($k \ll 1$). As an *a posteriori* argument, this fact adds

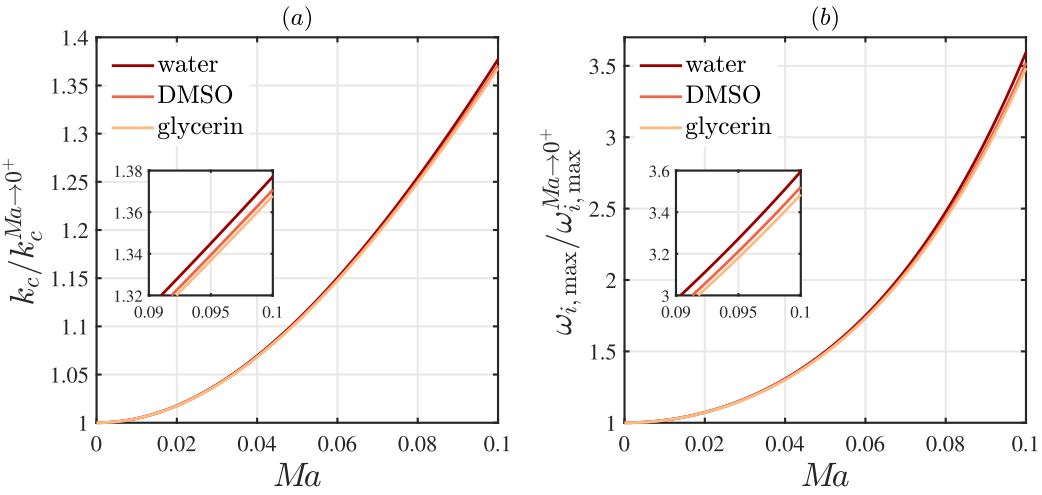

Fig. 8. Effect of the Mach number $Ma = O(\epsilon)$ on the stability of three falling film flows, each obtained employing one of the fluids detailed in Table 1 in terms of physical properties and listed in the legend. Curves represent the deviation of (*a*) the cut-off wavenumber k_c from its incompressible limit $k_c^{Ma\to 0^+}$ and (*b*) the maximum growth rate $\omega_{i,\max}$ from its incompressible limit $\omega_{i,\max}^{Ma\to 0^+}$ with reference to the temporal growth rate of linear disturbances $\omega_i(k) \equiv k\, c_i(k)$, for a fixed value of the Reynolds critical ratio (38), equal to RCR $= 1.05$, and inclination angle $\beta = 15°$.

legitimacy to the assumption of virtually non-dissipative fluid (Samanta et al., 2011), postulated in Section 3.1 behind the adoption of (14) as barotropic EoS. The dependence (40a) of the kinematic wave speed c_k on the squared wavenumber k^2 gives an estimate of the dispersive role of the streamwise second-order viscous terms, sometimes referred to as "viscous dispersive effect" (Ruyer-Quil et al., 2008).

6.1.1. Two-wave reframing of the critical threshold

Whitham (1974) proved that the film primary instability can be precisely reasoned in terms of competition between kinematic and dynamic waves. Whenever a multi-speed equation of the kind given in (41) holds, long-wave interfacial disturbances will damp on the condition that kinematic waves travel at a speed ranging between the speeds of dynamic waves:

$$c_{d^-} \le c_k \le c_{d^+}. \tag{42}$$

The origin of the temporal stability criterion (42) stems from the evolution of a localised precursory ripple (Ruyer-Quil, 2012). Since kinematic waves tend to emerge from the wave packet at long times, whereas its short-term dynamics is dominated by dynamic waves, the only stable situation is one where the back and front of the wave travel at dynamic wave speed c_{d^-} and c_{d^+} respectively, which implies constraint (42). The base state is marginally stable if $c_{d^-} = c_k$ or $c_{d^+} = c_k$. Here, in practice, only the latter condition has a binding character on the inception of the flow instability. Once evaluated in the limit of infinitely long waves ($k \to 0^+$), it is verified that equality:

$$c_{d^+} = c_k \tag{43}$$

is coherently able to recover (36), thus being in line with the expression for the neutral stability threshold previously found by means of an asymptotic expansion *à la* (Yih, 1963) for the wave celerity $c(k)$.

6.1.2. Elucidation of the compressibility-induced destabilising effect

To illustrate how compressibility enters Whitham's paradigm, we follow the methodology adopted by Samanta et al. (2011) and Samanta (2014) for liquid films falling along a slippery incline or in the presence of imposed shear stress, respectively. We consider the scenario discussed in Fig. 4(*a*, *d*), *i.e.* a water–glycerin film down a plane inclined at $\beta = 1.5°$ and $\beta = 12°$. For these two angles of inclination, Fig. 9 compares the kinematic wave speed c_k and the dynamic one c_{d^+} given by (40a) and (40b) as a function of the squared dimensionless wavenumber k^2, both within the incompressible limit $Ma \to 0^+$ (solid lines) and in a slightly compressible case, where $Ma = 0.1$ (dashed lines). Two values of the Reynolds critical ratio RCR – beyond the stability threshold, though in its vicinity – have been examined: (*a*, *c*) RCR $= 1.025$ and (*b*, *d*) RCR $= 1.075$.

Fig. 9 evidences that the compressibility contributes in lowering both the dynamic and the kinematic wave speeds. For further clarification, Fig. 9 has been completed with a proper close-up of the plane portion where curves cross each other. One easily realises that each compressible cut-off point (void circle) is always located at a higher squared wavenumber k^2 in comparison with its incompressible analogue (filled circle).

The kinematic wave speed c_k, however, is much less affected by the compressibility than the dynamic one c_{d^+}. This can be inspected by a brief discussion on the role of inertia. Let us first consider the low-angle configuration (upper panels). In such a scenario, the variation in the Reynolds critical ratio RCR in Fig. 9*a,b* seems to only have a minor impact on the compressible dynamic celerity c_{d^+} in terms of vertical shift. On the other hand, for the greatest RCR (panel *b*), the parabolic-like trend of the kinematic celerity c_k evolves with respect to k^2 in such a way that its descending tract gets drastically steeper in the vicinity of its point of intersection with the graph of the dynamic wave velocity c_{d^+}. As a consequence, the compressibility-induced destabilisation gets noticeably reduced when the Reynolds number increases.

We close this section by comparing panels (c – d), for which the inclination angle is $\beta = 12°$. Here we notice that the speed of kinematic waves c_k is less sensitive in comparison with the previous low-angle configuration to the same increase in the Reynolds critical ratio, from RCR $= 1.025$ (left) to RCR $= 1.075$ (right). Meanwhile, the dynamic wave speed c_{d^+}, which increases as a straight line with the square of the wavenumber k^2, undergoes deceleration by enhancing compressibility, but also by increasing RCR, leading to an attenuation of the compressibility-induced destabilisation.

6.2. Impact of compressibility on flow-related quantities

Aiming at finding a physical source to which the overflow uncovered in Section 4.1.1 may be attributed, we rephrase the pertinent perturbative analogue $\Delta q_{\mathrm{rel}}^{(2)} = \left(q^{(2)} - q^{(2)}\big|_{Ma\to 0^+}\right)/q^{(0)}$ in terms of dimensional variables, which gives:

$$\Delta q_{\mathrm{rel}}^{(2)} = \frac{\Lambda}{8}\frac{g\,\tilde{h}\cos\beta}{\tilde{a}_0^2}. \tag{44}$$

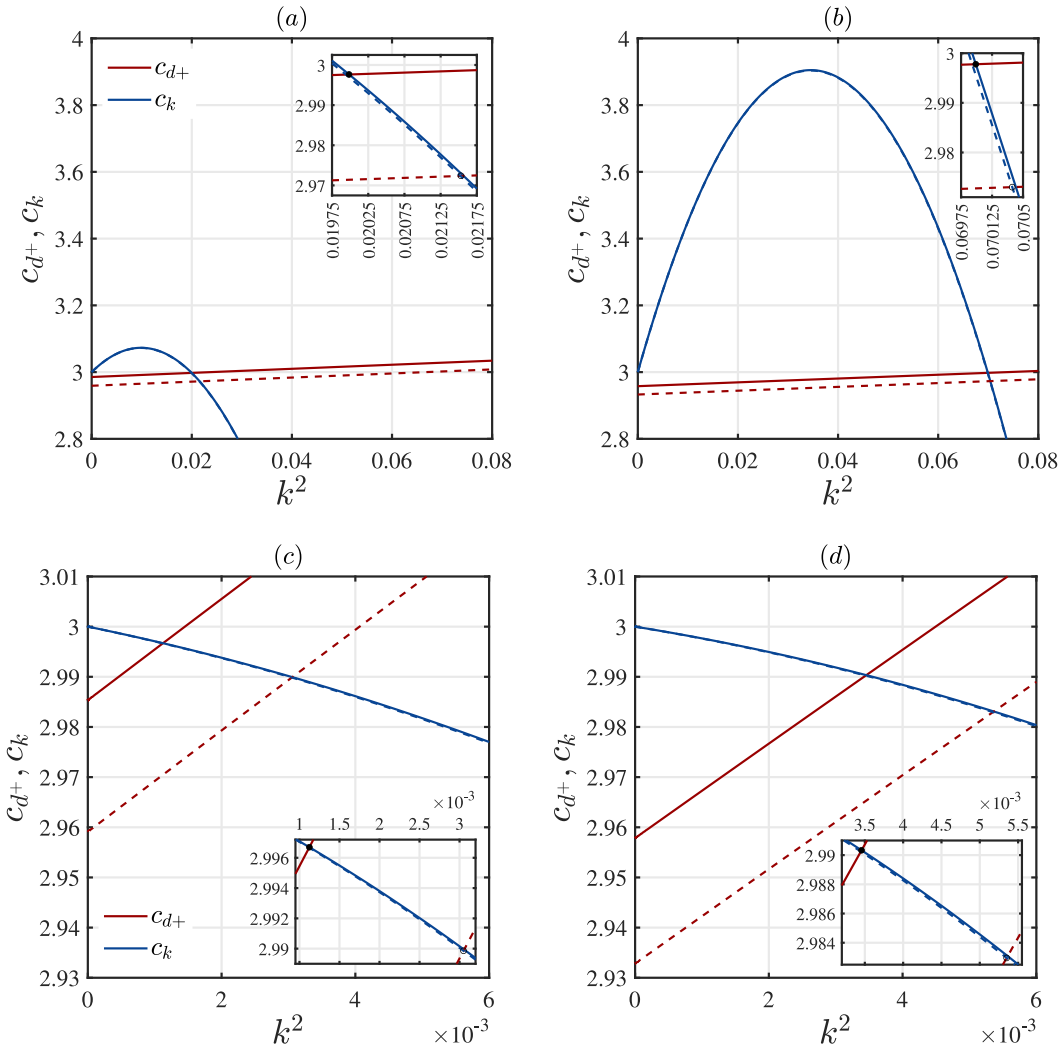

Fig. 9. The variation of dynamic c_{d^+} (in red) and kinematic c_k (in blue) wave speeds as a function of k^2 when the Mach number Ma passes from zero (solid lines) to a value of 0.1 (dashed lines), for different configurations in terms of angle of inclination β and Reynolds critical ratio RCR. (*a–b*): $\beta = 1.5°$. (*c–d*): $\beta = 12°$. Left panels: RCR $= 1.025$. Right panels: RCR $= 1.075$. (For interpretation of the references to colour in this figure legend, the reader is referred to the web version of this article.)

In a similar way, as the leading-order wall shear stress $\tau_w^{(0)} \equiv \partial_y u^{(0)}\big|_{y=0}$ is employed as normalising quantity for the extra wall shear stress profile, we obtain:

$$\Delta\,\tau^{(2)}_{w,\mathrm{rel}} = \frac{\Lambda}{6}\frac{g\,\tilde{h}\cos\beta}{\tilde{a}_0^2}. \tag{45}$$

The same functional form is manifestly shared by (44) and (45). A simple physical interpretation of the ratio therein contained, namely $g\,\tilde{h}\cos\beta/\tilde{a}_0^2$, can be given in the following terms:

$$\Delta\,q^{(2)}_{\mathrm{rel}},\ \Delta\,\tau^{(2)}_{\mathrm{rel}} \propto \frac{\tilde{\rho}\,g\,\tilde{h}\cos\beta}{\tilde{\rho}\,\tilde{a}_0^2} = \frac{\tilde{P}^{\mathrm{eff}}_{\mathrm{h}}}{\tilde{P}_{\mathrm{a}}}. \tag{46}$$

We can notice that (46) accounts for the ratio between the effective component of the hydrostatic pressure $\tilde{P}^{\mathrm{eff}}_{\mathrm{h}}$ exerted along the cross-stream direction by the wavy fluid column of height $\tilde{h}$, as stipulated by Stevin's law, and a reference acoustic pressure $\tilde{P}_{\mathrm{a}}$. As a matter of fact, the whole operating mechanism through which compressibility acts as a destabilising factor for the temporal development of long-wave linear disturbances should be intended as the competition of multiple effects: for decreasing angles of inclination, the gravitational effect is emphasised as $\cos\beta$ increases, but such a trigger for destabilisation is counterbalanced by the decrease of the uniform film thickness $\tilde{h}_N$, which is a function of $\sin\beta$, and so of $\tilde{h}$.

6.2.1. *Compressible lag of flow rate perturbations*

In order to explain the physical mechanism responsible for the compressibility-induced flow destabilisation, we adapt the basic rationale behind the methodology followed by Lavalle et al. (2019) in the context of confined falling liquid films in presence of an active upper phase. We start by recalling that the driving mechanism of Kapitza instability can be traced back to inertia, which is responsible for the time lag between the actual liquid flow rate $q\,(h(x,\,t))$ and its inertialess target value:

$$q^{\star}\,(h(x,\,t)) = \underbrace{\frac{\Lambda\,h^3}{3}}_{q^{\star,\,g}} + \underbrace{\frac{Ma^2\,h^4\,\Lambda^2\cot\beta}{8\,Re}}_{q^{\star,\,Ma}} + O(\varepsilon^2). \tag{47}$$

Here the second-order contribution arising from the flow compressibility has been highlighted individually, without expressly taking its limit as $Re \to 0^+$ owing to its divergent behaviour. Instead, two other Re–independent second-order terms contained within the expression of $q^{(2)}$ and arising in particular from the normal stress continuity condition (10b) at order $O(\varepsilon^2)$ have not been explicitly written in (47) and disregarded for simplicity in subsequent calculations. Such a decomposition therefore appears to be accurate at $O(\varepsilon)$ and it is used only as a means to gain insight at the mechanism at work by estimating the

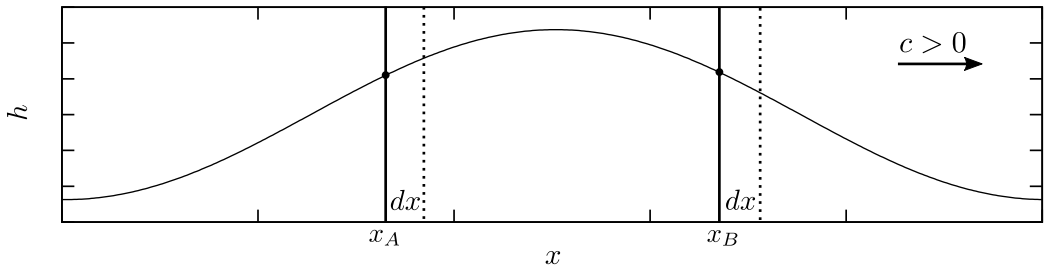

Fig. 10. Description scheme of the inertia-based mechanism of the Kapitza instability: by comparison between two points of abscissa x_A and x_B, located at opposite sides of a wave peak, the local film flow rate $q(x,t)$ is delayed in accommodating itself to film thickness variations induced by the passage of the superficial disturbance of speed c.

relative importance of each individual component in the destabilisation of the weakly-compressible flow.

The destabilising role of inertia on single-peaked Kapitza waves can be explained resorting to the analysis followed by Dietze (2016), who considered the history of two points located along the film free-surface either side of a wave crest. With reference to Fig. 10, at the abscissa x_B upstream of the wave hump, where $\partial_x h < 0$, the film thickness increases in time as the wave covers a distance dx, and so does the flow rate q along the x direction, in accordance with Benney's leading-order asymptotic expansion (B.1c). Conversely, at the abscissa x_A downstream of the wave hump, the film thickness and the flow rate decrease when the wave covers dx. In the presence of inertia, the flow rate cannot adapt instantaneously to such a film thickness variation. As a result, the flow rate in x_A will be too high while it will be too low in x_B. The ensuing discrepancy in flow across the wave peak accounts for its growth. Such a response is more intense as the lag phase of the actual flow rate q behind its target value $q^\star$ increases.

According to (47), the effect of gravity through the cubic dependence of $q^{\star,g}(h)$ on h tends to promote variations in $q^\star$ between the wave hump and the wave trough as an outcome of the change in film thickness h. The non-negative compressible contribution $q^{\star,Ma}(h)$ exacerbates such an effect, increasingly so as the corresponding term in (47) gains relevance. For a pertinent quantification, variables appearing in Eq. (47), *viz.* the wavy film thickness h and the inertialess film flow rate $q^\star$, are linearly perturbed around the aforediscussed (see Section 4.1.1) base state vector $\mathbf{Q}_0$, via superimposition of infinitesimal disturbances of amplitude $\|\hat{\mathbf{Q}}\| \ll \|\mathbf{Q}_0\|$:

$$h(x,t) = h_0 + \hat{h}(x,t) \tag{48a}$$

$$q^\star(h) = q_0 + \hat{q}(h). \tag{48b}$$

By virtue of (48a) it is now possible to discriminate between the magnitude of perturbations $\hat{q}^g$ and $\hat{q}^{Ma}$, which are, respectively, of gravitational and compressible provenance:

$$\hat{q}(\hat{h}) = \underbrace{\Lambda h_0^2 \hat{h}}_{\hat{q}^g} + \underbrace{\frac{Ma^2 h_0^3 \hat{h} \Lambda^2 \cot\beta}{2\,Re}}_{\hat{q}^{Ma}}. \tag{49}$$

The following expression can be obtained for the so-defined compressible-to-total amplitude ratio $\hat{q}^{Ma}/\hat{q}$:

$$\left|\frac{\hat{q}^{Ma}}{\hat{q}}\right| = \frac{3\,Ma^2\cot\beta}{2\,Re + 3\,Ma^2\cot\beta} \overset{(*)}{=} \frac{9\,Ma^2}{5\,\mathrm{RCR} + 9\,Ma^2}, \tag{50}$$

in which use has been made of the equality $\Lambda = 3$ and of the identity $h_0 \equiv 1$, $(*)$ together with the definition of the Reynolds critical ratio RCR (38), coupled with the incompressible evaluation of the critical threshold $\lim_{Ma\to 0^+}$(36), in lieu of the Reynolds number Re. Fig. 11 shows that the ratio expressed by (50) (*a*) increases with the Mach number Ma and (*b*) decreases with the Reynolds critical ratio RCR, which is in accordance with the most prominent role played by compressibility in the film flow destabilisation shown in section Section 5.

7. Conclusions

Liquid films occur over a wide range of length scales and are central to numerous areas of pure and applied sciences (Craster and Matar, 2009). The development of long-wave instabilities along its interface leads to self-excitation of non-trivial dynamics (Sharma and Dandapat, 2006). The motivation behind this study is addressing theoretically how changes in the fluid density fit into this context. For such purpose, we have discussed three guiding questions.

(i) How does compressibility affect the structure of a depth-integral model? We considered a barotropic relation involving the Mach number of the mean flow. Under the assumption of weak compressibility $Ma \ll 1$, the density of the fluid is found to be exponentially stratified against gravity along the crosswise direction. In the final depth-averaged system (25a) this is reflected in two additional terms: one $\propto \cot\beta\, Ma^2/Re$ in the continuity equation, and the other $\propto \cot\beta\, Ma^2/Re^2$ in the momentum conservation equation.

(ii) To what extent does compressibility take part in long-wave instability? According to our linear analysis, a low degree of compressibility boosts the inception of interfacial instability. This effect is most marked in low-inertial regimes. For instance, with reference to Fig. 5*b*, the instability threshold of a water–glycerin film flow having $Re = 2.40$, $\beta = 20°$ and $Ma = 0.1$ as set of distinctive parameters is seen to increase by 35% in terms of the cut-off wavenumber with respect to its incompressible analogue. A higher-order additive correction of the base flow rate, hydrostatic in nature, has been highlighted via (44). As perspective on future research, the derived depth-integrated model (25a) will be also of interest to simulate the non-linear dynamics of weakly-compressible falling liquid films, on condition that proper manipulations are performed for the numerical treatment of capillary terms (Lavalle et al., 2015).

(iii) Which is the underlying physical foundation? Albeit of small magnitude, differences between the compressible and incompressible nature of the long-wave instability can be traced back to a compressible-induced deceleration of dynamic waves (Fig. 9) or, equivalently, to an additional inertia-induced delay (relative to the kinematic waves) of the flow rate in adapting to a time-varying film-thickness (Fig. 11).

CRediT authorship contribution statement

P. Botticini: Methodology, Software, Validation, Formal analysis, Writing – original draft. **G. Lavalle:** Conceptualization, Methodology, Software, Writing – review & editing, Supervision, Funding acquisition. **D. Picchi:** Conceptualization, Writing – review & editing, Supervision. **P. Poesio:** Conceptualization, Writing – review & editing, Supervision.

Declaration of competing interest

The authors declare that they have no known competing financial interests or personal relationships that could have appeared to influence the work reported in this paper.

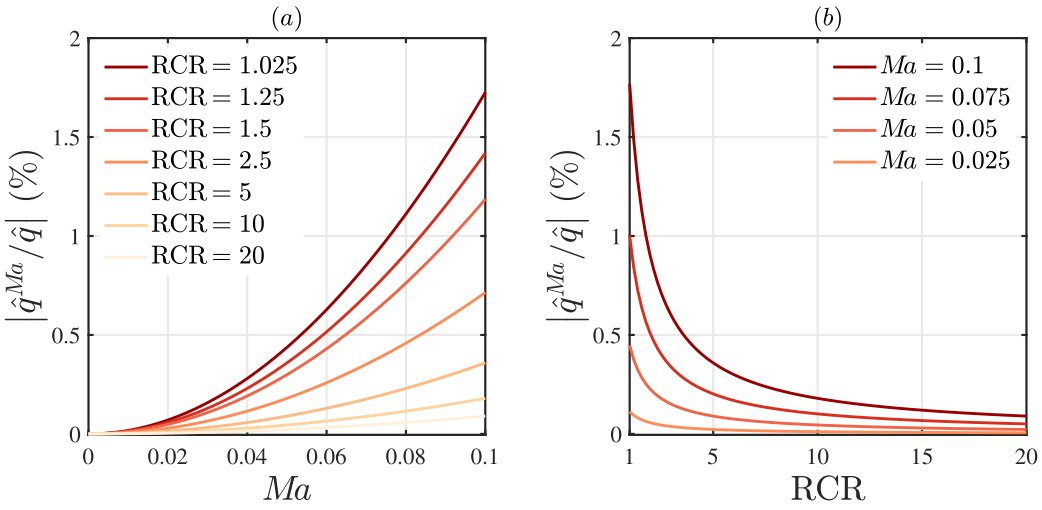

Fig. 11. Percentage contribution of the compressibility-related perturbation $\hat{q}^{Ma}$ to the total inertialess flow rate perturbation $\hat{q}$ (49) (*a*) as a function of the Mach number $Ma = O(\varepsilon)$ for different fixed values of the Reynolds critical ratio RCR (displayed in the legend) and (*b*) *vice versa*.

Data availability

Data will be made available on request.

Acknowledgements

Authors record their sincerest gratitude for financial support allocated during the course of this work by the Auvergne–Rhône–Alpes region as part of the project "MuscaFlow" (21 007147), agreed between Mines Saint–Etienne and Università di Brescia, Italy.

Appendix A. Reduction of the pressure profile

The complete solution of (16) is given by:

$$p(x,y,t;\vartheta) = p_i + \overbrace{\frac{\exp\left[\frac{\cos\beta}{Fr}Ma^2\,(h-y)\right]-1}{Ma^2}}^{\blacklozenge} - \frac{\varepsilon^2}{We}\partial_{xx}h + \\ + \frac{\varepsilon}{Re}\left[\mathcal{W}-\mathcal{W}|_h\overbrace{\exp\left[\frac{\cos\beta}{Fr}Ma^2\,(h-y)\right]}^{\blacklozenge} - \left(\frac{2}{3}-\vartheta\right)\left(\partial_x u+\partial_y v\right)\Big|_h + \right. \\ \left. +2\left(\partial_y v\right)\Big|_h - 2\overbrace{\partial_x h\left(\partial_y u\right)\Big|_h}^{\lozenge}\right] - \mathcal{I}(y,\mathcal{W})\exp\left(-\frac{\cos\beta}{Fr}Ma^2\,y\right), \tag{A.1}$$

where $\mathcal{I}(y,\mathcal{W})$ is the so-defined primitive

$$\mathcal{I}'(y,\mathcal{W}) = \varepsilon\,Ma^2\,\frac{\cos\beta}{Re\,Fr}\,\mathcal{W}\exp\left(\frac{\cos\beta}{Fr}Ma^2\,y\right), \tag{A.2}$$

the prime mark denoting total differentiation with respect to y. By inspection of (A.2), since it is assumed $Re \sim Fr = O(1)$, $\mathcal{I}'$ can be regarded as an $O(\varepsilon\,Ma^2)$ residual contribution, originating from the process of integration by parts in the context of the application of Duhamel's technique. Given that its analytical integration would at least require *a priori* knowledge concerning the explicit expression for the unknown spatial derivatives of the velocity field $\mathbf{v} = (u, v)$ involved within $\mathcal{W}$ as part of the integrand function (A.2), we seek for a low-compressibility restriction of the kind

$$\varepsilon\,Ma^2 \lesssim \varepsilon^3, \tag{A.3}$$

a condition wherein it is legitimate to consistently ignore its respective contribution within the ultimate problem (9a) via (14). Indeed, assignment (A.3) has been formalised in asymptotic terms through the equivalence relation (19), with $\alpha \geq 1$ and $M = O(1) \in \mathbb{R}_0^+$. By recalling expansion (20) with (A.3) in mind, the $O(\varepsilon)$–exponential term denoted as ⧫ can be shortened to the unitary value only. Furthermore, starting from the definition of $\mathcal{W}$ – jointly given with (16) – it is straightforward to verify that

$$-\mathcal{W}|_h - \left(\frac{2}{3}-\vartheta\right)\left(\partial_x u+\partial_y v\right)\Big|_h + 2\left(\partial_y v\right)\Big|_h \equiv -\left(\partial_x u\right)\Big|_h. \tag{A.4}$$

Finally, the boundary condition (10c) highlights the fact that $\left(\partial_y u\right)\Big|_h = O(\varepsilon^2)$, thereby allowing for the removal of ◊, which ultimately contributes as an $O(\varepsilon^3)$ term within (A.1). As a result, (A.1) is consistently tantamount to (17).

Appendix B. Asymptotic expansions

B.1. Leading order $O(\varepsilon^0)$

$$u^{(0)}(h(x,t),y) = -\frac{\Lambda\left(y^2-2\,h\,y\right)}{2} \tag{B.1a}$$

$$v^{(0)}(h(x,t),y) = -\frac{\Lambda\left(\partial_x h\right)\,y^2}{2} \tag{B.1b}$$

$$q^{(0)}(h(x,t)) = \frac{\Lambda\,h^3}{3} \tag{B.1c}$$

The steady-state flat-film solution, corresponding to Nusselt flow (Nusselt, 1916), can be recovered by substituting unity for h in Eqs. (B.1a). This shows that the leading order of Benney's development corresponds to local equilibrium.

B.2. First order $O(\varepsilon^1)$

$$u^{(1)}(h(x,t),y) = \frac{Re\,\varepsilon^2}{We}\,\partial_{xxx}h\left(hy-\frac{y^2}{2}\right) + \frac{Re\cos\beta}{Fr}\,\partial_x h\left(-hy+\frac{y^2}{2}\right) + \\ + Re\,\Lambda^2\partial_x h\left(\frac{hy^4}{24}-\frac{h^4 y}{6}\right) + Re\,\Lambda\,\partial_t h\left(\frac{y^3}{6}-\frac{h^2 y}{2}\right) \tag{B.2a}$$

$$v^{(1)}(h(x,t),y) = \frac{Re\,\varepsilon^2}{We}\left[\partial_{4x}h\left(\frac{y^3}{6}-\frac{hy^2}{2}\right) - \left(\partial_x h\right)\left(\partial_{xxx}h\right)\frac{y^2}{2}\right] + \\ + \frac{Re\cos\beta}{Fr}\left[\partial_{xx}h\left(-\frac{y^3}{6}+\frac{hy^2}{2}\right) + \partial_x^2 h\,\frac{y^2}{2}\right] + \\ + Re\,\Lambda\,y^2\left[\partial_{tx}h\left(-\frac{y^2}{24}+\frac{h^2}{4}\right) + \left(\partial_t h\right)\left(\partial_x h\right)\frac{h}{2}\right] + \\ + Re\,\Lambda^2\left[\partial_{xx}h\left(-\frac{hy^5}{120}+\frac{h^4 y^2}{12}\right) + \partial_x^2 h\left(-\frac{y^5}{120}+\frac{h^3 y^2}{3}\right)\right] \tag{B.2b}$$

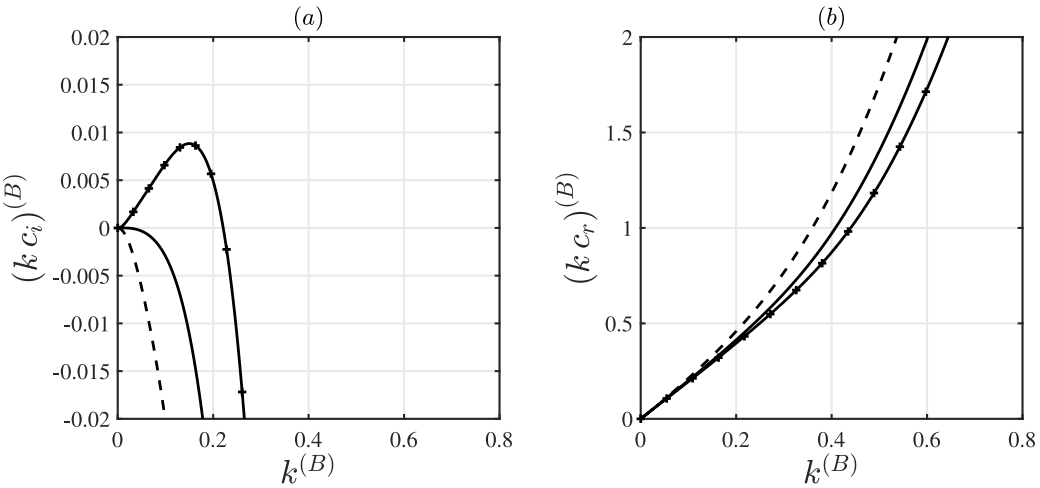

Fig. C.12. Comparison of the dimensionless (*a*) temporal growth rate $k\,c_i(k)$ and (*b*) angular wave frequency $k\,c_r(k)$ between our work and Brevdo et al. (1999) (figure 2 there). Parameter values: $g = 9.81$ m s^{-2}, $\beta = 4.6°$, $\tilde{\rho}_0 = 1130$ kg m^{-3}, $\tilde{\mu}_0 = 5.673\,10^{-3}$ Pa s, $\tilde{\gamma}_0 = 69.0\,10^{-3}$ N m^{-1}. Values of the Reynolds number $Re^{(B)} = (3/2)\,Re$ according to Brevdo's scaling: 10 (dashed line), $Re^{(B)}_{cr} = (5/4)\cot\beta$ (bare solid line), 20 (pluses). Note that $k^{(B)}$, $(k\,c_r)^{(B)}$ and $(k\,c_i)^{(B)}$ are scaled as in Brevdo et al. (1999), *i.e.* using the Nusselt film thickness $\tilde{h}_N$ and the free-surface velocity $(3/2)\,\tilde{U}_N$ as length and velocity scales, respectively, instead of the film mean velocity $\tilde{U}_N$ as done here.

B.3. Second order $O(\varepsilon^2)$

$$
\begin{aligned}
u^{(2)}(h(x,t),y) = {} & \frac{Re^2\,\Lambda\,\varepsilon^2}{We}\,\partial_{xxxx}h\left(\frac{y^6}{360}-\frac{hy^5}{60}+\frac{h^2y^4}{12}-\frac{h^3y^3}{6}+\frac{7h^5y}{30}\right)+\\
& +\frac{Re^2\,\Lambda\,\varepsilon^2}{We}\,\partial_x h\,\partial_{xxx}h\left(\frac{5hy^4}{12}-\frac{3h^2y^3}{2}+\frac{17h^4y}{6}\right)+\\
& +\frac{Re^2\,\Lambda\,\varepsilon^2}{We}\,\partial^2_{xx}h\left(\frac{hy^4}{4}-h^2y^3+2h^4y\right)+\\
& +\frac{Re^2\,\Lambda\,\varepsilon^2}{We}\,\partial^2_{x}h\,\partial_{xx}h\left(\frac{y^4}{2}-2hy^3+4h^3y\right)+\\
& +\frac{Re^2\,\Lambda\,\cos\beta}{Fr}\,\partial^2_{x}h\left(-\frac{hy^4}{6}+\frac{h^2y^3}{2}-\frac{5h^4y}{6}\right)+\\
& +\frac{Re^2\,\Lambda\,\cos\beta}{Fr}\,\partial_{xx}h\left(-\frac{y^6}{360}+\frac{hy^5}{60}-\frac{h^2y^4}{12}+\frac{h^3y^3}{6}-\frac{7h^5y}{30}\right)+\\
& +\Lambda\,\partial_{xx}h\left(-\frac{y^3}{3}-\frac{hy^2}{2}+\frac{5h^2y}{2}\right)+\\
& +Re^2\,\Lambda^3\,\partial_{xx}h\left(-\frac{hy^8}{4480}+\frac{h^2y^7}{560}-\frac{h^3y^6}{180}+\frac{h^4y^5}{120}+\frac{h^5y^4}{72}-\frac{h^6y^3}{18}+\frac{29h^8y}{315}\right)+\\
& +Re^2\,\Lambda^3\,\partial^2_{x}h\left(-\frac{y^8}{4480}+\frac{hy^7}{560}-\frac{7h^2y^6}{720}+\frac{h^3y^5}{30}+\frac{5h^4y^4}{72}-\frac{h^5y^3}{3}+\frac{38h^7y}{63}\right)+\\
& +\Lambda\,\partial^2_{x}h\left(5hy-\frac{y^2}{2}\right)+\frac{M^2\Lambda\,\cos\beta}{Fr}\left(\frac{y^3}{6}-\frac{hy^2}{2}+\frac{h^2y}{2}\right)
\end{aligned}
\tag{B.3}
$$

Appendix C. Validation with Orr–Sommerfeld problem within the incompressible limit

Our second-order model (25a) correctly recovers the expressions for $c^{(0)}$, $c^{(1)}\big|_{Ma\to0^+}$ and $c^{(2)}\big|_{Ma\to0^+}$, which show accordance with the asymptotic expansions of solutions to Orr–Sommerfeld boundary-value problem – reported in Ruyer-Quil and Manneville (1998). However, it is expected that higher-order expressions of $c^{(j)}$ with $j > 2$ are not correctly captured. Specifically, when the incompressible limit of $c^{(3)}$, expressed by $(34d)|_{Ma\to0^+}$, is contrasted with its exact Orr–Sommerfeld (O–S) analogue, we notice that all terms are present, but with different numerical coefficients in front of them in almost every occurrence $\star$. As shown in Table C.2, such discrepancies can be quantified in terms of relative percentage deviation

$$
\frac{\star^{(3)}_{(34d)}\big|_{Ma\to0^+} - \star^{(3)}_{\text{O–S}}}{\star^{(3)}_{\text{O–S}}}\cdot 100\% \quad [\%]\,. \tag{C.1}
$$

Table C.2
Percent errors [%] (expressed to one decimal place) committed by the incompressible evaluation of the present second-order model $(25a)|_{Ma\to0^+}$ in the estimate of polynomial coefficients $\star$ of the $O(k^3)$ incompressible wave celerity $c^{(3)}|_{Ma\to0^+}$, given by $(34d)|_{Ma\to0^+}$ by comparison with the exact ones (Ruyer-Quil and Manneville, 1998; Chang and Demekhin, 2002) provided by the Orr–Sommerfeld theory.

$Re\cot^2\beta$	$Re^2\cot\beta$	$\cot\beta$	Re/We	Re^3	Re
−16.7	21.6	−63.0	0	28.9	7.8

A numerical validation of the present second-order weakly-compressible model within its incompressible limit $(25a)|_{Ma\to0^+}$ can be accomplished by comparing its predictions to data from the literature concerning the long-wave interfacial instability for a liquid falling film flow. Fig. C.12 compares growth rate and angular frequency of linear surface waves with results of Brevdo et al. (1999) for the case of a liquid film falling down an incline within a passive atmosphere. We remark that agreement is achieved between the two sets of data with reference to the immediate proximity to the limit of infinitely long-wave ($k \to 0^+$), as long as the Reynolds number Re is chosen to be compliant with the pertinent assumption $Re = O(1)$ made in Section 3.

References

Alekseenko, S., Nakoryakov, V., Pokusaev, B., 1985. Wave formation on vertical falling liquid films. Int. J. Multiph. Flow 11 (5), 607–627. http://dx.doi.org/10.1016/0301-9322(85)90082-5.

Alekseenko, S., Nakoryakov, V., Pokusaev, B., 1994. Wave Flow of Liquid Films. Begell house.

Almqvist, A., Burtseva, E., Pérez-Ráfols, F., Wall, P., 2019. New insights on lubrication theory for compressible fluids. Int. J. Eng. Sci. 145, 103170. http://dx.doi.org/10.1016/j.ijengsci.2019.103170.

Batchelor, G., 2000. An Introduction to Fluid Dynamics. In: Cambridge Mathematical Library, Cambridge University Press, pp. xviii–615. http://dx.doi.org/10.1017/CBO9780511800955.

Benjamin, T., 1957. Wave formation in laminar flow down an inclined plane. J. Fluid Mech. 2 (6), 554–573. http://dx.doi.org/10.1017/S0022112057000373.

Benney, D., 1966. Long waves on liquid films. J. Math Phys 45 (1–4), 150–155. http://dx.doi.org/10.1002/sapm1966451150.

Bresch, D., Cellier, N., Couderc, F., Gisclon, M., Noble, P., Richard, G.L., Ruyer-Quil, C., Vila, J.P., 2020. Augmented skew–symmetric system for shallow–water system with surface tension allowing large gradient of density. J. Comput. Phys. 419, 109670. http://dx.doi.org/10.1016/j.jcp.2020.109670.

Brevdo, L., Laure, P., Dias, F., Bridges, T.J., 1999. Linear pulse structure and signalling in a film flow on an inclined plane. J. Fluid Mech. 396, 37–71. http://dx.doi.org/10.1017/S0022112099005790.

Cellier, N., Ruyer-Quil, C., 2020. A new family of reduced models for non-isothermal falling films. Int. J. Heat Mass Transfer 154, 119700. http://dx.doi.org/10.1016/j.ijheatmasstransfer.2020.119700.

Chang, H.-C., 1986. Nonlinear waves on liquid film surfaces - I. Flooding in a vertical tube. Chem. Eng. Sci. 41 (10), 2463–2476. http://dx.doi.org/10.1016/0009-2509(86)80032-x.

Chang, H.-C., 1994. Wave evolution on a falling film. Annu. Rev. Fluid Mech. 26 (1), 103–136. http://dx.doi.org/10.1146/annurev.fl.26.010194.000535.

Chang, H.-C., Demekhin, E., 2002. Complex Wave Dynamics on Thin Films. Elsevier.

Colinet, P., Legros, J.C., Velarde, M.G., 2001. Nonlinear Dynamics of Surface-Tension-Driven Instabilities, Vol. 527. Wiley Online Library.

Craster, R.V., Matar, O.K., 2009. Dynamics and stability of thin liquid films. Rev. Modern Phys. 81, 1131–1198. http://dx.doi.org/10.1103/RevModPhys.81.1131.

Dietze, G.F., 2016. On the kapitza instability and the generation of capillary waves. J. Fluid Mech. 789, 368–401. http://dx.doi.org/10.1017/jfm.2015.736.

Frisk, D.P., Davis, E.J., 1972. The enhancement of heat transfer by waves in stratified gas–liquid flow. Int. J. Heat Mass Transfer 15 (8), 1537–1552. http://dx.doi.org/10.1016/0017-9310(72)90009-9.

Gjevik, B., 1970. Occurrence of finite-amplitude surface waves on falling liquid films. Phys. Fluids 13 (8), 1918. http://dx.doi.org/10.1063/1.1693186.

Jeffreys, H., 1926. XVI. On the relation to physics of the notion of convergence of series. Lond. Edinb. Dublin Philos. Mag. J. Sci. 2 (7), 241–244.

Kalliadasis, S., Ruyer-Quil, C., Scheid, B., Velarde, M., 2013. Falling Liquid Films. Springer.

Kapitza, P.L., 1948. Wave flow of thin layers of a viscous fluid: I. Free flow. In: Haar, D.T. (Ed.), Collected Papers of P. L. Kapitza (1965). Zh. Ekper. Teor. Fiz., 18, I. 3–18), Pergamon, pp. 662–679, (Original paper in Russian).

Kapitza, P.L., Kapitza, S.P., 1949. Wave flow of thin fluid layers of liquid. In: Haar, D.T. (Ed.), Collected Papers of P. L. Kapitza (1965). Zh. Ekper. Teor. Fiz., 19: 105–120), Pergamon, pp. 662–679, (Original paper in Russian).

Kelly, R.E., Goussis, D.A., Lin, S.P., Hsu, F.K., 1989. The mechanism for surface wave instability in film flow down an inclined plane. Phys. Fluids A 1 (5), 819–826.

Kinsler, L., Frey, A., Coppens, A., Sanders, J., 2000. Absorption and attenuation of sound. In: Fundamentals of Acoustics. John Wiley & Sons, New York, pp. 210–245.

Lavalle, G., Li, Y., Mergui, S., Grenier, N., Dietze, G.F., 2019. Suppression of the Kapitza instability in confined falling liquid films. J. Fluid Mech. 860, 608–639. http://dx.doi.org/10.1017/jfm.2018.902.

Lavalle, G., Vila, J.-P., Blanchard, G., Laurent, C., Charru, F., 2015. A numerical reduced model for thin liquid films sheared by a gas flow. J. Comput. Phys. 301, 119–140. http://dx.doi.org/10.1016/j.jcp.2015.08.018.

Lavalle, G., Vila, J.-P., Lucquiaud, M., Valluri, P., 2017. Ultraefficient reduced model for countercurrent two-layer flows. Phys. Rev. Fluids 2, 014001. http://dx.doi.org/10.1103/PhysRevFluids.2.014001.

Lin, S., 1974. Finite amplitude side-band stability of a viscous film. J. Fluid Mech. 63 (3), 417–429. http://dx.doi.org/10.1017/s0022112074001704.

Liu, J., Gollub, J., 1994. Solitary wave dynamics of film flows. Phys. Fluids 6 (5), 1702–1712. http://dx.doi.org/10.1063/1.868232.

Lu, H., Ma, X., Huang, K., Fu, L., Azimi, M., 2020. Carbon dioxide transport via pipelines: A systematic review. J. Clean. Prod. 266, 121994. http://dx.doi.org/10.1016/j.jclepro.2020.121994.

Meliga, P., Sipp, D., Chomaz, J.-M., 2010. Effect of compressibility on the global stability of axisymmetric wake flows. J. Fluid Mech. 660, 499–526. http://dx.doi.org/10.1017/S002211201000279X.

Noble, P., Vila, J.-P., 2013. Thin power-law film flow down an inclined plane: Consistent shallow-water models and stability under large-scale perturbations. J. Fluid Mech. 735, 29–60. http://dx.doi.org/10.1017/jfm.2013.454.

Noble, P., Vila, J.-P., 2014. Stability theory for difference approximations of Euler–Korteweg equations and application to thin film flows. SIAM J. Numer. Anal. 52 (6), 2770–2791. http://dx.doi.org/10.1137/130918009.

Nusselt, W., 1916. Die oberflachenkondensation des wasserdampfes. Z. Verein. Deutsch. Ing. 50, 541–546.

Ooshida, T., 1999. Surface equation of falling film flows with moderate Reynolds number and large but finite Weber number. Phys. Fluids 11 (11), 3247–3269. http://dx.doi.org/10.1063/1.870186.

Orr, W.M., 1907. The stability or instability of the steady motions of a perfect liquid and of a viscous liquid. Part II: A viscous liquid. Proc. R. Irish Acad. 27, 69–138. http://dx.doi.org/10.2307/20490591.

Richard, G., 2021. An extension of the Boussinesq-type models to weakly compressible flows. Eur. J. Mech. B/Fluids 89, 217–240. http://dx.doi.org/10.1016/j.euromechflu.2021.05.011.

Richard, G., Gisclon, M., Ruyer-Quil, C., Vila, J., 2019. Optimization of consistent two-equation models for thin film flows. Eur. J. Mech. B/Fluids 76, 7–25. http://dx.doi.org/10.1016/j.euromechflu.2019.01.004.

Richard, G., Ruyer-Quil, C., Vila, J., 2016. A three-equation model for thin films down an inclined plane. J. Fluid Mech. 804, 162–200. http://dx.doi.org/10.1017/jfm.2016.530.

Ruyer-Quil, C., 2012. Instabilities and modeling of falling film flows. fluids mechanics [physics.class-ph]. p. 285, Université Pierre et Marie Curie - Paris VI, URL https://theses.hal.science/tel-00746483.

Ruyer-Quil, C., Manneville, P., 1998. Modeling film flows down inclined planes. Eur. Phys. J. B 6 (2), 277–292. http://dx.doi.org/10.1007/s100510050550.

Ruyer-Quil, C., Manneville, P., 2000. Improved modeling of flows down inclined planes. Eur. Phys. J. B 15 (2), 357–369. http://dx.doi.org/10.1007/s100510051137.

Ruyer-Quil, C., Manneville, P., 2002. Further accuracy and convergence results on the modeling of flows down inclined planes by weighted-residual approximations. Phys. Fluids 14 (1), 170–183. http://dx.doi.org/10.1063/1.1426103.

Ruyer-Quil, C., Treveleyan, P., Giorgiutti-Dauphiné, F., Duprat, C., Kalliadasis, S., 2008. Modelling film flows down a fibre. J. Fluid Mech. 603, 431—462. http://dx.doi.org/10.1017/S0022112008001225.

Samanta, A., 2014. Shear-imposed falling film. J. Fluid Mech. 753, 131–149. http://dx.doi.org/10.1017/jfm.2014.351.

Samanta, A., Ruyer-Quil, C., Goyeau, B., 2011. A falling film down a slippery inclined plane. J. Fluid Mech. 684, 353–383. http://dx.doi.org/10.1017/jfm.2011.304.

Shapiro, A.H., 1953. The Dynamics and Thermodynamics of Compressible Fluid Flow, Vol. 1. John Wiley & Sons, New York.

Sharma, A., Dandapat, B.S., 2006. Wave Dynamics and Stability of Thin Film Flow Systems. Alpha Science Int'l Ltd.

Shkadov, V.Y., 1967. Wave flow regimes of a thin layer of viscous fluid subject to gravity. Izv. Akad. Nauk SSSR Mekh. Zhidk. Gaza 1, 43–51. http://dx.doi.org/10.1007/bf01024797, (translation in 1970 Fluid Dyn. 2, 29–34).

Simmonds, J.G., Mann Jr., J.E., 1998. A First Look at Perturbation Theory. Courier Corporation.

Smith, M.K., 1990. The mechanism for the long-wave instability in thin liquid films. J. Fluid Mech. 217, 469–485.

Sommerfeld, A., 1908. Ein beitrag zur hydrodynamischen erklarung der turbulenten flussigkeisbewegung. Atti Congr. Int. Math. 4th.

Thompson, A.B., Gomes, S.N., Denner, F., Dallaston, M.C., Kalliadasis, S., 2019. Robust low-dimensional modelling of falling liquid films subject to variable wall heating. J. Fluid Mech. 877, 844–881. http://dx.doi.org/10.1017/jfm.2019.580.

Trevelyan, P.M.J., Scheid, B., Ruyer-Quil, C., Kalliadasis, S., 2007. Heated falling films. J. Fluid Mech. 592, 295–334. http://dx.doi.org/10.1017/S0022112007008476.

Van Dael, W., 1968. Thermodynamic properties and the velocity of sound. In: Le Neindre, B., Vodar, B. (Eds.), Experimental Thermodynamics Volume II: Experimental Thermodynamics of Non-Reacting Fluids. Springer US, Boston, MA, pp. 527–577. http://dx.doi.org/10.1007/978-1-4899-6569-1-17.

Van Dyke, M., Rosenblat, S., 1975. Perturbation Method in Fluid Mechanics. The Parabolic Press.

Weinstein, S.J., Ruschak, K.J., 2004. Coating flows. Annu. Rev. Fluid Mech. 36 (1), 29–53. http://dx.doi.org/10.1146/annurev.fluid.36.050802.122049.

Whitham, G., 1974. Linear and Nonlinear Waves. Wiley–Interscience, pp. xvi–636.

Yih, C.-S., 1963. Stability of liquid flow down an inclined plane. Phys. Fluids 6 (3), 321. http://dx.doi.org/10.1063/1.1706737.

Chapter 2

Conclusions

This thesis has addressed the modelling of two-phase thin-film flows through a reduced-order multiscale framework, bridging the gap between first-principles physical descriptions and computationally tractable models. The central focus has been the derivation of low-dimensional formulations that capture essential transport phenomena, including mass, momentum, and heat transfer – while incorporating multiphysics effects (such as capillarity, viscous dissipation, compressibility, and phase interactions).

The work demonstrates that perturbation-based techniques, grounded in multiple-scale analysis, provide a rigorous pathway to reduce complex governing equations into effective macroscopic representations, thereby enabling the identification of the dominant flow parameters. The four papers included in this thesis highlight complementary aspects of thin-film multiphase transport and, collectively, establish the versatility of the reduced-order multiscale framework in describing a broad class of transport phenomena.

Beyond theoretical contributions, the thesis aims to connect detailed physical modelling with application-oriented predictive tools. Practical implications include the design and optimisation of heat exchangers operating in core-annular and Taylor-flow regimes, as well as rheological models for two-phase flow in porous media. Moreover, the methodology lays the foundation for extending reduced-order models to problems involving phase change – such as in-tube boiling and condensation – where transitions between flow regimes are strongly influenced by interphase thermal exchange. Applying the multiscale formalism to such systems represents a natural progression of this research. Specifically, future directions involve:

- extending the framework to the bubble regions close to the spherical caps, where the assumption of scale separation no longer holds and matched asymptotic methods are required to capture the transition between near-film dynamics and far-field flow;
- investigating the axial evolution of the volumetric gas-fraction in internal flows with phase change, enabling a complete description of multiphase transport under dynamic operating conditions and across the different flow patterns;
- developing predictive boiling-curve models that capture the full spectrum of heat-transfer regimes – from single-phase convection to nucleate and film boiling – and quantifying

critical transition points such as the onset of the critical heat flux;
- incorporating richer rheological behaviours in thin-film flows, providing a more realistic representation of pore-scale geometry and transport conditions, and studying the impact of a capillary pressure threshold, e.g., developing bundle models composed of wavy tubes with spatially varying radius.

In summary, this thesis demonstrates that first-principles reduced-order modelling, grounded in multiscale asymptotics and perturbation theory, provides a powerful and flexible tool for understanding and predicting two-phase thin-film flows across a wide range of engineering and scientific applications.

Bibliography

[1] E. Chatzigiannakis, N. Jaensson and J. Vermant, 'Thin liquid films: Where hydrodynamics, capillarity, surface stresses and intermolecular forces meet', *Current Opinion in Colloid & Interface Science*, vol. 53, p. 101 441, 2021, ISSN: 1359-0294. DOI: 10.1016/j.cocis.2021.101441.

[2] R. V. Craster and O. K. Matar, 'Dynamics and stability of thin liquid films', *Rev. Mod. Phys.*, vol. 81, pp. 1131–1198, 3 2009. DOI: 10.1103/RevModPhys.81.1131.

[3] D. C. Venerus and H. C. Öttinger, *A Modern Course in Transport Phenomena*. Cambridge: Cambridge University Press, 2018, p. 538, ISBN: 9781107129207.

[4] A. Quarteroni and G. Rozza, Eds., *Reduced Order Methods for Modeling and Computational Reduction*, ser. MS&A. Cham: Springer, 2014, vol. 9, p. 334, ISBN: 9783319020907. DOI: 10.1007/978-3-319-02090-7.

[5] Y. Kuramoto, *Chemical Oscillations, Waves, and Turbulence*, ser. Springer Series in Synergetics. Berlin, Heidelberg: Springer, 1984, p. 158, ISBN: 9783642696893. DOI: 10.1007/978-3-642-69689-3.

[6] H. Haken, 'A nonlinear theory of laser noise and coherence. i', *Zeitschrift für Physik*, vol. 181, no. 1, pp. 96–124, 1964, ISSN: 0044-3328. DOI: 10.1007/BF01383921.

[7] H. Haken, *The Science of Structure: Synergetics*. Van Nostrand Reinhold, 1984, p. 255, ISBN: 9780442237035.

[8] E. T. Vasily and V. T. Valentina, *Economic Dynamics with Memory: Fractional Calculus Approach*. Berlin, Boston: De Gruyter, 2021, ISBN: 9783110627459. DOI: 10.1515/9783110627459.

[9] H. Haken, *Principles of Brain Functioning: A Synergetic Approach to Brain Activity, Behavior and Cognition*, ser. Springer Series in Synergetics. Berlin, Heidelberg: Springer, 1996, p. 350, ISBN: 9783642795701. DOI: 10.1007/978-3-642-79570-1.

[10] B. Asare, M. Sah and R. Hona, 'Alternative methods of regular and singular perturbation problems', *Applied Mathematics*, vol. 15, pp. 687–708, 2024. DOI: 10.4236/am.2024.1510040.

[11] C. M. Bender and S. A. Orszag, *Advanced Mathematical Methods for Scientists and Engineers I: Asymptotic Methods and Perturbation Theory*, 1st ed. Springer New York, NY, 1999, p. 593, Originally published by McGraw Hill, 1978, ISBN: 9780387989310. DOI: 10.1007/978-1-4757-3069-2.

[12] E. J. Hinch, *Perturbation Methods*, ser. Cambridge Texts in Applied Mathematics. Cambridge University Press, 1991, ISBN: 9780521378970.

[13] M. Van Dyke, *Perturbation Methods in Fluid Mechanics*, ser. Applied Mathematics and Mechanics. New York: Academic Press, 1964, ISBN: 9780127130507.

[14] R. Mauri, *Non-Equilibrium Thermodynamics in Multiphase Flows*, ser. Soft and Biological Matter. Dordrecht: Springer Dordrecht, 2013, p. 270. DOI: 10.1007/978-94-007-5461-4.

[15] K. Pietrzyk, S. Korneev, M. Behandish and I. Battiato, 'Upscaling and automation: Pushing the boundaries of multiscale modeling through symbolic computing', *Transport in Porous Media*, vol. 140, no. 1, pp. 313–349, 2021, ISSN: 1573-1634. DOI: 10.1007/s11242-021-01628-9.

[16] S. Whitaker, *The Method of Volume Averaging*, ser. Theory and Applications of Transport in Porous Media. Dordrecht: Springer Dordrecht, 1999, p. 210, ISBN: 9780792354864. DOI: 10.1007/978-94-017-3389-2.

[17] U. Hornung, *Homogenization and Porous Media*, ser. Interdisciplinary Applied Mathematics. Springer New York, 1997, ISBN: 9780387947860.

[18] I. Babuška, 'Solution of interface problems by homogenization. i', *SIAM Journal on Mathematical Analysis*, vol. 7, no. 5, pp. 603–634, 1976. DOI: 10.1137/0507048.

[19] A. Bensoussan, J.-L. Lions and G. Papanicolaou, *Asymptotic Analysis for Periodic Structures*, ser. Studies in Mathematics and Its Applications. Amsterdam New York Oxford: North-Holland, Elsevier, 1978, vol. 5, p. 700.

[20] E. Sanchez-Palencia, *Non-Homogeneous Media and Vibration Theory*, ser. Lecture Notes in Physics. Berlin, Heidelberg: Springer Berlin, Heidelberg, 1980, vol. 127, p. 400, ISBN: 9783540100003. DOI: 10.1007/3-540-10000-8.

[21] D. Cioranescu and P. Donato, *An Introduction to Homogenization*. Oxford University Press, Nov. 1999, ISBN: 9780198565543. DOI: 10.1093/oso/9780198565543.001.0001.

[22] J. Auriault, C. Boutin and C. Geindreau, *Homogenization of Coupled Phenomena in Heterogenous Media*. Wiley, 2009, p. 476. DOI: 10.1002/9780470612033.

[23] J. Wloka, *Partial Differential Equations*. Cambridge University Press, 1987, ISBN: 9780521277594.

[24] C. J. van Duijn, A. Mikelić, I. S. Pop and C. Rosier, 'Effective dispersion equations for reactive flows with dominant Péclet and Damköhler numbers', in *Advances in Chemical Engineering*, ser. Advances in Chemical Engineering, G. B. Marin, D. West and G. S. Yablonsky, Eds., vol. 34, Academic Press, 2008, pp. 1–45. DOI: 10.1016/S0065-2377(08)00001-X.

[25] B. Ling, A. M. Tartakovsky and I. Battiato, 'Dispersion controlled by permeable surfaces: Surface properties and scaling', *Journal of Fluid Mechanics*, vol. 801, pp. 13–42, Jul. 2016, ISSN: 1469-7645. DOI: 10.1017/jfm.2016.431.

[26] Z. Dai, Z. Guo, D. F. Fletcher and B. S. Haynes, 'Taylor flow heat transfer in microchannels—unification of liquid–liquid and gas–liquid results', *Chemical Engineering Science*, vol. 138, pp. 140–152, Dec. 2015, ISSN: 0009-2509. DOI: 10.1016/j.ces.2015.08.012.

[27] R. K. Shah and A. L. London, *Laminar Flow Forced Convection in Ducts*. Elsevier BV, 1978.

[28] S.-M. Kim, J. Kim and I. Mudawar, 'Flow condensation in parallel microchannels - part 1: Experimental results and assessment of pressure drop correlations', *International Journal of Heat and Mass Transfer*, vol. 55, no. 4, pp. 971–983, 2012, ISSN: 0017-9310. DOI: 10.1016/j.ijheatmasstransfer.2011.10.013.

[29] J. Lee and I. Mudawar, 'Fluid flow and heat transfer characteristics of low temperature two-phase micro-channel heat sinks – part 1: Experimental methods and flow visualization results', *International Journal of Heat and Mass Transfer*, vol. 51, no. 17, pp. 4315–4326, 2008, ISSN: 0017-9310. DOI: 10.1016/j.ijheatmasstransfer.2008.02.012.

[30] S.-M. Kim and I. Mudawar, 'Review of databases and predictive methods for heat transfer in condensing and boiling mini/micro-channel flows', *International Journal of Heat and Mass Transfer*, vol. 77, pp. 627–652, 2014, ISSN: 0017-9310. DOI: 10.1016/j.ijheatmasstransfer.2014.05.036.

[31] M. M. Shah, *Two-Phase Heat Transfer*. Wiley, Feb. 2021, ISBN: 9781119618652. DOI: 10.1002/9781119618652.

[32] W. M. Rohsenow, J. P. Hartnett and Y. I. Cho, *Handbook of Heat Transfer*, ser. McGraw-Hill handbooks. McGraw-Hill Education, 1998, ISBN: 9780070535558.

[33] T. Ding, X. Chen, Z. Li, H. Liu, C. Zhu, T. Zhao, Z. Li, Y. Zhang, J. Yang, H. Zhang and L. Hou, 'A review of flow boiling heat transfer: Theories, new methods and emerging applications', *Renewable and Sustainable Energy Reviews*, vol. 215, p. 115 615, 2025, ISSN: 1364-0321. DOI: 10.1016/j.rser.2025.115615.

[34] V. Talimi, Y. S. Muzychka and S. Kocabiyik, 'A review on numerical studies of slug flow hydrodynamics and heat transfer in microtubes and microchannels', *International Journal of Multiphase Flow*, vol. 39, pp. 88–104, 2012, ISSN: 0301-9322. DOI: 10.1016/j.ijmultiphaseflow.2011.10.005.

[P1] P. Botticini, D. Picchi and P. Poesio, 'Forced convection in two-phase core-annular flows', *Journal of Fluid Mechanics*, vol. 1011, A41, May 2025, ISSN: 1469-7645. DOI: 10.1017/jfm.2025.360.

[P2] P. Botticini, D. Picchi and P. Poesio, *Convective heat transfer around an elongated bubble in the absence of phase change*, submitted to *Physical Review Fluids*, Jan. 2026.

[P3] P. Botticini, D. Picchi, S. Sinha and A. Hansen, *Origin of pressure-flow nonlinearity in two-phase intermittent flow in porous media*, submitted to *Physical Review Fluids*, Oct. 2025. arXiv: 2510.12588 [physics.flu-dyn].

[P4] P. Botticini, G. Lavalle, D. Picchi and P. Poesio, 'Compressibility-induced destabilisation of falling liquid films: An integral approach', *International Journal of Multiphase Flow*, vol. 171, p. 104 667, 2024, ISSN: 0301-9322. DOI: 10.1016/j.ijmultiphaseflow.2023.104667.